Combining Fischer-Tropsch Synthesis (FTS) and Hydrocarbon Reactions in one Reactor

zur Erlangung des akademischen Grades eines
DOKTORS DER INGENIEURWISSENSCHAFTEN (Dr.-Ing.)

der Fakultät für Chemieingenieurwesen und Verfahrenstechnik der
Universität Fridericiana Karlsruhe (TH)

genehmigte
DISSERTATION

von
Ingeniera Química (Universitat de Barcelona) Alba Mena Subiranas
aus Vic in Spanien

Referent: Prof. Dr.-Ing. Georg Schaub
Korreferent: Prof. Dr. Bettina Kraushaar-Czarnetzki
Tag der mündlichen Prüfung: 12.12.2008

En memòria a la Dolors Magret

Als meus pares i al Christian

„Sehet im Studium nie eine Pflicht, sondern die beneidenswerte Gelegenheit, die befreiende Schönheit auf dem Gebiet des Geistes kennen zu lernen zu Eurer eigenen Freude und zugunsten der Gemeinschaft, der Euer späteres Wirken gehört."
Albert Einstein, 1933

Danksagung

Die vorliegende Arbeit entstand im Zeitraum von August 2004 bis Dezember 2007 während meiner Tätigkeit als wissenschaftliche Mitarbeiterin am Engler-Bunte-Institut, Bereich Gas, Erdöl und Kohle der Universität Karlsruhe (TH).

Meinem Doktorvater, Herrn Prof. Dr.-Ing. Georg Schaub, danke ich sehr herzlich für das Vertrauen, das er mir erst während der Diplomarbeit und später während der Promotion entgegen gebracht hat. Seine Hilfe und Anleitung in vielen Gesprächen und Diskussionen, sowie das gute Arbeitsgruppenklima haben maßgeblich zum Gelingen dieser Arbeit beigetragen.

Frau Prof. Dr. Bettina Kraushaar-Czarnetzki möchte ich nicht nur für die Übernahme des Korreferats danken, sondern auch für die Möglichkeit, an ihrem Institut einige der verwendeten Katalysatoren herzustellen. Ein Dank auch an Jens Freiding und Gerrit Waters, die mir dabei sehr geholfen haben.

Herr Prof. Dr. Hans Schulz hatte immer ein offenes Ohr für mich. Durch die anregenden Gespräche und vielen guten Ideen war er mir während der gesamten Zeit eine große Hilfe. Herzlichen Dank dafür.

Prof. Dr.-Ing. Rainer Reimert, Marion Benoit, Sabina Hug, Robert Mussgnug, Gabi Ell, Frank Herter und allen anderen Kollegen des Instituts danke ich für die Hilfe, die Zusammenarbeit und das gute Arbeitsklima.

Nico Fischer, Daniel Kiesel, Soontaree Vongpeng, Silvia Aguado und Dirk Klukowski mit ihren Diplom- und Studienarbeiten waren eine große Hilfe für meine Dissertation. Auch Ardo Adidiwidija, Daniel Schlösser, William Stamato, Michael Bock und Bernhard Seyfang haben mich durch ihre Arbeit unterstützt. Die Zeit mit Euch wird mir immer in guter Erinnerung bleiben.

Besonders wichtig sind mir Martin Rohde und Dominik Unruh, die mir ihr ganzes Fischer-Tropsch Know-how weiter gegeben haben. Zusammen mit Markus Brune und Sebastian Zürcher sind sie mir enge Freunde geworden. Die Zeit mit Euch am Institut und außerhalb machte und macht immer noch sehr viel Spaß.

Mein besonderer Dank gilt meinem Freund Christian, für seine Unterstützung, seine Hilfe und die unendliche Geduld, die mir fehlt.

Les gràcies més especials estan dirigides a la meva família, en especial els meus pares, el meu germà i l'àvia Lola que sempre han estat al meu costat i han recolzat sempre amb entusiasme les meves estades a l'estranger.
Moltíssimes gràcies.

List of contents

1. Introduction and background……………………………………………….. 1

2. Objectives………………………………………………………………….. 3

3. Literature survey…………………………………………………………….. 4

3.1 Synthetic fuels production via Fischer-Tropsch Synthesis...................... 4

3.1.1 Fischer-Tropsch Synthesis... 4

3.1.1.1 Chemical reactions.. 4

3.1.1.2 Catalysts.. 5

3.1.1.3 Mechanism... 6

3.1.1.4 Reactors.. 7

3.1.1.5 Selectivity: Product distribution, chain-growth probability... 9

3.1.1.6 Kinetics………………………………………………………. 11

3.1.2 Product upgrading……………………………………………….... 12

3.2 Zeolites as acid catalysts……………………………………………….. 13

3.2.1 General remarks…………………………………………………. 13

3.2.2 Properties and characterization…………………………………. 14

3.2.2.1 Definitions and terminology……………………………….. 14

3.2.2.2 Characterization…………………………………………… 15

3.2.2.3 Shape selectivity of acid zeolites…………………………. 17

3.2.2.4 Diffusion in zeolites……………………………………….. 18

3.2.3 Modification of zeolites…………………………………………….. 19

3.2.3.1 Ion exchange……………………………………………….. 19

3.2.3.2 Introduction of metals into the pore………………………. 20

3.2.4 Application of zeolites as catalysts in hydrocarbon reactions……. 20

3.2.4.1 Isomerisation……………………………………………….. 20

3.2.4.2 Hydrocracking……………………………………………. 21

3.2.4.3 Oligomerisation…………………………………………….. 21

3.2.5 Isomerisation and hydrocracking reaction mechanisms on bifunctional catalysts…………………………………………….. 22

3.2.6 Reaction kinetics: hydrocracking and isomerisation of n-alkanes.. 24

3.3 Combination of FTS and hydrocarbon reactions………………………. 27

4. Preliminary studies – Potential of combining FT and HC reactions……. 31

4.1 Gas phase composition in FT reactors………………………………….. 31

4.2 Temperature and pressure effect on hydrocarbon reactions…………… 32

5. Procedure and experimental methods……………………………………….. 35

5.1 Outline………………………………………………………………………. 35

5.2 Catalysts……………………………………………………………………. 35

5.2.1 Fischer-Tropsch catalysts……………………………………………….. 35

5.2.2 Bifunctional catalysts……………………………………………………….. 36

5.3 Experimental procedure and methods……………………………………... 40

5.3.1 Experimental set-up………………………………………………………. 40

5.3.2 Execution of the experiments………………………………………… 42

5.3.3 Product analysis……………………………………………………….. 43

5.3.4 Data analysis and definitions………………………………………… 46

5.4 Mathematical reactor model: fixed-bed reactor balance…………………. 49

5.5 Experimental conditions and experimental plan…………………………... 52

6. Experimental results and discussion…………………………………………. 56

6.1 Preliminary experiments with model compounds on bifunctional catalysts…………………………………………………………………… 56

6.1.1 Effect of CO on 1-octene reactions on Pt/ZSM-5………………….. 57

6.1.2 Effect of CO on 1-octene reactions on Pt/Beta…………………….. 59

6.1.3 Effect of CO and H_2 on ethene and propene oligomerisation reactions on Pt/ZSM-5 and Pt/Beta……………………………... 60

6.2 Fischer-Tropsch experiments - Reference……………………………… 63

6.2.1 Co-based catalyst………………………………………………………... 63

6.2.1.1 Kinetic analysis: effect of residence time, temperature and gas composition…………………………………………….. 64

6.2.1.2 Product distribution………………………………………… 65

6.2.2 Fe-based catalyst…………………………………………………………. 68

6.2.2.1 Kinetic analysis: effect of residence time, temperature and gas composition…………………………………………….. 68

6.2.2.2 Product distribution………………………………………… 70

6.2.3 Comparison of catalyst activities………………………………….. 73

6.3 Combination of FT and bifunctional catalysts……………………………... 74

6.3.1 Co-based configurations: dual layer with Pt/ZSM-5 or Pt/Beta, physical mixture with Pt/ZSM-5……………………………………. 74

6.3.2 Fe-based configurations: dual layer with Pt/ZSM-5………………. 80

7. Reaction network model…………………………………………………...... 85

7.1 Assumptions and reaction network………………………………………… 85
7.2 Model formulation and validation of rate equations, example Pt/ZSM-5.. 86
7.2.1 Dual layer……………………………………………………………… 91
7.2.2 Physical mixture……………………………………………………….. 95
7.2.3 Reaction rates of hydroprocessing reactions……………………… 97
8. Conclusions and outlook…………………………………………………….. 100
9. Summary / Zusammenfassung……………………………………………… 103
10. References……………………………………………………………………. 120
11. Notation………………………………………………………………………. 128
12. Appendix……………………………………………………………………….. 134
12.1 Gas chromatography……………………………………………………….. 134
12.1.1 Inorganic compounds…………………………………………………... 134
12.1.2 Organic compounds……………………………………………………. 135
12.2 FID factors for oxygenates compounds…………………………………... 141
12.3 Additional experimental results……………………………………………. 141
12.3.1 Ethene/propene reactions on Pt/ZSM-5…………………………… 141
12.3.2 Ethene/propene reactions on Pt/Beta……………………………… 142
12.3.3 Fischer-Tropsch Synthesis……………………………………………... 142
12.3.4 Combination FT and bifunctional catalysts………………………... 144
12.4 Analysis of Pt/ZSM-5 and Pt/Beta after one month on stream……… 146
12.5 Temperature-programmed desorption (TPD) – Method………………… 148
12.6 Complementary calculations for the plug-flow reactor model…………. 148
12.7 Additional kinetic model results……………………………………………. 153
12.7.1 Dual layer: Co/Al_2O_3 + Pt/ZSM-5... 153
12.7.2 Dual layer: K-promoted Fe + Pt/ZSM-5…………………………… 154
12.7.3 Stoichiometric coefficients……………………………………………... 156
12.8 Estimation of errors…………………………………………………………. 156
12.9 Applications of zeolites as catalysts ……………………………………… 160

1 Introduction and background

World primary energy consumption (PEC) increased by a factor of 1.4 from 1989 to 2006 (BP 2007). The predictions forecast not only an increase of primary-energy consumption but also an increase of gasoline and diesel-fuel consumption. To give an example, the International Energy Agency (IEA) reported an increase of motor gasoline and diesel-fuel demand in China of about 11 and 13 % from year 2004 to 2006, respectively (IEA 2006). The length of time that natural gas and coal reserves would last, if production were to continue at the level 2006, are longer than that of oil (63, 147 and 41 years, respectively, from BP 2007). The increasing fuel demand together with high oil/gas prices, geopolitical uncertainty of oil/gas supply and new regulations for CO_2 emissions are the driving forces for the development of synthetic fuels.

The Fischer-Tropsch synthesis (FTS), which converts synthesis gas to hydrocarbons, offers a way to produce synthetic fuels from various raw materials such as natural gas, coal or biomass (Gas-to-liquids GTL, Coal-to-liquids CTL and, Biomass-to-liquids BTL) (Fig. 1.1). At present, commercial GTL and CTL plants are operating, mainly in Asian Pacific and in African regions by Sasol and Shell. A BTL plant will start operating in 2008 in Freiberg (Germany, in a cooperation between Choren and Shell). More large capacity synfuel plants, mainly in Qatar and China will follow (e.g. Pearl GTL project in Qatar with 140000 bpd, Shell 2007).
Synthesis gas production occurs via oxygen/steam gasification or partial oxidation reactions. In the case of feedstock coal, analogous to biomass, the synthesis gas has to be cleaned of impurities and adjusted to the needs of the subsequent synthesis step (e.g. CO-shift). Fischer-Tropsch synthesis, catalysed most commonly by Co- or Fe-based catalysts, is a polymerisation reaction with CH_2 as monomer, leading to mainly linear alkanes and alkenes hydrocarbons, ranging from methane to high-molecular-weight waxes. The carbon number distribution of FT products ideally follows a statistical model (Anderson-Schulz-Flory, ASF) with a chain-growth probability parameter α. However, the maximum gasoline and diesel yield is limited by approximately 40 wt-% respectively. Gasoline (C_{5-9}) obtained through low temperature FTS has a very low octane number (RON ≤ 43) due to the low-branched hydrocarbons selectivity. Hence, the C_{5-9}-fraction must be upgraded, mainly through isomerisation and reforming processes. Diesel from FTS has a high cetane number (> 70) due to its high n-alkane and low aromatic content. The cetane number is even higher than determined by the specifications (> 51). Viscosity and density values are close to the common specifications (de Klerk 2007, Fröhling 2002).

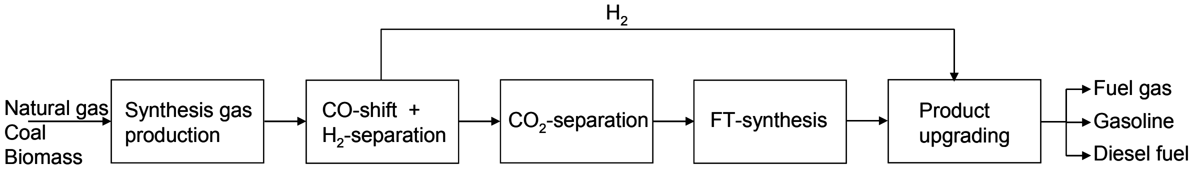

Fig. 1.1: Overall flow scheme for the conversion of organic feedstocks (natural gas, coal and biomass) to liquid hydrocarbon fuels through Fischer-Tropsch synthesis (on the basis of Hamelinck et al. 2004).

If diesel fuel (C_{10-20}) is the desired product, present strategies achieve maximum yields by a two-step approach. During FT synthesis, long-chain hydrocarbons (C_{21+}) are produced which are subsequently hydrocracked and hydroisomerised to produce a high-quality diesel product (i.e. product upgrading). Product upgrading via hydroprocessing reactions (i.e. hydroisomerisation, hydrocracking, and hydrogenation) usually takes place on bifunctional catalysts.

The combination of FT synthesis (on Co- or Fe-based catalysts) with hydrocarbon reactions (on bifunctional catalysts) in one reactor under FT synthesis conditions may be interesting for BTL plants as they will probably have smaller capacities than GTL or CTL plants. This combination could simplify the overall process and improve the yield and quality of the gasoline and diesel fuel produced. GTL or CTL plants usually have higher synthetic-fuels production capacities than BTL plants (1000-150000 bpd, Fleisch et al. 2002). Small plants often do not posses the technical and human resources know-how for the product upgrading, whereas big plants (e.g. GTL-Shell in Malaysia or Qatar, CTL-Sasol in South Africa) can take advantage of the resources available. In addition, high hydrogen partial pressure is required for the hydroprocessing reactions. The hydrogen can be obtained from a separation unit (e.g. Pressure Swing Adsorption, PSA), which is placed behind the CO-shift.

Hamelinck et al. 2004 reported estimates for investment for a BTL plant with 400 MW_{HHV} input and 168 $MW_{FT,HHV}$ FT products (~ 2000 bpd). Remarkable costs for the complex FTS and hydrocarbon reactions include hydrogen separation, the FT reactor and the product upgrading. Thus, effects on the investment of these units can be estimated on the basis of literature data (Hamelinck et al. 2004, Bechtel 1998, Katofsky 1993), (Tab. 1.1). Assuming an ideal situation in which the combination FTS and hydrocarbon reactions produce gasoline and diesel fuel with an acceptable quality and the wax fraction is completely cracked, the investment for the three units mentioned could be lowered by about 30 %. However, the FT reactor must be larger since it must contain the two catalysts (i.e. FT and bifunctional catalysts). Based on this simple estimate, an economic incentive for combining FTS and hydroprocessing reactions in one reactor only exists if the investment is lower than a factor of 2.5 of the state-of-the-art FTS reactor (Tab. 1.1, Fig. 1.1).

Tab. 1.1: Estimates of investment in $M€_{2002}$ for H_2-separation unit, FTS reactor, and product upgrading for a BTL plant with 400 MW_{HHV} input and with 168 $MW_{FT,HHV}$ FT products (~ 125000 t/a). Investment for the state-of-the-art process. On the basis of Hamelinck et al. 2004, Bechtel 1998 and Katofsky 1993 data.

Process	H_2-separation unit ($M€_{2002}$)	FTS-reactor ($M€_{2002}$)	Product upgrading ($M€_{2002}$)	Total ($M€_{2002}$)
State of the art	33	38	27	98

2 Objectives

The present study should help to assess the potential and the limiting factors of the combination of Fischer-Tropsch synthesis and hydrocarbon reactions in a single reactor. In an exploratory study, the hydrocarbon reactions should take place on a hydroprocessing catalyst (e.g. Pt/zeolite as bifunctional catalyst) under FT synthesis conditions (i.e. temperature, presence of CO and water vapour and at relatively low H_2 partial pressure), which are not the optimum for hydroprocessing reactions and bifunctional catalysts.

The study should address the following tasks:

- Experimental work by combining a typical FT catalyst (Co- and Fe-based) with selected examples of bifunctional catalysts (noble metal/zeolite) in a fixed-bed reactor.
- Measure detailed product distributions for Co- and Fe-catalysts (by means of gas chromatography).
- Measure detailed product distributions for different combinations of a FT and a hydroprocessing catalyst (also by means of gas chromatography).
- Study the effects of reaction conditions on hydroprocessing reactions (i.e. temperature, p_{CO}, p_{H2}) and the effects of catalyst-bed configuration (dual-layer and physical-mixture, Fig. 2.1).
- Development of a simplified reaction network for the hydroprocessing reactions taking place on the bifunctional catalyst.
- Mathematical calculations based on the simplified reaction network to understand the kinetic of the hydroprocessing reactions and comparison with the experimental data.

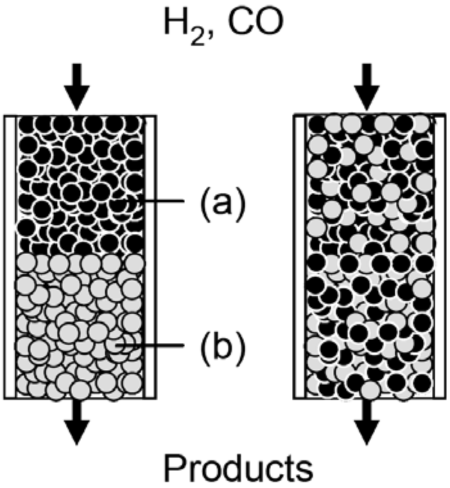

Fig. 2.1: Scheme of possible catalyst-bed configurations for combining FTS and hydrocarbon reactions in a fixed-bed reactor. Left: dual-layer, right: physical-mixture. (a) FT catalyst, (b) bifunctional catalyst.

3 Literature survey

3.1 Synthetic fuels production via Fischer-Tropsch Synthesis

3.1.1 Fischer-Tropsch Synthesis

The transformation of coal-based synthesis gas into liquid fuels was reported for the first time by Franz Fischer and Hans Tropsch in 1923, who used an alkali-promoted Fe catalyst at 10 MPa and 400-450 °C. The main development took place at the Kaiser Wilhelm Institute for Coal Research (presently Max Plank Institute) at Mülheim/Ruhr (Germany) in collaboration with the company Ruhrchemie (Fischer et al. 1923). At that times, strategic arguments for liquid-fuel production from coal exceeded economic aspects. In the period after World War II (~ 1945-1955), the discovery of major oil fields (e.g. Saudi Arabia, Alaska etc.) changed the scenario regarding the lack of coal competitiveness, except for the South African case. In 1955, the Sasol I plant (capacity ~ $700 \cdot 10^3$ t/a) came on stream in South Africa with coal-based synthesis gas. Both fixed-bed and circulating-fluidised-bed FT reactors were used (Dry 1996). In the period 1955-1970, the world energy scene was governed by cheap oil supplies and FTS had a marginal interest in a few research groups. During the 1970s and 1980s, energy programs in the US, Japan and Europe enforced the development of coal-based FT processes due to the oil boycotts by major oil-producing countries (Schulz 1999). In the seventies, Sasol expanded its operations. Sasol II and III came on stream with a total production of $4200 \cdot 10^3$ t/a using only fluidised-beds. In the eighties, Shell developed its SMDS (Shell Middle Distillate Synthesis) process. It has been operating since 1993 in Bintulu (Malaysia) with a Co-based low-temperature FTS with a fixed-bed reactor (14700 bpd). The obtained wax products are then hydrocracked over a bifunctional catalyst to produce the desired middle distillate products (Shell 2007). In 1992 the Mossgas FT complex (South Africa) with fluidised-bed reactors came on stream with synthesis gas produced from offshore natural gas.

In the last few years as a consequence of environmental demands (e.g. CO_2-emission reduction, flaring of associated natural-gas charged with taxes), technological developments and decreasing fossil energy reserves, the interest in FTS has grown. Present areas for FTS implementation include countries around the Arabian Gulf, particularly Qatar with its large natural gas reserves (e.g. Pearl GTL project with Qatar Petroleum and Shell), Nigeria (Sasol Chevron Joint Venture), South Africa (e.g. Sasol complex at Sasolburg), the North Sea in Europe (e.g. Statoil in Norway); and the US state of Alaska (e.g. BP in Nikiski, ANGTL in Prudhoe Bay).

3.1.1.1 Chemical reactions

The hydrogenation of CO under typical FT conditions leads to a broad distribution of products on the basis of carbon number. This type of product distribution has been explained assuming chain-growth polymerisation kinetics that implies a step-by-step insertion of CH_2 monomers into the growing chain:

$$2n\ H_2 + n\ CO \longrightarrow -(CH_2)-_n + n\ H_2O \qquad \Delta_R H^0_{250°C} = -158.5\ \text{kJ/mol}\ (n=1) \qquad (3.1)$$

The main reactions leading to the formation of alkanes, alkenes and alcohols during FTS can be written as follows:

$$(2n+1)\ H_2 + n\ CO \longrightarrow C_nH_{2n+2} + n\ H_2O \qquad (3.2)$$
$$2n\ H_2 + n\ CO \longrightarrow C_nH_{2n} + n\ H_2O \qquad (3.3)$$
$$2n\ H_2 + n\ CO \longrightarrow C_nH_{2n+2}O + (n-1)\ H_2O \qquad (3.4)$$

Water is a primary product of the FT reaction. Water-gas-shift (WGS) activity can be significant for K-promoted Fe catalysts and is negligible over Co or Ru catalysts.

$$CO + H_2O \rightleftarrows CO_2 + H_2 \qquad \Delta_RH^0_{250°C} = -39.5\ \text{kJ/mol} \qquad (3.5)$$

Undesired reactions include the methanation (Eq. 3.6) and the Boudouard reactions (Eq. 3.7):

$$3\ H_2 + CO \longrightarrow CH_4 + H_2O \qquad \Delta_RH^0_{250°C} = -213.0\ \text{kJ/mol} \qquad (3.6)$$
$$2CO \rightleftarrows CO_2 + C \qquad \Delta_RH^0_{250°C} = -175.6\ \text{kJ/mol} \qquad (3.7)$$

Regarding the chemical equilibrium of the reactions involved, it can be concluded that: i) methane, the least-desired product, is thermodynamically favoured over the other hydrocarbons, ii) the formation of alkanes is preferred over alkenes and alcohols, iii) the formation of methanol is very unfavourable, and iv) ethene is the least-favoured alkene at temperatures below 430 °C. Therefore, the synthesis reaction has to be performed under kinetically controlled conditions in order to yield the desired hydrocarbons in significant amounts.

3.1.1.2 Catalysts

The most-active metals for FT synthesis are Co, Fe, Ru and Ni. Co and Ru are preferred for the synthesis of higher hydrocarbons at low temperatures and high pressures. However, despite Ru high catalytic activity, it has not found commercial application because of the high price and limited world reserves for this metal compared to Co or Fe. At elevated pressure, Ni tends to form nickel carbonyl and, with increasing temperature, the selectivity changes to mainly methane (Schulz 1999). Until today, Fe and Co remain the only catalysts for industrial application.
Pichler et al. 1970 compared the active catalysts for FTS in order to identify common properties: i) they are active for hydrogenation reactions, ii) they are capable of metal carbonyl formation, and iii) the FT reaction conditions (T, p) are not far from those where thermodynamics would allow the metals to be converted into metal carbonyls.
Espinoza et al. 1999 concluded that for Co, most active are supported catalysts; while for Fe, most active are precipitated catalysts. The different preparation procedures result in a higher metal area for Fe catalysts as compared to Co catalysts. However, this advantage of precipitated Fe catalysts over supported Co catalysts will tend to decrease and then disappear as conversion, and therefore the water partial pressure, increases.

Co catalysts

For the preparation of Co-based FTS catalysts, the metal precursor is usually impregnated on a porous support (e.g. SiO_2, Al_2O_3), and then activated by means of calcination-reduction treatments to obtain the final metallic active sites. Co/SiO_2 catalysts are easier to reduce than Co/Al_2O_3. The weak interaction of Co with SiO_2 usually leads to low Co dispersions due to metal sintering during the reduction treatments (Corma et al. 2002). The reducibility, final metal dispersion and FT activity of Co catalysts are strongly influenced by: i) nature of the support, ii) cobalt precursor salt used in the impregnation step, iii) presence of promoters (e.g. Zr, Re, Ti, (Schulz 1999)), and iv) activation conditions. In order to avoid less-selective reactions in the centre of a catalyst particle and thereby counteracting pore blockage by high-molecular-weight product molecules, "egg-shell" Co catalysts in which the active metal is located close to the particle surface have been developed by Exxon (Iglesia et al. 1995).

Today, Co catalysts for FT-diesel production from natural gas are designed for maximum wax selectivity and they are mainly used in fixed-bed reactors (e.g. SMDS).

Fe catalysts

An active Fe-based catalyst for FTS is only obtained after reduction with H_2. During the initial period of synthesis, several iron carbide phases and elemental carbon are formed, whereas iron oxides (hematite, α-Fe_2O_3, magnetite, Fe_3O_4, and Fe_xO) are still present in combination with some metallic iron (Schulz 1999, Corma et al. 2002). The contribution of the different phases to the FT activity is still a matter of controversy (Shroff 1995). The formation of carbon and iron carbide species is greatly influenced by the reaction conditions and, in supported catalysts, by the nature of the support (e.g. Al_2O_3, ZrO_2, TiO_2, SiO_2) (Corma et al. 2002). Supports are used in order to provide special attrition resistance (e.g. bubble column reactor, high-pressure conditions, etc.). Bukur et al. 2002 found that Fe supported on SiO_2 shows good attrition resistance and activity compared to the unsupported catalyst.

Generally, Fe-based catalysts have been used in two directions regarding product selectivity: i) production of low alkenes at high reaction temperature in an entrained phase or fluid-bed process (Sasol Synthol process), or ii) production of high-molecular-weight hydrocarbons at low reaction temperature.

Alkali promotion (e.g. K_2O), to attain high activity and stability, decreases iron oxide dispersion and selectivity towards long-chain alkanes (Corma et al. 2002, Schulz 1999). Choi et al. 1996 reported that the addition of K increases the chemisorption ability of CO_2 but decreases that of H_2. Low alkene (C_2-C_4) selectivity increases. These catalysts have a high water-gas-shift activity and appear to be stable when synthesis gas with a high H_2/CO ratio is converted (Jager et al. 1995). Addition of Mn (usually combined with alkali promoters) was found to increase the alkenes (C_3-C_5) selectivity and decrease methane selectivity (Abbott et al. 1986, Kreitman et al. 1987).

3.1.1.3 Mechanism

Various mechanisms have been proposed over the years. All reaction pathways include three different reaction sections: i) generation of the chain initiator, ii) chain growth or propagation, and iii) chain-growth termination or desorption (Claeys et al. 2004). Fischer 1926 proposed the "carbide" mechanism with iron carbides as intermediates. This mechanism was discarded when no carbides phases were discovered with Co and Ru catalysts (Schulz 1999). For the formation of alcohols and other oxygenated products, Storch et al. 1951 proposed the "Enol" mechanism where the hydrogen is added first to the adsorbed CO to form oxymethylene species. Meanwhile, this mechanism appears obsolete (Schulz 1999). Pichler and Schulz 1970 proposed a CO insertion mechanism. The general consensus has been that carbide (=CH_2) species are involved in the chain-growth mechanism with CO insertion accounting for the formation of oxygenates. In the "alkyl" mechanism, CH_3 surface species is regarded as the chain initiator, and CH_2 as the monomer in this reaction scheme (Fig. 3.1). Chain growth is thought to take place by successive incorporation of CH_2 monomers. Product formation takes place by either ß-hydrogen abstraction or hydrogen addition yielding α-alkenes and n-alkanes as primary products (Claeys et al. 2004). This mechanism was developed on the basis of the "carbide" mechanism proposed by Fischer in 1926.

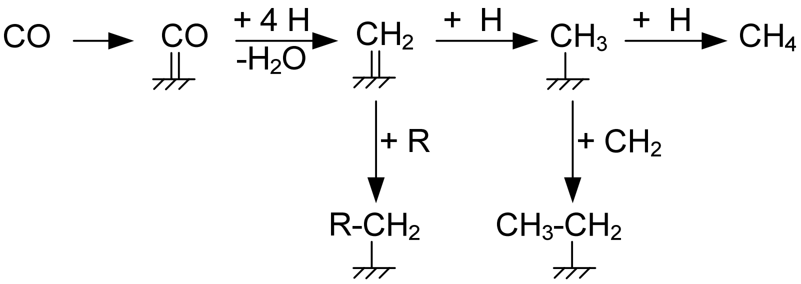

Fig. 3.1: Kinetic scheme of CO consumption reaction during Fischer-Tropsch synthesis according to the "alkyl" mechanism, R = C_nH_{2n+1} with n ≥ 0 (Schulz et al. 1994).

Direct hydrogenation of individual CH_2 units results in CH_4 formation. Metals like Ni and Co, which are more active for hydrogenation, tend to yield larger amounts of methane than the less active Fe catalysts (Dry 1996).
The active surface of a FT catalyst is very heterogeneous, and many active intermediate species are likely to be present. However, it must be kept in mind that the presence of any particular species on the surface does not prove that it is involved in the synthesis; it might simply be an inactive "spectator" (Dry 1996, Schulz 1999).

3.1.1.4 Reactors

At present there are three types of FT reactors in commercial use: i) tubular fixed-bed reactor, ii) slurry phase reactor, iii) fluidised-bed reactor (bubbling or circulating fluidised bed), (Fig. 3.2).

The FT reaction is highly exothermic (about 145 kJ per "CH_2" formed). Rapid removal of this heat and control of temperature is a major consideration in the design of suitable reactors in order to avoid undesirable increased methane production and catalyst damage. The rate of heat transfer from the catalyst particles to the heat exchanger surfaces in the reactor must be high in order to achieve near-isothermal conditions. Heat exchangers are fed with water and produce useful steam.

Tubular fixed bed and slurry reactors are used for the low-temperature FTS (around 220 to 250 °C) to obtain long-chain hydrocarbons with Fe- or Co-based catalysts. Thereby, three phases are present (solid, liquid, gas). When alkenes and/or straight-run fuels are the desired products high-temperature FTS (around 320 to 350 °C) is applied using two-phase fluidised systems (FFB or CFB) with Fe-based catalysts.

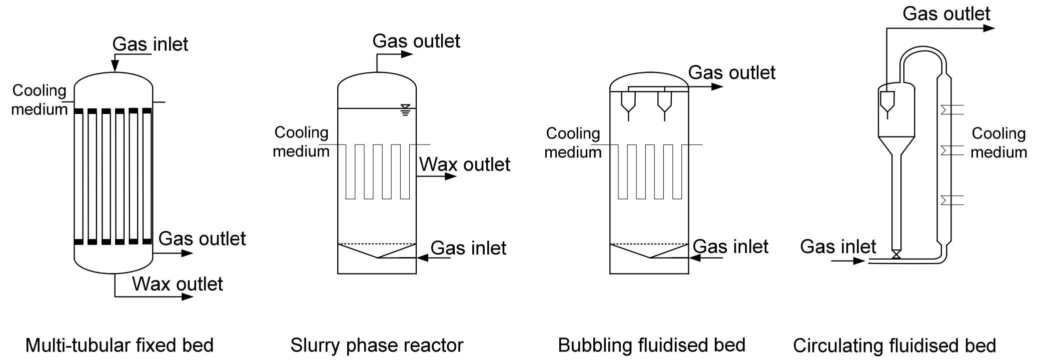

Multi-tubular fixed bed Slurry phase reactor Bubbling fluidised bed Circulating fluidised bed

Fig 3.2: Types of Fischer-Tropsch reactors in commercial use at present (Steynberg et al. 2004, Dry 2002, Steynberg et al. 1999).

In a **tubular fixed-bed reactor** the catalyst (smaller catalyst pellets or extrudates) is packed into narrow tubes (≤ 5 cm id for Fe-based catalysts, Espinoza et al. 1999) which are surrounded on the outside by water. A high flow of synthesis gas is passed through the tubes which results in turbulent flow. These factors ensure rapid heat exchange and minimise temperature rises (axial and radial temperature differences). Multi-tubular fixed-bed reactors are simple to operate and can be used over a wide range of temperature. There is no problem separating liquid products from the catalyst. The main disadvantages of this reactor type are: i) high capital cost, ii) scale-up is mechanically difficult, iii) it is not possible to replace the catalyst during operation, iv) high pressure drop (0.3-0.7 MPa). This last disadvantage is coupled with high gas compression costs (Espinoza et al. 1999, Steynberg et al. 2004).
Sasol has 5 multi-tubular ARGE reactors (3 m diameter with 2050 tubes each, 5 cm id and 12 m long), (Espinoza et al. 1999) in the Sasolburg plant (South Africa), operating with Fe-based catalyst at approximately 2.7 MPa and 230 °C with a capacity of 500 bpd/reactor. Shell also uses multi-tubular reactors (~ 7 m diameter, < 5 cm id) in Bintulu plant (Malaysia), operating with Co-based catalyst and a capacity of 8000 bpd/reactor (Steynberg et al. 2004).

The concept of a **slurry phase reactor** was developed by Kölbel and co-workers (Kölbel et al. 1980) during the fifties and until the late seventies. In that case, the liquid wax product is the medium in which the fine catalyst is suspended. The main difficulty with the commercial application is the separation of the wax product from the catalyst. In 1990 Sasol demonstrated a suitable system to overcome this problem (Espinoza et al. 1999). The rate of the FT reaction is often pore diffusion-limited (even at low temperatures) and hence the smaller the catalyst particle the higher the observed activity. For that reason, the slurry system offers a higher activity per mass of catalyst than the fixed-bed reactor. The slurry phase is well mixed and tends towards isothermal operation. It also offers a better control of product selectivity at high conversion. The pressure drop is about four times lower than of a multi-tubular reactor which results in lower gas-compression costs (Dry 2002). On-line catalyst removal can be done without difficulty. Scale-up of a slurry phase reactor can be done by increasing both diameter and height of the reactor. However, large pilot units are required to successfully design commercial slurry units since the gas hold-up of a three-phase fluidisation system is difficult to predict (Espinoza et al. 1999). However, the cost of a slurry reactor is only 25 % of the multi-tubular reactor (Steynberg et al. 2004). At present, Sasol operates slurry bed reactors with Fe-based catalysts.

Reactors with a capacity of 17000 bpd are currently in the start-up phase in Qatar (Steynberg et al. 2004, SasolChevron 2007).

Two-phase **fluidised-bed reactors** are applied for high-temperature FTS. The circulating fluidised bed (CFB) was developed by Kellogg and applied by Sasol in Sasolburg, Secunda and Mossel Bay (Synthol reactors). Currently the only CFB reactors operating are those at Mossel Bay (Steynberg et al. 2004). The other reactors have been replaced by bubbling fluidised bed reactors with capacities between 11000 and 20000 bpd (SAS, Sasol Advanced Synthol). In the CFB the catalyst is swept up the reaction section by the preheated feed gas. The bulk of any catalyst fines still entrained in the gas is knocked out in the cyclones and returned to the standpipe. To achieve a high conversion rate it is necessary to have a high catalyst loading in the reaction zone. However, the pressure drop over the reaction zone must not exceed the pressure drop over the standpipe, and online catalyst removal and addition of fresh catalyst is necessary (Steynberg et al. 2004). The advantages of the SAS reactor compared to the CFB reactor are: i) about two times higher catalyst/gas ratio in the reaction zone, ii) lower construction costs (about 40 %), iii) better temperature control (more cooling coils can be installed and more space for heat exchange surface due to the larger diameter of the reactor), iv) lower recycle ratio, v) lower gas and catalyst linear velocities (no abrasive problems), vi) about the half of pressure drop across the reactor, and consequently vii) lower compression costs (Steynberg et al. 2004, 1999).

3.1.1.5 Selectivity: Product distribution, chain-growth probability

According to Anderson 1956 the distribution of n-alkanes can be described by the Anderson-Schulz-Flory (ASF) equation:

$$y_{N_c,n} = (1-\alpha)\cdot\alpha^{N_c-1} \tag{3.8}$$

$$y_{N_c,m} = N_C\cdot(1-\alpha)^2\cdot\alpha^{N_c-1} \tag{3.9}$$

The chain-growth probability (α) is assumed as independent of the C-number (N_C) and is defined as the rate of propagation (r_p) divided by the sum of propagation and termination (r_t) rates (Eq. 3.10). With this assumption, the entire hydrocarbon product spectrum can be calculated for α values between zero and one (Fig. 3.3).

$$\alpha = \frac{r_p}{r_p + r_t} \tag{3.10}$$

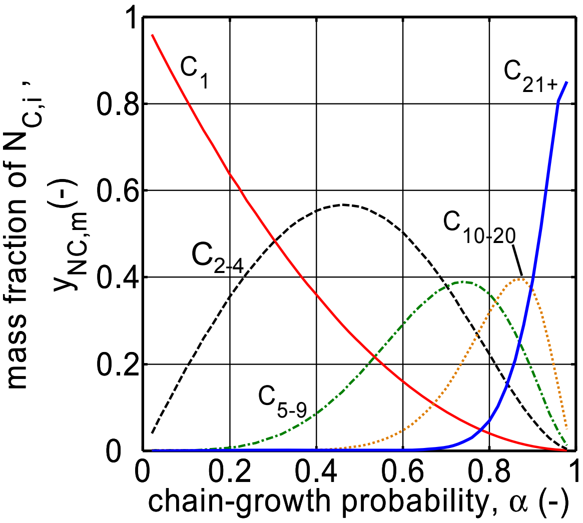

Fig. 3.3: Calculated hydrocarbons selectivity (in weight) with the assumption of ideal ASF distribution (Eq. 3.9).

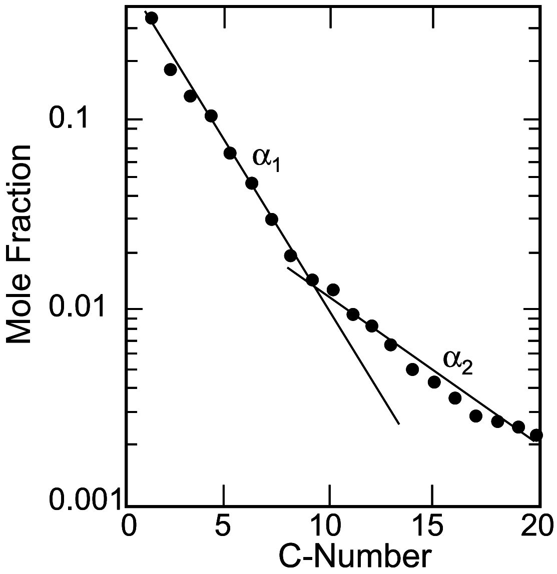

Fig. 3.4: Double-α ASF distribution of volatile products from a precipitated Fe catalyst (Donelly et al. 1989).

The ASF plots are useful to describe FT product selectivities but adjustments are required to predict the lower ethylene selectivity and high methane selectivity that are usually observed (“extra-methane” centres). For reactors containing a liquid phase (i.e. wax under FT conditions), the pores of the catalysts are presumably filled with a vapour/liquid mixture. This could lead to re-adsorption of the primary alkenes and result in further chain growth. Schulz et al. 1988 and Kuipers et al. 1995 agreed that re-adsorption of long-chain hydrocarbons is responsible for the deviation from ideal polymerisation. On the other side, Iglesia et al. 1994 concluded that mass transport effects are the responsible for this deviation.

The product selectivity on alkalised and unalkalised Fe catalysts have been found to follow a modified ASF distribution with two chain-growth probabilities, sometimes referred to as a “double-α” distribution (Donnelly et al. 1989). It suggests that two independent chain-growth mechanisms contribute to the overall distribution (Fig. 3.4).

The FT product distribution can be varied by altering the operating variables such as temperature, feed gas composition, operating pressure, type of reactor used, or type of catalyst (e.g. composition, promoters, reduction), (Tab. 3.1).

Tab. 3.1: Trends of selectivity changes in the FT synthesis. (+) increase with increasing parameter, (-) decrease with increasing parameter, (~) more complex relation, less pronounced dependency (from Schulz 1979).

Parameter	α	Chain branching	alkene / alkane	$S_{alcohol}$	C-deposition	S_{CH4}
T	- - -	+ +	+ , -	(-)	+ +	+ +
P	+ +	- -	~	+ +	~	-
(p_{H2}/p_{CO})	- -	+ +	- -	- -	- -	+ +
Conversion	~	~	- -	- -	+	(+)
Space velocity	~	~	+ +	+ +	~	(-)
Alkali (Fe-catalysts)	+ +	- -	+ +	+	+	-

Higher reaction temperature will increase the rate of desorption, and consequently lower molecular mass hydrocarbons are favoured, especially methane (which is favoured according to chemical equilibrium). As the temperature is increased hydrogenation rates are faster and the ratio alkene/alkane decreases as well as the alcohol selectivity, but the degree of branching increases (also expected from thermodynamics). An increase of hydrogen partial pressure will increase the probability of chain termination by hydrogenation. Short-chain hydrocarbons and methane are favoured and alkene selectivity decreases. An increase of total pressure increases the wax selectivity, but only with Co-based catalysts (Dry 2004).

3.1.1.6 Kinetics

A literature review of Fischer-Tropsch synthesis kinetics with Co- and Fe-based catalysts is given by van der Laan et al. 1999a. They also present a review of water-gas-shift kinetics on Fe-based catalysts.

The FTS kinetics with **Co catalysts** is less complex than with Fe catalysts, due to the absence of the water-gas shift (WGS) reaction. However, only a limited number of kinetic studies are available in the literature. Sarup and Wojciechowski 1989 developed six different rate equations for the formation of the CH_2 monomers, based on both the carbide and the enol/carbide mechanism (see Chapter 3.1.1.3). Yates and Satterfield 1991 were able to reproduce the data of Sarup et al. 1989 with the kinetic equation presented in Table 3.2. It contains only two adjustable parameters: the kinetic parameter (k_{FT}) represents a surface rate constant, and the other parameter represents an adsorption coefficient (a_{FT}).

Tab. 3.2: Kinetic expression and parameter values of FTS reaction on Co-based catalyst in a slurry reactor. Temperature between 220 and 240 °C (from Yates et al. 1991).

$r_{FT} = \frac{k_{FT} \cdot p_{CO} \cdot p_{H_2}}{(1 + a_{FT} \cdot p_{CO})^2}$	(3.11)	$k_{FT,240°C}$	(mol /(s·kg·Pa^2))	$1.26 \cdot 10^{-12}$
		$k_{FT,220°C}$	(mol /(s·kg·Pa^2))	$8.85 \cdot 10^{-13}$
		$E_{A,FT}$	(kJ/mol)	92.7-94.5
		$a_{FT,240°C}$	(Pa^{-1})	$1.16 \cdot 10^{-5}$
		$a_{FT,220°C}$	(Pa^{-1})	$2.23 \cdot 10^{-5}$

Reviews of kinetic equations for **Fe catalysts** are given by Huff and Satterfield 1984 and Zimmerman and Bukur 1990 (Tab. 3.3-3.4). In general, the FT reaction rate of Fe-based catalysts increases with the H_2 partial pressure and decreases with the partial pressure of H_2O. Generally, CO_2 inhibition is not as strong as H_2O inhibition due to the large difference in adsorption coefficients (Dry et al. 1969). However, Ledakowicz et al. 1985 included a CO_2 inhibition term in the FT reaction rate equation. CO_2 inhibition is particularly important over K-promoted iron catalysts (Zimmerman et al. 1990), which can have significant shift activity.

Tab. 3.3: Kinetic expressions of FTS and CO-shift reactions on $Fe/Al_2O_3/Cu/K$ catalysts (Newsome 1980, Zimmerman et al. 1990, Riedel 2003).

FT reaction

$$r_{FT} = k_{FT} \cdot \frac{p_{CO} \cdot p_{H_2}}{(p_{CO} + a_{FT} \cdot p_{H_2O} + b_{FT} \cdot p_{CO_2})} \tag{3.12}$$

CO-shift

$$r_{WGS} = k_{SH} \cdot \frac{p_{H_2} \cdot p_{CO_2} - (p_{CO} \cdot p_{H_2O})/K_{p,CO_2}}{(p_{CO} + a_{SH} \cdot p_{H_2O} + b_{SH} \cdot p_{CO_2})} \tag{3.13}$$

Equilibrium constant of WGS reaction

$$K_{p,CO_2} = 1/K_{p,CO} = \frac{p_{CO} \cdot p_{H_2O}}{p_{CO_2} \cdot p_{H_2}} \tag{3.14}$$

$$K_{p,CO} = \exp\left(\frac{2073}{T} - 2.029\right)$$

Tab. 3.4: Kinetic parameters for the FTS and CO_2/CO-shift reactions on $Fe/Al_2O_3/Cu/K$ catalyst (Zimmerman et al. 1990, Riedel 2003).

	$k_{0,i}$ (mol / (s·kg·Pa))	$E_{A,i}$ (kJ/mol)	a_i -	b_i -
FT reaction				
Zimmerman et al. (1990)	8.58	86	4.8	0.33
Riedel (2003)	1.77	72	33	2.7
CO_2/CO-shift				
Zimmerman et al. (1990)	$9.33 \cdot 10^{6}$	132	21	0
Riedel (2003)	$3.34 \cdot 10^{-2}$	55	65	7.4

3.1.2 Product upgrading

The refining processes required depend on the composition of the FT products. For that reason, product upgrading of high-temperature FTS (Tab. 3.5) and low-temperature FTS (Tab. 3.6) must be distinguished. The main objectives of the further downstream operations are to: i) improve yields and selectivities of the desired fractions, and ii) improve fuel properties to target the fuel specifications.

The main products of **HTFT** are low-boiling-point hydrocarbons. The lighter alkenes (e.g. propene, butene) can be oligomerised over acidic zeolites (see Chapter 3.2.4.3). Nowadays, propylene is being used in the manufacture of polypropylene, acrylonitrile and other petrochemicals. Ethylene is mainly used for polyethylene and PVC production. Heavier linear α-alkenes (C_{12-15}) can be extracted to produce detergent alcohols via hydroformylation. The critical point in the processing of HTFT products is the oxygenates content since it restricts the metallurgy of processing equipment. Hydrodeoxygenation produces water which creates problems in catalysis and complicates the product work-up. In the future, HTFT plants are likely to target bulk commodity chemicals to decrease the reliance on high oil prices (Dancuart et al. 2004).

Tab. 3.5: Refining processes required for high-temperature FT primary products.

Process	Objective
Oligomerisation of light products	Increase the diesel/gasoline ratio Reduce the vapour pressure of gasoline
Aromatisation, isomerisation and alkylation	Improve octane number, density and poor cold properties
Hydrogenation	Remove unwanted oxygenates, alkenes and dienes for better stability during storage

The product spectrum obtained from **LTFT** is wider than from HTFT. It mainly contains linear alkanes and lower contents of alkenes, oxygenates and iso-alkanes. The LTFT primary products are ideally suited for upgrading to middle distillates with naphtha as main co-product. Another option is to process wax for the production of lubricant base oils.

Tab. 3.6: Refining processes required for low-temperature FT primary products.

Process	Objective
Hydrocracking of heavy products (wax)	Reduce boiling range to middle distillate Improve the cold flow properties
Hydrotreating	Saturate alkenes and remove oxygenates for stability during storage
Catalytic dewaxing / hydroisomerisation	Produce lubricant oils

Detailed information (e.g. reaction conditions, catalysts) of the different refining processes mentioned in Table 3.5-3.6 can be found in Tables 12.11-12.13.

3.2 Zeolites as acid catalysts

3.2.1 General remarks

Zeolites are members of a large family of crystalline aluminosilicates. In 1950 Barrer reported that nitrogen and oxygen could be separated using synthetic zeolites that had been treated to provide the necessary shape selectivity to discriminate between the molecular dimension of oxygen and nitrogen (Barrer et al. 1955). In 1959 Union Carbide marketed the “ISOSIV” process for normal/iso-alkane separation, which was the first major bulk separation process to use true molecular sieving selectivity. In the same year, Y zeolite was marketed by Union Carbide as an isomerisation catalyst (Davis et al. 2002). The small pore entrances in zeolites (e.g. 0.4 nm in zeolite A) first attracted commercial interest because they provided the opportunity for selective adsorption based on small differences in the size of gaseous molecules. A significant stage in the development of zeolite catalysts was the disclosure by Mobil Oil in 1972 of the synthesis of the zeolite now universally known as ZSM-5 (i.e. Zeolite Socony Mobil-5). This was the first and most important member of the pentasil family of zeolites.

The natural and early synthetic zeolites were comprised of silica and alumina tetrahedra arranged to provide crystalline microporous materials. It was soon recognized that the use of zeolites was limited by the maximum pore opening allowed by the 12-ring tetrahedral arrangement, and major efforts were made to enlarge this opening. This approach was not successful with the aluminosilicate zeolites, but it worked with other framework elements. For example, Davis synthesized a new aluminophosphate (ALPO) structure with an 18-tetrahedral ring opening (Davis et al. 2002).

In 1992 a completely new family of so-called “mesoporous molecular sieves” was described by Mobil scientists (Kresge et al. 1992). The most important member of this family is MCM-41 (i.e. Mobil catalytic material number 41); the family was later collectively designated M41S. Ideally, MCM-41 pore structure consists of hexagonal arrays of non-intersecting uniform channels of controlled size. They are not strictly “molecular sieves” in the classical sense, but they have a great potential value for the separation of large molecules or microbiological organisms and also as tailor-made catalysts (Davis et al. 2002).

3.2.2 Properties and characterization (based on Schüth et al. 2002)

3.2.2.1 Definitions and terminology

The importance of the pore size has long been recognized in diverse fields such as catalysis. For this reason it seems logical to distinguish between small pores (micropores) and larger pores (macropores). In 1985, as a result of a wide-ranging survey, the International Union of Pure and Applied Chemistry (IUPAC) specified some of the terminology used in the zeolite field (Tab. 3.7).

Tab. 3.7: Terms and definitions (Sing et al. 2002).

Term	Definition
Porous solid	Solid with cavities or channels that are deeper than they are wide
Open pore	Cavity or channel with access to the surface
Closed pore	Cavity not connected to the surface
Cage	Intracrystalline pore with windows allowing no passage of molecules bigger than H_2O
Channel	Intracrystalline pore extending infinitely in one direction allowing passage of molecules
Effective channel width	The smallest free aperture along the dimension of infinite extension
Cavity	Not infinitely extended intracrystalline pore with at least one window bigger than water molecule
Windows	The n-rings of atoms defining the faces of a polyhedral pore
Micropore	Pore of internal width less than 2 nm
Mesopore	Pore of internal width between 2 and 50 nm
Macropore	Pore of internal width greater than 50 nm
Pore size	Pore width. The available inner diameter of a tubular pore or distance between the opposite walls
Pore volume	Volume of pores determined by stated method
Porosity	Ratio of pore volume to overall volume occupied by solid
Total porosity	Ratio of volume of pores and voids to overall volume
Surface area	Extent of total surface area, as determined by stated method
External surface area	Area of surface outside pores
Internal surface area	Area of pore walls

True density	Density of solid, excluding pores and voids
Apparent density	Density of material including pores, as determined by stated method
Tortuosity	The path available for diffusion through a porous bed in relation to the shortest distance across the bed

3.2.2.2 Characterization

Many different experimental methods are now available for the characterization of porous solids. However, IUPAC pointed out that no experimental method is capable of yielding absolute values of surface area, pore size, etc. (Rouquerol et al. 1994). In order to obtain catalytic systems with tailor-made properties a profound knowledge of the relationship between structure and catalytic behaviour is required.

Microscopy

A structural characterization is divided into three steps: The first step is the application of an adequate preparation procedure for the selected analytical method: light microscopy (LM), scanning electron microscopy (SEM) or transmission electron microscopy (TEM). This preparation procedure can cause a change in the porous material. They often contain electrically nonconducting materials. Hence the interaction with the imaging electron beam results in ionization of atoms and charge accumulation on the specimen surface, which leads to a destruction of the specimen structure. This loss of structure induced by the electron beam can be dramatic, especially with zeolite structures with a channel diameter ≤ 1 nm (Terasaki 1999, Tesche 2002). The second step is the interaction of the incident beam with the specimen to produce the spectroscopic or image signal. The third step is the recording procedure. Table 3.8 summarizes the expected structural information depending on the applied analytical method.

Tab. 3.8: Expected structural information depending on the applied analytic method (Tesche 2002). Resolution limited by: [a] wavelength, [b] spot size, [c] lenses. Abbreviations: see Chapter 11. [x]: limited information.

Method	TEM	SEM	STM	AFM	AES	EDX	LM
Information	[a,c]	[b]	[b]	[b]	[b]	[b]	[a]
Structure determination (amorphous or crystalline)	x						
Crystal imperfection or disorder	x						
Entire morphology, surface (topography)	[x]	x	[x]	x			x
Electronic structure			x				
Composition					x	x	
Particle size and distribution	[x]	x		x			

Density

The density of a porous material is an elusive property. True density can be defined as the mass of a powder or particle divided by its volume excluding all pores and voids. Strictly, the true density can be evaluated only by X-ray diffraction measurements on single crystals. It is often assumed that He-pycnometry can also be used to obtain the true density, but this assumption is valid only if there is independent evidence that the He is not absorbed and that the solid does not contain closed pores. With Hg-porosimetry the bulk and skeletal density can be calculated. The bulk density is calculated at the lowest pressure when no pores below a given cut-off size are filled with Hg. Skeletal density is measured when all pores are filled with Hg at the highest pressure point. The derived density values are accurate to about 2-5 % under normal conditions (Giesche 2002).

Pore size distribution and pore volume

Hg-porosimetry analysis gives information about the pore size and pore volume. However, pore size should not be understood as the cavity size, but rather as the largest entrance of throat opening towards that pore. The pore size determined by Hg-porosimetry is always smaller than the corresponding pore size determined from micrographs (Giesche 2002).

Surface area determination

The fundamental role of the specific surface area of adsorbents and catalysts has long been recognized. The BET (Brunauer-Emmett-Teller) method has remained one of the most popular techniques for determining the surface area of a wide range of porous materials (Rouquerol et al. 2002). However the limitations of the BET method must be kept in mind. Another fundamental problem that should be taken into account when adsorption methods are used for surface-area determination is that the adsorbate may be too large to penetrate into narrow micropores (ultramicropores) or there may be a significant number of closed pores. If at least one of these conditions applies, the adsorption will be confined to the accessible area of the total surface. With most porous adsorbents, the extent of the internal surface is much greater than that of the external surface.

Surface acidity

Characterisation of acidity is necessary for understanding reactions catalysed by zeolites. An enormous amount of research has gone into understanding the nature of acidity in solids and developing methods for measuring acidity in solids. Solid acids are composed of discrete active sites and, therefore, the concentration of acid sites must be determined separately from the catalytic activity of those sites.
In the early days of acid-catalysed hydrocarbon cracking, there was a debate on whether Lewis-acid sites or Brønsted-acid sites were most important. It now seems clear that Brønsted acidity is required for this reaction (as well as for others). Brønsted-acid sites arise in zeolites when the negative charge associated with the substitution of framework Si^{4+} with Al^{3+} is formally balanced by a hydrogen ion (Fig. 3.5).

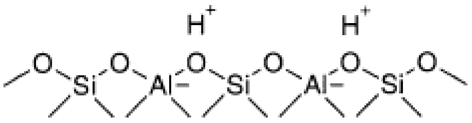

Fig 3.5: Brønsted-acid sites in zeolites (Stöcker 2005).

The Al content is known to play a crucial role in the acidity of zeolites. Since both site density and specific site activity affect the overall activity of a catalyst, one must determine the site concentration before attempting to determine the properties of the sites. Different techniques have been found to be useful for the measurement of Brønsted sites densities: X-Ray diffraction, infrared spectroscopy with adsorbed bases, NMR methods, XPS or adsorbed pyridine, temperature-programmed desorption method (TPD) and alpha test (Bhatia 1990, Gorte 2002). The X-Ray diffraction technique depends on the fact that AlO_4 tetrahedra are slightly larger than SiO_4 tetrahedra, so that the lattice size allows calculating the Al content for some zeolites. The acid site is best viewed as a bridging hydroxyl with partial charge on hydrogen. Real materials contain a large number of hydroxyls: some active and some not. Using IR spectroscopy the hydroxyl groups can be characterised. Protonic sites are directly observable by ^{1}H NMR, however most real solids contain far too many hydroxyls to allow the number of ^{1}H spins to be equated to Brønsted-site densities. Usually other nuclei, such as ^{29}Si or ^{27}Al, are used to determine the framework composition. X-ray photoelectron spectroscopy (XPS) is applied to determine the concentration of pyridinium ions following the adsorption of pyridine on acidic solids. However, this is a very relative surface-sensitive technique and it must be performed in a high vacuum. TPD is a deceptively simple technique for characterising solid acids. Ammonia is the most widely used base for TPD measurements on solid acids but there are some problems in obtaining site densities from ammonia TPD results. The primary difficulty is that ammonia interacts with both Brønsted and Lewis sites and it is not always possible to distinguish which type of site is being counted. One should be suspicious of adsorption energies determined from TPD data in porous solids. Improper analysis of TPD results is likely to be one of the primary reasons for the wide discrepancies in the literature values for adsorption enthalpies on solid acids (Gorte 2002). The alpha test measures the cracking rate of n-hexane under specific conditions since hydrocarbon cracking reaction is one of the most important commercial processes that uses solid acids (Miale et al. 1966). It has been shown that cracking rates increase linearly with Al content, and therefore with site density at least for HZSM-5.

3.2.2.3 Shape selectivity of acid zeolites

In 1960, Weisz and Frilette introduced the expression “shape-selective catalysis” by demonstrating that Ca-A-zeolite dehydrated 1-butanol at 260°C but not iso-butanol. The mechanisms of molecular shape-selectivity catalysis can be described and summarized as follows:

i) *Reactant selectivity*: microporous catalysts act as molecular sieves and exclude bulky molecules from entering the intra-crystalline void-structure while allowing smaller molecules to enter. The critical exclusion limit can be varied over a wide range of different zeolites and related microporous solids (Martens et al. 2001).

ii) *Product selectivity*: refers to discrete diffusivities of the reaction products formed with respect to the microporous pore architecture and crystal size of the catalyst particles. Sterically less-hindered product molecules may easily leave the microporous framework, whereas bulky molecules may stay much longer in the cavities of the zeolites (Stöcker 2005, Bhatia 1990).

iii) *Restricted transition state-type selectivity*: it was first proposed by Csicsery in 1971 and occurs when the spatial configuration around a transition state or a reaction intermediate located in the intra-crystalline volume is such that only certain configurations are possible. For that reason, the formation of reaction intermediates and/or transition states is sterically limited due to the shape and size of the microporous lattice allowing the access of the species formed to interact with the active sites. This type of selectivity is usually connected to the suppression of undesired side reactions like coke formation (Stöcker 2005).

The same geometric principles that govern shape-selectivity of zeolites in their acidic mode remain valid for zeolites containing metal clusters (Sachtler 1993).

3.2.2.4 Diffusion in zeolites

An important characteristic property of zeolite-based catalysts is their well-defined pore size. This has major implications in terms of diffusion phenomena, which was demonstrated by Weisz in 1973 by means of a diffusivity/pore-size diagram (Fig. 3.6). Zeolites, which have pore diameters in the range 0.4-0.9 nm are shown to exhibit diffusivities which occur in a range beyond the regular (bulk) and Knudsen regions. This so-called configurational region of diffusivities is shown to span some ten orders of magnitude in diffusivity depending on: size and nature of the sorbate species, type of molecular sieve and temperature. It is this feature which gives rise to their application in shape-selectivity catalysis and in selective adsorption/separation. Weisz 1973 estimated that a useful reactor for catalytic transformation of hydrocarbons using zeolites must convert about 1 mol/s for every cubic metre invested in catalyst material. Only if the physical mass transport rate exceeds the intrinsic chemical conversion rate are limitations due to restricted mobility of reactants and/or products likely to be absent. Only then, the inner surface area of a porous catalyst can be utilised (Weisz et al. 1954, Satterfield et al. 1963).

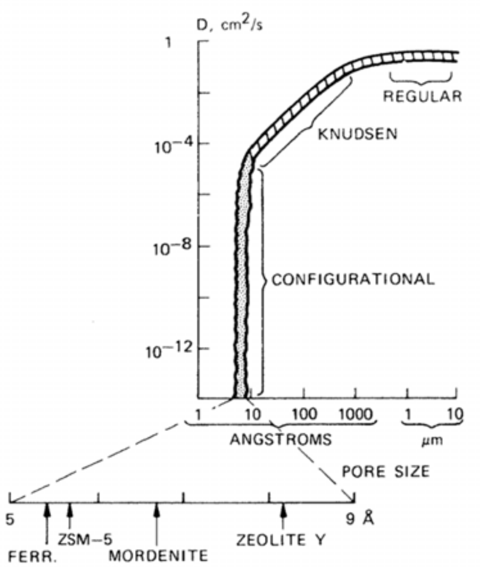

Fig. 3.6: Molecular diffusivity (D) as a function of catalyst pore aperture (Weisz 1973).

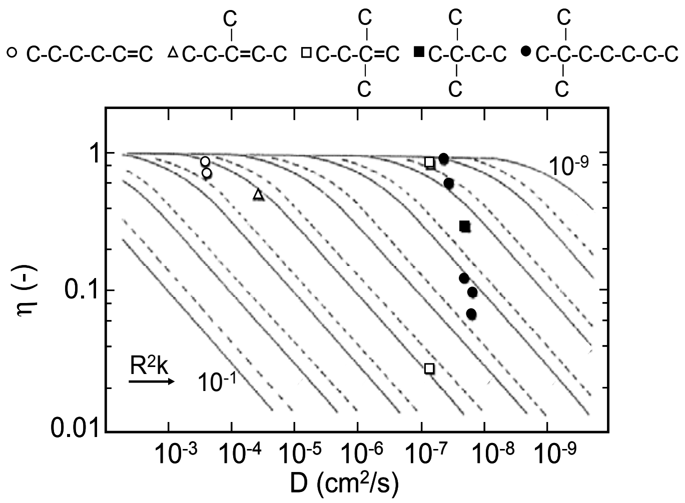

Fig. 3.7: Relation between the effectiveness factor and diffusivity at different values of R^2k (determined with C_{6-9} alkanes and alkenes in ZSM-5 at 538 °C. The dashed curves indicate the half values), (Haag et al. 1981).

If a transport selectivity mechanism is operative in a particular reaction scheme, the size of the molecular sieve crystal may strongly influence the extent of selectivity attained. Many commercial molecular sieves consist of small microporous crystals formed into a meso- or macroporous pellet. Such materials may offer three distinct resistances to mass transfer: i) the micropore resistance of the zeolite crystal (r^2_c/D_c), ii) the resistance related to transport through the outer layer of the zeolite crystal, iii) the meso- or macropore diffusional resistance of the pellet (R_p^2/D_p), (Post 1991). The extent to which diffusional transport limits the rate of conversion of a single reactant can be qualified using the Thiele relation-step. Haag et al. 1981 observed the crystal size effect which helped in the calculation of the effective diffusivities. This was the first known case for determination of molecular diffusivities in a zeolite at steady-state and actual reaction conditions. Diffusivities were found by determination of effectiveness factor (η) of a catalyst and with the knowledge of Thiele modulus (Φ), reaction rate constant (k) and particle size (R):

$$\Phi = R \cdot \left(\frac{k}{D} \right)^{1/2} \tag{3.15}$$

Diffusivity decreases by four orders of magnitude from n-alkanes to dibranched alkanes (Fig. 3.7). While branching has a large effect, the influence of the length of the molecule is small. Alkenes have similar diffusivities to the corresponding alkanes.

3.2.3 Modification of zeolites

The properties of zeolites can be varied considerably by modifying them either during or after the actual synthesis. The types of modifications can be classified into three groups: i) modification of internal pores, ii) modification of the framework through the incorporation or removal of elements (M) other than Si, therefore varying the Si/M ratio, iii) modification of the external surface (Tatsumi 2002).

3.2.3.1 Ion exchange

Cations in zeolites can act as active sites in catalytic reactions. Therefore, ion-exchanged zeolites are quite frequently used as catalysts in industrial processes (Blauwhoff et al. 1999). Protonated zeolites, such as HX, HY or HZSM-5, are highly acidic catalysts due to their ability to easily release protons that are located in the zeolite pores as charge-compensation cations (Tatsumi 2002). Ion exchange is usually carried out in aqueous solutions. When the zeolite crystals are immersed in an aqueous electrolyte, ion exchange between the zeolite (solid phase) and the solution proceeds. In general, zeolite synthesis yields the form neutralised by Na ions. The template-removal step is followed by removal of Na by the ion-exchange method. The most effective and gentle method for converting the Na form into the hydrogen form is exchanging the cation by ammonium from an aqueous solution of ammonium salt. Subsequently, thermal treatment of the ammonium-exchanged zeolites results in the liberation of NH_3 and the formation of the proton (acidic) form of the zeolites (Z), (Eq. 3.16).

$$NH_4^+Z \rightarrow H^+Z + NH_3 \uparrow \tag{3.16}$$

3.2.3.2 Introduction of metals into the pore

Bifunctional (metallic and acid functions) catalysts are applied in a variety of oil refining and petrochemical processes. Zeolite-supported noble metal catalysts are conveniently prepared by ion exchange using an aqueous solution of a cationic metal complex (Sachtler 1993). For platinum and palladium $[Pt(NH_3)_4]^{2+}$ and $[Pd(NH_3)_4]^{2+}$ are used respectively. The ion-exchange product is then reduced in a stream of hydrogen to produce small metal particles inside the zeolite pores ideally. This reduction is accompanied by formation of the Brønsted acid sites:

$$[M\,(NH_3)_4]^{2+}Z + H_2 \rightarrow M + 4\,NH_3 + (H^+)_2Z \qquad (M = Pt \text{ or } Pd) \qquad (3.17)$$

Impregnation is an alternative to the ion-exchange method for the introduction of other metal elements. It must be kept in mind that ion exchange could occur using the impregnation technique. In that case, not only the cation that was originally present and replaced with the cation of the added salt but also the counter anion might remain inside the pore under the conditions where salt imbibition can occur (Tatsumi 2002). For this reason it is favourable to employ nitrates or salts of organic acids such as acetates. These anions are easily decomposed by heating (no residual poisonous elements).

3.2.4 Application of zeolites as catalysts in hydrocarbon reactions

The world market of zeolites is still in a period of strong development. Currently about 1.6 million t/a are used, of which about 1.3 million t/a refers to synthetic zeolites and about 0.3 million t/a to natural zeolites. The latter are mainly applied as adsorbent and ion-exchangers (Marcilly 2001). Concerning the application of synthetic zeolites, 1.05 million t/a are used as detergent builders, 0.15 million t/a on catalysis and 0.1 million t/a on adsorption (Stöcker 2005).

The following chapters focus on the application of zeolites as catalysts for the relevant hydrocarbon reaction in this study. Tables 12.11-12.13 summarise other applications of zeolites as catalysts.

3.2.4.1 Isomerisation

In principle, there are two types of catalysts for skeletal isomerisation of alkane via carbenium ions as intermediates (see Chapter 3.2.5): monofunctional acidic catalysts (e.g. $HCl/AlCl_3$), and bifunctional catalysts that combine the acidic function with the hydrogenation-dehydrogenation function of a metal.

Monofunctional catalysts suffer from the disadvantage that chain termination reactions give rise to catalyst deactivation. For economic and ecological reasons most of the processes that used this type of catalyst are now using bifunctional catalysts. The main advantage of bifunctional catalysts is that stable operation is possible under sufficiently high hydrogen pressure. The hydrogen pressure will affect the steady-state concentration of carbenium ions by the equilibrium reaction so that the rate of isomerisation will be reduced:

$$R^+ + H_2 \rightleftarrows RH + H^+ \qquad (3.18)$$

However, the effect of hydrogen pressure on the chain termination reactions is much stronger. With noble metal present on the catalyst and under hydrogen pressure, the selectivity of isomerisation is improved since there are fewer disproportionation products (Sie 1997).

Crystalline silica-aluminas such as zeolites are used in combination with a noble metal. In particular the H-form of Y, Mordenite or Beta zeolite are strongly acidic components. The latter two are among the most acidic, and the activity may be further enhanced by partial dealumination.

The main isomerisation processes that apply zeolites as catalysts are: i) isomerisation of C_5 and C_6 for octane enhancement, ii) combining C_5 and C_6 alkane isomerisation with physical separation, iii) isomerisation of long-chain alkanes, iv) conversion of n-C_4 to iso-C_4, and v) n-alkenes isomerisation (see Tab. 12.11).

3.2.4.2 Hydrocracking

Hydrocracking catalysts are bifunctional. An obvious design parameter is the relative importance of de/hydrogenation and the cracking (acidic) functions. The combination of operating temperature and pressure is critical in the hydrocracking process because these parameters significantly influence catalyst activity and stability, and product quality. The presence of H_2S has a very deleterious effect on the hydrogenation activity of noble-metal-based catalysts, such as Pd (Maxwell et al. 1997).

When the de/hydrogenation function dominates the acidic function or they are in close proximity, so-called ideal hydrocracking conditions exist whereby consecutive reactions (after isomerisation and primary cracking) play a subordinate role. Non-ideal conditions occur when the rate of de/hydrogenation is less than that of cracking. In this case, secondary isomerisation is possible and higher iso/n-alkane ratio than in the ideal case will be observed.

Hydrocracking catalytic activity is expected to increase with the rate of formation of alkenes (see Chapter 3.2.5). On the one hand, hydrogen pressure suppresses the dehydrogenation reactions (negative order in hydrogen for the rate of n-alkane hydrocracking, see Chapter 3.2.6), (Maxwell et al. 1997). On the other hand, catalyst performance increases with increasing hydrogen partial pressure. The reason for this difference is due to the relatively high levels of coke precursors (e.g. in oil). Under practical operation conditions the primary role of the de/hydrogenation function is to hydrogenate the coke precursors. Zeolites, with molecular-sized pore systems, tend to be significantly less prone to coke formation. This can be attributed to shape-selective coke suppression (see Chapter 3.2.2.3). To date, almost all commercial zeolitic hydrocracking catalysts have been based on the Y-zeolite structure which has large pores, and especially ultrastable Y-zeolite for thermal and hydrothermal stability. A reduction of isomerisation/cracking ratio can be observed by decreasing zeolite pore size (diffusional limitations). Alternative zeolitic materials (e.g. Omega, Beta) have been studied but they have not yet led to commercial application (Stöcker 2005). More details about hydrocracking process conditions can be found in Table 12.12.

3.2.4.3 Oligomerisation

Oligomerisation is an acid-catalysed reaction which involves the conversion of low-molecular-weight alkenes (e.g. propene, butene) to products which represent essentially dimers, trimers and tetramers. At low temperatures, oligomerisation is favoured thermodynamically but molecular weight growth is kinetically limited. Oligomers can undergo further reactions such as cracking, double-bond or skeletal isomerisation and aromatization which lead to a continuous distribution of components over carbon numbers in the product spectrum. As temperature is increased all reaction rates increase with cracking eventually dominating kinetically, resulting in a thermodynamic limitation to molecular weight growth (Quann et al. 1991, O´Connor 1997).

Zeolites are the most important acid catalysts for oligomerisation and in particular the protonated form of ZSM-5 zeolite. The higher-carbon-number products are dominated by the presence of single methyl branches. This phenomenon is due to the so-called shape-selectivity property of ZSM-5 (see Chapter 3.2.2.3). The pore size of the zeolite prevents the formation of bulky intermediate or transition state products. Hence, typical bulky coke precursors do not readily form, thus increasing the lifetime of the catalyst. Other zeolites (e.g. Y, Mordenite) or medium pore molecular sieves (e.g. SAPO-11, -31, -34) have been reported to be alkene oligomerisation catalysts but none of them had lifetimes or selectivities that were in any way comparable to those of ZSM-5 (O´Connor 1997).

Industrial applications of ZSM-5 for alkene oligomerisation are the MOGD (Mobile Olefin to Gasoline and Distillate) and COD (Conversion of low-molecular-weight olefins to distillate). Both of them produce, according to the operation mode, synthetic diesel fuel or gasoline. More information about these two industrial processes can be found in Table 12.13 and also in Tabak et al. 1986, Quann et al. 1991, O´Connor 1997, and Knottenbelt 2002.

3.2.5 Isomerisation and hydrocracking reaction mechanisms on bifunctional catalysts

Zeolites have been used as catalysts for the major classes of reactions, such as Brønsted acid, metal and bifunctional catalysis. This chapter is only focused on the hydrocracking and/or isomerisation reaction mechanisms of hydrocarbons (n-alkane as main product of the FTS) occurring on bifunctional catalysts.

The conversion of hydrocarbons involves the formation of carbocations as reaction intermediates. According to the classical bifunctional reaction scheme (Fig. 3.8), the metal dehydrogenates the alkane feed molecules into alkenes. The alkenes are protonated over the Brønsted-acid sites into alkylcarbenium ions. These cations undergo isomerisation and scission reactions, after which they desorb from the acid sites under the form of alkenes. Finally, saturated products are recovered after hydrogenation on the metal phase. Consequently, it gives rise to only primary cracking of isomerised hydrocarbons on the Brønsted-acid sites. Aluminosilicates zeolites containing Pt or Pd generally work according to the classical bifunctional mechanism (especially at elevated conversion and hydrogen partial pressure). The presence of methane and ethane in the reaction products is evidence for the additional occurrence of metal catalysed cracking (hydrogenolysis). During hydrocracking reactions, the carbenium ion can suffer ß-scission to give an alkene and a smaller carbenium ion, or isomerise into a more stable carbenium ion until a configuration suitable for ß-scission is attained. The isomerised carbenium ion can, again, suffer ß-scission or desorb from the acid site as a branched alkene, while restoring the proton to the catalyst (Fig. 3.8).

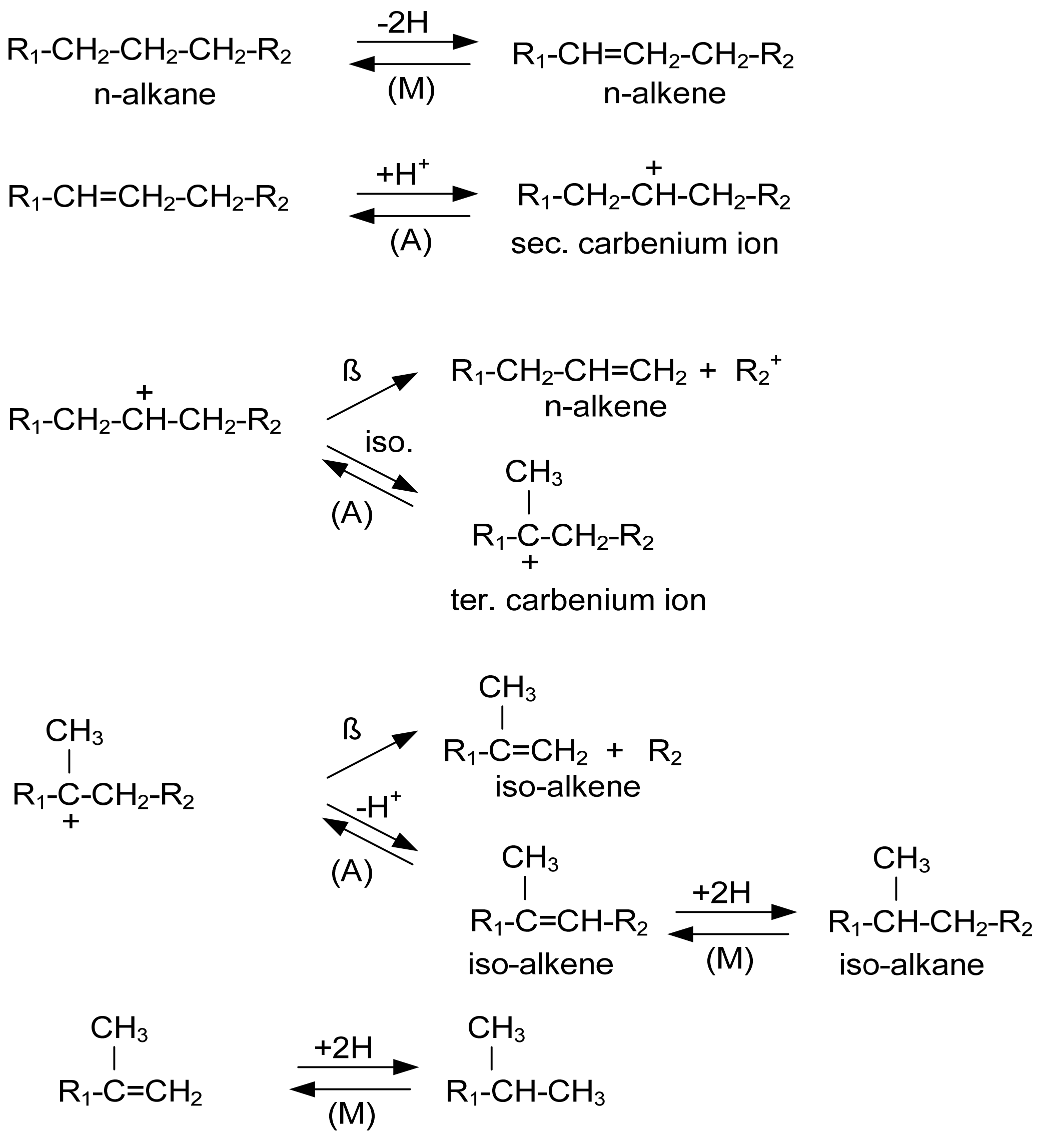
R_1-CH_2-CH_2-CH_2-R_2
n-alkane
-2H
(M)
R_1-CH=CH_2-CH_2-R_2
n-alkene
+H$^+$
(A)
R_1-CH_2-$\overset{+}{C}$H-CH_2-R_2
sec. carbenium ion
ß
R_1-CH_2-CH=CH_2 + R_2^+
n-alkene
iso.
(A)
ter. carbenium ion
R_1-C=CH_2 + R_2
iso-alkene
-H$^+$
R_1-C=CH-R_2
iso-alkene
+2H
(M)
R_1-CH-CH_2-R_2
iso-alkane
R_1-C=CH_2
R_1-CH-CH_3
CH_3

Fig. 3.8: Typical reaction path in hydrocracking of n-alkane. ß: beta scission, A: acid site, M: metal site (from Scherzer et al. 1996), based on earlier mechanistic studies.

The rearrangement of secondary alkylcarbenium ions may lead to another secondary carbenium ion through an alkyl shift (type A isomerisation), or it may lead to a tertiary alkylcarbenium ion (branching) via a protonated cyclopropane (PCP) intermediary (type B isomerisation), (Fig. 3.9). The rate of type A isomerisation is usually higher than that of type B.

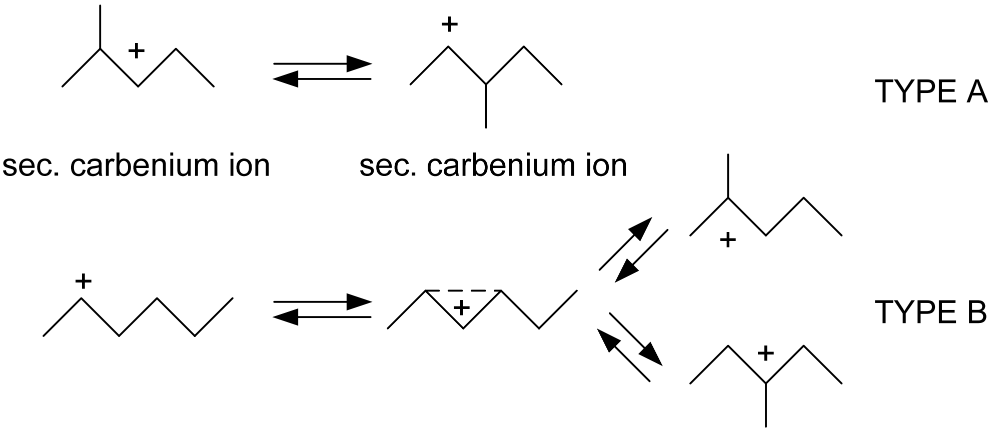

Fig. 3.9: Skeletal isomerisation mechanisms (from Scherzer et al. 1996, based on Jacobs et al. 1991).

ß-scission can lead to the formation of tertiary and secondary carbenium ions, but no primary carbenium ions are formed. Several ß-scission mechanisms have been suggested for the cracking of branched secondary and tertiary carbenium ions (Fig. 3.10). Type A ß-scission, which converts a tertiary carbenium ion to another tertiary carbenium ion, has the highest reaction rate and is the most likely to occur. The reaction rates decrease from type A to type D ß-scissions. One should note that each type of reaction requires a minimum number of carbon atoms (n) in the molecule and a certain type of branching in order to take place (Weitkamp et al. 1983, Jacobs et al. 1991, Scherzer et al. 1996).

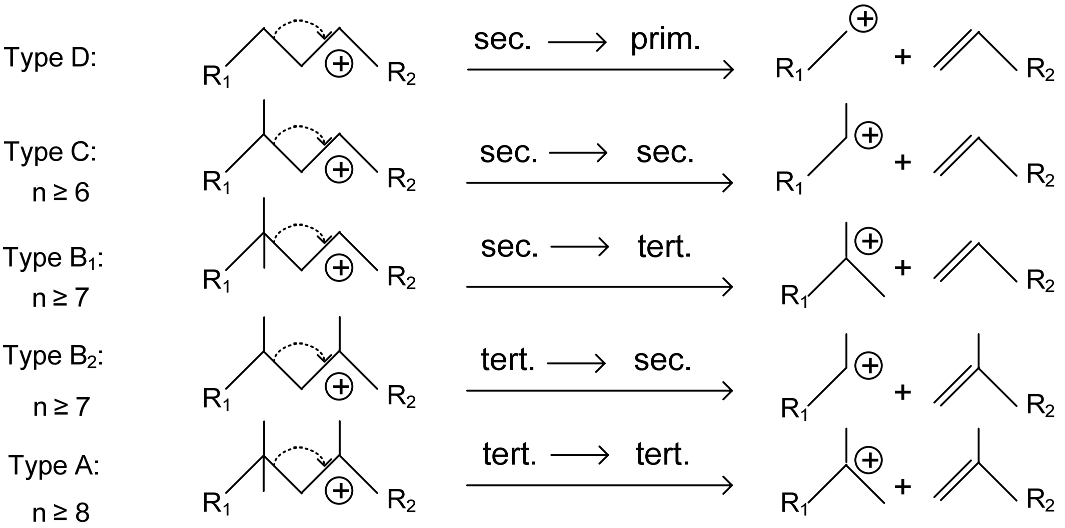

Fig. 3.10: Modes of ß-scission of alkylcarbenium ions (from Weitkamp et al. 1983).

3.2.6 Reaction kinetics: hydrocracking and isomerisation of n-alkanes

Steijns et al. 1981 and Froment 1987 performed experiments with n-C_8, n-C_{10}, n-C_{12} as model hydrocarbons on ultrastable Y zeolite impregnated with 0.5 wt-% of Pt in a Berty reactor at T = 130-250 °C and p = 0.5-10 MPa. They varied the partial pressure of n-alkane and hydrogen and paid special attention to the relation between the distribution of feed isomers and cracked products for the development of the reaction network and reaction kinetics. The catalyst was 700 h on stream and no deactivation was observed, even at low hydrogen partial pressure (0.1 MPa). The cracked products obtained followed the “ideal behaviour” (symmetrical product distribution). Consequently no secondary cracking reactions took place (methane and ethane were virtually absent), (see Chapter 3.2.5).

It was found that isomerisation conversion is a unique function of the total conversion over a wide range of experimental conditions. The isomerisation selectivity is close to 100 % at low conversion levels. This indicates that hydrocracking is preceded by hydroisomerisation. Dibranched, respectively multibranched structures, are formed in consecutives reactions from the monobranched isomers of the feed. However, monobranched were found to be predominant, even higher than thermodynamic equilibrium would predict, which indicates that these species are the predominant products of the cleavage reactions (Steijns et al. 1981a). Even more, isomerisation has to be considered as being reversible (demonstrated by Weitkamp et al. 1978), whereas cracking is an irreversible reaction (Scherzer et al. 1996).

The experiments mentioned above demonstrated that even with simple feedstocks the reaction scheme is complex. Therefore, simplifications which involve the lumping of reaction steps and products are required. These simplifications should reduce the number of reactions and, therefore, the number of parameters by lumping components. Steijns et al. 1981b proposed the followed simplified reaction network for hydrocracking and isomerisation of n-alkane on bifunctional catalysts:

$$\text{n-alkane} \rightleftarrows \text{monobranched} \rightleftarrows \text{dibranched} \longrightarrow \text{cracked}$$

Fig. 3.11: Proposed reaction network for hydrocracking and hydroisomerisation reactions of n-alkane on bifunctional catalysts (Steijns et al. 1981b).

The aim of Steijns et al. 1981b was to develop a kinetic model based on the reaction network from Figure 3.11, which reflects as much as possible the true physicochemical nature of the process. Two relations were required to arrive at a kinetic model: i) an expression for the physical adsorption isotherm, relating the hydrocarbons concentration inside the zeolite to the partial pressure in the gas phase and, ii) an expression for the reaction rate in terms of hydrocarbon concentration in zeolite pores. A Langmuir isotherm was assumed for chemisorption and the following expression was retained for the adsorption term (AD) in the rate equations:

$$\mathrm{AD} = \mathrm{p}_{\mathrm{H}_2} \cdot \left(1 + \mathrm{K}_{\mathrm{L}} \cdot \left(\mathrm{p}_{\text{n-Alkane}} + \mathrm{p}_{\mathrm{MB}} + \mathrm{p}_{\mathrm{DB}}\right)\right) \tag{3.19}$$

The following simplifying assumptions were made by Steijns et al. 1981a,b:

- The adsorption constants (K_L) of feed n-alkane and its respective isomers (MB and DB) were assumed to have the same values.
- Adsorption of the cracked products was negligible. They considered that only in the cases where the feed contains large amounts of lower-boiling-point hydrocarbons, this term has to be included.
- Hydrocracking and hydroisomerisation reactions do not give rise to any volume change.
- Hydrocracking and hydroisomerisation have the same activation energy.

- Lumped equilibrium constants (K_{eq}) for the reversible isomerisation reactions were calculated using thermodynamic data from Stull et al. 1969 for C_{10} at a temperature of 227 °C. These values were assumed to be constant across the whole temperature range studied and also the same values were used for C_{12} and C_8 (Tab. 3.9).

The reaction rate equations of formation of monobranched (MB), multibranched (DB) and cracked products (cr) are presented in Equations 3.20-3.22 respectively. Table 3.9 presents the kinetic parameter values (AD: see Eq. 3.19).

$$r_{iso,_{MB}} = \frac{(k_{iso,MB} \cdot (p_{n-Alkane} - p_{iso,MB}/K_{eq,1}) - k_{iso,DB} \cdot (p_{iso,MB} - p_{iso,DB}/K_{eq,2}))}{AD} \tag{3.20}$$

$$r_{iso,DB} = \frac{(k_{iso,DB} \cdot (p_{iso,MB} - p_{iso,DB}/K_{eq,2}) - k_{cr} \cdot p_{iso,DB})}{AD} \tag{3.21}$$

$$r_{cr} = \frac{k_{cr} \cdot p_{iso,DB}}{AD} \tag{3.22}$$

Tab. 3.9: Kinetic parameter values for hydroisomerisation and hydrocracking reactions of n-alkanes (Steijns et al. 1981b, Froment 1987)

		n-C_8	n-C_{10}	n-C_{12}
$k_{0,iso,MB}$	mol / (h·g)	$1.1 \cdot 10^{14}$	$(1.8 \pm 0.3) \cdot 10^{15}$	$(4.0 \pm 0.3) \cdot 10^{16}$
$k_{0,iso,DB}$	mol / (h·g)	$4.8 \cdot 10^{13}$	$(1.9 \pm 0.3) \cdot 10^{15}$	$(8.7 \pm 2.1) \cdot 10^{16}$
$k_{0,cr}$	mol / (h·g)	$6.0 \cdot 10^{13}$	$(1.4 \pm 0.3) \cdot 10^{15}$	$(5.0 \pm 1.4) \cdot 10^{16}$
E_A	kJ / mol	136.8 ± 1.7	138.9 ± 2.5	149.8 ± 5.0
K_L	bar^{-1}	8.5	13.9 ± 2.7	13.8 ± 3.9
$K_{eq,1}$	-	7.6	7.6	7.6
$K_{eq,2}$	-	2.2	2.2	2.2

Froment 1987 concluded that extrapolation of the rate parameters to higher alkanes is still hazardous and further experimentation is required for such feeds.

Pellegrini et al. 2004, 2007 proposed a reaction network and a kinetic model for the hydrocracking and hydroisomerisation reactions of a C_{4-70} mixture of n-alkanes on a Pt/amorphous silica-alumina catalyst. Temperature was varied between 343 and 373 °C and pressure between 3.5 and 6 MPa. The reaction network and the kinetic expressions proposed are based on Steijns et al. 1981b and Froment 1987. Pellegrini and co-workers do not differentiate among the different types of isomers. The kinetic model from Pellegrini et al. 2004, 2007 contains a large number of parameters since the proposed reaction network contains nine different fractions: C_{22+}, C_{15-22}, C_{10-14}, C_{5-9} (respectively n- and iso-alkane), C_{1-4}. They presented different values for isomerisation and cracking activation energies. Each lump has also a different value for adsorption and equilibrium constants. This kinetic model contains 29 kinetic parameters in total. It is difficult to prove if the proposed values for the adsorption and equilibrium constants are physically plausible or if they are the results of the numerical validation algorithm used. These values differ quite a lot from those proposed by Steijns et al. 1981b and Froment 1987. But it must be kept in mind that the catalyst, the feed and the reaction conditions are also different. The kinetic model proposed by Pellegrini et al. 2004, 2007 is in qualitative agreement with the theory proposed by Sie et al. 1988. They proposed that the rate of acid-catalysed alkane hydrocracking under mild conditions is strongly dependent upon the length of the alkane chain. C_{17} exhibits relative cracking reactivity about 90 times higher than that of C_{10} (Fig. 3.12). Not only the reaction mechanism but also the process conditions are responsible for this difference. Process conditions are chosen as to allow lighter hydrocarbons to be partially evaporated; they then have only limited contact with the catalyst and hence display a low reactivity (Eilers et al. 1990).

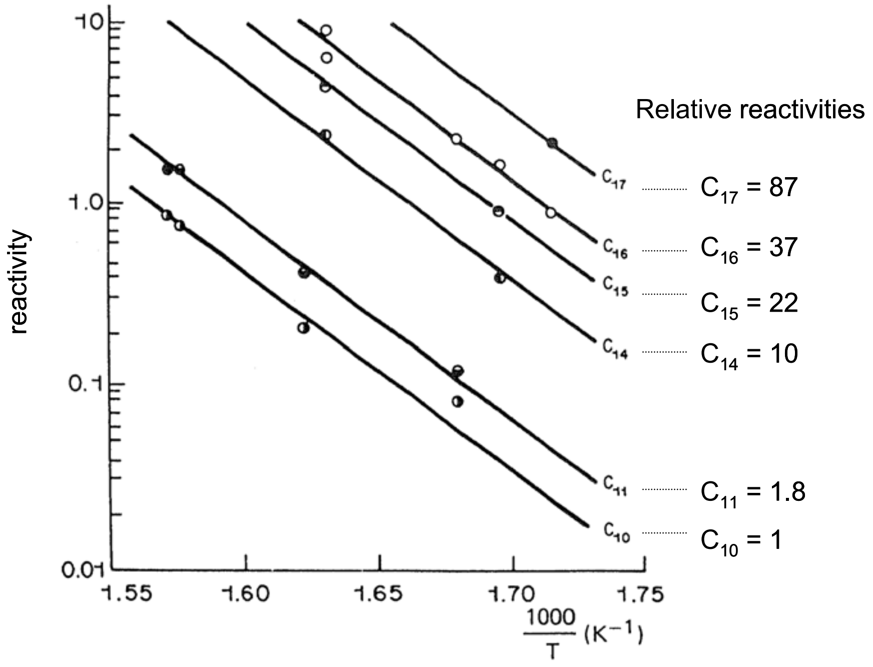

Fig. 3.12: Arrenhius plot of the hydrocracking rates of n-alkane in the temperature range 300-370 °C and pressure between 30 and 50 bar (Sie et al. 1988), reactivity in arbitrary units.

3.3 Combination of FTS and hydrocarbon reactions

The aim of combining FTS and hydrocarbon reactions is to overcome the typical ASF product distribution (see Chapter 3.1.1.5) arising from conventional Fischer-Tropsch catalysts and to result in a gasoline with enhanced octane number. Until now, none of the published literature has reported a combination directed towards increasing the selectivity of middle distillates (diesel).

Most of the recent literature about this topic (e.g. those in Tab. 3.10) used HZSM-5 zeolite as acid catalyst. ZSM-5 zeolite is preferred for bifunctional catalyst compositions when gasoline production is targeted because of its characteristic properties (Rao et al. 1990):

i) Its mesopore structure provides shape selectivity (10-membered ring channels which are connected with sinusoidal channels).
ii) Its high acidity promotes oligomerisation, isomerisation, cracking and aromatisation reactions.
iii) Its resistance to coking owing to the medium-pore size which prevents the formation of coke precursors.

iv) Its high stability and resistance to dealumination under FT reaction conditions.

Most of the studies reported a combination with Co-based FT catalyst. Concerning the high temperatures required for hydrocracking reactions, Fe-based catalysts seem more attractive. In all studies reported, only limited efforts were spent to characterise the broad product spectrum and the effects of the integrated hydrocarbon reactions.

FT catalyst: Fe

The earliest mention of an Fe catalyst mixed with ZSM-5 is a patent from the Mobil Oil Corporation (Chang et al. 1978). The experiments were carried out at high temperature (370 °C) and consequently methane selectivity (30 wt-%) was high, as well as the amount of aromatics.

Butter et al. 1980, Schulz et al. 1991, Botes et al. 2004, and Yoneyama et al. 2005 reported the effects of a physical mixture of K-promoted Fe-based catalyst and HZSM-5 in a fixed-bed reactor or in a Berty microreactor. They worked at temperatures between 280 and 330 °C. Butter et al. 1980 and Botes et al. 2004 reported a decrease of CO conversion when combining FT and zeolite catalyst. This decrease was attributed to alkali migration from the iron to the HZSM-5 catalyst. It also caused a severe shift in the selectivity of the FT towards methane. On the contrary, Schulz et al. 1991 and Yoneyama et al. 2005 achieved nearly the same CO conversion with the combination of both catalysts as with Fe catalyst alone.

Concerning the product distribution, all of them reported a maximum at around C_4 due to cracking reactions of long-chain aliphatic molecules. The C_4-fraction consists mainly of iso-C_4. Schulz et al. 1991 and Botes et al. 2004 reported a second maximum at around C_8, which corresponds to the favoured distribution of aromatics due to the pore size of ZSM-5. They also reported deactivation of the acid catalyst. Schulz et al. 1991 proposed a regeneration method with temperature-programmed oxidation followed by reduction with H_2. Yoneyama et al. 2005 did not report any deactivation. However, the maximal time on stream was 10 h. This could explain that C_{16} was the longest hydrocarbon obtained from the Fe catalyst and C_{10} from the combination Fe-HZSM-5.

None of the Fe-zeolite combinations mentioned above contained a noble metal which may be useful for retarding or avoiding zeolite deactivation. At the reaction conditions applied (high temperature) and in absence of a metal, most probably catalytic cracking reactions took place instead of hydrocracking reactions.

FT catalyst: Co

Table 3.10 presents some of the published concepts of combining Co-based and hydroprocessing catalysts in one reactor under FTS reaction conditions. The concepts presented can be divided into three groups: i) physical-mixture configuration in fixed-bed reactor, ii) physical-mixture configuration in a slurry phase (autoclave), and iii) capsule catalysts. It is not possible to conclude which is the best concept, since reaction conditions and catalysts were different in each study. In most of the cases the CO conversion did not remain constant compared with that achieved with Co catalyst alone (Bessell 1995, Jothimurugesan et al. 1998, Li et al. 2004, Ngamcharussrivichai et al. 2006).

Most of the studies used HZSM-5 as acid catalyst but also larger pore zeolites (e.g. Y, Beta, Mordenite) were studied by Bessell 1995, Li et al. 2004, Liu et al. 2005, Ngamcharussrivichai et al. 2006, Martínez et al. 2007. Zeolites with smaller pores and with most complex and constrained channel systems (e.g. ZSM-34) were investigated by Bessell 1995. Concerning only the zeolite pore topology, it can be concluded that highly acidic zeolites with channels structure allowing ready accessibility to internal acid sites (e.g. zeolites defined by 10-membered rings and above) are suitable acid catalysts for increasing branched hydrocarbons selectivity in gasoline fraction. Larger pores zeolites were found to deactivate faster than smaller zeolites (Martínez et al. 2007).

Liu et al. 2004 and Li et al. 2005 studied the influence of Pt and Pd on the hydrocarbon reactions. Surprisingly, in the results presented by Li et al. 2004, alkenes were not hydrogenated in the presence of Pd and H_2. The presence of Pd improved the C_{2+} and iso-alkane selectivity, especially with Pd/Beta. Hydrocracking reactions were also reported to take place and CH_4 selectivity increases compared with Co alone. A possible explanation of these results could be the occurrence of hydrogenolysis or secondary cracking reactions. On the contrary, Liu et al. 2005b reported nearly constant CH_4 selectivity (compared with Co alone) when using Pd/Beta, but alkene selectivity increases. Iso-alkane selectivity also increases in the gasoline fraction (especially in C_{4-6} fraction). This increase was higher when using granular catalysts instead of powder. Liu et al. 2005b also reported selectivity of C_{11+} fraction around 15 % for Co alone. With the combination, C_{10} was the longest hydrocarbon produced. This would indicate a strong hydrocracking activity of Pd/Beta at 230 °C and 1 MPa. Similar results were presented by Tsubaki et al. 2003, even though in some cases no noble metal was presence. They also reported an increase of alkene selectivity by using ZSM-5 or Pd/ZSM-5. A possible explanation could be that catalytic cracking took place which results in iso-alkene and n-alkane. However, it is questionable if catalytic cracking takes place at 230-250 °C.

Martínez et al. 2007 also performed model compounds experiments with n-C_{16} on Co-ZSM-5 catalyst. Their studied the influence of H_2O on the zeolite activity. They concluded that at the conditions studied, H_2O competes with n-C_{16} molecules for adsorption on the zeolite acid sites, thus decreasing the amount of sites available for cracking reactions. This competition is supposed to be stronger with highly hydrophilic zeolites.

A new concept was presented by He et al. 2005 by coating catalyst pellets (0.38-0.5 mm, 0.85-1.7 mm) with a 10 µm thickness ZSM-5 membrane. The reactants permeate through the layer into the FT catalyst. The hydrocarbons formed are forced to diffuse through the zeolite layer and undergo hydrocracking and isomerisation reactions. Lower CO conversion values were achieved (compared with Co alone), possibly due to diffusional limitations. Methane and alkene selectivity increased, due to secondary reactions and unfavourable H_2/CO-ratio within the pellets. A sharp cut-off at C_9-C_{10} and higher iso-alkane selectivity were also reported which indicates a strong cracking and isomerisation activity of the membrane. He et al. 2005a mentioned that the catalyst was precoated with Pt before characterisation. Catalyst deactivation was not reported.

Tab. 3.10: Concepts from the literature to combine Co-based FT and hydroprocessing catalysts in one reactor.

References	Catalyst, reactor configuration	Objective	Zeolite	Noble metal
Martínez et al. (2007)	physical mixture - fixed bed	- influence of zeolite pore topology on activity - H_2O effect on zeolite activity	USY, Beta, Mordenite, ZSM-5	-
Liu et al. (2005a)	two fixed beds in series: 1st reactor: physical mixture 2nd reactor: Pd or Pt/Beta	- influence of noble metal type and loading weight - influence of the bifunctional catalysts on iso-alkane selectivity in gasoline range	Beta	Pd, Pt
Liu et al. (2005b)	physical mixture	- influence of particle size (granular and powder) on activity and iso-alkane selectivity	Beta	Pd
Li et al. (2004)	physical mixture - fixed bed	- influence of zeolite pore topology and noble metal presence on activity and iso-alkane selectivity in gasoline range	USY, Beta, Mordenite, ZSM-5	Pd (with Beta and ZSM-5)
Tsubaki et al. (2003)	physical mixture - fixed bed	- influence of noble metal and zeolite on iso-alkane selectivity	ZSM-5	Pd/SiO_2
Jothimurugesan et al. (1998)	physical mixture, dual layer, impregnated zeolite - fixed bed	- influence of catalyst configuration and alloys (Co-Fe, Fe-Ni, Co-Ni) on activity and hydrocarbons selectivity	ZSM-5	-
Bessel (1995)	physical mixture - microreactor	- influence of zeolite pore structure, acid strength and concentration on activity	ZSM-34, ZSM-11, ZSM-12, ZSM-5	-
Ngamcharussrivichai et al. (2006)	slurry phase (autoclave)	- influence of Co support (SiO_2, Al_2O_3, Montmorillonite) on FT catalyst activity - influence of zeolite pore structure and acidity on activity and hydrocarbons selectivity	USY, ZSM-5, MCM-22	-
He et al. (2005 a,b)	capsule catalyst - fixed bed	- influence of catalyst configuration on iso-alkane selectivity	ZSM-5	(Pt)

4 Preliminary studies - Potential of combining FT and HC reactions

4.1 Gas phase composition in FT reactors

Fischer-Tropsch reaction conditions are not favourable for bifunctional catalysts. H_2/CO-ratio at reactor inlet and conversion levels of CO determine the local gas composition. For Co-based catalysts a H_2/CO-ratio near 2 is optimal for activity, chain-growth probability and low-methane selectivity. CO_2 partial pressure is very low, since Co-based catalysts usually are not active towards the CO/CO_2-shift reaction. Partial pressure of water vapour may be high, as it is the main by-product of the FT synthesis (Fig. 4.1).

In the case of Fe-based catalysts, the H_2/CO-ratio at FT reactor inlet is more flexible. Synthesis gas from biomass usually has H_2/CO-ratios below 2 (Unruh 2006). Since Fe-based catalysts are CO/CO_2-shift active, CO_2 may be produced from CO decreasing the hydrocarbon yield. As a result, water vapour partial pressure is lower than with Co catalysts (Fig. 4.2).

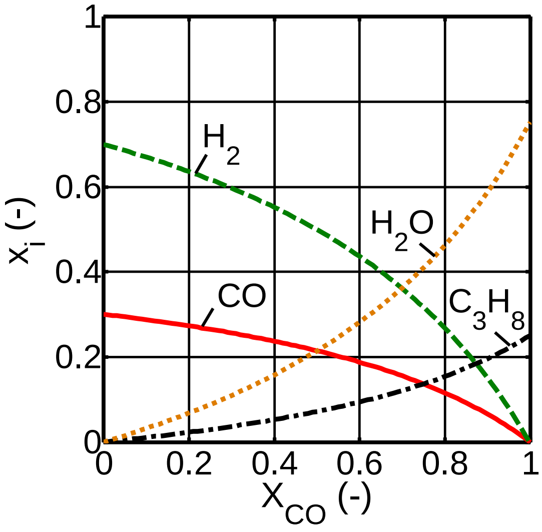

Fig. 4.1: Calculated molar fraction in gas phase FT product versus CO conversion on a Co catalyst (zero CO/CO_2-shift activity). $(p_{H2}/p_{CO})_{in}$ = 2.33, stoichiometry with C_3H_8 as product molecule.

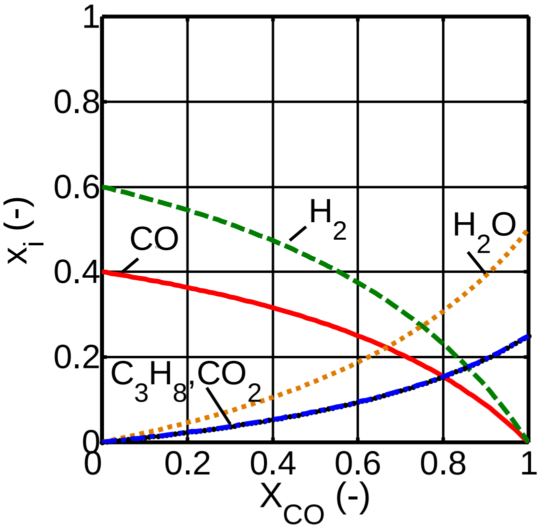

Fig. 4.2: Calculated molar fraction in gas phase FT product versus CO conversion on a Fe catalyst with CO/CO_2-shift activity. $(p_{H2}/p_{CO})_{in}$ = 1.5, stoichiometry with C_3H_8 as product molecule.

In general, synthesis gas conversion between 60 and 90 % may be obtained in industrial FT reactors. Figures 4.1 and 4.2 show that at these conversions, CO concentrations are still significant in the FT product. CO is known to affect the (de)/hydrogenation activity of noble metals (Scherzer et al. 1996, Weiss et al. 1984). In addition, water vapour may affect the hydrocracking/hydroisomerisation activity of the acidic support (such as zeolites), especially at high synthesis gas conversion (Martínez et al. 2007). Moreover, the hydrocracking process in petroleum refining operates at high hydrogen partial pressure (5-20 MPa) in order to enhance hydrogenation of coke precursors and cleaning of the catalyst surface (Stöcker 2005). At high levels of CO conversion, p_{H2}/p_{HC}-ratio may be low, even below the stoichiometric requirements of hydrocracking. This could affect the catalyst lifetime in the case of combining FT and hydrocarbons reactions.

4.2 Temperature and pressure effect on hydrocarbon reactions

Temperatures between 180 and 270 °C, as used for low-temperature FTS, are comparatively low for hydrocracking reactions (300-450 °C), (Scherzer et al. 1996, Stöcker 2005). Figure 4.3 shows characteristic temperature intervals for FT reactions on the Co- and Fe-based catalysts used in this study. Schulz et al. 1972 and Weitkamp et al. 1983 studied model hydrocarbon reactions (e.g. with n-C_{12}, n-C_{15}) on bifunctional catalysts (Pt/CaY, Pt/ZSM-5) at temperatures between 210 and 300 °C and pressure between 2 and 4 MPa. Figure 4.3 shows that conversion by isomerisation increases with temperature and then goes through a maximum when cracking becomes predominant (see Fig. 3.8). It can be observed that cracking reactivity increases with increasing hydrocarbon chain length. This relation indicates the possibility to crack C_{20+} molecules with bifunctional catalysts at FT temperatures.

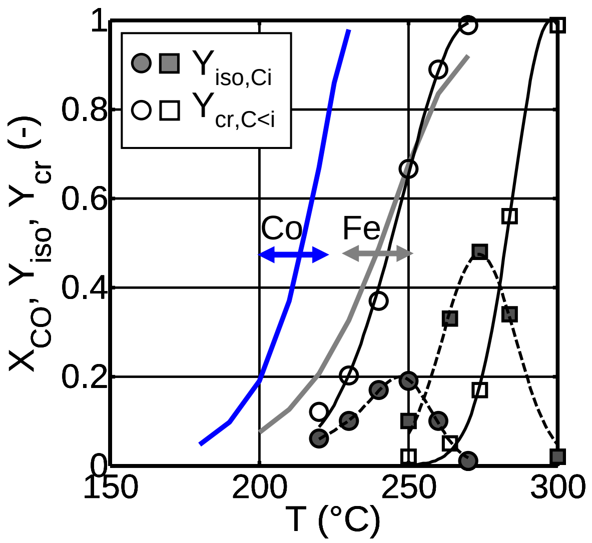

Fig. 4.3: Characteristic temperature intervals for FT reactions on Co- and Fe-based catalysts (calculated with kinetic model, see Chapter 6) and for model hydrocarbon hydrocracking and hydroisomerisation reactions. Squares: n-C_{12} as feed with Pt/CaY (0.5 wt-% Pt) catalyst, $(H_2/n\text{-}C_{12})_{molar,in}$ = 20 , p = 4 MPa (Schulz et al. 1972). Circles: n-C_{15} as feed with Pt/ZSM-5 (0.5 wt-% Pt) catalyst, $(H_2/n\text{-}C_{15})_{molar,in}$ = 100, p = 2 MPa (Weitkamp et al. 1983).

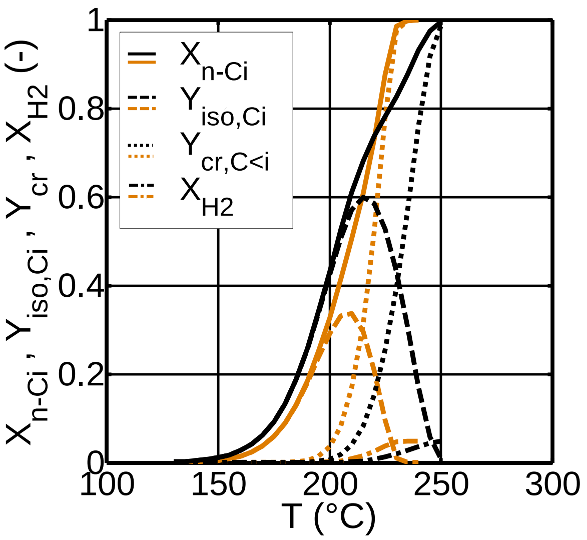

Fig. 4.4: Effect of chain length on conversion and yields. Feed: n-C_8H_{18} (black curves), n-$C_{12}H_{26}$ (grey curves). p = 1 MPa, $(H_2/C_nH_{2n+2}/Ar)_{molar,in}$ = 0.65 / $3.12 \cdot 10^{-2}$ / 0.32, τ_{mod} = 3000 kg·s/m^3. Calculated with kinetic model from Steijns et al. 1981, Froment 1987 with Pt/USY (0.5 wt-% Pt) catalyst (see Chapter 3.2.6).

A kinetic model for model hydrocarbon reactions (n-C_8, n-C_{10}, n-C_{12}) on Pt/USY catalyst, as presented in Chapter 3.2.6 (Steijns et al. 1981, Froment 1987), considers that all components are present in the gas phase. This model was used to carry out some case studies in order to understand the effects of hydrocarbon chain length, total pressure and p_{H2}/p_{HC}-ratio on isomerisation and cracking reaction kinetics. Reaction conditions of these studies were chosen to be close to those of the own experiments (see Chapter 6). The kinetic model distinguishes between mono- and dibranched hydrocarbons, of which the isomerisation yield curves presented in the case studies are the sum (Fig. 4.4-4.5). The application of the kinetic model of Steijns et al. 1981, Froment 1987 shows again the relation between cracking activity and hydrocarbon chain length. Figure 4.4 also shows a low hydrogen conversion since hydrogen is in excess. The kinetic model predicts cracking reactions of iso-C_8 and iso-C_{12} to take place above 220 °C at 1 MPa and p_{H2}/p_{HC}-ratio of about 20. However, it must be kept in mind that this kinetic model does not consider the presence of CO or water vapour. The ratio of isomerisation/cracking activities depends on the type of catalyst (hydrogenation and acidic compounds).

Figure 4.5a shows the effects of hydrogen partial pressure on isomerisation/cracking activity when keeping constant the partial pressure of n-C_8. According to the own model compound experiments, p_{H2}/p_{C8}-ratio of 20 was chosen (see Chapter 6.1). A ratio of 1.5 was chosen according to the later experiments with Co-based FT catalyst at 80 % CO conversion. According to the isomerisation/cracking reaction rate equations (Eq. 3.20-3.22), it is obvious that by increasing hydrogen partial pressure the reaction rates decrease. It seems that low p_{H2}/p_{HC}-ratio could be an advantage for the combination of FT and hydrocarbon reactions.

Figure 4.5b shows the effect of increasing total pressure when keeping p_{H2}/p_{C8}-ratio constant. Total pressure of 1 MPa was chosen according to the own experiments (see Chapter 6). At higher total pressure, higher temperature is required to achieve the same conversion level of n-C_8.

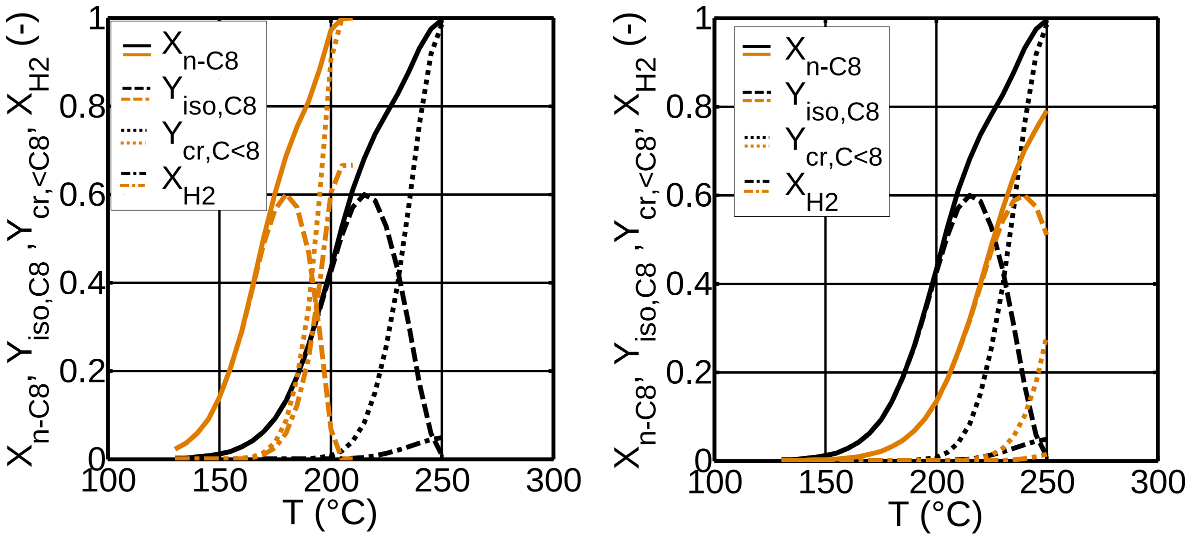

(a) (b)

Fig. 4.5a: Effect of H_2 partial pressure on conversion and yields. Black curves: $(p_{H2}/p_{C8H16}/p_{Ar})_{in}$ = 0.65 / $3.12 \cdot 10^{-2}$ / 0.32 MPa. Grey curves: $(p_{H2}/p_{C8H16}/p_{Ar})_{in}$ = $4.68 \cdot 10^{-2}$ / $3.12 \cdot 10^{-2}$ / 0.92 MPa, p = 1 MPa, τ_{mod} = 3000 kg·s/m^3.

Fig. 4.5b: Effect of total pressure on conversion and yields. Black curves: p = 1 MPa. Grey curves = 6 MPa, $(H_2/C_8H_{16}/Ar)_{molar,in}$ = 0.65 / $3.12 \cdot 10^{-2}$ / 0.32, τ_{mod} = 3000 kg·s/m^3.

a+b: Calculated with kinetic model from Steijns et al. 1981, Froment 1987 with Pt/USY (0.5 wt-% Pt) catalyst (see Chapter 3.2.6).

These case studies show the possibility to crack short-chain hydrocarbons (C_8-C_{12}) on Pt/USY catalyst at lower pressure and temperature than those used in a hydrocracking process in petroleum refining or in FT-wax hydrocracking. The pores of Y zeolite exhibit nearly no shape-selectivity. The use of zeolites with smaller pores (e.g. ZSM-5) should improve the long-chain cracking reactions. Smaller pores will help to crack the long-chain hydrocarbons (C_{21+}), since their respective isomers could be too large for the small pores (see Chapter 3.2.2.3).

Until today there are no experiments or kinetic model known which describe the effects of CO and H_2O on hydrocracking reactions. For that reason, experiments were carried out within the present study to support the case studies presented (see Chapter 6).

5 Procedure and experimental methods

5.1 Outline

Figure 5.1 presents the procedure followed in this study. First of all, a literature survey was carried out concerning hydrocarbon reactions taking place on bifunctional catalysts and concerning the combination of FTS and hydrocarbon reactions in one reactor (Chapter 3). This survey was conducted with parallel case studies on the basis of a kinetic reaction model for hydrocarbon compounds presented in the literature survey (Chapter 4). The experimental work can be divided into three parts: i) preliminary hydrocarbon reactions with model compounds (1-octene, ethene/propene) on bifunctional catalysts (Pt/ZSM-5, Pt/Beta), ii) FT synthesis with Co- and Fe-based catalysts with reaction conditions varied for kinetic studies, and iii) combination of FTS and hydrocarbon reactions with FT and bifunctional catalysts in two different reactor configurations (dual layer, physical mixture), (Chapter 6). The preliminary model compounds experiments help to assess the influence of CO on the reactions taking place on bifunctional catalysts. The FT-synthesis experiments provide a basis for the combination of FTS and hydrocarbon reactions. The hydrocarbon product analysis plays a central role in the experiments evaluations. The results obtained allow the establishment of a reaction network draft which was validated on the basis of kinetic models from the literature (Chapter 7).

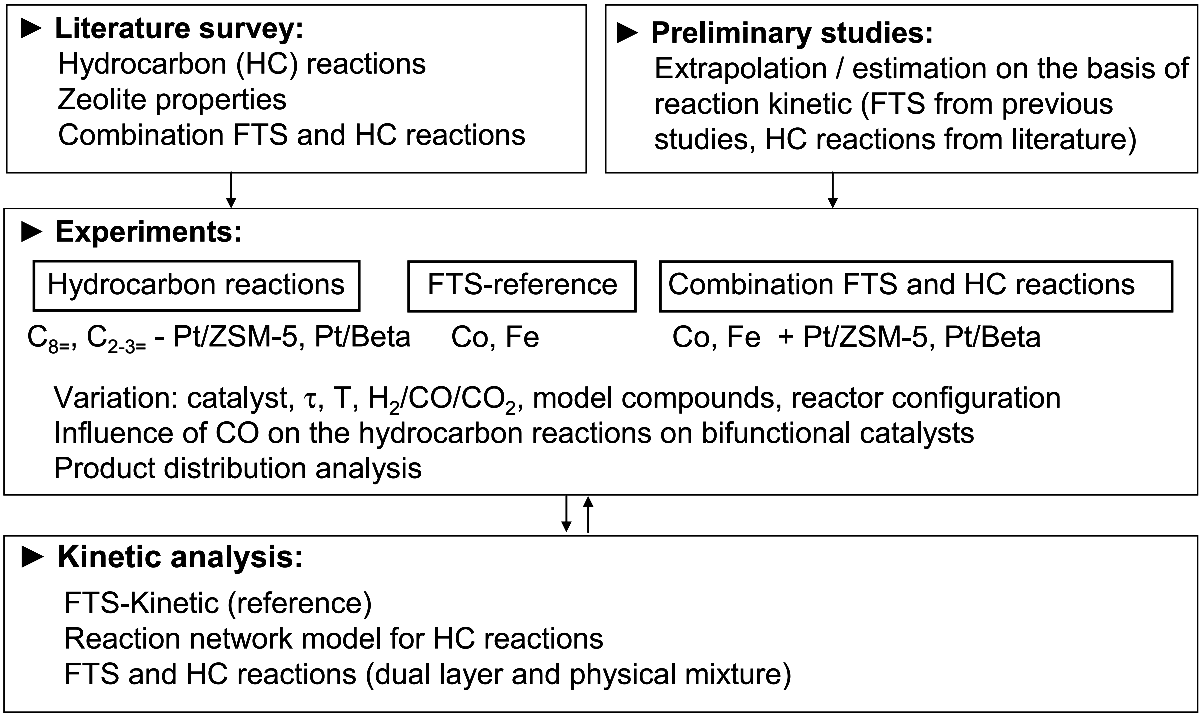
► Literature survey:
Hydrocarbon (HC) reactions
Zeolite properties
Combination FTS and HC reactions
► Preliminary studies:
Extrapolation / estimation on the basis of reaction kinetic (FTS from previous studies, HC reactions from literature)
► Experiments:
Hydrocarbon reactions
FTS-reference
Combination FTS and HC reactions
$C_{8=}$, $C_{2-3=}$ - Pt/ZSM-5, Pt/Beta
Co, Fe
Co, Fe + Pt/ZSM-5, Pt/Beta
Variation: catalyst, τ, T, $H_2/CO/CO_2$, model compounds, reactor configuration
Influence of CO on the hydrocarbon reactions on bifunctional catalysts
Product distribution analysis
► Kinetic analysis:
FTS-Kinetic (reference)
Reaction network model for HC reactions
FTS and HC reactions (dual layer and physical mixture)

Fig. 5.1: Schema of the procedure followed.

5.2 Catalysts

5.2.1 Fischer-Tropsch catalysts

The FT catalysts were chosen according to the following requirements:

i) Fischer-Tropsch activity. The Co-based catalysts should show high activity at relatively high temperatures (> 200 °C), with respect to the desired cracking and isomerisation reactions on bifunctional catalysts.
ii) The Fe-based catalyst should contain K as chemical promoter for the CO/CO_2-shift activity.
iii) Measurable yields of FT-wax should help to quantify the effect of the cracking reactions taking place on the bifunctional catalyst.

The Co-based catalyst chosen includes Al_2O_3 as structural promoter (i.e. support) and no reduction promoter. The Fe-based catalyst chosen included K as chemical promoter. Further composition details about the Fe catalyst are restricted due to industrial secrecy. Table 5.1 summarises some properties of the FT catalysts.

Tab. 5.1: Composition and characterization of the Fischer-Tropsch catalysts used.
$^{1)}$ Maximum in distribution function , $^{2)}$ Data provided by catalysts manufacturers,
$^{3)}$ Analysis of A_{BET} and pore diameter by Quantachrome GmbH&Co.KG.

Catalyst	Composition $^{2)}$ (wt-%)	A_{BET} $^{3)}$ (m^2/g)	Pore diameter $^{1), 3)}$ (nm)	Specific pore volume $^{3)}$ (cm^3/g)
Co/Al_2O_3	14.1 Co, 38.5 Al_2O_3	131	8.0	0.313
K-promoted Fe	K < 10	94	-	0.754

5.2.2 Bifunctional catalysts

Bifunctional catalysts contain a well-dispersed metal in the pores of an acidic support. The relative strength of the two functions determines the type and the distribution of the products. If a strong hydrogenation function such as that of Pt is used, high selectivities for hydroisomerisation as well as ideal primary cracking can be obtained (i.e. no methane formation, symmetrical product distribution, Steijns et al. 1981). For that reason, Pt was chosen as a noble metal in this study.

Zeolites were selected as acidic support (Chapter 3.2) and among them HZSM-5 and HBeta where chosen (in H-form), exhibiting different structure (Fig. 5.2). ZSM-5 zeolite is well known for its shape selectivity (Chapter 3.2.2.3) due to its intersecting two-dimensional pore structure. ZSM-5 has two types of pores, both formed by 10-membered oxygen rings. The first type is straight and elliptical in cross section (0.55 x 0.51 nm in [100] direction); the second type pores intersect the straight pores at right angles (0.56 x 0.53 nm in [010] direction), in a zig-zag pattern and are circular in cross section (IZA 2007). Published applications of ZSM-5-zeolite in hydrocarbon reactions include hydrocracking, catalytic dewaxing of middle distillates, conversion of alkenes to diesel, conversion of methanol to gasoline, xylene isomerisation, etc. (Tab. 12.11-12.13).
Beta zeolite has a tetragonal crystal structure with straight 12-membered ring channels (0.76 x 0.64 nm in [100] direction) with crossed 10-membered ring channels (0.55 x 0.65 nm in [001] direction). Published applications of Beta zeolite in hydrocarbon reactions include catalytic alkylation of aromatics, Friedel Crafts reactions (alkylation and acylation), isomerisation of waxes, etc. (Tab. 12.11-12.13).

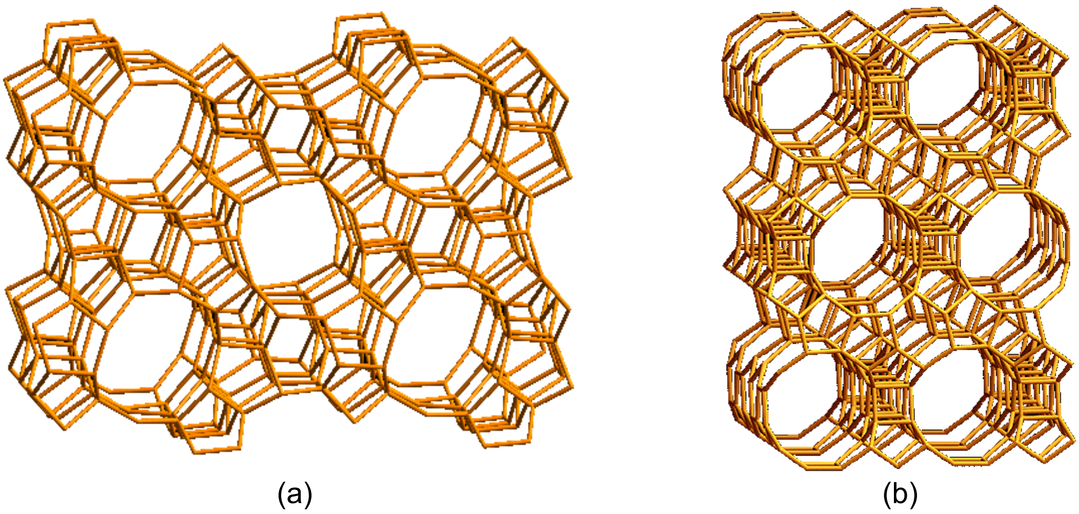
(a) (b)

Fig. 5.2: (a) ZSM-5 framework viewed along [010] direction, (b) Beta framework viewed along [100] direction (IZA 2007).

Samples of HZSM-5 were obtained from the Institut für Chemische Verfahrenstechnik (Universität Karlsruhe, TH) and HBeta from Süd-Chemie AG, with some differences in SiO_2/Al_2O_3-ratio and crystal size (Tab. 5.2). HBeta zeolite has a higher surface area (from BET method) than HZSM-5. The SiO_2/Al_2O_3-ratio is inversely proportional to the number of acidic sites. Crystal size is inversely proportional to the ratio between number of acid sites on the external surface and sites on the porous structure.

Tab. 5.2: Composition and characterization of the powder zeolites used. Analysis of A_{BET} by Quantachrome GmbH&Co.KG with Ar at 87 K in AUTOSORB-3-Kr. Pt loading analysis by Institut für Wasserchemie (Universität Karlsruhe, TH) with ICP-OES method. Other data from the zeolite suppliers.

Zeolite	SiO_2/Al_2O_3 (-)	A_{BET} (m^2/g)	Crystal size (nm)	Pt (wt-%)
HZSM-5	64	387	300-500	1
HBeta	25	611	< 100	1

Both zeolite powders (HZSM-5 and HBeta) were loaded with 1 wt-% Pt. Firstly, the zeolite powder was calcinated at 400 °C for 4 hours. The ion exchange was carried out at 25 °C for 24 h with $Pt(NH_3)_4(OH)_2$ aqueous solution (4.96 wt-% Pt, Alfa Aesar GmbH&Co.KG) under stirring (600 rpm). The excess of the aqueous solution was evaporated at 35 °C and 15 mbar for 2 h under rotation (60 min^{-1}), then was dried at 120 °C for 24 h. In order to avoid a high pressure drop along the reactor, the Pt/ZSM-5 was mixed with γ-Al_2O_3 (Pural SB1, Condea Chemie GmbH) and hydroxyethylcellulose (8.5 wt-% HEC, Fluka GmbH) and extrudated ($m_{Pt/ZSM-5}/m_{Pural}/m_{HEC}$ = 1/1.5/1.5). Then it was dried at 25 °C for 24 h and calcinated at 550 °C (2 K/min) for 3 h. The extrudates were milled to the desired particle size (d_p = 100-160 μm). Inductively coupled plasma-optical emission spectroscopy (ICP-OES) analysis confirmed the amount of Pt on the catalyst. The surface area (from the BET method) of each bifunctional catalyst is lower than of the powder zeolite, which may indicate that a significant number of pores were closed during Pt loading (Tab. 5.3). Pt/Beta catalyst has a greater surface area, total pore volume and mesopore specific surface area than Pt/ZSM-5. The micropore specific surface area is nearly the same for both catalysts. The surface area values measured using the BET method differ from those measured using the NLDFT method which uses information about the pores structure (i.e. pore volume and diameter, Tab. 5.3).

Tab. 5.3: Characterization of the bifunctional catalysts used. Analysis by Quantachrome GmbH&Co.KG. A_{BET} with Ar at 87 K in AUTOSORB-3-Kr, pore volume and micro-/mesopore surface area with NLDFT Kernel with Ar and assuming cylindrical pores.

Zeolite	A_{BET}	Total pore volume	Micropore (< 2 nm)		Mesopore (2-50 nm)	
			Spec. surface area	Spec. pore volume	Spec. surface area	Spec. pore volume
	(m^2/g)	(cm^3/g)	(m^2/g)	(cm^3/g)	(m^2/g)	(cm^3/g)
Pt/ZSM-5	286	0.438	706	0.089	140	0.349
Pt/Beta	571	0.737	694	0.099	256	0.638

Both bifunctional catalysts were examined under a transmission electron microscope (TEM) and a scanning electron microscope (SEM) (Fig. 5.3-5.4). The black spots in the TEM pictures were confirmed to be platinum (Fig. 5.3). Platinum cluster size for both Pt/ZSM-5 and Pt/Beta is approx. 11 nm. Zeolite materials are electron-beam sensitive. Terasaki 1999 reported that it is difficult to indicate the electron dose sufficient to destroy the crystallinity of zeolites. It is strongly dependent on the type of zeolite, Si/Al-ratio, water content, crystals quality and energy of incident electrons (see Chapter 3.2.2.2). Due to the instability of the crystal it was not possible to determine the degree of Pt dispersion. The SEM pictures show that ZSM-5 crystals are larger than those from Beta zeolite (Tab. 5.2, Fig. 5.4).

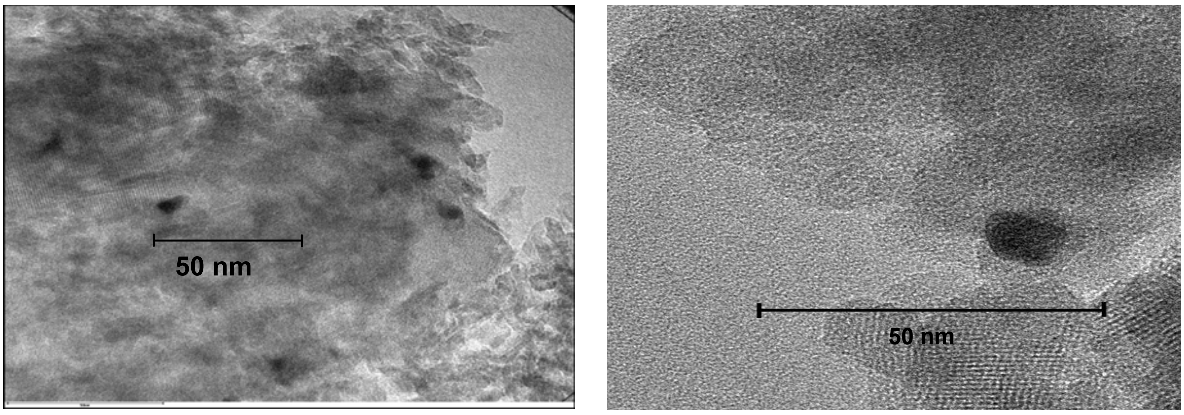

(a) (b)

Fig. 5.3: Transmission electron microscope (TEM) pictures. (a) Pt/ZSM-5, (b) Pt/Beta. Pictures taken at Laboratorium für Elektronenmikroskopie (Universität Karlsruhe, TH).

The SiO_2/Al_2O_3-ratio of a zeolite gives an indication of the number of acidic sites but not about the acidic strength, which is a function of the zeolite microstructure and independent of the acid amount. Temperature-programmed desorption (TPD) of ammonia is frequently used to reveal the acidic property of zeolites (see Chapter 3.2.2.2). Ammonia is selected as probe due to the size of the molecule (critical diameter = 0.36 nm), which is smaller than that of the zeolites pores (Niwa et al. 1997).

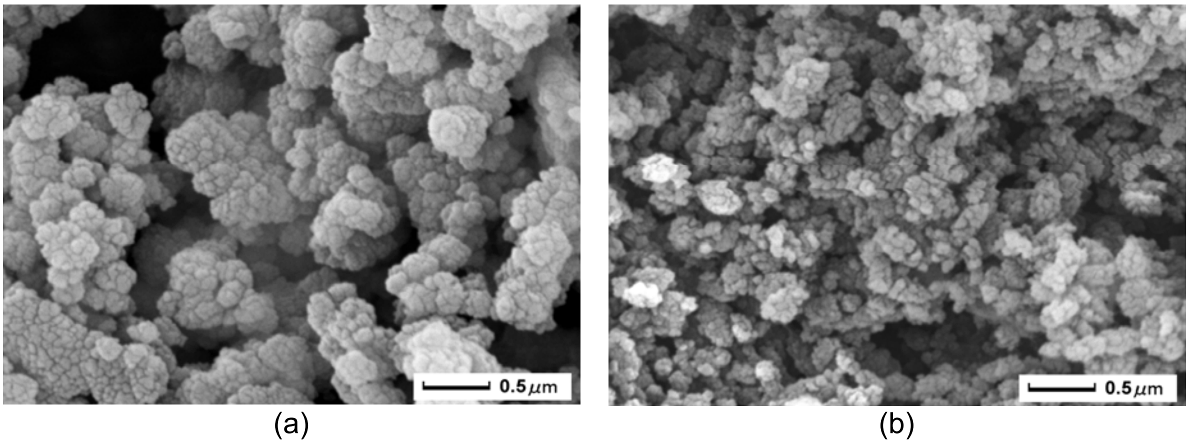

Fig. 5.4: Scanning electron microscope (SEM) pictures. (a) Pt/ZSM-5, (b) Pt/Beta. Pictures taken at the Laboratorium für technische Chemie (Universität Kaiserslautern).

TPD analysis of the two zeolite powders and bifunctional catalysts were performed and the ammonia signal was measured by means of mass spectroscopy (MS). The results obtained were used qualitatively (Fig. 5.5). The MS signal shows two maxima, of which the first one at lower temperatures is due to weakly held or physically adsorbed ammonia. The height of the second maximum gives information about the strength of the ammonia adsorption and consequently the acidic strength by means of heat of ammonia desorption can be calculated (Niwa et al. 1997). Figure 5.5 shows that the second maximum is higher for HZSM-5 than for HBeta. This gives an indication that the acidic strength of HZSM-5 is higher and may result in higher activity. The second maximum decreases by loading the zeolite powder with Pt, which suggests again that some pores get plugged during this process. This decrease is more pronounced by Pt/ZSM-5 since the ZSM-5 zeolite has smaller pores than Beta and can easily get plugged.

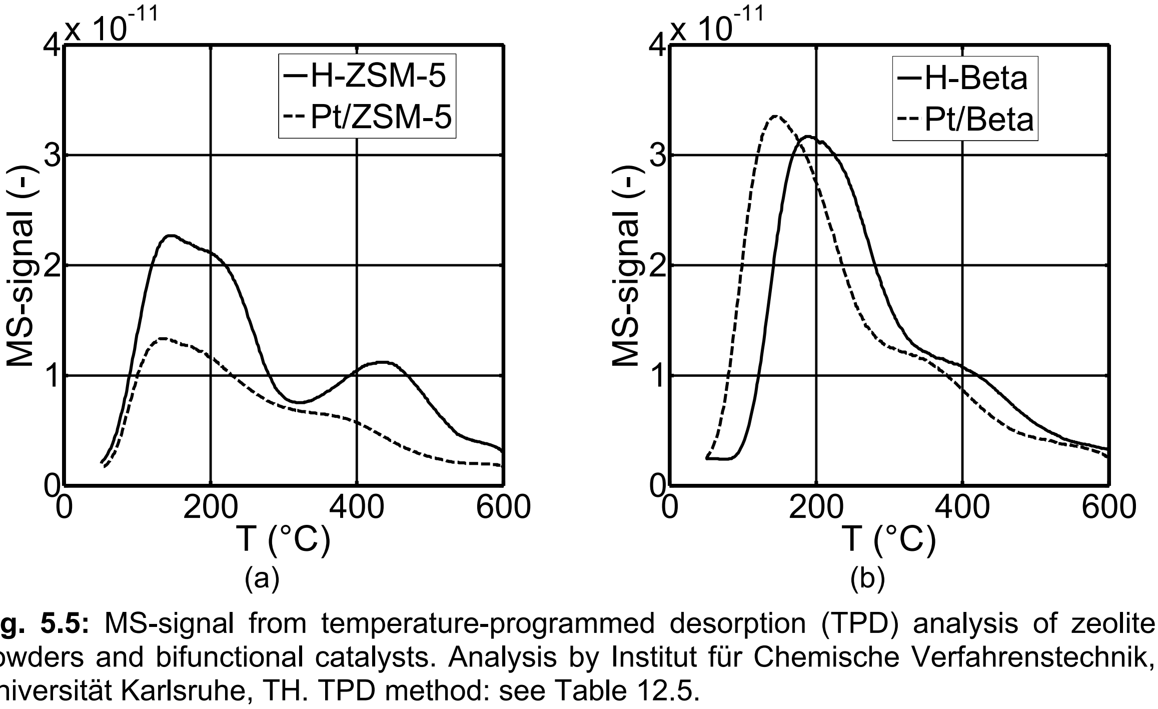

Fig. 5.5: MS-signal from temperature-programmed desorption (TPD) analysis of zeolite powders and bifunctional catalysts. Analysis by Institut für Chemische Verfahrenstechnik, Universität Karlsruhe, TH. TPD method: see Table 12.5.

5.3 Experimental procedure and methods

5.3.1 Experimental set-up

All the experiments were performed in a lab-scale fixed-bed reactor (Fig. 5.6).

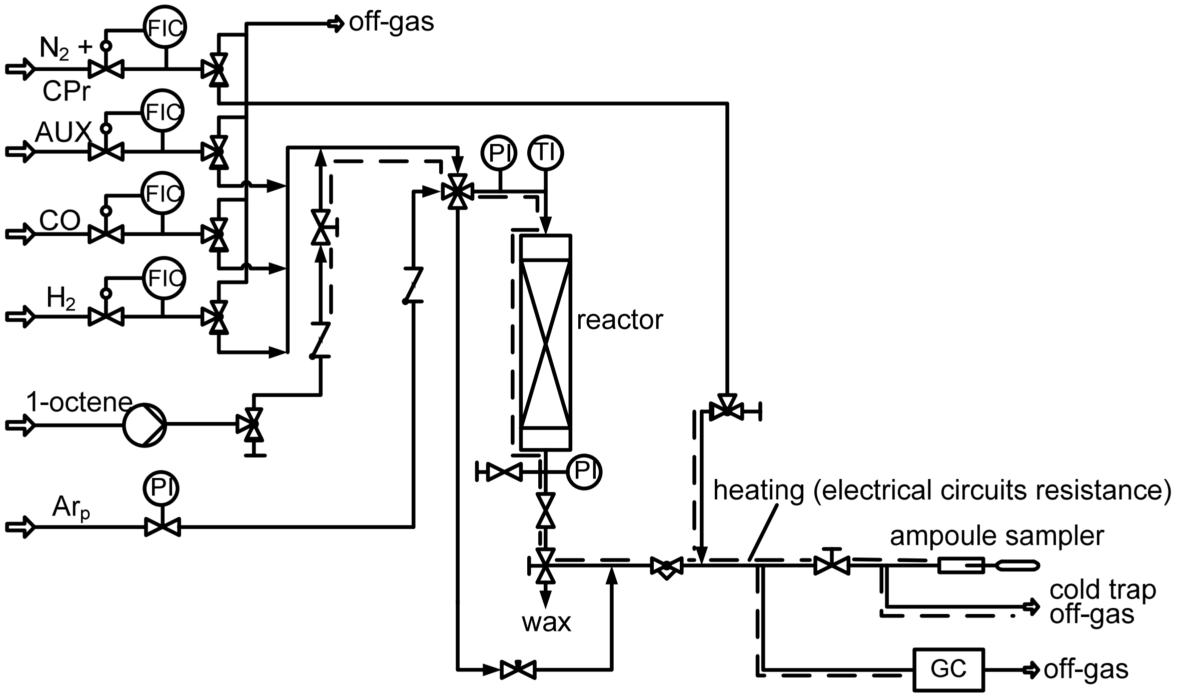

Fig. 5.6: Flow scheme of the lab-scale Fischer-Tropsch rig with a fixed-bed reactor.

Test rig

The lab-scale fixed-bed reactor used in this work is connected to 5 gas bottles (Air Liquide GmbH and BASI Schöberl GmbH&Co.) and to a high-pressure pump (M16, Reichelt Chemietechnik GbmH&Co.), used for feeding liquid 1-octene (Merck KGaA). CO, H_2 and AUX (Ar, CO_2 or $C_2H_4/C_3H_6/N_2$) are fed into the reactor, with volume flows adjusted by analogue mass flow controllers (Brooks Instruments). Liquid 1-octene evaporates in the heated pipes and is led into the reactor. In order to keep a constant pressure inside the reactor tube (1 or 0.5 MPa), Ar is added via a pressure reducer (Bezner OHG). The relation between product and Ar flows can be controlled by means of a fine regulating valve (Swagelok GmbH). Just before the reactor inlet, a 4-port valve allows to switch from reactor to bypass. When the valve is set to bypass, the feed gases flow through the bypass and argon flows through the reactor. On the contrary, the feed gases flow through the reactor and argon through the bypass. After the reactor, the product stream is led to a wax trap (165 °C and 1MPa, 200 °C and 0.5 MPa for the experiments with 1-octene), where the gas and liquid phases are separated. The liquid product stream (wax) is removed discontinuously (~ every 24 h) through a valve (Swagelok GmbH) and analysed in an offline gas chromatograph. After expansion of the product stream to atmospheric pressure, a reference gas stream (0.5 vol-% cyclopropane in N_2, Air Liquide GmbH) is added via another mass flow controller (Brooks Instruments), and mixed with the gas product stream. The gas product stream is led to the cold trap (25 °C), where it partially condensates, and also to the online gas chromatograph and to the ampoule sampler. Cyclopropane is used as reference gas for the organic product analysis (because it is not produced during FT synthesis), and N_2 as reference gas for the inorganic product analysis (Chapter 5.3.3). Figure 5.7 shows a picture of the test rig.

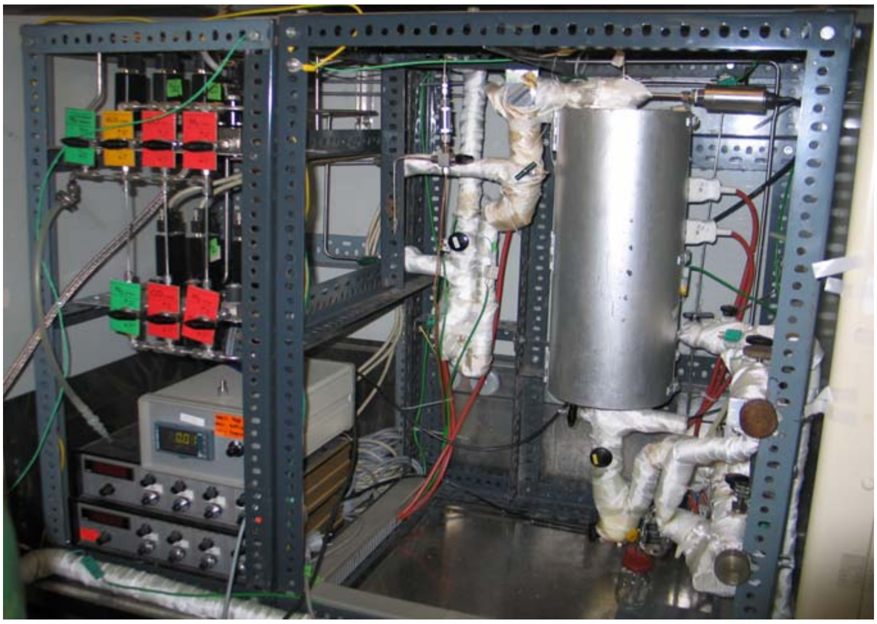

Fig. 5.7: Picture of the lab-scale fixed-bed reactor. Left: mass flow controllers, centre: fixed-bed reactor and wax trap, right: ampoule sampler, cold trap and pipe to online gas chromatograph.

Reactor

The reactor itself consists of a glass tube (d_{ext} = 11 mm, d_{int} = 8 mm, L = 400 mm, s = 1.5 mm), filled with catalyst (Fig. 5.8). In order to ensure isothermal conditions, since FTS is an exothermal reaction ($\Delta_R H^0_{250°C}$ = -156.5 kJ/mol), silicon carbide is mixed with the catalysts for dilution (see Fig. 5.8). Above, between and below the catalyst beds are white quartz wool plugs and SiC layers. The catalyst beds are positioned on a sintered quartz frit to prevent the catalyst and SiC from being blown out of the reactor tube. The glass tube is placed for pressure relief in a bolted steel tube (d = 16 mm, s = 2 mm). To avoid any gas bypassing the reactor, the glass tube was pressed onto a rubber seal with a spring (O-Ring: Simriz (75 FFPM 495), Freudenberg&Co.KG, d_{int} = 9.5 mm, s = 3mm). Temperature is measured and controlled by a set of Eurotherm GmbH controllers. The difference in temperature along the reactor centre axis measured with a moveable thermocouple (d = 4 mm, s = 0.9 mm) was in the range between ± 1 and ± 3 K (20 cm "isothermal" zone). The reactor is heated with heating cartridges (Helios GmbH), which are placed in a metal shell. The reactor heating is split into 2 separate zones, each with its own temperature controller. The pressure at the inlet and outlet of the reactor is measured with a pressure transducer (WIKA GmbH).

Figure 5.8 presents the different catalyst bed configurations used in this study. For the FT synthesis experiments, the catalyst bed contains only the FT catalyst mixed with SiC (Fig. 5.8a), whereas for the experiments with combination of FTS and hydrocarbon reactions, the catalyst bed contains the FT and the hydroprocessing catalysts each mixed with SiC (Fig. 5.8b,c). The catalyst bed for the model compounds experiments contains only the bifunctional catalyst mixed with SiC (Fig. 5.8d). The mass of both catalysts is the same in all configurations.

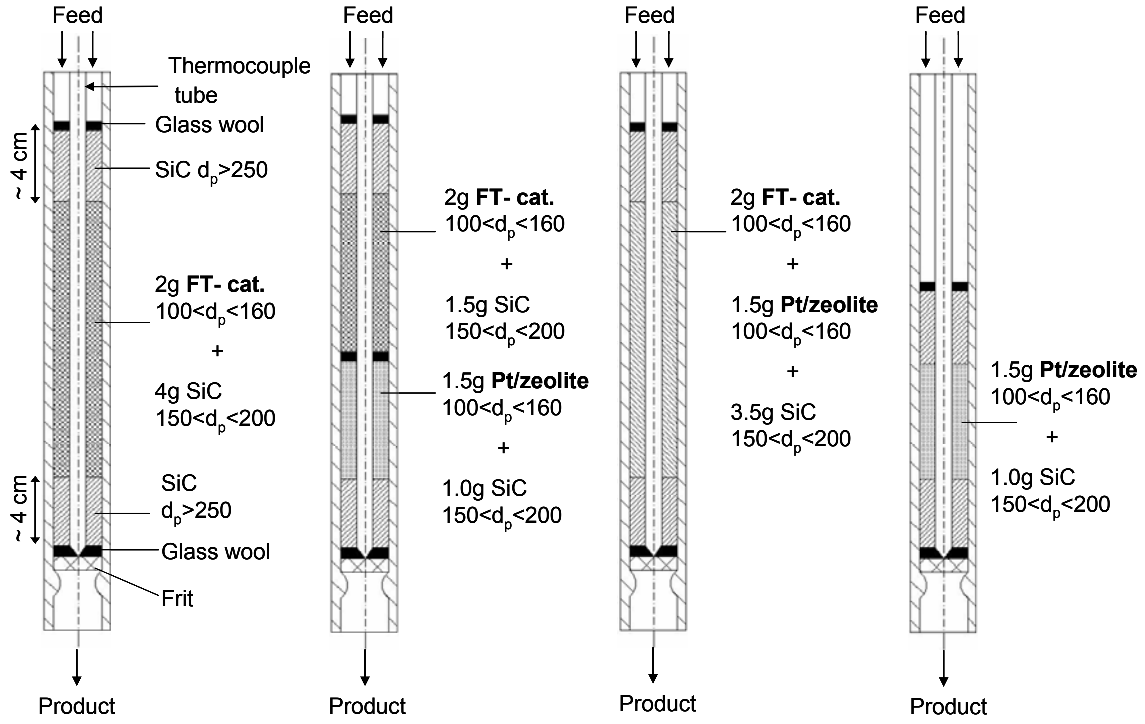
Feed
Thermocouple tube
Glass wool
~ 4 cm
SiC d$_p$>250
2g FT- cat.
100<d$_p$<160
+
4g SiC
150<d$_p$<200
~ 4 cm
SiC
d$_p$>250
Glass wool
Frit
Product
Feed
2g FT- cat.
100<d$_p$<160
+
1.5g SiC
150<d$_p$<200
1.5g Pt/zeolite
100<d$_p$<160
+
1.0g SiC
150<d$_p$<200
Product
Feed
2g FT- cat.
100<d$_p$<160
+
1.5g Pt/zeolite
100<d$_p$<160
+
3.5g SiC
150<d$_p$<200
Product
Feed
1.5g Pt/zeolite
100<d$_p$<160
+
1.0g SiC
150<d$_p$<200
Product

(a) (b) (c) (d)

Fig. 5.8: Cross section of the different catalyst-bed configurations (glass reactor). (a) FT catalyst alone, (b) dual layer with FT and hydroprocessing catalysts, (c) physical mixture with FT and hydroprocessing catalysts, (d) hydroprocessing catalyst alone. Particle diameter (d_p) in µm.

5.3.2 Execution of the experiments

Before starting each experimental campaign, the test rig is tested with pressurized hydrogen in order to ensure that there are no leaks. After that procedure, all catalysts used are reduced in-situ in the fixed-bed reactor (Tab. 5.4-5.5). The Fe-based powder has a small particle size (d_p < 100 µm) resulting in a high pressure drop along the reactor length (Δp = 0.153 bar, $\dot{V}_{H2,n}$ = 120 cm^3/min, T = 25 °C, p = 0.1 MPa, m_{cat} = 3 g + 4 g SiC). To reduce the pressure drop, the catalyst powder was mixed with distillate water and calcinated at 400 °C for 16 h.

Tab. 5.4: Reduction conditions for the FT catalyst or for the combination FT and hydroprocessing catalysts.

		Temperature program				
Gas	$\dot{V}_n / m_{FT-cat}$ cm^3 / (min·g)	p (MPa)	T_{start} (°C)	heating rate (°C/min)	T_{end} (°C)	t (T_{end}) (h)
H_2/Ar (1/3)	20	0.1	20	2	400	16

Tab. 5.5: Reduction conditions for the hydroprocessing catalysts used for the model compounds experiments.

		Temperature program				
Gas	$\dot{V}_n / m_{cat}$ cm^3 / (min·g)	p (MPa)	T_{start} (°C)	heating rate (°C/min)	T_{end} (°C)	t (T_{end}) (h)
H_2/Ar (1/3)	27	0.1	20	2	400	16

At the end of the reduction procedure, the reactor is cooled down to the desired reaction temperature (230 or 250°C) and reaction pressure is set (1 or 0.5 MPa). The feed composition and volume flow are adjusted with the mass flow controllers and flows through the bypass. The feed composition is controlled with online gas chromatographic analysis (Chapter 5.3.3). To begin an experiment, the 4-port valve is switched from bypass to reactor. This moment is defined as the start of the reaction (t = 0).

Table. 5.6: Activation conditions for the Fischer-Tropsch catalysts used.

Catalyst	Gas	p (MPa)	$\dot{V}_n / m_{cat}$ cm^3 / (min·g)	T (°C)	t (h)
Fe-based	H_2/CO (2/1)	1	15	250	~ 415
Co-based	H_2/CO (2/1)	1	15	230	~ 165

The first four days approximately are considered as activation and conditioning period for FT catalysts (Fig. 6.10, 6.16). During this period, online gas chromatographic analysis of the outlet gas flow are carried out each 40 min. Once a steady state is achieved (constant conversion and yields), reaction parameters are varied. After each reaction parameter variation, a period of 12-18 h is necessary to reach a steady-state. After this time, around 20 online-GC analyses are done and the mean value calculated. After that, five ampoule samples are taken (of which two are routinely analysed in the offline GC and the mean value calculated). A wax sample is analysed for each temperature and synthesis gas composition. Wax sample analyses are not necessary for the model compound experiments.

5.3.3 Product analysis

The product analysis is performed by gas chromatography. Organic compounds in the liquid phase (wax) and in the gas phase are analysed offline. The inorganic components are analysed online. The hydrocarbon peaks are identified by comparison with gas chromatograms from Riedel 2003, Claeys 1997 and Schulz 2007. Branched hydrocarbons are calculated cumulatively.

Ampoule technique

The ampoule sampling and analysis technique was developed in earlier studies at the Engler-Bunte Institut (Universität Karlsruhe, TH) and described by Schulz et al. 1984. Gas samples are taken using preevacuated glass ampoules (V ~ 2 ml, L ~ 120 mm, d_{ext} ~ 6.5 mm, s ~ 1.5 mm). The long capillary is pushed through a sealing rubber into the sampling chamber, which is filled with the mixture of product stream and reference gas (Fig. 5.9). By breaking the capillary tip with a fork, the ampoule is filled very quickly with gas (t << 1 s). Finally the ampoule is pulled a little way out and sealed by means of capillary fusion with a small gas burner. In this way a representative and storable gas mixture sample is obtained.

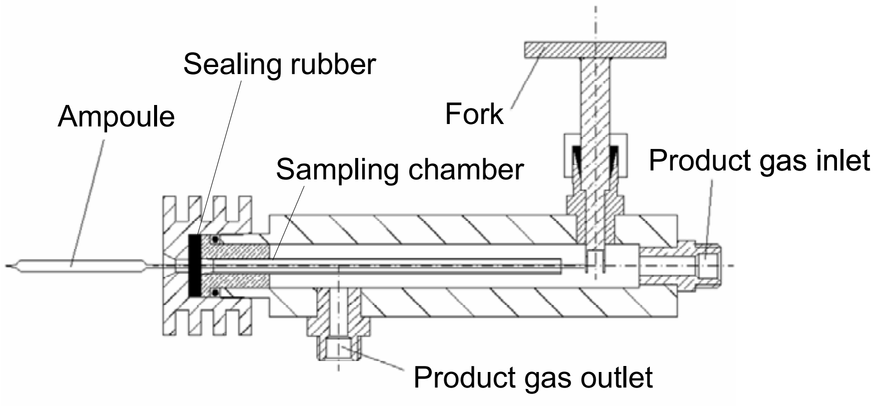

Fig. 5.9: Cross section of the ampoule sampler (Schulz 1984).

Inorganic compounds

The inorganic compounds (CO_2, H_2, N_2, CO) and CH_4 are analysed online with a HP6890N gas chromatograph (Agilent Technologies) equipped with a thermal conductivity detector (TCD), (Fig. 5.10). The sample is mixed with the carrier gas (Ar) in V1 valve and then carried to the HP1 precolumn (L = 30 m, d = 0.53 mm, s_{film} = 2.65 μm). When V3 valve switches to the "off" position, the HP1 column is cleaned and the long-chain hydrocarbons are sent to the off-gas. The other components are led to Plot Q (L = 30 m, d = 0.53 mm, s_{film} = 40 μm). When H_2, N_2, CH_4, CO reach V4 valve, this switches to the "off" position. CO_2 and H_2O flow directly to the TCD and the rest of the components are led to the Molesieve column (L = 30 m, d = 0.53 mm, s_{film} = 25 μm). The components are detected in the following order: CO_2, H_2, N_2, CH_4, CO, H_2O. Argon is also the reference gas for the thermal conductivity detector. A typical chromatogram and more details of the HP5890 gas chromatograph can be found in Table 12.1 and Figure 12.1.

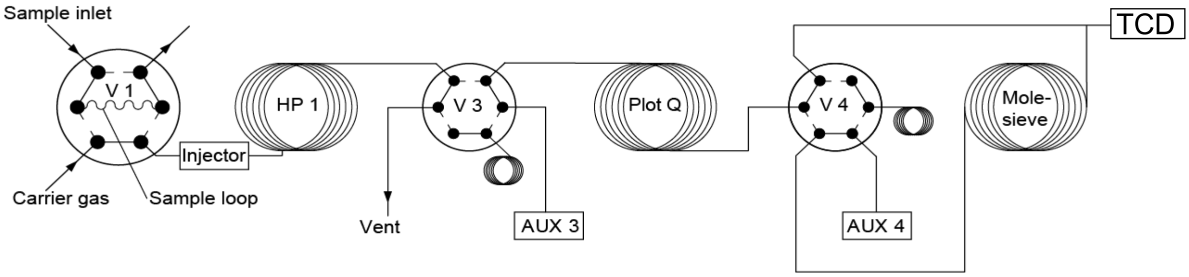

Fig. 5.10: Set-up of columns in the online gas chromatograph (HP6890N) for inorganic compounds analysis, HP6890N (Unruh 2006). ─ "off" position, --- "on" position.

Organic compounds in the gas phase

The online HP6890N gas chromatograph (Agilent Technologies) is also equipped with a flame ionization detector (FID). This online GC has no cooling system and the oven temperature is limited (290 °C). For that reason, it is only possible to analyse hydrocarbons from C_1 to C_{13} (Fig. 12.2). Furthermore, it is not possible to separate ethene/ethane and propene/propane. The carrier gas (He) leads the hydrocarbon products and cylopropane to the HP1 column (L = 30 m, d = 0.32 mm, s_{film} = 0.52 μm) where they are separated and detected in the FID (Fig. 5.11). These online analyses were used for monitoring the achievement of steady state.

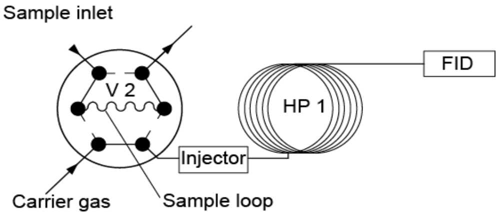
Sample inlet
V 2
HP 1
FID
Injector
Carrier gas
Sample loop

Fig. 5.11: Set-up of columns in the online gas chromatograph (HP6890N) for organic products in the gas phase analysis (Unruh 2006). ─ “off” position, --- “on” position.

A quantitative analysis of the hydrocarbon products in the gas phase (C_1-C_{20}) is carried out using the ampoule sample technique in an adapted GC (HP5890). The ampoules are injected using a heated ampoule breaker (260 °C) to ensure vaporisation of the ampoule content. The ampoule is broken by a pneumatically controlled metal rod and the ampoule content is carried to the split injector (with He as carrier gas). The hydrocarbons are separated in a fused-silica capillary column (L = 50 m, d = 0.25 mm, s_{film} = 0.25 μm) with H_2 as carrier gas and are detected in a FID. The adapted GC is equipped with two ampoule breakers and two FIDs which allow the analysis of two ampoules at the same time (Fig. 5.12). A typical chromatogram and more details of the HP6890 gas chromatograph can be found in Table 12.2 and Figures 12.4-12.6.

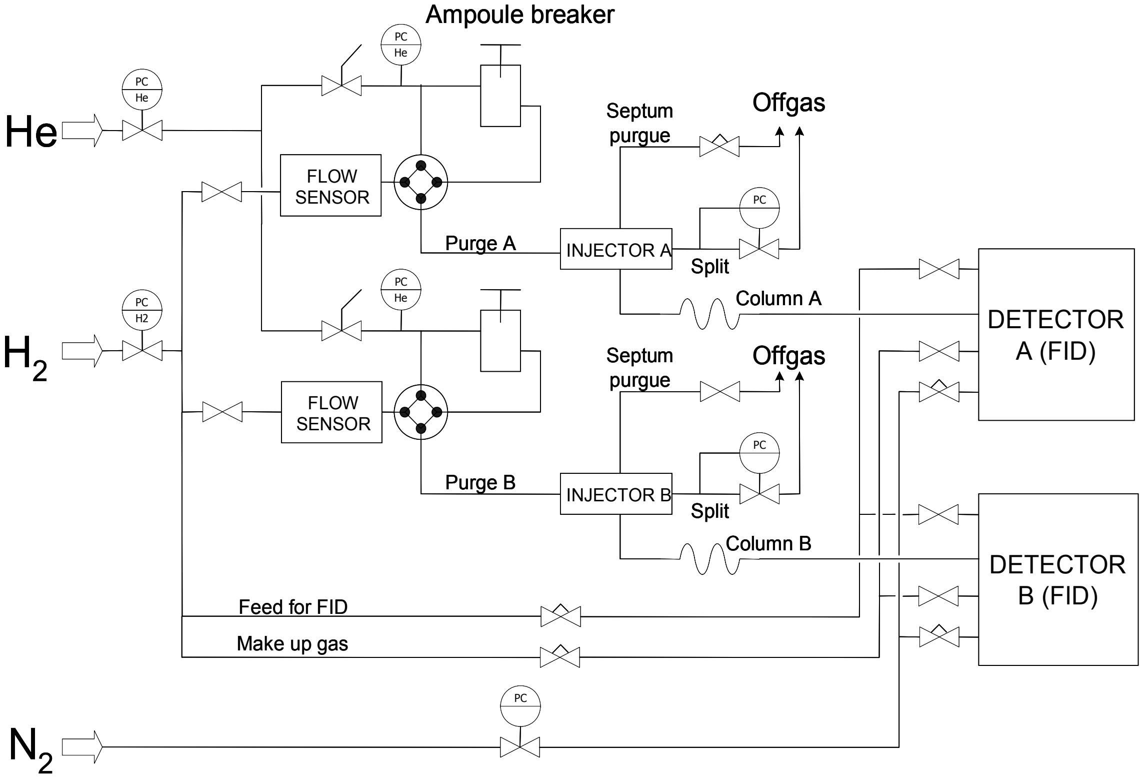
Ampoule breaker
PC He
He
H2
PC H2
N2
FLOW SENSOR
FLOW SENSOR
Septum purgue
Offgas
PC
Purge A
INJECTOR A
Split
Column A
DETECTOR A (FID)
Septum purgue
Offgas
Purge B
INJECTOR B
Split
Column B
DETECTOR B (FID)
Feed for FID
Make up gas
PC

Fig. 5.12: Process flow diagram of HP5890 offline gas chromatograph.

Organic compounds in the liquid phase (wax)

Circa 10 mg of the long-chain hydrocarbons collected in the hot wax trap are dissolved in cyclohexane in an ultrasonic bath at 50-60 °C. Approximately 1 µl of this solution is injected in an offline gas chromatograph (HP5890 Series II Plus) equipped with a FID and a HP-SiMDiST column (L = 15 m, d = 0.53 mm, s_{film} = 0.15 µm), with He as carrier gas. A typical chromatogram and more details of the HP6890 gas chromatograph can be found in Table 12.3 and Figure 12.3.

5.3.4 Data analysis and definitions

Fischer-Tropsch synthesis and FT + bifunctional catalyst experiments

With the data obtained from the online GC-TCD analysis, the ratio of the peak areas of the inorganic gases and of CH_4 related to the peak area of the internal standard (N_2) are calculated (Eq. 5.1). These ratios are multiplied with the exactly known molar flow of N_2 (15 cm^3/min) in order to obtain the molar flows of these gases, which are used to calculate the conversion of CO and H_2, and the yield of CO_2 and CH_4.

$$\frac{\dot{N}_j}{\dot{N}_{N_2}} = f_j \cdot \frac{A_j}{A_{N_2,\mathrm{Ref}}} \tag{5.1}$$

The factors (f_j) for the inorganic compounds and CH_4 analysis with the thermal conductivity detector are calculated by analysing different calibration gas bottles (Air Liquide GmbH, BASI Schöberl GmbH&Co.).

The peak area of the organic products in the gas phase (proportional to $N_{C,i}$) obtained from the adapted offline GC-FID analysis are referred to the peak area of cyclopropane and muliplied with the exactly known molar flow of cyclopropane (0.5 vol-%). The peaks of oxygen-containing compounds exhibit some degree of tailing, which widens the peak. A factor (f_j) has to be introduced for the oxygenated compounds. This is calculated by means of the increment method from Kaiser 1969 (Tab. 12.4). For the other hydrocarbons, it can be assumed that the correction factor is equal to 1 (Claeys 1997). The molar flow of each hydrocarbon is calculated with the following equations (Claeys 1997):

$$\frac{N_j}{N_{N_2}} = \frac{N_{\mathrm{Re}f}}{N_j} \cdot \left(\frac{f_j \cdot A_j}{f_{\mathrm{Re}f} \cdot A_{\mathrm{Re}f}} \right) \cdot \left(\frac{y_{C\,\mathrm{Pr},\mathrm{Re}f}}{1 - y_{C\,\mathrm{Pr},\mathrm{Re}f}} \right) \tag{5.2}$$

$$\dot{N}_j = \left(\frac{N_j}{N_{N2}} \right) \cdot \dot{N}_{N_2} = \left(\frac{N_j}{N_{N2}} \right) \cdot x_{N_2,\mathrm{Re}f} \cdot \dot{V}_{N_2} / V_A \tag{5.3}$$

To calculate the molar flow on carbon basis the following equations are used (Claeys 1997):

$$\frac{N_{C,j}}{N_{N_2}} = N_{\mathrm{Re}f} \cdot \left(\frac{f_j \cdot A_j}{f_{\mathrm{Re}f} \cdot A_{\mathrm{Re}f}} \right) \cdot \left(\frac{y_{C\,\mathrm{Pr,Re}f}}{1 - y_{C\,\mathrm{Pr,Re}f}} \right) \tag{5.4}$$

$$\dot{N}_{C,j} = \left(\frac{N_{C,j}}{N_{N2}} \right) \cdot \dot{N}_{N_2} = \left(\frac{N_{C,j}}{N_{N2}} \right) \cdot x_{N_2,\mathrm{Re}f} \cdot \dot{V}_{N_2} / V_A \tag{5.5}$$

In the long-chain hydrocarbon sample (wax), no reference gas is present. The peak areas obtained from the offline GC-FID are referred to the C atoms (Eq. 5.6) and multiplied with the wax molar flow (Eq. 5.10) calculated from an overall carbon balance (Eq. 5.7-5.9). This balance assumes that the carbon balance is closed to 100 %. In reality, the carbon balance is closed within -5 and +2 C-% (Co catalyst) and -9 and +2 C-% (Fe catalyst). The hot wax trap is emptied approx. every 24 h and the product was weighed and assumed as CH_2.

$$y_{j,wax} = \frac{\left(A_j / N_{C,j} \right)}{\sum_{j=12}^{j=60} \left(A_j / N_{C,j} \right)} \tag{5.6}$$

$$\dot{N}_{C,in} = \dot{N}_{CO,in} = \dot{N}_{C,out} \tag{5.7}$$

$$\dot{N}_{C,out} = \dot{N}_{C,CO,out} + \dot{N}_{C,CO_2,out} + \dot{N}_{C,HC,out} \tag{5.8}$$

$$\dot{N}_{C,HC,out} = \dot{N}_{C,HC,ampoule} + \dot{N}_{C,HC,wax} \tag{5.9}$$

$$\dot{N}_{C,j,HC,wax} = y_{j,wax} \cdot \dot{N}_{C,HC,wax} \tag{5.10}$$

In the hot wax trap (T = 165°C, p = 1 MPa), the liquid and the gas phases are separated (equilibrium gas-liquid phases). At these operation conditions, some components (~C_{12}-C_{20}) are found in the two phases. For that reason, it is necessary to combine both gas and liquid phase analyses (Fig. 6.12, Fig. 6.19).

The molar flow of the produced water is calculated with an oxygen balance:

$$\dot{N}_{H_2O,out} = \dot{N}_{CO,in} - \dot{N}_{CO,out} - 2 \cdot \dot{N}_{CO_2,out} - \dot{N}_{alcohol,out} \tag{5.11}$$

The conversion of the reactants H_2, CO, CO_2, C_2H_4 and C_3H_6 is calculated with the following equation:

$$X_i = \frac{\dot{N}_{i,in} - \dot{N}_{i,out}}{\dot{N}_{i,in}} \tag{5.12}$$

The yield of a component *j* on carbon basis is calculated as:

$$Y_{C,j} = \frac{\dot{N}_{C,j,out}}{\dot{N}_{C,i,in}} \tag{5.13}$$

The selectivity on carbon basis is defined as the yield on carbon basis divided by conversion:

$$S_{C,j} = \frac{Y_{C,j}}{X_i} \tag{5.14}$$

The hydrocarbon mol fraction of a component *j* is defined as:

$$y_{NC} = \frac{\dot{N}_{j,HC}}{\sum_{j=1}^{j=N} \dot{N}_{j,HC}} \tag{5.15}$$

For the experiments with 1-octene, the n-C_8 conversion, the iso-C_8 and cracked product yields, and the isomers molar fraction are calculated using the following equations:

$$X_{n-C8} = \frac{\dot{N}_{1-C8H16,in} - \dot{N}_{1-C8H18,out}}{\dot{N}_{1-C8H16,in}} \tag{5.16}$$

$$Y_{iso-C8} = \frac{\dot{N}_{iso-C8,out}}{\dot{N}_{1-C8H16,in}} \tag{5.17}$$

$$Y_{cr,<C8} = \frac{\sum_{j=1}^{7} \dot{N}_{j,out}}{\dot{N}_{1-C8H16,in}} \tag{5.18}$$

$$y_{NC,iso} = \frac{\dot{N}_{j,iso}}{\sum_{j=1}^{j=8} \dot{N}_{j}} \tag{5.19}$$

The weight hourly space velocity for the experiments with 1-octene is calculated with the following equation:

$$WHSV = \frac{\dot{m}_{1-C8H16,in}}{m_{cat}} \tag{5.20}$$

The modified residence time is defined as weight mass of catalyst divided by the volume flow at reactor inlet and standard conditions:

$$\tau_{mod} = \frac{m_{cat}}{\dot{V}_{n,in}} \tag{5.21}$$

The reaction rate of a reaction *j* is defined as the change in moles of a component with respect to time, per unit volume of reaction mixture. In heterogeneous reactions, particularly those with solid phases (e.g. solid catalyst), it may be convenient to base the rate on a unit mass rather than volume (Eq. 5.22).

$$r_j = \frac{1}{m_{cat}} \cdot \frac{d\zeta_j}{dt} \tag{5.22}$$

The reaction rate for a component *i* involved in multiple reactions is defined as:

$$r_i = \sum_{j=1}^{N} r_{i,j} \quad ; \qquad r_{i,j} = \nu_{i,j} \cdot r_j \tag{5.23}$$

5.4 Mathematical reactor model: fixed-bed-reactor balance

Fixed-bed-reactor model

The derivation of differential material balance or continuity equations for the components *i* flowing in a reactor is treated in detail in textbooks on chemical reaction engineering (e.g. Baerns et al. 1987). The material balance for a fixed-bed reactor considering only one dimension and gas phase is defined as:

$$\frac{\partial(C_i)}{\partial t} = -div(u \cdot C_i) + div(D_{i,eff} \cdot gradC_i) + \rho_{cat} \cdot (1-\varepsilon)/\varepsilon \cdot \sum_{j=1}^{N} \nu_{i,j} \cdot r_j \tag{5.24}$$

which results in Equation 5.25 for constant $D_{i,eff}$:

$$\frac{\partial(C_i)}{\partial t} = -\frac{\partial(C_i \cdot u_g)}{\partial z} + D_{i,eff} \frac{\partial^2(C_i)}{\partial z^2} + \rho_{cat} \cdot (1-\varepsilon)/\varepsilon \cdot \sum_{j=1}^{N} \nu_{i,j} \cdot r_j \tag{5.25}$$

Equation 5.25 can also be expressed by using the density of the catalyst bed:

$$\frac{\partial(C_i)}{\partial t} = -\frac{\partial(C_i \cdot u_g)}{\partial z} + D_{eff} \frac{\partial^2(C_i)}{\partial z^2} + \rho_s / \varepsilon \cdot \sum_{j=1}^{N} \nu_{i,j} \cdot r_j \tag{5.26}$$

For the fixed-bed reactor described in Chapter 5.3.1, a pseudohomogeneous one-dimensional model is applied, based on the following assumptions (Eq. 5.27):

- steady state,
- one-dimensional (axial direction),
- homogenous temperature along the reactor (isothermal),

- internal mass transfer limitations and wall effects can be neglected as the particle size of the fixed bed does not exceed 160 µm (Chapter 12.6),
- axial dispersion effects are negligible under the reaction conditions used (Bo > 50, Chapter 12.6),
- pressure drop along the reactor can be neglected.

$$\frac{d\left(C_i \cdot u_g\right)}{dz} = \rho_s / \varepsilon \cdot \sum_{j=1}^{N} \nu_{i,j} \cdot r_j \tag{5.27}$$

By multiplying Equation 5.27 with the cross-sectional area, the following simplified material balance equation can be obtained:

$$\frac{d\dot{N}_i}{dz} = \frac{m_{cat}}{L_s} \cdot \sum_{j=1}^{N} \nu_{i,j} \cdot r_j \tag{5.28}$$

with the following initial conditions at z = 0

$$\dot{N}_{i,z=0} = \dot{N}_{i,in} \tag{5.29}$$

The integration of this system of ordinary differential equations is carried out by means of a Runge-Kutta method from Matlab Software.

Reaction rates - FT synthesis and CO/CO$_2$-shift reactions

The reaction rate for the FT synthesis reaction on the *Co-based catalyst* was chosen from Yates et al. 1991:

$$\mathrm{r_{FT,Co}} = \mathrm{k_{FT,Co}} \cdot \frac{\mathrm{p_{CO} \cdot p_{H_2}}}{\left(1 + \mathrm{a_{FT,Co} \cdot p_{CO}}\right)^2} \tag{5.30}$$

The reaction rate for the FT synthesis and CO/CO$_2$-shift reactions on the *Fe-based catalyst* was chosen from Zimmerman et al. 1990, Riedel et al 2001, Riedel 2003 and Unruh 2006 (Eq. 5.31-5.32). The CO/CO$_2$-shift reaction is an equilibrium reaction, being close to equilibrium under FT reaction conditions. For the temperature effect on the equilibrium constant, Equation 5.33 is used (Newsome 1980, van der Laan et al. 1999a).

$$\mathrm{r_{FT,Fe}} = \mathrm{k_{FT,Fe}} \cdot \frac{\mathrm{p_{CO} \cdot p_{H_2}}}{\mathrm{(p_{CO} + a_{FT,Fe} \cdot p_{H_2O} + b_{FT,Fe} \cdot p_{CO_2})}} \tag{5.31}$$

$$\mathrm{r_{CO_2-SH}} = \mathrm{k_{SH}} \cdot \frac{\mathrm{p_{H_2} \cdot p_{CO_2} - (p_{CO} \cdot p_{H_2O})/K_{p,CO_2}}}{\mathrm{(p_{CO} + a_{SH} \cdot p_{H_2O} + b_{SH} \cdot p_{CO_2})}} \tag{5.32}$$

$$\mathrm{K_{p,CO_2}} = 1/\mathrm{K_{p,CO}} = \frac{\mathrm{p_{CO} \cdot p_{H_2O}}}{\mathrm{p_{CO_2} \cdot p_{H_2}}}; \qquad \mathrm{K_{p,CO}} = \exp\left(\frac{2073}{\mathrm{T}} - 2.029\right) \tag{5.33}$$

With the reaction rates presented above (Eq. 5.31-5.33) and the material balance equation (Eq. 5.28) it is possible to determine the kinetic constants of the FTS and CO/CO_2-shift reactions by using the least-square method. This method minimises the summed square of residuals (difference between calculated and the observed experimental value):

$$\chi^2 = \sum_{j}^{m}\sum_{i=1}^{n}\left(\frac{f(x_i,P)-y_i)}{y_i}\right)^2 \tag{5.34}$$

The term *n* accounts for the number of experimental points for each residence time (2-4 experimental points per temperature) and *m* accounts for the number of functions (e.g. CO conversion, CO_2 yield).

Hydroprocessing hydrocarbon reactions

The material balance for the hydrocarbons reacting on a bifunctional catalyst (Pt/zeolite) is based on Equation 5.28 with the following initial conditions:

$$\dot{N}_{i,z=inlet\ \text{sec}ond\ layer} = \dot{N}_{i,z=oulet\ first\ layer} \quad \text{; for a dual-layer configuration} \tag{5.35}$$

$$\dot{N}_{i,z=0} = \dot{N}_{i,in} \quad \text{; for a physical-mixture configuration} \tag{5.36}$$

The detailed kinetic model and the reaction rates for the hydrocarbon reactions on a bifunctional catalyst are presented in Chapter 7. Due to the large number of molecules involved in these reactions, the hydrocarbons are grouped into nine fractions distinguishing between n- and iso-alkanes (C_{21+}, C_{15-20}, C_{10-14}, C_{5-9}, C_{2-4}). Assuming that only hydrocracking, isomerisation, hydrogenation and short-chain alkenes oligomerisation reactions take place on the Pt/zeolite catalyst (see Chapter 7.1), nine material balance equations are required. Equation 5.37 presents the change of the molar flow of the n-alkane fractions along the reactor length.

$$\frac{d\dot{N}_{n-i}}{dz} = \frac{m_{cat}}{L_s}\cdot(-r_{i,iso}) \tag{5.37}$$

Equations 5.38-5.41 present the change of the molar flow of the iso-C_i fractions along the reactor length:

$$\frac{d\dot{N}_{iso-21+}}{dz} = \frac{m_{cat}}{L_s}\cdot(r_{21+,iso} + (-1+2\cdot(1-\sum_{i=15-20}^{i=2-4}\nu_{21+/i}))\cdot r_{21+,cr}) \tag{5.38}$$

$$\frac{d\dot{N}_{iso-15-20}}{dz} = \tag{5.39}$$

$$\frac{m_{cat}}{L_s}\cdot(r_{15-20,iso} + (-1+2\cdot(1-\sum_{i=10-14}^{i=2-4}\nu_{15-20/i}))\cdot r_{15-20,cr} + 2\cdot\nu_{21+/15-20}\cdot r_{21+,cr})$$

$$\frac{d\dot{N}_{iso-10-14}}{dz} = \frac{m_{cat}}{L_s} \cdot \left(r_{10-14,iso} + \left(-1 + 2 \cdot \left(1 - \sum_{i=5-9}^{i=2-4} \nu_{10-14/i}\right)\right) \cdot r_{10-14,cr} + \sum_{i=21+}^{i=15-20} 2 \cdot \nu_{i/10-14} \cdot r_{i,cr}\right) \tag{5.40}$$

$$\frac{d\dot{N}_{iso-5-9}}{dz} = \frac{m_{cat}}{L_s} \cdot \left(r_{5-9,iso} + \left(-1 + 2 \cdot \left(1 - \nu_{5-9/2-4}\right)\right) \cdot r_{5-9,cr} + \sum_{i=21+}^{i=10-14} 2 \cdot \nu_{i/5-9} \cdot r_{i,cr} + r_{ol}\right) \tag{5.41}$$

The fraction C_{2-4} includes the iso-C_4 and its molar-flow change along the reactor can be described with the following equation:

$$\frac{d\dot{N}_{2-4}}{dz} = \frac{m_{cat}}{L_s} \cdot \left(\sum_{i=21+}^{i=5-9} 2 \cdot \nu_{i/2-4} \cdot r_{i,cr} - 2 \cdot r_{ol}\right) \tag{5.42}$$

The determination of the kinetic constants for the hydrocarbon reactions on Pt/zeolite catalyst is performed by means of a trial and error method (see Chapter 7.2). Considering the amount of experimental data, the number of kinetic parameters to be determined is too large to use the least-square method.

5.5 Experimental conditions and experimental plan

The following tables summarise all the experiments carried out in the present study. Tables 5.7-5.8 include the experiments with model compounds (1-octene, ethene/propene) on bifunctional catalysts (Pt/ZSM-5, Pt/Beta). Table 5.9 includes the Fischer-Tropsch synthesis experiments on Co- and Fe-based catalysts. The experiments on Co-based catalysts in combination with bifunctional catalysts in different catalyst-bed configurations (dual-layer, physical-mixture) are included in Tables 5.10-5.12. The combination Fe-based and Pt/ZSM-5 catalyst in a dual-layer configuration is presented in Table 5.13. Pt/ZSM-5 was also tested with H_2/CO_2 for CO/CO_2-shift activity (Tab. 5.14). Pt/ZSM-5 and Pt/Beta catalysts were also tested alone with synthesis gas at temperatures between 200 and 300 °C (τ_{mod} = 3000 kg·s/m^3, p = 1 MPa, $(p_{H2}/p_{CO})_{in}$ = 2).

Experimental plan

Tab. 5.7: Reaction conditions for the 1-octene experiments on bifunctional catalysts (* related to 1-octene).

Catalyst	m_{cat} (g)	p (MPa)	WHSV * (h^{-1})	T (°C)	$(p_{H2}/p_{CO}/p_{Ar}/p_{CO2})_{in}$ (-)	$(p_{H2}/p_{1\text{-}C8H16})_{in}$ (-)	$(p_{CO}/p_{1\text{-}C8H16})_{in}$ (-)	$(p_{Ar}/p_{1\text{-}C8H16})_{in}$ (-)	$\dot{V}_{n,in}$ (cm^3/min)
Pt/ZSM-5	1.5	0.5	0.22	230, 250, 300	2/1/0/0, 2/0/1/0	17.1 - 21.4	0, 10.7	0 - 8.5	30
Pt/Beta	1.5	0.5	0.65	230, 250, 300	2/1/0/0, 2/0/1/0 1/0/0/0, 1/1/0/0 3/1/0/0, 2/1/0/1	3.2 - 18.5	0 - 4.7	0 - 8.4	20 - 84

Tab. 5.8: Reaction conditions for the oligomerisation experiments with ethene:propene (50:50 vol-%) on bifunctional catalysts.

Catalyst	m_{cat} (g)	p (MPa)	T (°C)	$\dot{V}_{n,C2H4,in}$ (cm^3/min)	$\dot{V}_{n,C3H6,in}$ (cm^3/min)	$\dot{V}_{n,N2,in}$ (cm^3/min)	$\dot{V}_{n,H2,in}$ (cm^3/min)	$\dot{V}_{n,CO,in}$ (cm^3/min)	τ_{mod} (g·s/cm^3)
Pt/ZSM-5	1.5	1.0	215	0.3, 0.7	0.3, 0.7	6.0, 13.1	0, 20	0, 10	2.0 - 13.6
		1.0	230	0.3 - 0.7	0.3 - 0.7	6.0 - 13.1	0, 20	0, 10	
		0.5, 1.0	250	0.3 - 0.7	0.3 - 0.7	6.0 - 13.1	0, 20	0, 10	
		0.5, 1.0	270	0.3, 0.7	0.3, 0.7	6.0, 13.1	0, 20	0, 10	
Pt/Beta	1.5	0.5, 1.0	250	0.3	0.3	6.0	0	0	13.6

Tab. 5.9: Reaction conditions of the FTS experiments.

Catalyst	m_{cat} (g)	T (°C)	p (MPa)	$(p_{H2}/p_{CO}/p_{CO2})_{in}$ (-)	$\dot{V}_{n,in}$ (cm^3/min)
Co-based	2	200	1	2/1/0	30 / 60
		215		2/1/0	30 / 60
		230		2/1/0	30 / 40 / 60 / 120
				1/1/0	30 / 60
				3/1/0	60
Fe-based	2	235	1	2/1/0	30 / 40
		250		2/1/0	30 / 40 / 60 / 120
				1/1/0	30 / 60
				3/0/1	30 / 40 / 60 / 120
		260		2/1/0	30 / 40 / 60
				1/1/0	30
		270		2/1/0	30 / 60
				1/1/0	30 / 60
				3/0/1	30 / 40 / 60 / 120
		280		3/0/1	30 / 40 / 60 / 120

Tab. 5.10: Reaction conditions of the Co-based + Pt/ZSM-5 experiments. *Dual-layer* configuration.

Catalyst	m_{cat} (g)	T (°C)	P (MPa)	$(p_{H2}/p_{CO}/p_{CO2})_{in}$ (-)	$\dot{V}_{n,in}$ (cm^3/min)
Co-based	2	200	1	2/1/0	30 / 60
		215		2/1/0	30 / 60
+	+	230		2/1/0	30 / 40 / 60 / 120
				1/1/0	30 / 60
Pt/ZSM-5	1.5			3/1/0	60

Tab. 5.11: Reaction conditions of the Co-based + Pt/Beta experiments. *Dual-layer* configuration.

Catalyst	m_{cat} (g)	T (°C)	p (MPa)	$(p_{H2}/p_{CO}/p_{CO2})_{in}$ (-)	$\dot{V}_{n,in}$ (cm^3/min)
Co-based	2	200	1	2/1/0	30 / 60
		215		2/1/0	30 / 60
+	+	230		2/1/0	30 / 40 / 60 / 120
				1/1/0	30 / 60
Pt/Beta	1.5			3/1/0	60

Tab. 5.12: Reaction conditions of the Co-based + Pt/ZSM-5 experiments. *Physical-mixture* configuration.

Catalyst	m_{cat}	T	p	$(p_{H2}/p_{CO}/p_{CO2})_{in}$	$\dot{V}_{n,in}$
	(g)	(°C)	(MPa)	(-)	(cm^3/min)
Co-based	2	200	1	2/1/0	30 / 60
		215		2/1/0	30 / 60
+	+	230		2/1/0	30 / 40 / 60 / 120
				1/1/0	30 / 60
Pt/ZSM-5	1.5			3/1/0	30 / 60

Tab. 5.13: Reaction conditions of the Fe-based + Pt/ZSM-5 experiments. *Dual-layer* configuration.

Catalyst	m_{cat}	T	p	$(p_{H2}/p_{CO}/p_{CO2})_{in}$	$\dot{V}_{n,in}$
	(g)	(°C)	(MPa)	(-)	(cm^3/min)
Fe-based	2	250	1	2/1/0	30 / 60
+	+			1/1/0	30 / 60
Pt/ZSM-5	1.5	270		2/1/0	30 / 60
				1/1/0	30 / 60

Tab. 5.14: Reaction conditions of water-gas-shift activity of Pt/ZSM-5 catalyst.

Catalyst	m_{cat}	T	p	$(p_{H2}/p_{CO}/p_{CO2})_{in}$	$\dot{V}_{n,in}$
	(g)	(°C)	(MPa)	(-)	(cm^3/min)
Pt/ZSM-5	1.5	200	1	1/0/1	30
		230			
		250			
		300			

6 Experimental results and discussion

6.1 Preliminary experiments with model compounds on bifunctional catalysts

For the combination of FTS and hydrocarbon reactions it is important to know if the bifunctional catalysts show a synthesis gas activity. The bifunctional catalysts used in this study (Pt/ZSM-5, Pt/Beta) were reduced with H_2 following the procedure presented in Table 5.5. First, the bifunctional catalysts were tested alone with synthesis gas at temperatures between 200 and 300 °C (τ_{mod} = 3000 kg·s/m^3, $(p_{H2}/p_{CO})_{in}$ = 2, p = 1 MPa), where no synthesis activity was observed. They were also tested with H_2/CO_2 for CO/CO_2-shift activity (see Tab. 5.14), where 0.5 % CO yield was measured at 200 °C and 2 % at 300 °C, indicating that Pt has a low CO/CO_2-shift activity at these reaction conditions. Measured exit concentrations are far away from the equilibrium (Fig. 6.1).

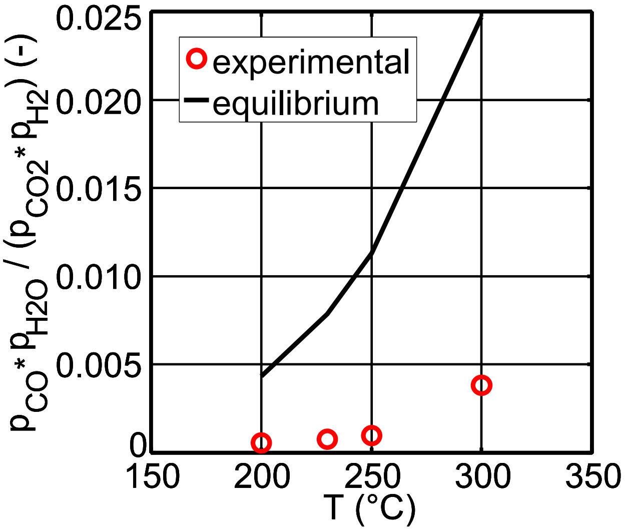

Fig. 6.1: CO/CO_2-shift activity of Pt/ZSM-5 catalyst: measured exit gas composition compared with chemical equilibrium. Reaction conditions see Table 5.14.

The first set of experiments with model compounds on bifunctional catalysts was carried out with 1-octene. This compound is not representative for the wax fraction (C_{21+}) but it is easy to handle in the experiments (liquid at room temperature, boiling temperature moderately low, VDI-Wärmeatlas 1984). In addition, the experimental results can be compared with the results predicted from the kinetic model used in Chapter 4. Considering the theory that cracking activity is proportional to hydrocarbon chain length, it can be concluded that if the model compound experiments show C_8 cracking activity, wax molecules (C_{21+}) should also crack under the same conditions.

Several research groups (as described in Chapter 3.2) have investigated hydroisomerisation/hydrocracking reactions of hydrocarbon model compounds (n-C_{6-16}). They used bifunctional catalysts (Pt/ZSM5, Pt/Beta, Pt/Y) at temperatures between 180 and 300 °C. However, none of them investigated the effect of CO on these reactions. The effect of CO will be presented in the next section. All the previous studies used n-alkane as model compound. In the present study, an n-alkene was chosen in order to test the hydrogenation activity of Pt.

Liquid 1-octene was fed with a high-pressure pump and evaporated. Then, it was mixed either with H_2/CO or H_2/Ar (Ar as inert gas) and fed into the reactor. The high-pressure pump allowed operation only at maximum pressure of 0.5 MPa. Pressure and H_2/1-C_8H_{16} molar ratio was kept constant in all the experiments (Tab. 5.7).

6.1.1 Effect of CO on 1-octene reactions on Pt/ZSM-5

Platinum showed a high hydrogenation activity since 1-octene was totally hydrogenated even in the presence of CO. For that reason, it was considered appropriate to use n-C_8 conversion for the discussion (see definition in Eq. 5.16).

In absence of CO, n-C_8 conversion was close to 100 % between 230 and 300 °C. As shown in Figure 6.2 cracking yield is higher than isomerisation yield. The typical maximum of the isomerisation yield curve cannot be observed indicating that cracking reactions of iso-alkane dominate. Figure 6.2 also compares experimental and calculated values (with Steijns et al. 1981, Froment 1987 kinetic model, see Chapter 3.2.6). Higher temperatures are necessary to achieve the conversion and yields predicted from the kinetic model. Considering that the kinetic model was developed for a different type of bifunctional catalyst (Pt/USY), the agreement between experimental and calculated data is surprisingly good.

In the presence of CO, n-C_8 conversion was also close to 100 %. However, iso-C_8 yield is higher than in absence of CO, thus resulting in lower cracking yield. The rate of iso-C_8 cracking reactions is more strongly affected by the presence of CO than the rate of isomerisation. However, this effect of CO decreases as the temperature is raised (Fig. 6.3).

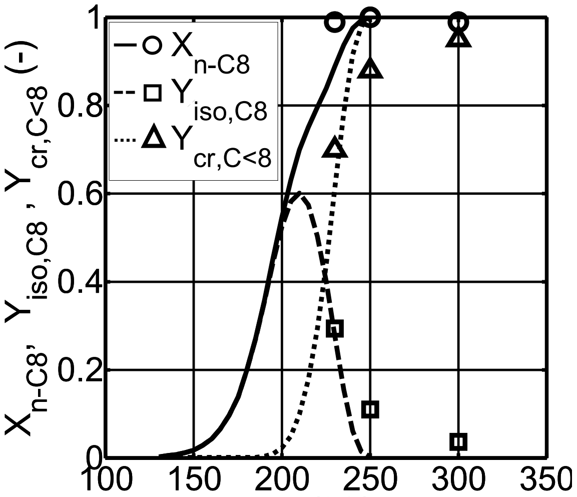

Fig. 6.2: Reactions of 1-C_8H_{16} without CO. Feed: 1-C_8H_{16} + H_2 + Ar. Catalyst: Pt/ZSM-5. Points: experimental, curves: calculated with Steijns et al. 1981, Froment 1987 kinetic model with Pt/USY catalyst (see Chapter 3.2.6). p = 0.5 MPa, WHSV = 0.22 h^{-1}. Other reaction conditions see Table 5.7.

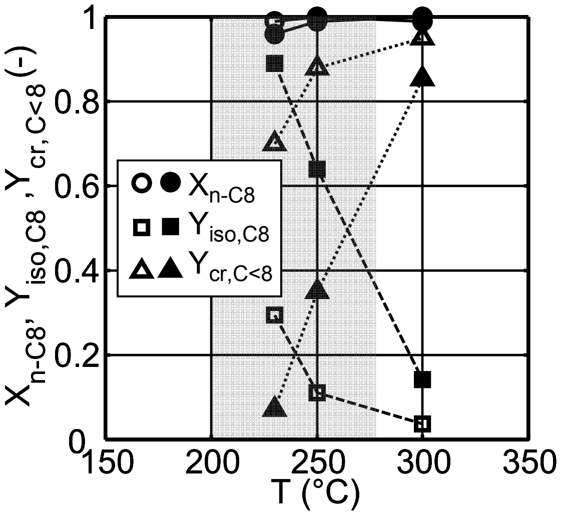

Fig. 6.3: Reactions of 1-C_8H_{16} without CO (open symbols) and with CO (full symbols). Feed: 1-C_8H_{16} + H_2 + Ar or CO. Catalyst: Pt/ZSM-5. Points: experimental, curves: trends. p = 0.5 MPa, WHSV = 0.22 h^{-1}. Other reaction conditions see Table 5.7. Grey range: FTS temperature range.

Figure 6.3 shows that in the FTS temperature range and in the presence of CO mainly isomerisation reactions take place (grey range in Fig. 6.3).
In the absence of CO, the distribution of the cracked products is nearly symmetrical with respect to C_4, with approximately the same values for C_3 and C_5 (Fig. 6.4a). This result, together with relatively small values of C_1, C_2, C_6, C_7, indicates that primary hydrocracking reactions are predominant. Primary hydrocracking is typical of bifunctional catalysts with a good metal/acid-ratio (see Chapter 3.2.4.2). The presence of low amounts of methane and ethane could be an evidence for the occurrence of metal-catalysed cracking (hydrogenolysis). In the presence of CO, this symmetrical product distribution is only observed at 300 °C, since at lower temperatures, iso-C_8 and in particular monomethyl isomers are the main product according to ZSM-5 shape-selectivity (Fig. 6.5).

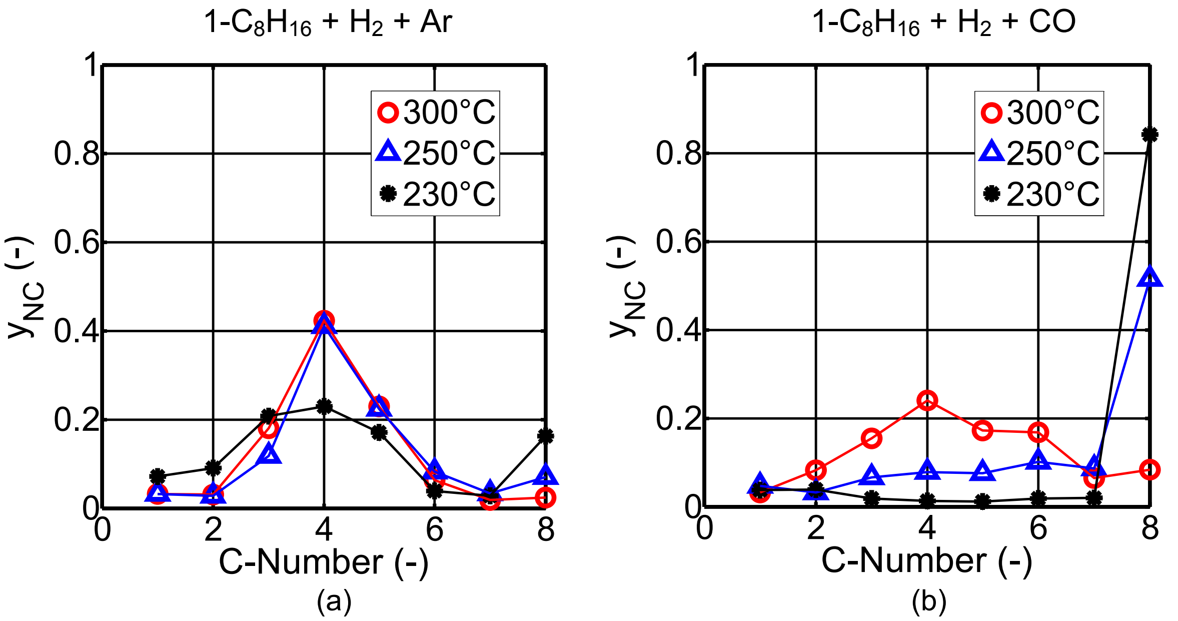

(a) (b)

Fig. 6.4: Effect of CO and temperature on hydrocarbon molar fractions after hydrogenation, hydrocracking and hydroisomerisation reactions of 1-C_8H_{16} with Pt/ZSM-5. Points: experimental, curves: trends. p = 0.5 MPa, WHSV = 0.22 h^{-1}. Other reaction conditions see Table 5.7.

As for the interpretation of the measured CO effect, Weiss et al. 1984 concluded that CO decreases the hydrogenation activity of noble metals. On the other side, Al-Ammar et al. 1978 and Arnold et al. 1997, concluded that CO competes with H_2 for adsorption.

As a consequence, if CO is not totally converted during FTS, the main product of the combination FTS and hydrocarbon reactions should be isomers. But as already mentioned, C_8 is not representative for the wax fraction. Propane and higher n-alkanes have a critical molecule diameter around 0.49 nm (Turro et al. 1990). These molecules should be able to diffuse and react in the ZSM-5 pores (see Chapter 5.2.2). Following the correlation of Sie et al. 1988 (Fig. 3.12), it could be assumed that long-chain hydrocarbons (C_{21+}) should also undergo isomerisation and cracking reactions at FT temperatures.

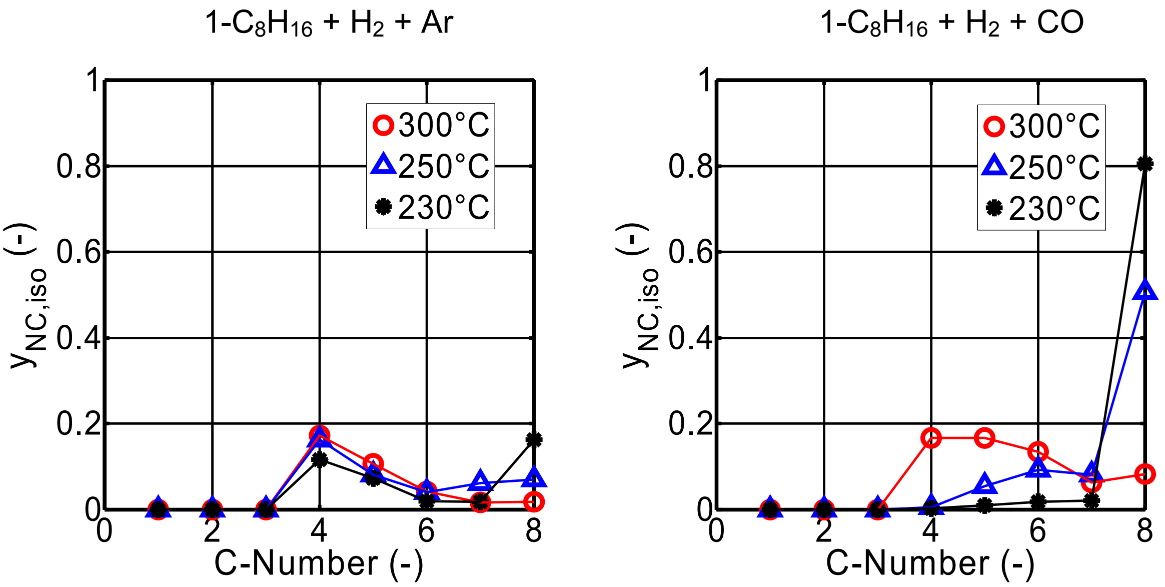

(a) (b)

Fig. 6.5: Effect of CO and temperature on isomer content. Reactions of 1-C_8H_{16} with Pt/ZSM-5. Points: experimental, curves: trends. Definition of $y_{NC,iso}$ see Equation 5.19. p = 0.5 MPa, WHSV = 0.22 h^{-1}. Other reaction conditions see Table 5.7.

6.1.2 Effect of CO on 1-octene reactions on Pt/Beta

The same type of experiments with 1-octene was performed on Pt/Beta. The feed hydrocarbon 1-octene is also completely hydrogenated, but n-C_8 conversion is lower than with Pt/ZSM-5 (Fig. 6.6). The main products are C_8 isomers. Beta zeolite is used especially in n-alkane isomerisation processes to enhance gasoline octane numbers (see Tab. 12.11). The pores of Beta zeolite are larger than the pores of ZSM-5 and should allow the formation and diffusion of dibranched hydrocarbons (Fig. 3.6-3.7). The gas chromatographic technique used was not sensitive enough to separate these C_8 isomers.

Weitkamp et al. 1983 reported that the cracking mechanism in Pt/ZSM-5 is basically different from that in large-pore catalysts like Pt/Beta. In large-pore zeolites, ß-scission of types A and B_2 of alkylcarbenium ion is operative, thus resulting in high yields of branched molecules (see Chapter 3.2.5, Fig. 3.10). It was proposed that inside ZSM-5 pores type C of ß-scission is involved to a considerable extent in the cracking mechanism.
The different types of ß-scission mechanisms are most probably not the only reason for the different activity of Pt/ZSM-5 and Pt/Beta catalysts. The two zeolites used here have not only different geometry and pore size, but also different Si/Al-ratio, acid strength, crystal size and specific surface area (Tab. 5.2-5.3). Therefore, it is difficult to explain their activity. The TPD analysis shows that Beta-zeolite has lower acid strength than ZSM-5 (Fig. 5.5) which leads to higher isomerisation activity (Yashima et al. 1996, Wang et al. 1997). Beta crystal size is smaller than that of ZSM-5, meaning that the number of acid sites on the external surface of Beta zeolite is higher than of ZSM-5 (Tab. 5.2, Fig. 5.4). It is also known that external acid sites are less strong, also leading to a higher isomerisation activity. The shape-selectivity of ZSM-5 also plays a role, as it tends to crack the hydrocarbons molecules in order to reduce their size and favours the diffusion.

In the presence of CO, n-C_8 conversion on Pt/Beta catalyst is lower than in absence of CO, but the main products are also C_8 isomers. Only at 300 °C, a limited cracking activity is observed (Fig. 6.6).

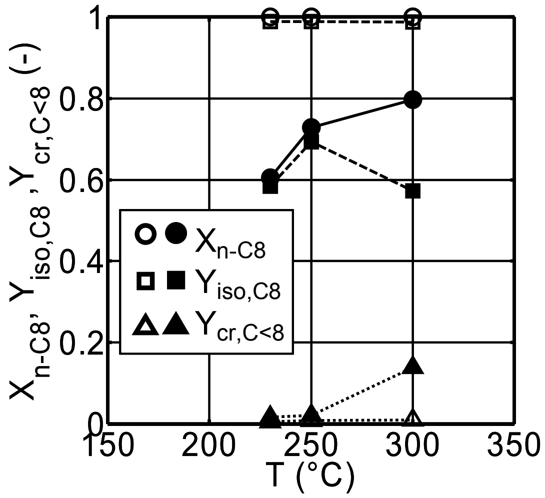

Fig. 6.6: Reactions of 1-C_8H_{16} without CO (open symbols) and with CO (full symbols). Feed: 1-C_8H_{16} + H_2 + Ar or CO. Catalyst: Pt/Beta. Points: experimental, curves: trends. p = 0.5 MPa, WHSV = 0.65 h^{-1}, $(p_{H2}/p_{CO}/p_{Ar})_{in}$ = 2/1/0, 2/0/1, $(p_{H2}/p_{1\text{-}C8H16})_{in}$ = 6.

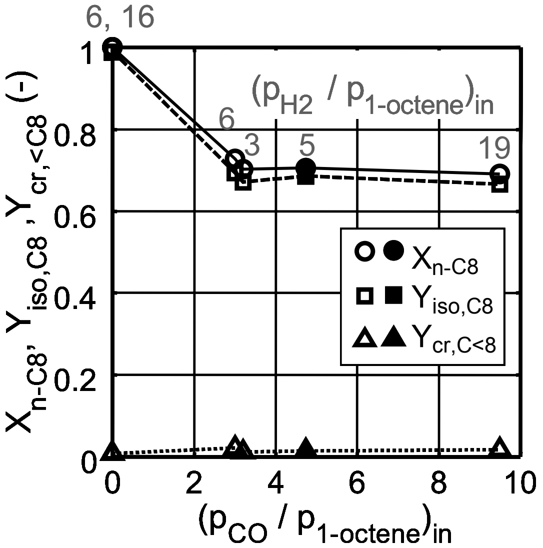

Fig. 6.7: Effect of CO and H_2 inlet partial pressure on 1-C_8H_{16} reactions. Catalyst: Pt/Beta. Feed: open symbols: 1-C_8H_{16} + H_2 + Ar or CO, full symbols: 1-C_8H_{16} + H_2 + CO + CO_2. Points: experimental, curves: trends. T = 250 ºC, p = 0.5 MPa, WHSV = 0.65 h^{-1}. Other reaction conditions see Table 5.7.

As for the influence of CO and H_2 partial pressures on Pt/Beta (Fig. 6.7) the ratio p_{H2}/p_{HC} (>1) seems not to have any effect on n-C_8 conversion. The presence of CO decreases the C_8-conversion.

After one month on stream, no catalyst deactivation was observed in both cases (Pt/ZSM-5, Pt/Beta). However, Pt/Beta changed its colour from grey to black during the experiments. Bulky hydrocarbons (e.g. aromatics, large isomers) may have deposited on the catalyst surface without affecting acidic sites activity.

6.1.3 Effect of CO and H_2 on ethene and propene oligomerisation reactions on Pt/ZSM-5 and Pt/Beta

ZSM-5 zeolite is applied as a catalyst in industrial alkene oligomerisation processes (Tab. 12.13) like MTG (Methanol-to-Gasoline), MOGD (Mobile Olefine to Gasoline and Distillate) or MtSynfuels®. These processes represent an important route for the production of synthetic liquid fuels (Stöcker et al. 1999, O'Connor 1989, Liebner et al. 2004). Alkenes are also products of the FT synthesis, especially on Fe-based catalysts. For that reason, alkene oligomerisation reactions were studied on bifunctional catalysts at FT temperatures and low pressure, as well as the effect of synthesis gas presence. Due to the limitation of the mass-flow controllers flow range it was not possible to keep the alkene partial pressure constant by addition of synthesis gas (Tab. 5.8).

The experimental results show that ethene and propene oligomerisation reactions take place. C_{13} was the largest hydrocarbon molecule obtained. Propene conversion is higher than ethene conversion, meaning that long-chain hydrocarbons are mainly formed from propene (Fig. 6.8). Propene conversion increases with temperature. This tendency cannot clearly be observed with ethene. O'Connor et al. 1989 reported that ethene is relatively unreactive, but its conversion can be strongly enhanced at temperatures between 285 and 375 °C and at pressure between 0.4 and 3 MPa.

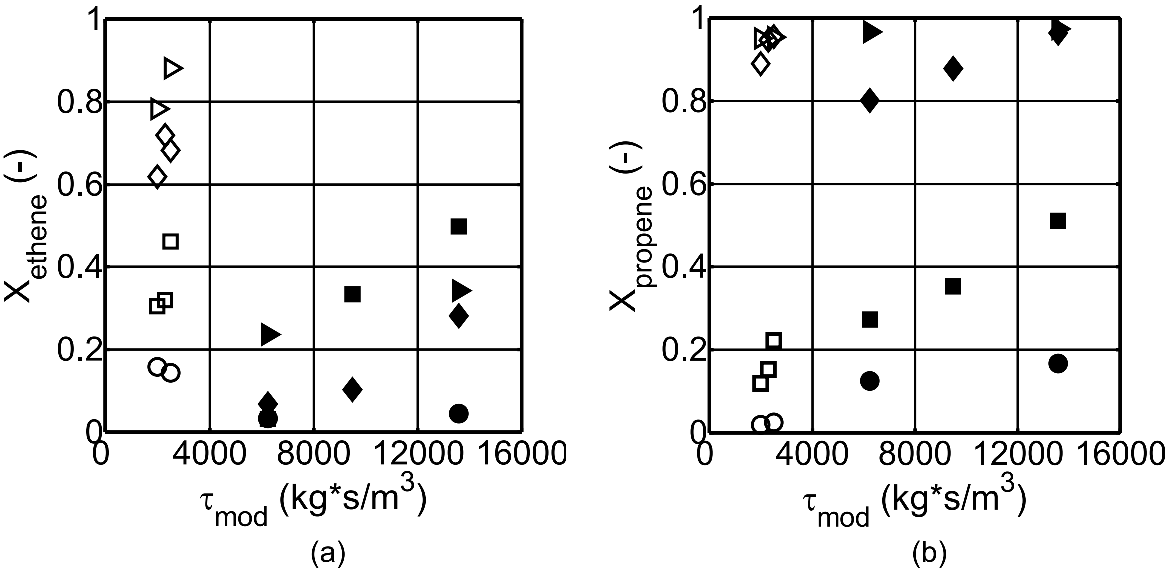

(a) (b)

Fig. 6.8: Effect of the presence of synthesis gas and temperature on ethene (a) and propene (b) conversion versus modified residence time on Pt/ZSM-5. Feed: C_2H_4 + C_3H_6 + H_2 + CO + N_2 (open symbols), C_2H_4 + C_3H_6 + N_2 (full symbols). T = 215 °C (circles), 230 °C (squares), 250 °C (diamonds), 270 °C (triangle), p = 1 MPa. Ranges of other reaction conditions see Table 5.8.

Oligomerisation processes at high conversion are accompanied by side reactions such as double bond and skeletal isomerisation or cracking, which lead to a continuous distribution of components carbon numbers (Fig. 6.9, also see Chapter 3.2.4.3). Odd-numbered hydrocarbons could also be formed by metathesis reactions (Mol 1997).

At 1 MPa and temperatures between 215 and 270 °C the main products are hydrocarbons in the gasoline range (C_{5-9}) and mainly monomethyl isomers, which improve the octane number (Fig. 6.9). The type of products is constrained by the pore geometry of ZSM-5 zeolite (i.e. shape selectivity). ZSM-5 will tend to linearise or crack highly branched structures formed from oligomerisation in order to minimize diffusion resistance. High pressure (4-10 MPa) is the driving force for condensation to higher-molecular-weight alkenes (i.e. diesel range). At low temperatures (190-310 °C), oligomerisation is favoured thermodynamically but molecular weight growth is kinetically limited. As temperature is increased, all reaction rates increase, with cracking eventually dominating kinetically, resulting in a thermodynamic limitation to molecular-weight growth (O´Connor 1997, Quann et al. 1991).

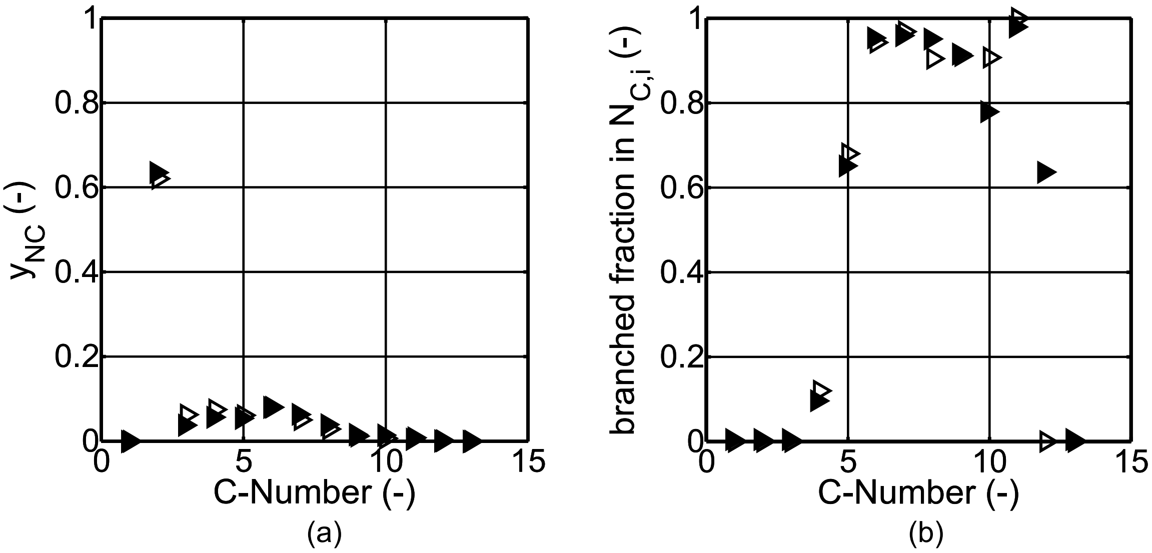

Fig. 6.9: Effect of the presence of synthesis gas on hydrocarbons molar fraction (a) and branched hydrocarbons content in carbon-number fractions on Pt/ZSM-5 (b). Feed: C_2H_4 + C_3H_6 + H_2 + CO + N_2 (open symbols, τ_{mod} = 2000 kg·s/m^3), C_2H_4 + C_3H_6 + N_2 (full symbols, τ_{mod} = 6250 kg·s/m^3), T = 270 °C, p = 1 MPa. Other reaction conditions see Table 5.8.

Experiments with ethene, propene and only H_2 in the feed lead to ethene and propene conversion of 100 %. The only products are ethane and propane, meaning that only hydrogenation reactions take place on Pt/ZSM-5. This is in contrast to ethene, propene, H_2 and CO as feed, where also oligomerisation reactions take place and ethene is partially hydrogenated. Therefore, ethene conversion in the presence of synthesis gas is higher than without synthesis gas (Fig. 6.8a). Once again, the main oligomerisation products are from propene reactions. Propene conversion remains nearly constant in the presence of synthesis gas (Fig. 6.8b taking into account that τ_{mod} was lower in the presence of synthesis gas). The product distribution of oligomerisation reactions in the presence of synthesis gas does not deviate much from that with pure ethene and propene as feed. In that case, monomethyl isomers are also the main products (Fig. 6.9). In the experiments at 0.5 MPa no pressure effect could be observed on conversion and product distribution (Fig. 12.7).

Beta zeolite, although it is not a typical oligomerisation catalyst, was tested with ethene and propene as feedstock. Ethene and propene conversion are lower than with Pt/ZSM-5 (i.e. lower oligomersation activity). Propene conversion is also higher than ethene conversion (X_{C2H4} = 0.12, X_{C3H6} = 0.58 at 250 °C, 1 MPa, τ_{mod} = 13600 kg·s/m^3). The product distribution is similar to that with Pt/ZSM-5 catalyst (Fig. 12.7a). The branched hydrocarbon fraction with Pt/Beta is slightly higher than with Pt/ZSM-5 (Fig. 12.7b), which is also observed in the experiments with 1-octene (see Chapters 6.1.1-6.1.2).

During the time on stream (one month) no catalyst deactivation was observed. Pore size of ZSM-5 prevents the formation of bulky coke precursors, thus increasing the lifetime of the catalyst. In addition, in the experiments described, hydrogen was present most of the time (hydrogenation of coke precursors).

These results confirm that oligomerisation reactions can also take place on a bifunctional catalyst under the reaction conditions investigated. They also confirm the deleterious effect of CO on the hydrogenation activity of Pt.

6.2 Fischer-Tropsch experiments - Reference

6.2.1 Co-based catalyst

The Co-based catalyst was first reduced following the procedure presented in Table 5.4. The reduction of the initial Co_3O_4 phase occurs in two steps:

$$Co_3O_4 + H_2 \longrightarrow 3\,CoO + H_2O \qquad (6.1)$$

$$CoO + H_2 \longrightarrow Co + H_2O \qquad (6.2)$$

The reduction procedure increases the number of cobalt surface sites, thus having an influence on catalyst activity. After reduction and following the procedure presented in Chapter 5.3.2, the Co-based catalyst was activated and FT synthesis reaction started (Fig. 6.10). During this “conditioning” period (about 20000 min) the catalyst can undergo structural and compositional changes like reconstruction of catalyst surface accompanied by the formation of the “active Fischer-Tropsch sites” (Schulz et al. 2002). This process can take place over several days. Figure 6.10 shows that, in the present case, steady state (i.e. constant conversion and yields) was achieved after one day on stream. Schulz et al. 2002 reported that the “conditioning” period in principle includes three kinetic episodes: i) during the first approx. 10 min, CO conversion decreases drastically due to saturation of CO adsorption on the catalyst, ii) after episode I, CO conversion increases slowly with time to a much higher value, and iii) in episode III (which is shown in Fig. 6.10) steady-state is achieved. Each online GC analysis cycle takes around 45-50 min making impossible to obtain data from episodes I and II.

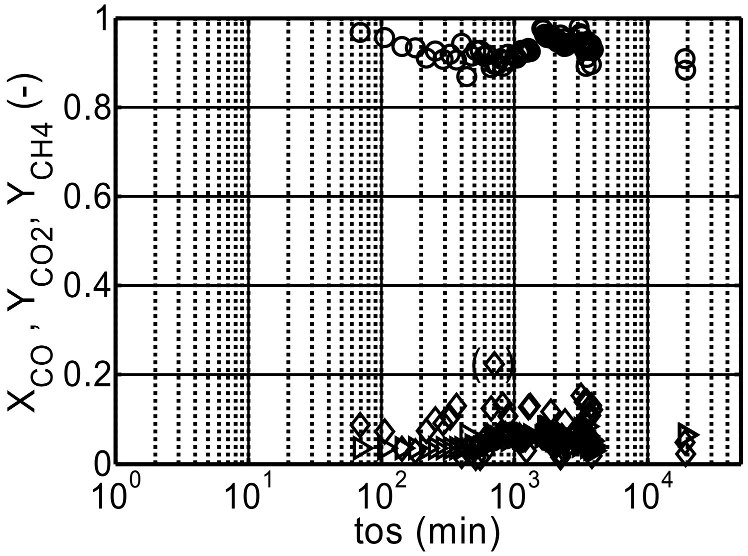

Fig. 6.10: Co-based catalyst activation and reproduction experiments after approximately two weeks on stream. CO conversion (circles), CH_4 yield (triangles), CO_2 yield (diamonds). Reaction conditions: T = 230 °C, $(p_{H2}/p_{CO})_{in} = 2$, p = 1 MPa, τ_{mod} = 4000 kg·s/m^3, at tos = 0 start H_2/CO flow.

The Co catalyst shows a low CO/CO_2-shift activity, which is typical for Co catalysts (values of Y_{CO2} > 10 % in Fig. 6.10 are due to difficulties in CO_2-peak integration with the online GC). Methane yield (about 8 %) is moderate considering the high temperature (230 °C) and high CO conversion. Reproduction experiments were performed after two weeks and after one month on stream. No change in activity was observed.

6.2.1.1 Kinetic analysis: effect of residence time, temperature and gas composition

As CO/CO_2-shift reaction plays a minor role, in modelling the reaction kinetics only CO-hydrogenation reaction was considered (Eq. 5.30). In that case, the CO-consumption rate is equivalent to the formation rate of hydrocarbons on carbon basis (assumption: no oxygenate compounds formed):

$$CO + 2H_2 \longrightarrow -(CH_2)- + H_2O \qquad (6.3)$$

Kinetic parameter values were determinated simultaneously for the experiments with H_2/CO-ratio of 2 and 1 (Fig. 6.11). Experiments at 230 °C with H_2/CO-ratio equal to 3 were also performed, but total CO conversion is achieved making these results not appropriate for kinetic analysis (at τ_{mod} = 2000 kg·s/m^3). Parameter values in the reactor model (Chapter 5.4) were determined via minimization of the sum of square errors (Eq. 5.35), with data points obtained for varying the modified residence time for each temperature. The kinetic parameter values obtained and the sum of residuals are presented in Table 6.1. They show a good agreement between calculated and experimental values. The obtained a_{FT-Co} value was assumed to be constant for all temperatures. Activation energy E_A was determined from an Arrhenius plot.

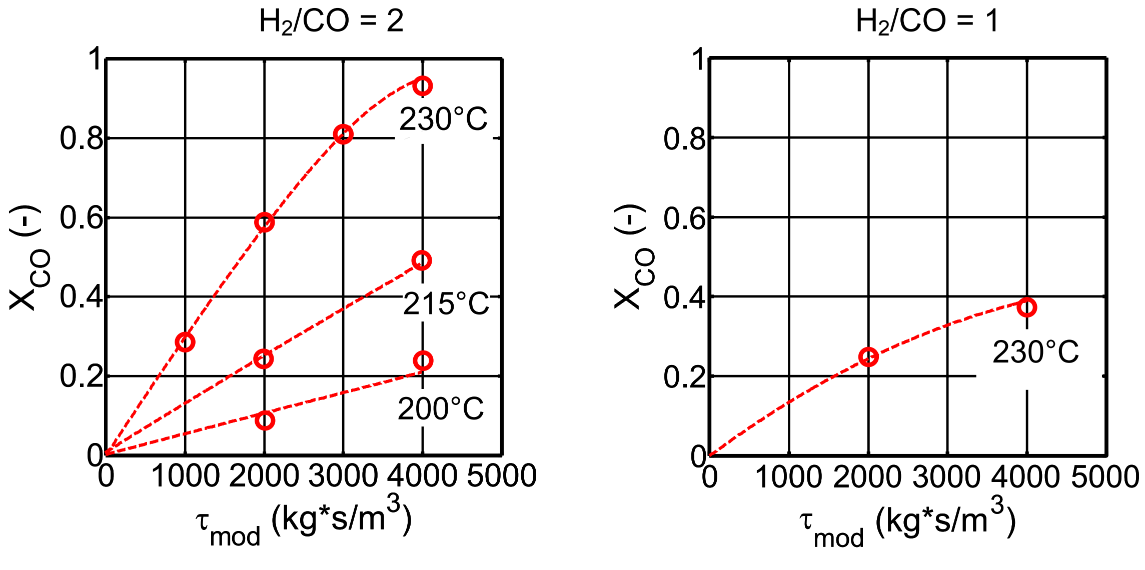

(a) (b)

Fig. 6.11: Effect of temperature and gas composition on CO conversion versus modified residence time. Catalyst: Co/Al_2O_3. Points: experimental, curves: calculated with kinetic model (Tab. 6.1, Eq. 5.30). Other reaction conditions see Table 5.9.

Conversion of CO increases by increasing modified residence time, temperature and H_2/CO-ratio (Fig. 6.11). Arrhenius' equation predicts an exponential increase of CO consumption rate with the temperature, which can be observed in the experimental results. An increase of CO partial pressure has a strong inhibiting effect on FT reaction on Co-based catalysts (Dry 1981, Schulz et al. 1995).

Tab. 6.1: Kinetic parameter values for Fischer-Tropsch reaction on Co catalyst resulting from model validation. FT rate equation from Yates et al. 1991 (see Eq. 5.30). χ^2: sum of square residuals.

		Fischer-Tropsch	χ^2
$k_{FT, Co, 200°C}$	(mol / (s·kg·Pa^2))	$3.76 \cdot 10^{-13}$	$5.28 \cdot 10^{-2}$
$k_{FT, Co, 215°C}$	(mol / (s·kg·Pa^2))	$8.80 \cdot 10^{-13}$	$1.17 \cdot 10^{-3}$
$k_{FT, Co, 230°C}$	(mol / (s·kg·Pa^2))	$2.15 \cdot 10^{-12}$	$2.17 \cdot 10^{-3}$
$E_{A, FT}$	(kJ / mol)	127	-
$a_{FT, Co}$	(Pa^{-1})	$2.85 \cdot 10^{-5}$	-

6.2.1.2 Product distribution

FT product distribution is usually presented in an Anderson-Schulz-Flory (ASF) diagram. The experimental set-up included a hot wax trap, which separates the liquid and the gas phase (Fig. 5.6). The established equilibrium phase distribution for each hydrocarbon species depends on its partial pressure and the temperature of the wax trap. Hydrocarbons in the range C_{12}-C_{23} are found in both gas and liquid phases (Fig. 6.12). The liquid phase (wax) is removed discontinuously by opening a valve. During the removal, some amounts of hydrocarbons may evaporate or remain in the wax trap. This explains the difficulty to close the C-balance to 100 % (see Chapter 5.3.4). Both liquid and gas phase analysis are combined following Equations 5.6-5.10 and defining the C-balance to be closed to 100% (see Tab. 12.9-12.10). This results in an adjustment of the wax fraction. In the diagram of the combined analysis (Fig. 6.13) hydrocarbon molar fractions in the range C_{12}-C_{23} appear nearly constant.

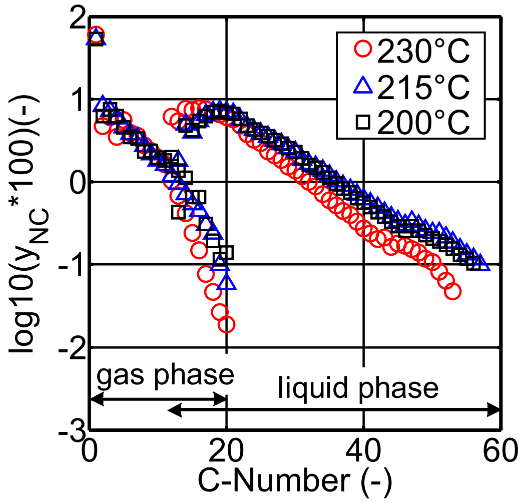

Fig. 6.12: ASF plot of separate gas and liquid phases in hot wax trap at different reaction temperatures. Catalyst: Co/Al_2O_3. Reaction conditions: $(p_{H2}/p_{CO})_{in}$ = 2, p = 1 MPa, τ_{mod} = 4000 kg·s/m^3. Hot wax trap: T = 165 °C, p = 1 MPa.

Figure 6.13 presents the product hydrocarbon distribution at different temperatures and H_2/CO ratios. An increase in temperature results in a shift towards products with a lower carbon number (decrease of chain-growth probability α_{C2-C53} from 0.88 at 200 °C to 0.85 at 230 °C) and methane selectivity on carbon basis increases (from 5.7 % at 200°C to 7.9 % at 230 °C). For cobalt catalysts, H_2/CO ratio often affects hydrocarbon product composition. An increase of CO partial pressure increases the chain-growth probability (from 0.86 at H_2/CO = 3 to 0.90 at H_2/CO = 1, T = 230 °C) and decreases methane selectivity (from 16.4 % at H_2/CO = 3 to 4.2 % at H_2/CO = 1, T = 230 °C). At low CO partial pressure, methane selectivity is high (Fig. 6.13b). These conditions should be avoided in a FT reactor working with Co-based catalyst.

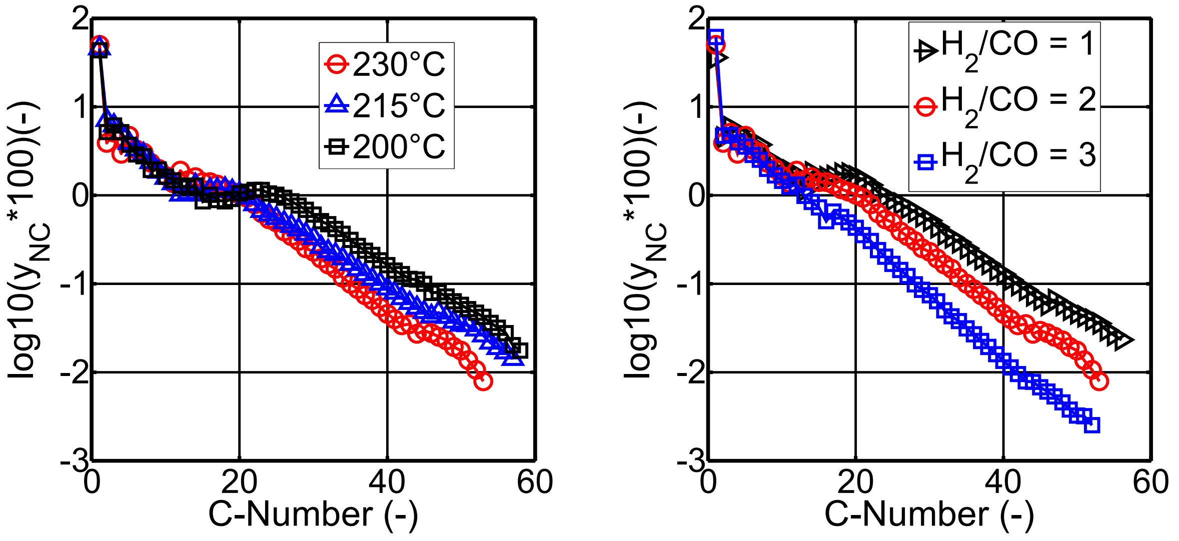

(a) (b)

Fig. 6.13: ASF plot of combined gas and liquid phases, and effect of temperature (a) and synthesis gas composition (b) on hydrocarbons distribution. Catalyst: Co/Al_2O_3. Reaction conditions: $(p_{H2}/p_{CO})_{in}$ = 2 (a), T = 230 ºC (b), p = 1 MPa, τ_{mod} = 4000 kg·s/m^3 and 2000 kg·s/m^3 for $(p_{H2}/p_{CO})_{in}$ = 3.

Liquid phase (wax) samples from experiments at different modified residence times (at constant temperature and synthesis gas composition) were also analysed. It was found that residence time has no influence on the wax product distribution.

Even with Co catalysts, which are much more active for hydrogenation reactions than Fe, alkenes selectivity exceeds alkanes selectivity for the low molecular mass hydrocarbons (C_3-C_5), especially at lower temperatures (Fig. 6.14a). The low value of ethene is due to its high reactivity at FTS conditions (Schulz 2006). The reactivity increases from C_3 to higher alkene since its adsorption probability also increases (Schulz 2006). The curves reflect secondary alkenes hydrogenation. Alkene with carbon number 3 or 4 appears to be the least affected by secondary reactions (Schulz 2002). An increase of temperature results in a decrease of alkenes selectivity (Fig. 6.14a), due to the attenuation of CO adsorption and an increase of secondary alkene hydrogenation (Claeys 1997). Alkenes selectivity increases with decreasing H_2/CO ratio due to lower H_2 partial pressure and stronger CO adsorption and inhibition of alkene readsorption (Fig. 6.14b).

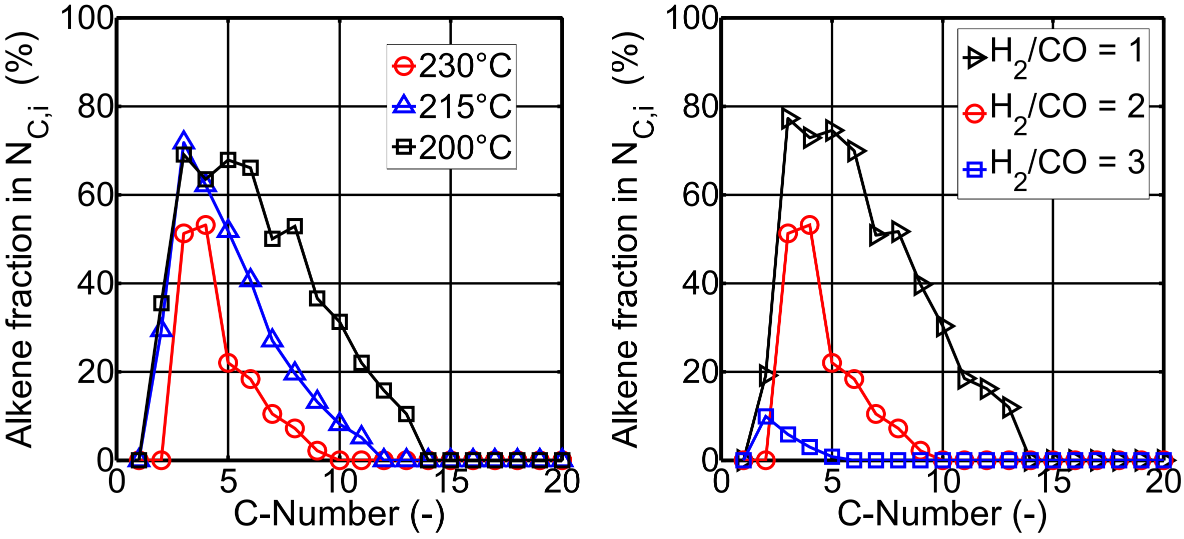

(a) (b)

Fig. 6.14: Effect of temperature (a) and synthesis gas composition (b) on n-alkene content in carbon-number fractions in the gas phase. Catalyst: Co/Al_2O_3. Reaction conditions: $(p_{H2}/p_{CO})_{in}$ = 2 (a), T = 230 °C (b), p = 1 MPa, τ_{mod} = 4000 kg·s/m^3 (2000 kg·s/m^3 for $(p_{H2}/p_{CO})_{in}$ = 3).

CO hydrogenation by FT synthesis preferentially produces linear chains of CH_2 groups. In addition, a small extent of methyl branching occurs (Fig. 6.15) but not enough to yield a gasoline fraction with good octane number. Schulz et al. 1988 concluded that branching reactions are more demanding in space at the active site than linear chain growth. This could explain the observed decrease of branching with chain length (Fig. 6.15). Figure 6.15a shows a moderate increase of branched hydrocarbons with temperature. Partial pressure of CO does not show a clear effect on branching selectivity (Fig. 6.15b). Oxygenates compounds are not formed.

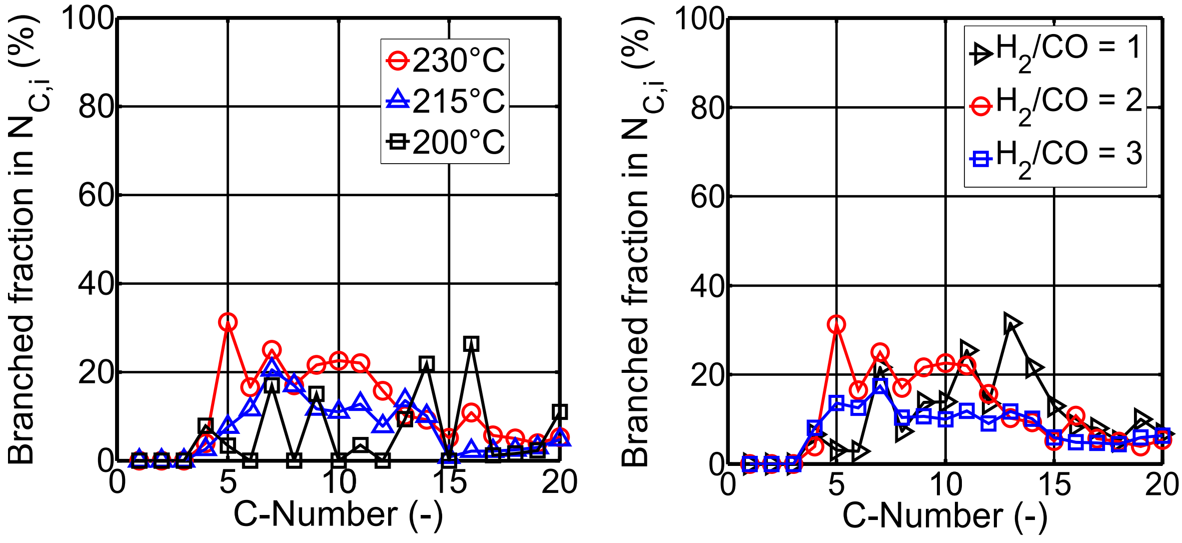

(a) (b)

Fig. 6.15: Effect of temperature (a) and synthesis gas composition (b) on branched isomers content in carbon-number fractions in the gas phase. Catalyst: Co/Al_2O_3. Reaction conditions: $(p_{H2}/p_{CO})_{in}$ = 2 (a), T = 230 °C (b), p = 1 MPa, τ_{mod} = 4000 kg·s/m^3 (2000 kg·s/m^3 for $(p_{H2}/p_{CO})_{in}$ = 3).

6.2.2 Fe-based catalyst

The K-promoted Fe catalyst was reduced following the procedure presented in Table 5.4. During the “conditioning” stage when the hydrogen is being replaced by synthesis gas, the Fe metal is rapidly converted to a mixture of carbides. The “conditioning” process can be divided into four episodes (Fig. 6.16). During episode I (the first 30 min), carbide formation is the main reaction. In episode II, FT and CO/CO_2-shift activity increases with the time until achieving steady state (episode III). During episode IV, FT and CO/CO_2-shift activities decrease due to carbon deposition (Boudouard reaction, Eq. 3.7) until reaching a new steady state. Formation of carbide is considered a prerequisite for FT activity, but it is still not known which carbides are responsible for the FT activity (Riedel 2003). Earlier studies showed that K_2O promotion of iron catalysts increases the rate of carbide formation as well as the CO/CO_2-shift activity (Dry 1981, also see Chapter 3.1.1.2).

K-promoted Fe catalyst has higher CO_2 yield and lower methane yield than the Co/Al_2O_3 catalyst (Fig. 6.16 and Fig. 6.10). A comparison of both catalysts activity is presented in Chapter 6.2.3.

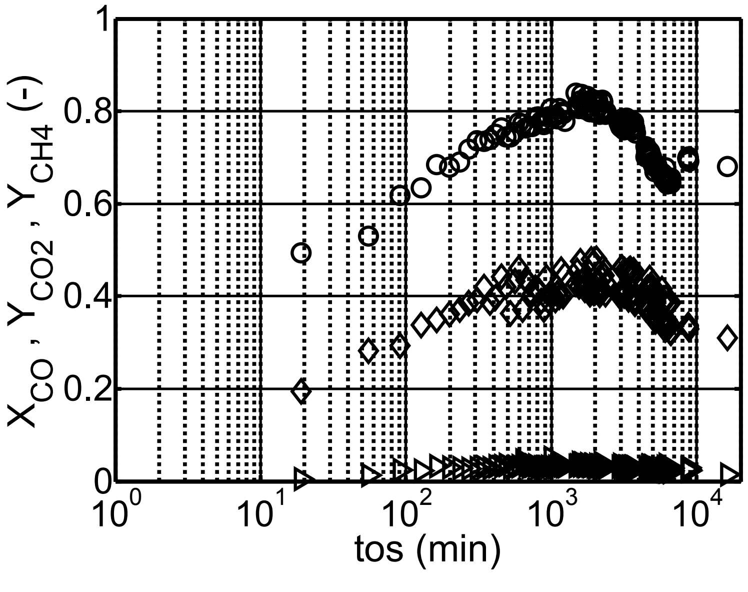

Fig. 6.16: K-promoted Fe catalyst activation and reproduction experiments (approximately 1 week after activation). CO conversion (circles), CO_2 yield (diamonds) and CH_4 yield (triangles). Reaction conditions: T = 250 °C, $(p_{H2}/p_{CO})_{in} = 2$, p = 1 MPa, $\tau_{mod} = 4000$ kg·s/m^3.

6.2.2.1 Kinetic analysis: effect of residence time, temperature and gas composition

Both FT and CO/CO_2-shift reactions take place on K-promoted Fe catalyst in contrast to Co/Al_2O_3 catalyst. CO reacts at the same time to hydrocarbons and CO_2 (parallel reaction). In the case of H_2/CO_2 feed gas, CO_2 may be converted to CO through the reverse CO/CO_2-shift reaction which can further react to hydrocarbons (Eq. 6.4), and oxygenates formation may be neglected (see Fig. 12.11).

$$CO_2 \rightleftarrows CO \longrightarrow -(CH_2)- \tag{6.4}$$

Determination of kinetic parameter values was done for the experiments with H_2/CO-ratio of 2 and 1 and H_2/CO_2-ratio of 3 (also see Fig. 12.12-12.13, Tab. 5.9). The reactor model used is presented in Chapter 5.4 as well as the kinetic rate equations (Eq. 5.31-5.32). Kinetic parameter values were determined via minimization of the sum of square errors (Eq. 5.34) simultaneously with data points obtained for varying the modified residence time for each temperature (Fig. 6.17-6.18). The obtained values and the sum of residuals are presented in Table 6.2. Calculated and experimental values show good agreement. The obtained a_i and b_i values (inhibition coefficients for H_2O and CO_2 respectively) were kept constant for all temperatures, since the kinetic parameter determination was carried out through $k_{FT\text{-}Fe}$ and $k_{CO2\text{-}SH}$ constants. The low values of b_i indicate that the CO_2 inhibition is lower than the H_2O inhibition.

With synthesis gas $H_2/CO = 2$, CO conversion and CO_2 and hydrocarbon yields increase with temperature and residence time (Fig. 6.17). Both experimental and calculated data show the usual progress of a parallel reaction.

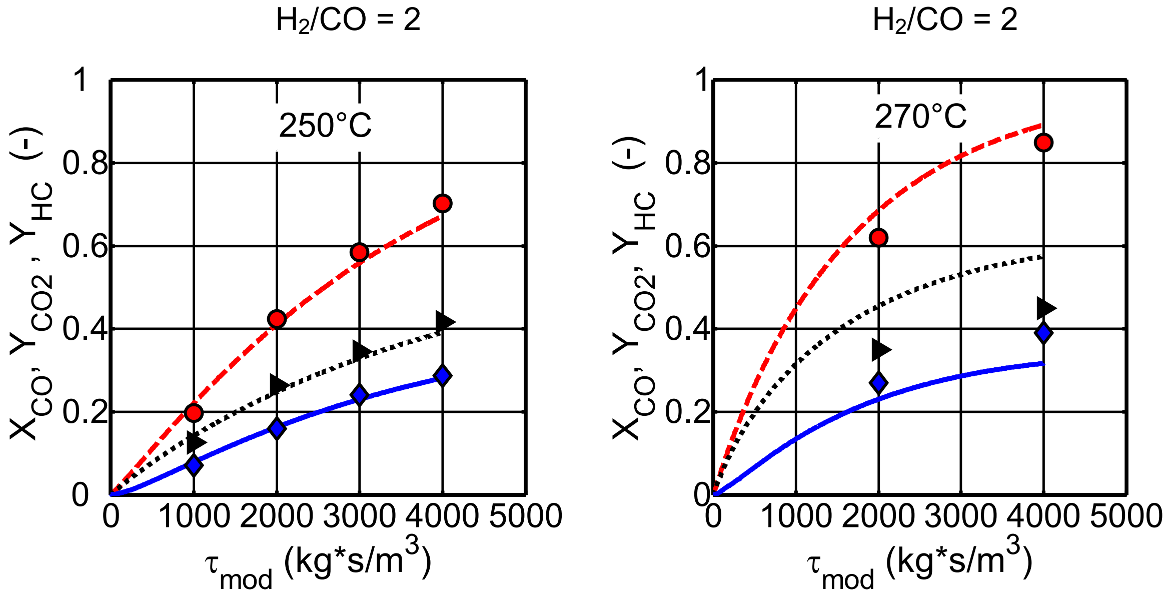

Fig. 6.17: Effect of temperature on CO conversion (circles, dashed curves), CO_2 (diamonds, solid curves) and hydrocarbons (triangles, dotted curves) yields versus modified residence time. Catalyst: K-promoted Fe. Points: experimental, curves: calculated with kinetic model (Tab. 6.2, Eq. 5.31-5.32). Reaction conditions see Table 5.9.

With $H_2/CO_2 = 3$ as feed, CO_2 conversion and CO and hydrocarbon yields increase also with temperature and residence time (Fig. 6.18). The residence time range investigated does not show the maximum of CO yield typical for an intermediate product. This maximum may be found at higher modified residence time.

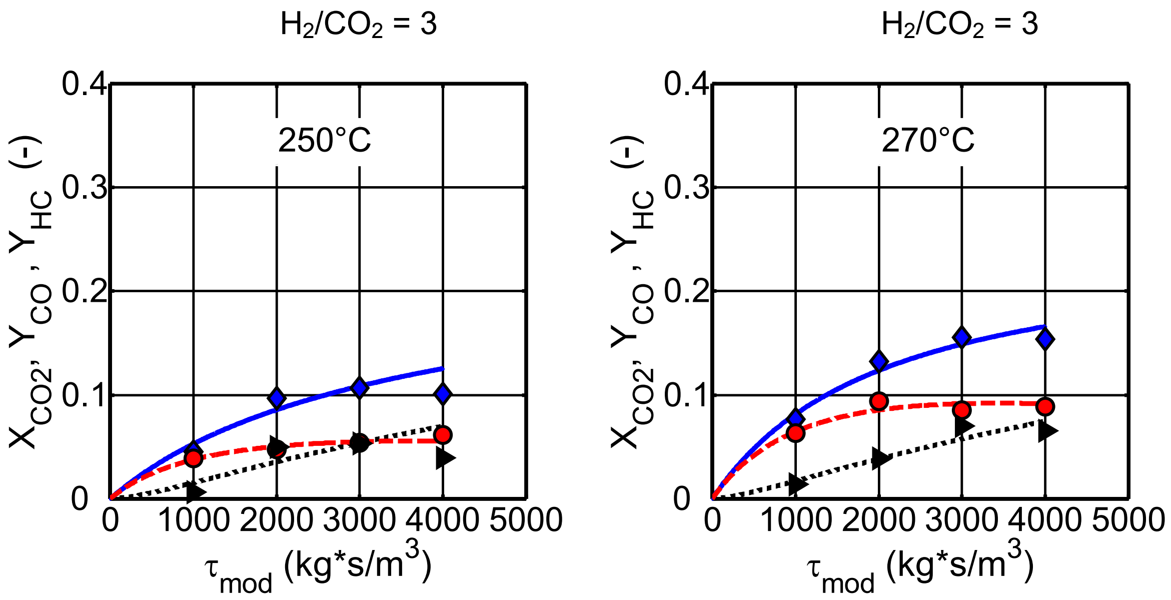

Fig. 6.18: Effect of temperature on CO_2 conversion (diamonds, solid curves), CO (circles, dashed curves) and hydrocarbons (triangles, dotted curves) yield versus modified residence time. Catalyst: K-promoted Fe. Points: experimental, curves: calculated with kinetic model (Tab. 6.2, Eq. 5.31-5.32). Reaction conditions see Table 5.9.

Tab. 6.2: Kinetic parameter values for Fischer-Tropsch and CO/CO_2-shift reactions on K-promoted Fe catalyst resulting from validation. Rate equations from Zimmerman et al. 1990 (Eq. 5.31-5.32). χ^2 : sum of square residuals.

		Fischer-Tropsch	CO/CO_2-shift	χ^2
$k_{i,\text{ Fe, }235°C}$	(mol / (s·kg·Pa))	$3.18 \cdot 10^{-9}$	$1.89 \cdot 10^{-11}$	$9.08 \cdot 10^{-2}$
$k_{i,\text{ Fe, }250°C}$	(mol / (s·kg·Pa))	$5.93 \cdot 10^{-9}$	$6.41 \cdot 10^{-11}$	$5.00 \cdot 10^{-2}$
$k_{i,\text{ Fe, }260°C}$	(mol / (s·kg·Pa))	$8.82 \cdot 10^{-9}$	$1.38 \cdot 10^{-10}$	$3.12 \cdot 10^{-2}$
$k_{i,\text{ Fe, }270°C}$	(mol / (s·kg·Pa))	$1.29 \cdot 10^{-8}$	$2.91 \cdot 10^{-10}$	$2.17 \cdot 10^{-3}$
$E_{A,i}$	(kJ / mol)	92	154	-
$a_{i,\text{ Fe}}$	(-)	4.8	21	-
$b_{i,\text{ Fe}}$	(-)	0.33	3	-

6.2.2.2 Product distribution

Like in the experiments with the Co/Al_2O_3 catalyst, the liquid and the gas phases were separated in the hot wax trap, under the same conditions (T = 165 °C, p = 1 MPa). Figure 6.19 shows the analysis of the two phases. A deviation in the overlapping range (~ C_{12}-C_{23}) and two different slopes can be observed. The combination of the two phases is presented in Figure 6.20. As compared with Co (Fig. 6.13), the combination results in a stronger deviation from ideal ASF distribution. In general, Fe-based catalysts yield higher alkenes and isomer hydrocarbon selectivities than Co-based catalysts. Alkenes and branched hydrocarbons have lower boiling points than the respective n-alkanes (VDI-Wärmeatlas 1984). Some amounts of these molecules may be lost when emptying the hot wax trap. In addition, like in the case with Co catalyst, the C-balance cannot be closed to 100 % (see Chapter 5.3.4). The wax fraction in the calculation is overweighed which could explain the deviation from ideal ASF distribution.

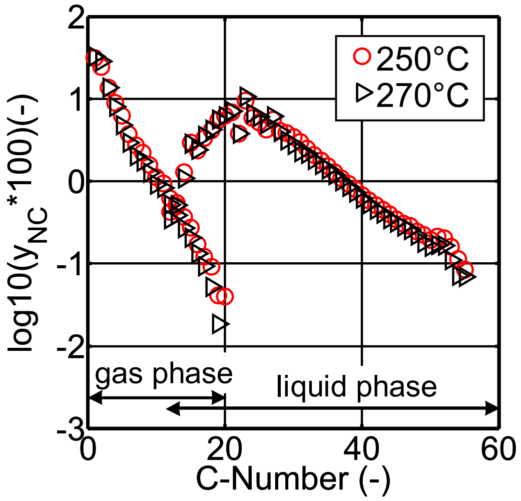

Fig. 6.19: ASF plot of separate gas and liquid phases in hot wax trap at different reaction temperatures. Catalyst: K-promoted Fe. Reaction conditions: $(p_{H2}/p_{CO})_{in}$ = 2, p = 1 MPa, τ_{mod} = 4000 kg·s/m^3. Hot wax trap: T = 165 °C, p = 1 MPa.

Like in Chapter 6.2.1.2 the influence of temperature and synthesis gas composition on FT product distribution is presented in combined ASF plots (Fig. 6.20). The hydrocarbon product distribution in the liquid phase sample is similar to the sample with Co (Fig. 6.13). However, methane selectivity with Fe is significantly lower than with Co, meaning no preferred methanation (Schulz 2006). The different slopes of gas phase and liquid phase agree with earlier findings (Donnelly et al. 1989). Product distribution on alkalised Fe catalyst follows a modified ASF distribution with two chain-growth probabilities, "double-α". No direct correlation between temperature and product distribution was found with the Fe catalyst in the (limited) temperature range investigated, as well as between synthesis gas composition and product distribution.

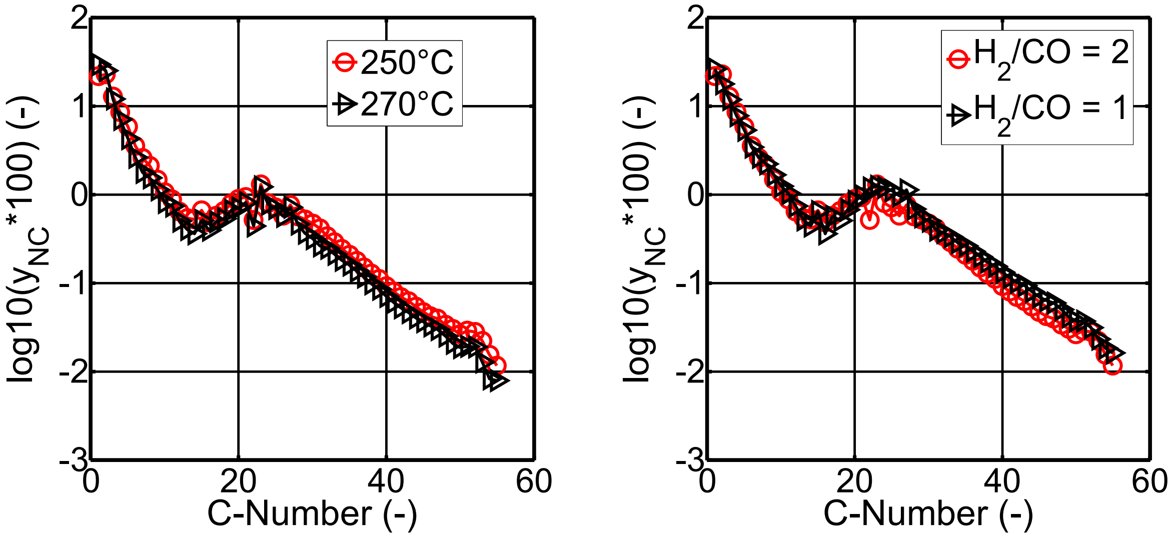

(a) (b)

Fig. 6.20: Effect of temperature (a) and synthesis gas composition (b) on hydrocarbon distribution. Catalyst: K-promoted Fe. Reaction conditions: $(p_{H2}/p_{CO})_{in}$ = 2 (a), T = 250 °C (b), p = 1 MPa, τ_{mod} = 4000 kg·s/m^3.

Fe-based catalysts have a lower hydrogenation activity than Co catalysts. Therefore, n-alkenes selectivity is higher with Fe catalysts, due to limited secondary alkene hydrogenation (Fig. 6.21). Claeys 1997 reported that K inhibits alkene consecutive reactions. Figure 6.21 shows that alkenes selectivity exceeds the alkanes between C_4 and C_{18}. Above C_{18}, alkenes selectivity decreases drastically.
The branching selectivity with Fe is moderately higher than with Co and leads mainly to monomethyl isomers. Temperature and synthesis gas ratio also do not show any influence on alkenes fractions (Fig. 6.21), nor on branching selectivity either (Fig. 6.22).

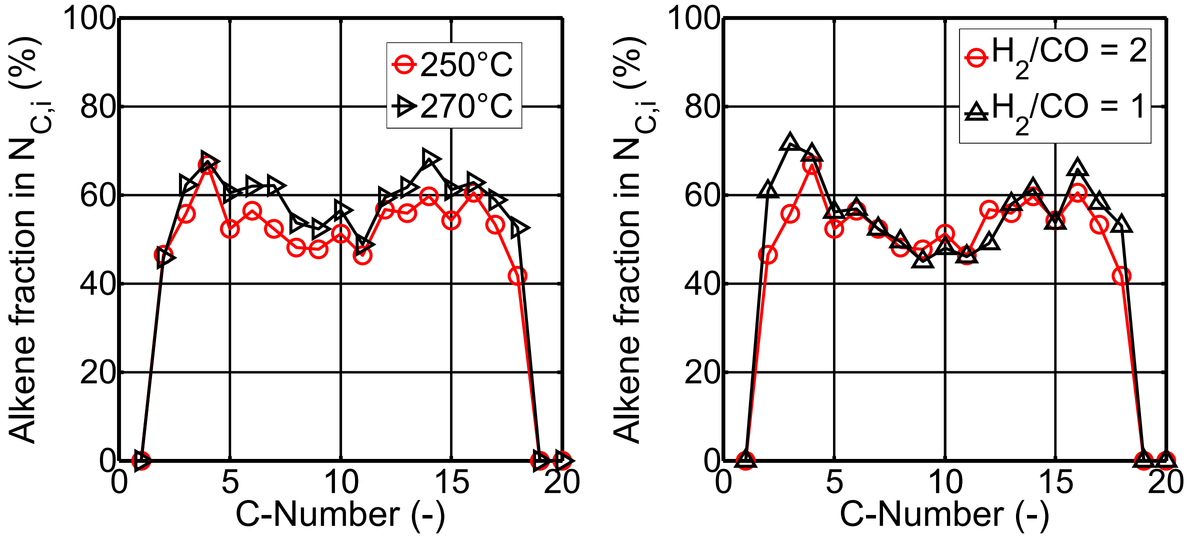

(a) (b)

Fig. 6.21: Effect of temperature (a) and synthesis gas composition (b) on n-alkene content in carbon-number fractions in the gas phase. Catalyst: K-promoted Fe. Reaction conditions: $(p_{H2}/p_{CO})_{in}$ = 2 (a), T = 250 ºC (b), p = 1 MPa, τ_{mod} = 4000 kg·s/m^3.

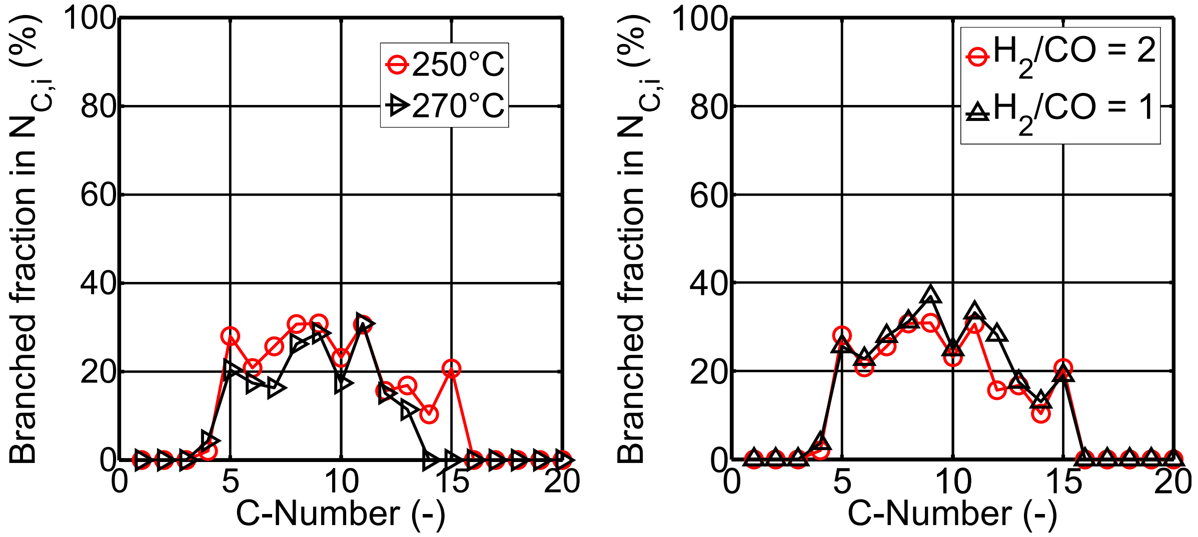

(a) (b)

Fig. 6.22: Effect of temperature (a) and synthesis gas composition (b) on branched isomers content in carbon-number fractions in the gas phase. Catalyst: K-promoted Fe. Reaction conditions: $(p_{H2}/p_{CO})_{in}$ = 2 (a), T = 250 ºC (b), p = 1 MPa, τ_{mod} = 4000 kg·s/m^3.

Oxygenates up to C_5 are produced with low selectivity, mainly alcohols (see Fig. 12.11). Riedel 2003 reported that alcohol selectivity declined with time on stream. It is still unclear through which mechanism the alcohols are produced during FT synthesis (see Chapter 3.1.1.3). By way of example, a sample of the aqueous phase (collected during all reaction conditions tested) was analysed qualitatively by means of gas chromatography and mass spectrometry (HP6890 Plus, HP5973 respectively). Alcohols, aldehydes, acetone and methyl esters were identified.

The presented effects of temperature, synthesis gas ratio on product selectivity are in agreement with the general effects in Table 3.1. Residence time effects are limited to alkenes selectivity as shown in Figures 12.9-12.10 for both Co and Fe catalysts.

6.2.3 Comparison of catalyst activities

The FT synthesis reaction rate was calculated for both catalysts used in the present study (Co/Al_2O_3 and K-promoted Fe) at different temperatures and for typical partial pressures in order to compare their FT synthesis activity. The FT reaction rates and the kinetic parameters used for this comparison are presented in Equations 5.31-5.32 and Tables 6.1-6.2 respectively. The Co/Al_2O_3 catalyst shows higher FT synthesis activity than the K-promoted Fe catalyst (Fig. 6.23).
The Co catalyst used in this study shows similar FT synthesis activity with the Co/MgO on SiO_2 catalyst from Yates et al. 1991, showing no influence of the support (Fig. 6.23).

Figure 6.24 shows that the CO/CO_2-shift activity of the K-promoted Fe catalyst is lower than its FT synthesis activity (calculated using Eq. 5.33 and kinetic parameters from Tab. 6.2). It was also considered interesting to compare the activity of the Fe catalyst used in this study with that of Zimmerman et al. 1990, Yates et al. 1991, Riedel 2003 and Unruh 2006 catalysts (reaction rates and parameters: Tab. 3.2-3.4, Unruh 2006).
Riedel 2003 and Unruh 2006 used similar Fe-based catalysts with Al_2O_3 as support, Cu as reduction promoter and K as chemical promoter. The Fe-based catalyst from Zimmerman et al. 1990 contains also Cu and K but in lower amounts. Zimmermann's catalyst shows similar FT activity to that of Riedel's but higher CO/CO_2-shift activity. Unruh's Fe catalyst shows the same FT activity as that of the Fe catalyst used in this study but higher CO/CO_2-shift activity. FT catalysts activity, however, is not only determined by the catalyst composition but also by the reduction and activation method.

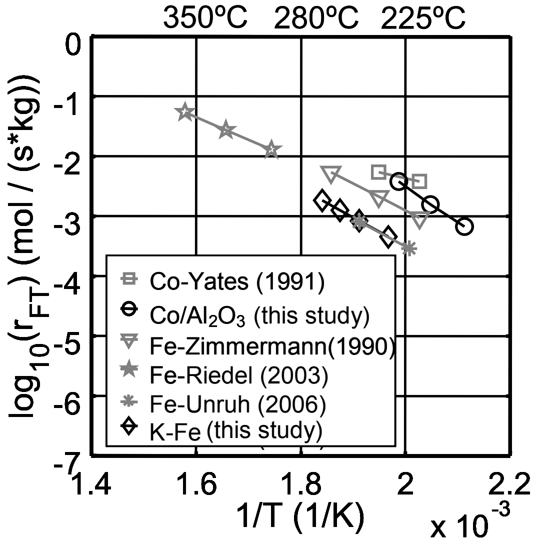

Fig. 6.23: Calculated FT reaction rates for the K-Fe and Co/Al_2O_3 catalysts used in this study (black lines and symbols), with kinetic parameters from Tables 6.1-6.2. Grey lines and symbols: catalysts from Zimmerman et al. 1990, Yates et al. 1990, Riedel 2003 and Unruh 2006. p_{H2} = 0.4 MPa, p_{CO} = 0.2 MPa, p_{H2O} = 0.3 MPa.

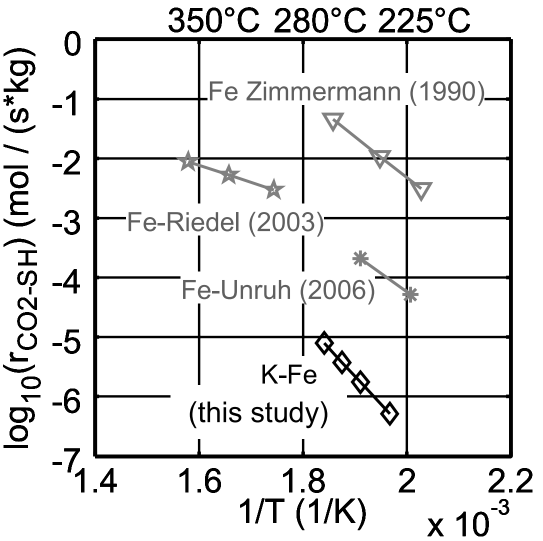

Fig. 6.24: Calculated CO_2-shift reaction rates for the K-Fe catalyst used in this study (black lines and symbols), with kinetic parameters from Table 6.2. Grey lines and symbols: catalysts from Zimmermann et al. 1990, Riedel 2002 and Unruh 2006. p_{H2} = 0.5 MPa, p_{CO} = 0.25 MPa, p_{CO2} = 0.125 MPa, p_{H2O} = 0.125 MPa.

6.3 Combination of FT and bifunctional catalysts

The two bifunctional catalysts (Pt/ZSM-5, Pt/Beta) were each combined with the Co or the Fe catalyst in different reactor configurations (Fig. 5.8). In this chapter, experimental results concerning the product distribution will be presented. Conversion of CO and CO_2 yields are not presented since they remain constant compared with the FTS experiments alone.

6.3.1 Co-based configurations: dual layer with Pt/ZSM-5 or Pt/Beta, physical mixture with Pt/ZSM-5

The Co/Al_2O_3 catalyst was combined with Pt/ZSM-5 or Pt/Beta in a dual layer (DL) and in a physical-mixture (MIX) configuration with Pt/ZSM-5.

Like in the FT experiments in Chapter 6.2, the gas and the liquid phases were analysed separately and then combined (Chapter 5.3.4). The first effect of combining a FT and a bifunctional catalyst is the selectivity shift towards lower chain hydrocarbons and a deviation from the typical ASF distribution (Fig. 6.25). The long-chain hydrocarbon fraction (C_{21+}) decreases in a similar way in all the configurations with Pt/ZSM-5 and less with Pt/Beta. This decrease leads to an increase of lighter hydrocarbon yields, especially in the gasoline range (C_{5-9}) with Pt/Beta in a dual-layer configuration and Pt/ZSM-5 in the mixture configuration (Fig. 6.25b). The dual-layer configuration with Pt/ZSM-5 results in an increase in the diesel range (C_{10-20}). These results indicate that hydrocracking reactions take place on the bifunctional catalysts. Long-chain hydrocarbons mainly undergo primary (“ideal”) cracking reactions since methane selectivity remains nearly constant compared with Co catalyst alone

(Fig. 6.25, Fig. 6.13a). These results indicate that long-chain hydrocarbons (C_{21+}) could diffuse through the micropores of ZSM-5 zeolite and of Beta zeolite. From the experimental results, it is not possible to conclude if the cracking reactions take place at the external surface or inside the porous structure.

Taking into account that 230 °C, 1 MPa and the presence of CO and water vapour are not the typical industrial conditions for hydrocracking, it is not surprising that the C_{21+} fraction is not totally cracked. Experiments were also performed at 215 and 200 °C where the cracking activity was even lower (see Fig, 12.14-12.15). At these low temperatures, CO conversion on the Co catalyst is also lower (Fig. 6.11). The resulting high CO partial pressure together with the low temperatures may explain the low cracking activity observed. At 200 and 215 °C, with Pt/ZSM-5 as a bifunctional catalyst, a decrease of the $C_{2\text{-}4}$ fraction is observed, which may be attributed to short-chain alkenes oligomerisation reactions (see Chapter 6.1.3).

230°C, $H_2/CO = 2$

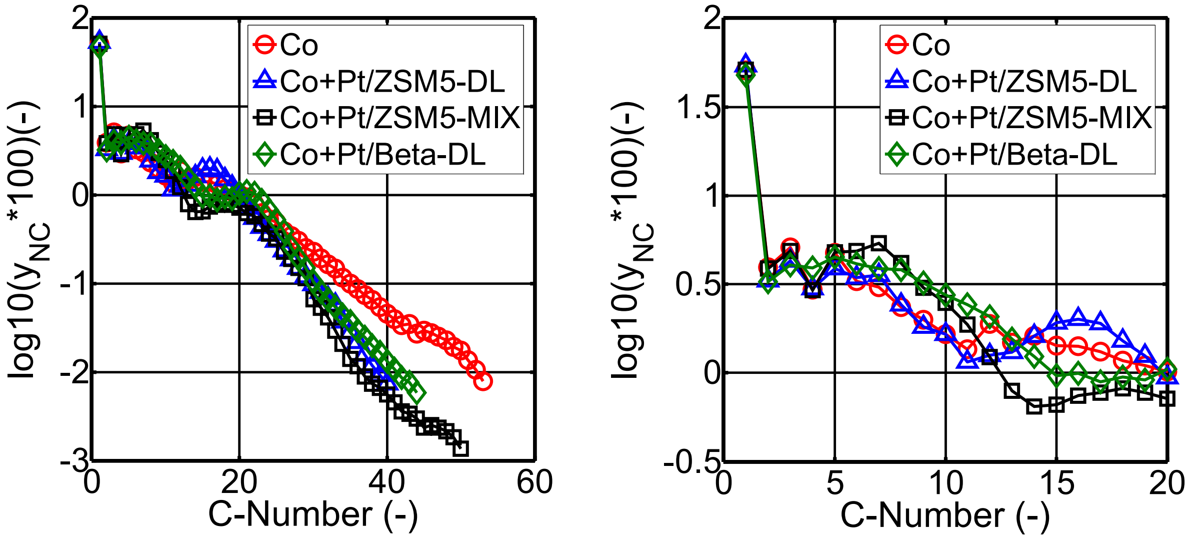

(a)

(b)

Fig. 6.25: Effect of catalyst-bed configuration (DL: dual layer, MIX: physical mixture) on hydrocarbons distribution. Catalysts: Co/Al_2O_3, Pt/ZSM-5, Pt/Beta. Reaction conditions: p = 1 MPa, $\tau_{mod} = 4000\ kg{\cdot}s/m^3$ (referred to $m_{FT\text{-}cat.}$), $m_{HP\text{-}cat.} / m_{FT\text{-}cat.} = 0.75$ (Tab. 5.9-5.13).

Since synthesis raw gas from biomass usually exhibits H_2/CO ratios below 2, the combination FT and bifunctional catalysts at a H_2/CO-ratio of 1 was also investigated. Figure 6.26 shows that the yield reduction of C_{21+} is less significant than in the case with H_2/CO-ratio of 2, as well as the increase of gasoline and/or diesel fractions. In that case, both bifunctional catalyst type and catalyst-bed configuration do not influence the extent of cracking reactions.

These results may be primarily attributed to the higher CO concentrations which are due to lower CO conversion during FTS at lower H_2/CO ratio (Fig. 6.11).

The significant hydrogenation activity of Pt was already proved with the 1-octene and ethene/propene experiments on Pt/ZSM-5 and Pt/Beta (see chapter 6.1). By combining these bifunctional catalysts with the Co catalyst, alkenes with $N_C > 5$ are nearly completely hydrogenated (Fig. 6.27). It seems from these results that hydrogenation activity of Pt does neither depend on temperature nor on the catalyst-bed configuration (Fig. 6.27).

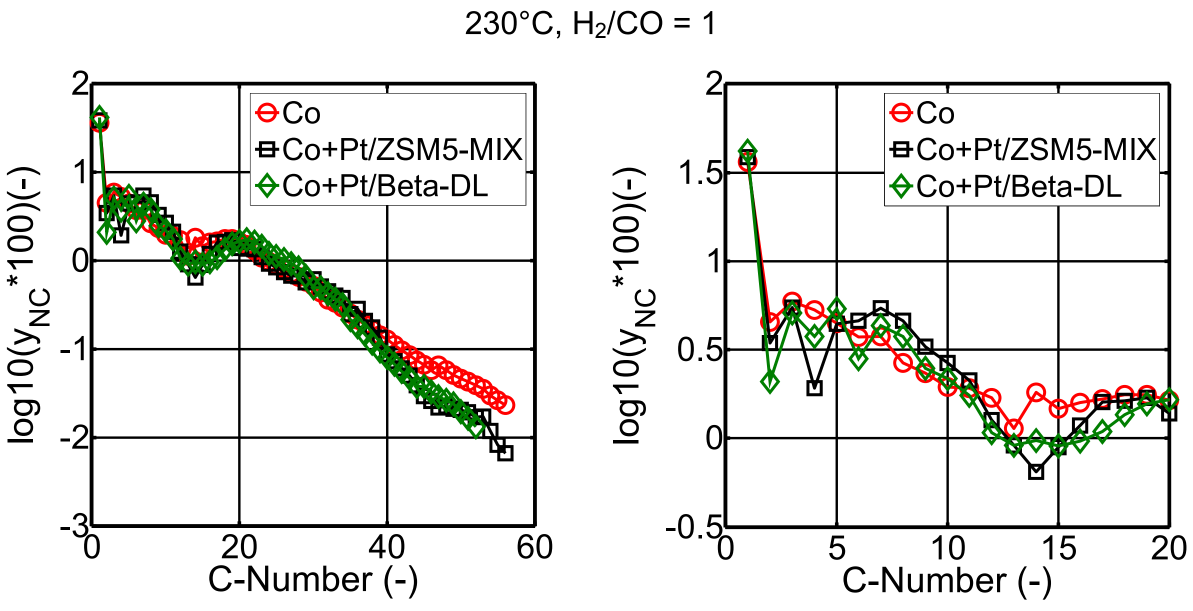

(a) (b)

Fig. 6.26: Effect of catalyst-bed configuration (DL: dual layer, MIX: physical mixture) on hydrocarbons distribution. (b) Zoom of Fig. 6.26a. Catalysts: Co/Al$_2$O$_3$, Pt/ZSM-5, Pt/Beta. Reaction conditions: see Fig. 6.25.

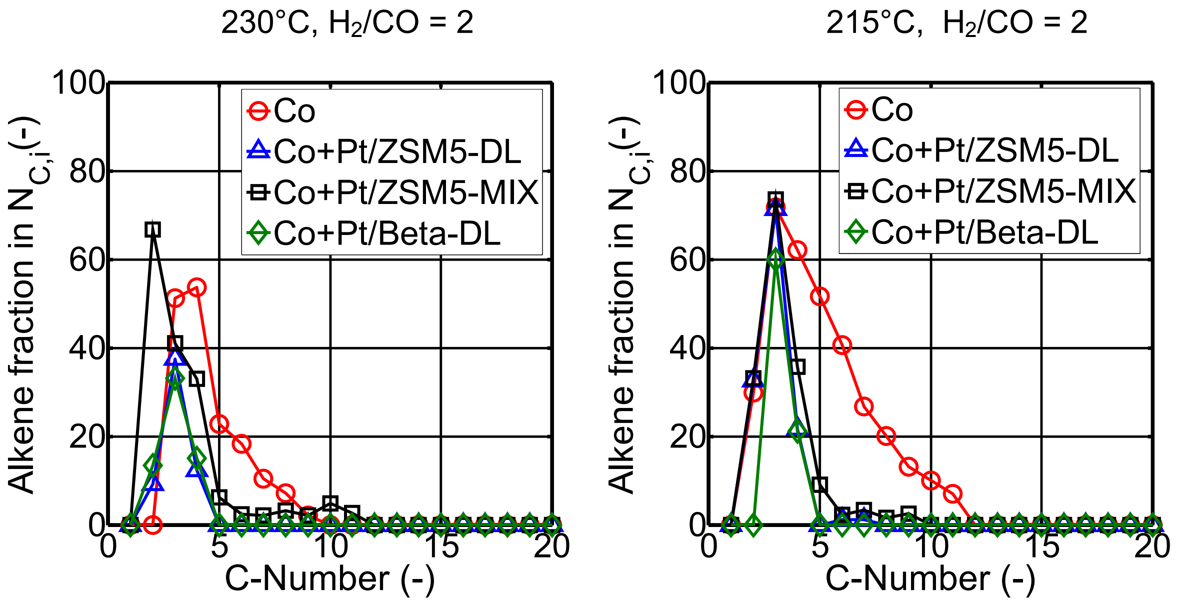

Fig. 6.27: Effect of temperature, bifunctional catalyst and catalyst-bed configuration on alkene content in carbon-number fractions in the gas phase. Catalysts: Co/Al$_2$O$_3$, Pt/ZSM-5, Pt/Beta. Reaction conditions: see Fig. 6.25.

The combination of Co and bifunctional catalysts leads to an increase of isomer selectivity, especially in the gasoline and diesel range (Fig. 6.28), with a physical-mixture configuration. Branched hydrocarbons selectivity is higher at lower temperatures indicating isomerisation is preferred at lower temperatures (215 °C), and cracking at higher temperatures (230 °C). The gas-chromatography technique was not sensitive enough to identify if dibranched hydrocarbons were produced.

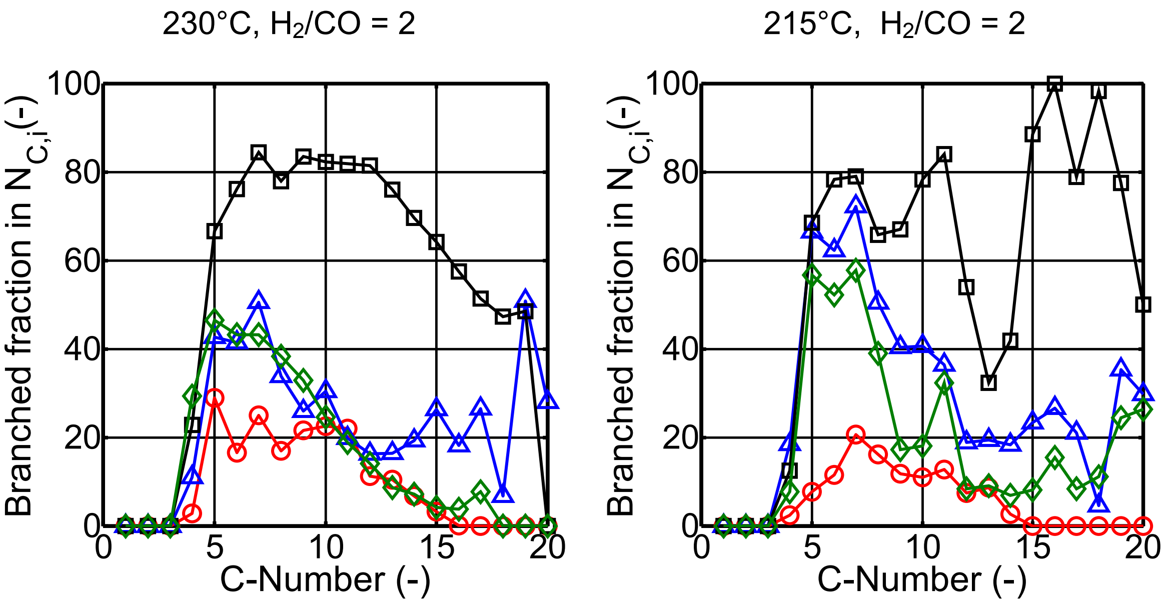

Fig. 6.28: Effect of temperature, bifunctional catalyst and catalyst-bed configuration on branched content in carbon-number fractions in the gas phase. Symbols see Fig. 6.27. Catalysts: Co/Al_2O_3, Pt/ZSM-5, Pt/Beta. Reaction conditions: see Fig. 6.25.

Table 6.3 and Figure 6.29a present the quantitative effects of the bifunctional catalyst and the catalyst configuration on different hydrocarbon product fractions. As explained in Chapter 1, straight-run gasoline from Co-based catalysts has a very low isomer selectivity (Fig. 6.15), which results in a poor research octane number (RON ≤ 43, de Klerk 2007). The research octane number for the gasoline fraction obtained with the different configurations was therefore estimated. It was calculated with the data available in the literature (ASTM Data Series DS 4B, 1991) and assuming a linear correlation between concentration and research octane number. The resulting values should be taken as indications, but not as absolute numbers. For instance, for the dual-layer configuration with Pt/ZSM-5 catalyst, 94 isomers were detected (in $C_{5\text{-}9}$ fraction) and octane number data for 52 of them could be found and used for the estimate. Only the components with research octane number available were considered. The physical-mixture configuration improves the research octane number considerably (to 63), and gasoline yield also increases (Tab. 6.3).

FT diesel has a high cetane number (> 70), even higher than the established values (cetane number > 51), (de Klerk 2007, Fröhling 2002). The dual-layer configuration with Pt/Beta leads to an increase of isomer selectivity in the diesel fraction. This effect could improve the cold flow properties of FT diesel (e.g. CFPP: cold filter plugging point). However, branched molecules reduce the self-ignition performance of diesel (cetane number, Pischinger et al. 2007). As cetane number data for isomers in the diesel range are rarely available in the literature, it was not possible to estimate this effect for the different catalyst configurations.

Table 5.2 shows that the Beta zeolite used has smaller crystal size than the ZSM-5 zeolite, indicating a higher number of acidic sites on the outer surface than inside the pore system. If isomerisation reactions take place at the outer surface, the reaction will proceed unaffected by geometrical restrictions. This would explain the increase of long-chain branched hydrocarbons on Pt/Beta catalyst. The experiments with 1-octene on Pt/Beta also show high isomer yield at 230 °C and nearly no cracking activity (see Chapter 6.1). On Pt/ZSM-5 catalyst, the isomerisation reactions most probably take place inside the pore system and shape selectivity may control the product selectivity by preferably cracking large molecules (see Chapter 3.2.2.3).

In the physical-mixture configuration the weight fraction of C_{1-4} increases, due to methane increase (approx. + 2 %). The long-chain hydrocarbons (C_{21+}) were cracked in all the configurations, especially in the dual-layer with Pt/ZSM-5 (Tab. 6.3).

Tab. 6.3: Effect of bifunctional catalysts on hydrocarbon fraction yields (on C-basis) and octane number (estimate, based on approx. 50 % of the identified isomers). Experimental data include gas and liquid phase analysis. Reaction conditions: T = 230 °C, $(p_{H2}/p_{CO})_{in} = 2$, $\tau_{mod} = 4000$ kg·s/m^3 (referred to $m_{FT\text{-}cat.}$), p = 1 MPa.

		Co	Co + Pt/ZSM-5	Co + Pt/Beta	Co + Pt/ZSM-5
		alone	dual layer	dual layer	physical mixture
y_{C1-4}	(C-%)	14.8	16.5	14.3	17.9
$y_{gasoline,C5-9}$	(C-%)	17.5	19.4	23.3	31.7
$y_{iso\ in\ C5-9}$	(%)	23.0	40.0	41.3	91.0
$y_{diesel,C10-20}$	(C-%)	38.7	47.5	37.9	33.2
$y_{iso\ in\ C10-20}$	(%)	11.7	22.0	42.7	41.0
y_{C21+}	(C-%)	29.0	16.6	24.5	17.2
$\sum y_{gasoline\ +\ diesel}$	(C-%)	56.2	66.9	61.2	64.9
RON	(-)	~ 37	~ 39	~ 39	~ 63

The results presented in Table 6.3 confirm that both zeolite type and catalyst-bed configuration have an influence on the product distribution. These effects can be explained with the partial pressures of the different compounds. In a dual-layer configuration, synthesis gas reacts in the first layer (Co catalyst). Gas composition at the end of the first layer depends on CO conversion. Figure 6.29a shows different gas composition at the outlet of the FT catalyst layer at different temperatures. At 230 °C, CO conversion and thus H_2O concentrations are high and the p_{H2}/p_{HC} is close to 1. In the case of a physical-mixture configuration, the bifunctional catalyst is present already at the reactor inlet. At this point, CO and H_2 partial pressures are high (0.33 and 0.66 MPa respectively at $H_2/CO = 2$) and no water vapour is present.

As found in the model compound reactions the presence of CO leads to lower cracking reactions rates, thus favouring isomerisation. From these results it is not clear to which extent water vapour affects the reaction rates.

The low CO partial pressure in the dual-layer configuration with Pt/ZSM-5 leads to a higher reduction of the C_{21+} fraction. The reduction of C_{21+} fraction in the physical-mixture configuration is lower than in the dual layer, due to the higher CO partial pressure. Cracking activity of Pt/Beta catalyst is considerably lower than that of Pt/ZSM-5. The dual-layer configuration with Pt/ZSM-5 seems to be the only configuration able to increase the diesel yield (Tab. 6.3).

The high isomer selectivity obtained with the physical mixture is also visible on the wax sample. The wax sample from the Co catalyst was hard and the wax sample from the physical mixture was soft and had a gel texture (Fig. 6.29b).

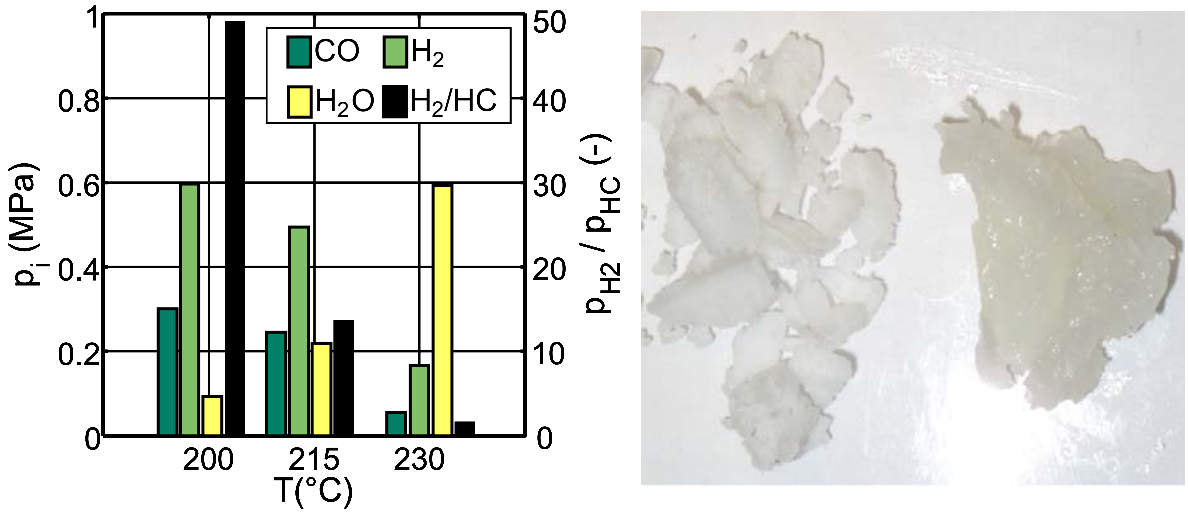

(a)

(b)

Fig. 6.29: (a) Partial pressure of the different compounds and H_2/HC-ratio at different temperatures at the outlet of the Co/Al_2O_3 catalyst layer. Reaction conditions: $(p_{H2}/p_{CO})_{in} = 2$, p = 1 MPa , τ_{mod} = 4000 kg·s/m^3 (referred to $m_{FT\text{-}cat.}$), $m_{HP\text{-}cat.} / m_{FT\text{-}cat.} = 0.75$ (Tab. 5.9-5.13), (b) Wax samples from Co-based catalyst (left) and from Co+Pt/ZSM5 in a physical-mixture configuration (right).

The industrial Shell Middle Distillate Synthesis (SMDS) process uses a Co-based catalyst with a high α value for the low-temperature FT synthesis leading to high selectivity of long-chain hydrocarbons (C_{21+} fraction, Fig. 6.30b with $\alpha \approx 0.95$). The produced C_{21+} fraction undergoes hydroprocessing treatments (hydrocracking, hydroisomerisation, hydrogenation) under mild reaction conditions (T = 300-370 ºC, p = 3-5 MPa) with recirculation of the non-converted C_{21+} fraction leading to an increase of the gasoline (approx. 20 C-% $C_{<10}$) and diesel (approx. 80 C-% $C_{10\text{-}20}$) selectivity (Fig. 6.30b).

The Co catalyst used in the present study has a lower α value than the catalyst used in the SMDS process (approx. 0.85 at 230 ºC) leading to lower C_{21+} selectivity. By combining the Co catalyst with Pt/ZSM-5 or Pt/Beta in a dual-layer or in a physical-mixture configuration it is possible to reduce the C_{21+} and increase the $C_{<10}$ and $C_{10\text{-}20}$ fractions selectivity via cracking reactions. The lower temperature and pressure applied in this combination, the presence of CO and the absence of recirculation of the non-converted C_{21+} fraction lead to lower gasoline and diesel selectivities than those achieve via the SMDS (Fig. 6.30a, b).

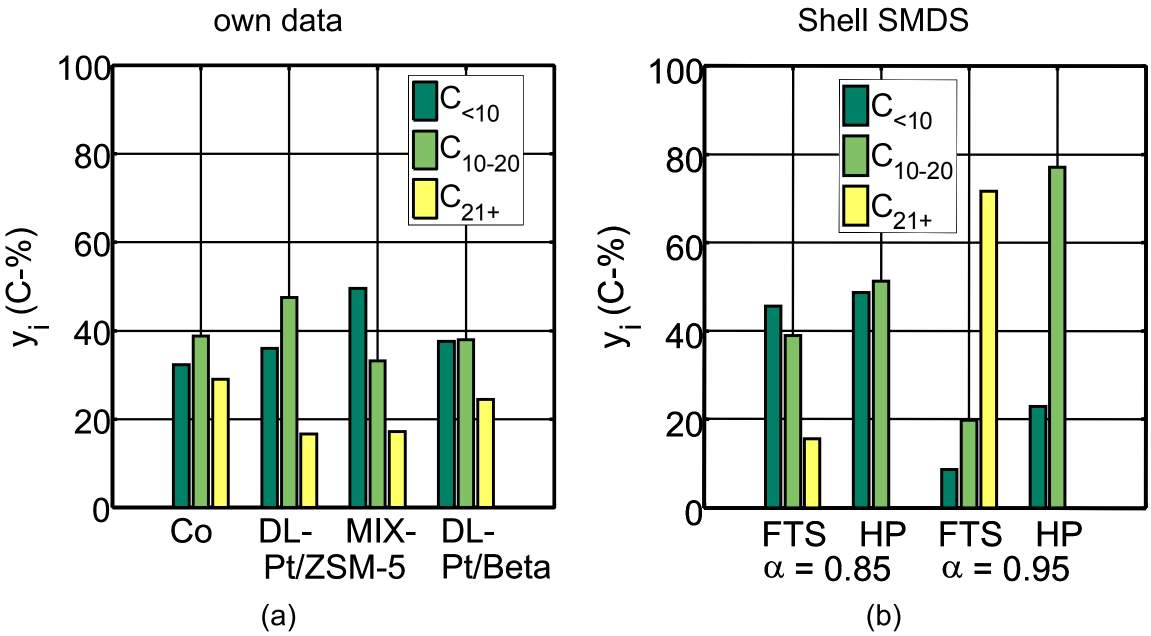

Fig. 6.30: (a) Effect of bifunctional catalyst and catalyst-bed configuration on hydrocarbon fraction yields (own data, on C-basis). DL: dual-layer, MIX: physical-mixture. Reaction conditions: see Fig. 6.25, (b) Shell Middle Distillate Synthesis (SMDS). FTS product distribution from Co-based catalysts with different α value and product distribution after hydroprocessing (HP), including recirculation of the non-converted C_{21+}-fraction (Data based on Eilers et al. 1990).

6.3.2 Fe-based configurations: dual layer with Pt/ZSM-5

The first experiments with a Pt/ZSM-5 catalyst layer underneath the Fe layer resulted in a decrease of CO conversion. Butter et al. 1980 reported that alkali promoters have a tendency to migrate to an adjacent acidic crystalline aluminosilicate component (i.e. zeolite). The Fe catalyst used in the present study contains potassium as promoter (Tab. 5.1) which perhaps could explain the activity decrease of the Fe catalyst in the dual-layer configuration. After one month on stream, the Pt/ZSM-5 used was analysed by ICP-OES method, and potassium could be found in small amounts (< 1 wt-%). In further experiments, the quartz-wool plug between the two catalyst layers was replaced by a silicon carbide layer and the same CO conversion and CO_2 yield values as with Fe catalyst alone were achieved.

As already explained in Chapter 6.2.2, Fischer-Tropsch temperatures for Fe-based catalysts are higher than for Co-based catalysts, which may be favourable for cracking reactions. Figure 6.31 shows the influence of Pt/ZSM-5 catalyst on the product distribution of Fe catalyst. The combination of the two catalysts leads to a decrease of C_{21+} selectivity and an increase of short-chain hydrocarbons. Methane selectivity remains constant at 250 ºC compared with Fe catalyst alone, whereas it increases (for approx. + 3 %) at 270 °C compared with Fe catalyst alone. This could be attributed to secondary cracking reactions taking place at higher temperatures.

The addition of the gas and liquid phase analysis for the combination Fe and Pt/ZSM-5 catalysts shows a deviation in the overlapping carbon number range. This problem was already mentioned for Fe catalyst in Chapter 6.2.2.2.

The combination of Fe and Pt/ZSM-5 was also tested with synthesis gas ratio of H_2/CO = 1, as the ratio in industrial applications with Fe-based catalysts may be below 2. As already mentioned, higher CO partial pressure at constant temperature and modified residence time leads to a lower FT activity (i.e. for CO hydrogenation). At higher CO partial pressure, cracking activity of long-chain molecules decreases, even at higher temperatures (270 °C). Figure 6.32 shows the same effect as Figure 6.26.

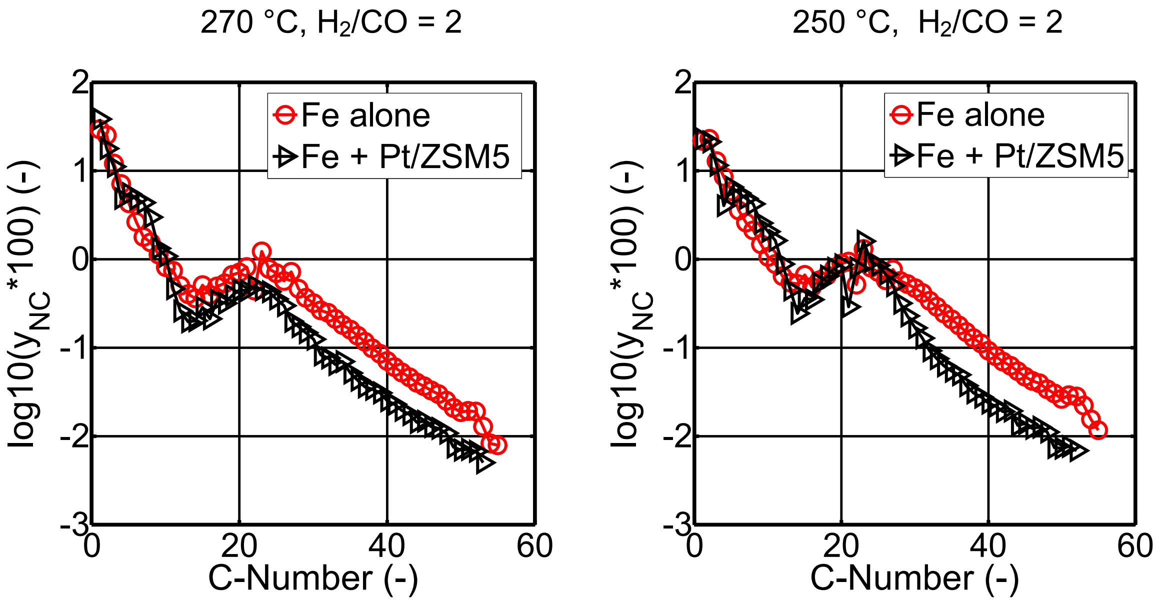

Fig. 6.31: Effect of bifunctional catalyst and temperature on hydrocarbons distribution. Catalysts: K-promoted Fe, Pt/ZSM-5. Reaction conditions: p = 1 MPa, τ_{mod} = 4000 kg·s/m^3 (referred to $m_{FT\text{-}cat.}$), $m_{HP\text{-}cat.}$ / $m_{FT\text{-}cat.}$ = 0.75 (Tab. 5.9-5.13).

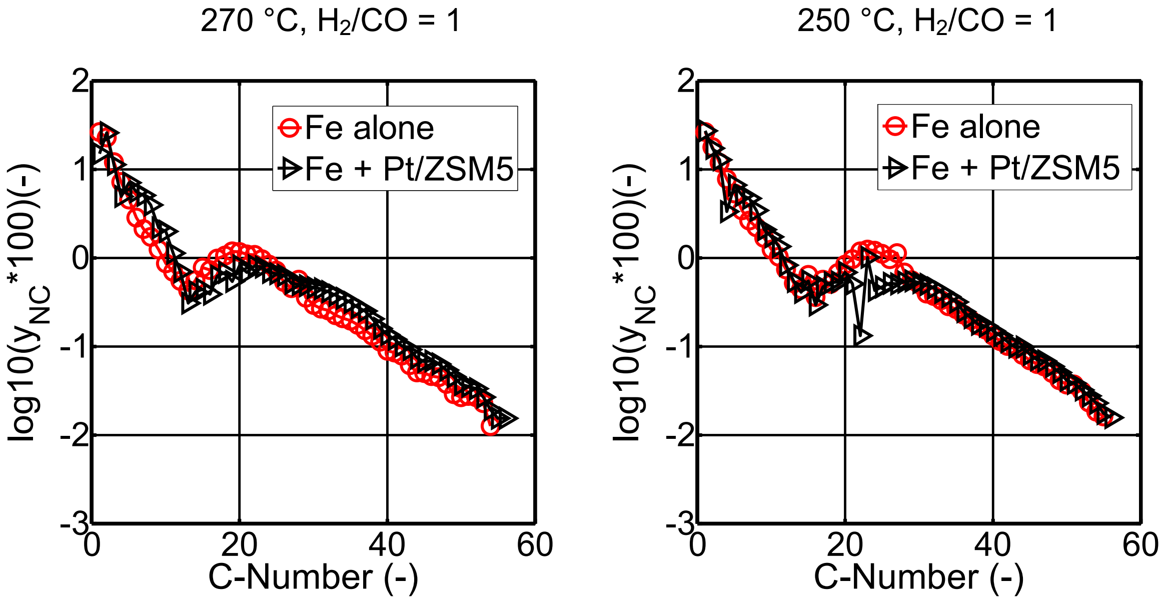

Fig. 6.32: Effect of synthesis gas, bifunctional catalyst and temperature on hydrocarbons distribution. Catalysts: K-promoted Fe, Pt/ZSM-5. Reaction conditions: see Fig. 6.31.

Alkenes selectivity with Fe catalyst is higher than with Co catalyst (Fig. 6.21 versus Fig. 6.14). However, the combination with Pt/ZSM-5 hydrogenates all alkenes with

$N_C > 5$ (Fig. 6.33). This result is analogous to the combination with Co (Fig. 6.27). It seems that at 270 ºC, hydrogenation activity is higher than at lower temperatures.

Pt/ZSM-5 catalyst layer underneath the Fe catalyst also leads to an increase of branched hydrocarbons in gasoline and diesel fraction (Fig. 6.34).

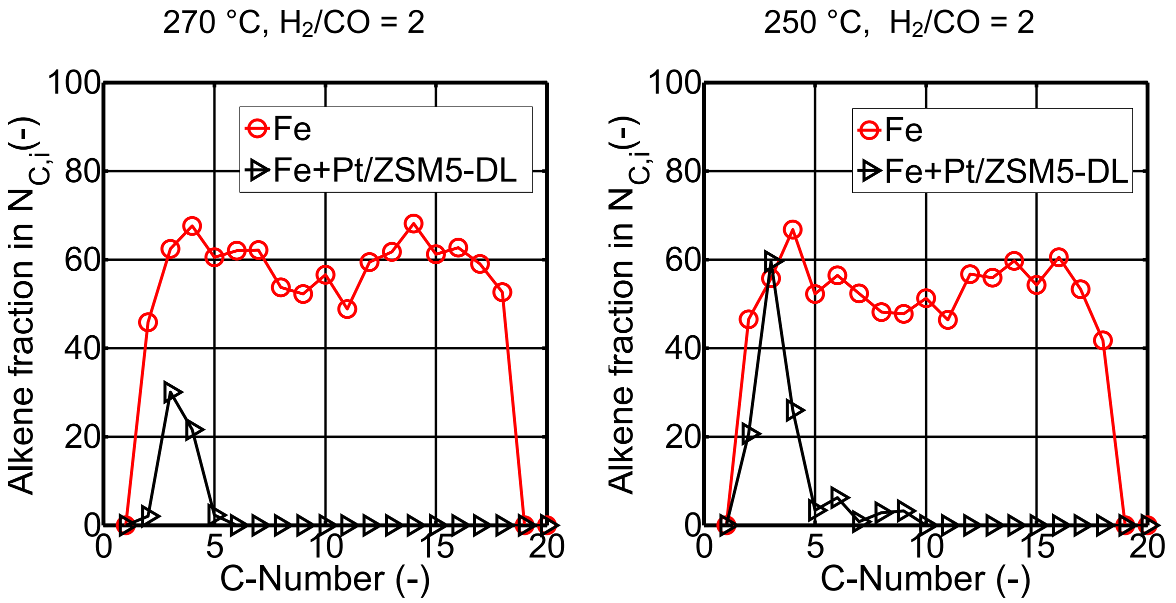

(a) (b)

Fig. 6.33: Effect of temperature and bifunctional catalyst on alkene content in carbon-number fractions in the gas phase. Catalysts: K-promoted Fe, Pt/ZSM-5. Reaction conditions: see Fig. 6.31.

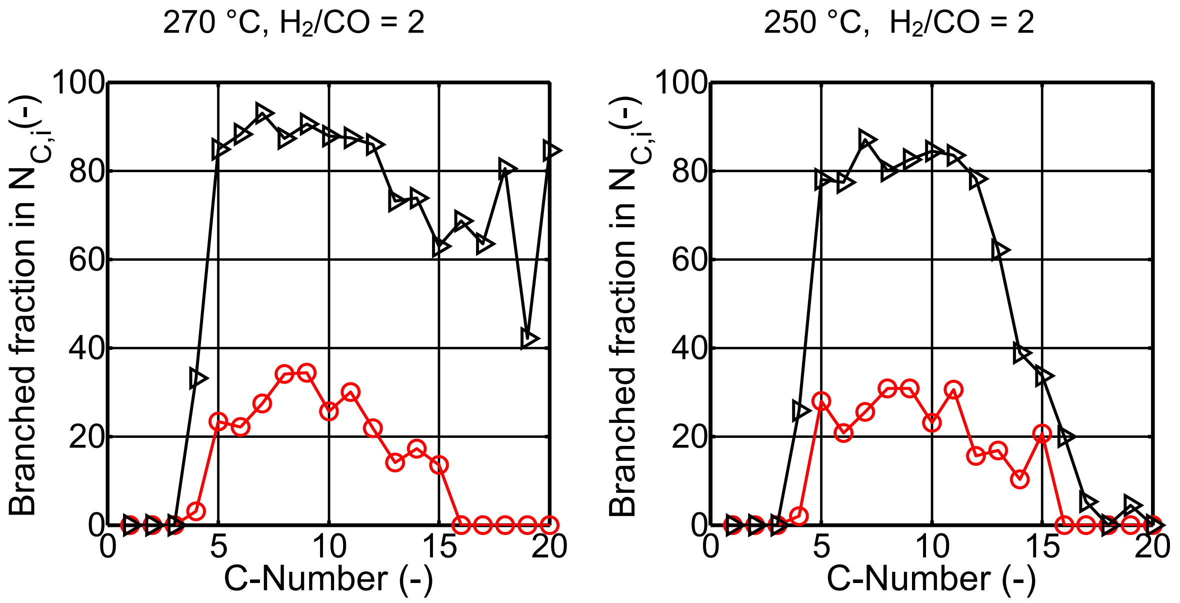

(a) (b)

Fig. 6.34: Effect of temperature and bifunctional catalyst on branched content in carbon-number fractions in the gas phase. Symbols see Fig. 6.33. Catalysts: K-promoted Fe, Pt/ZSM-5, Pt/Beta. Reaction conditions: see Fig. 6.31.

The combination of Fe and Pt/ZSM-5 at 270 °C increases the yield fraction of C_{1-4} (see Tab. 6.4, Fig. 6.35a). This increase indicates once again the possibility that secondary cracking or hydrogenolysis took place. The yield fraction of fuels (gasoline and diesel) also increases with the combination. The research octane number improved moderately at 250 and 270 °C. The calculated research octane number should be considered only as an indication (see discussion of Table 6.3).

Tab. 6.4: Effect of bifunctional catalyst and temperature on hydrocarbon fraction yields (on C-basis) and octane number (estimate, based on approx. 50 % of the identified isomers). Experimental data include gas and liquid phase analysis. Reaction conditions: $(p_{H2}/p_{CO})_{in} = 2$, $p = 1$ MPa, $\tau_{mod} = 4000$ kg·s/m^3 (referred to $m_{FT\text{-}cat.}$).

		T = 270°C		T = 250°C	
		Fe	Fe + Pt/ZSM-5	Fe	Fe + Pt/ZSM-5
		alone	dual layer	alone	dual layer
y_{C1-4}	(C-%)	26.8	31.1	23.4	20.8
$y_{gasoline,C5-9}$	(C-%)	13.4	29.9	15.6	27.3
$y_{iso,C5-9}$	(%)	21.2	83.7	27	81
$y_{diesel,C10-20}$	(C-%)	16.9	14.6	17.8	20.9
$y_{iso,C10-20}$	(%)	32.7	42.5	35.8	45.5
y_{C21+}	(C-%)	42.9	24.4	43.2	31.0
$\sum y_{gasoline + diesel}$	(C-%)	30.3	44.5	33.4	48.2
RON	(-)	~ 61	~ 69	~ 60	~ 68

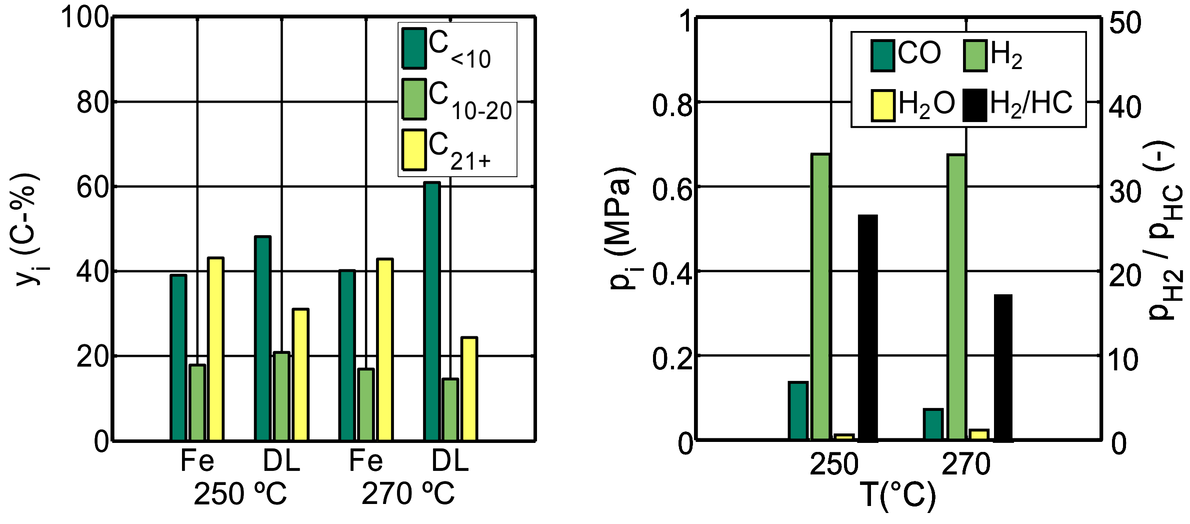

(a) (b)

Fig. 6.35: (a) Effect of Pt/ZSM-5 catalyst and temperature on hydrocarbon fraction yields (on C-basis), (b) partial pressure of the different compounds and H_2/HC-ratio at different temperatures at the outlet of K-promoted Fe catalyst layer. Reaction conditions: $(p_{H2}/p_{CO})_{in} = 2$, $p = 1$ MPa, $\tau_{mod} = 4000$ kg·s/m^3 (referred to $m_{FT\text{-}cat.}$).

The relative decrease of C_{21+} fraction from combining Fe and Pt/ZSM-5 at 250 °C is lower than with Co+Pt/ZSM-5 at 230 ºC (Fig. 6.35a versus Fig. 6.30a). The CO-hydrogenation activity is higher with Co than with Fe catalyst (for the same synthesis gas composition and modified residence time). This means that CO partial pressure at the bifunctional catalyst layer inlet is higher if Fe is the FT catalyst (Fig. 6.35b versus Fig. 6.29a). At 270 ºC with Fe+Pt/ZSM-5, the CO partial pressure at the inlet of the second layer is close to the CO partial pressure after the Co catalyst layer. In that case, nearly the same decrease of C_{21+} fraction was obtained (Fig. 6.35a versus Fig. 6.30a).

All bifunctional catalysts were on stream for approximately one month, and no deactivation was measured. Like in the experiments with model compounds, Pt/Beta catalyst changed its colour from grey to black (see Chapter 6.1). Pt/Beta catalyst was separated from SiC and dissolved with cyclohexane. A sample of this solution was analysed by means of gas chromatography (HP5890 Series II plus). It was found that hydrocarbons between C_{32} and C_{41} were deposited on the catalyst (see Fig. 12.17). A total carbon amount of 9 wt-% was determined by means of microelementary analysis (by Mikroanalytisches Labor Pascher). By means of thermal gravimetrical analysis (by Sachtleben Chemie GmbH) it could be concluded that organic and inorganic C also deposited on the catalyst (see Fig. 12.17-12.18). The pores of Beta zeolite accommodate these bulky molecules but they did not block the active sites. Pt/ZSM-5 catalyst was also analysed following the same procedure mentioned above. The pores of ZSM-5 zeolite are too small to accommodate bulky molecules rich in C (restricted transition state-type selectivity, see Chapter 3.2.2.3). The gas chromatographic analysis shows that no hydrocarbons were deposited in ZSM-5 structure (Fig. 12.18).

7 Reaction network model

7.1 Assumptions and reaction network

The experimental results presented in Chapter 6 show that hydrocracking, hydroisomerisation, hydrogenation and oligomerisation reactions take place on the bifunctional catalysts tested. These results were the basis to develop the simplified reaction network draft presented in Figure 7.1. This reaction network is an extension of the model from Steijns et al. 1981 presented in Figure 3.11 and Pellegrini et al. 2004.

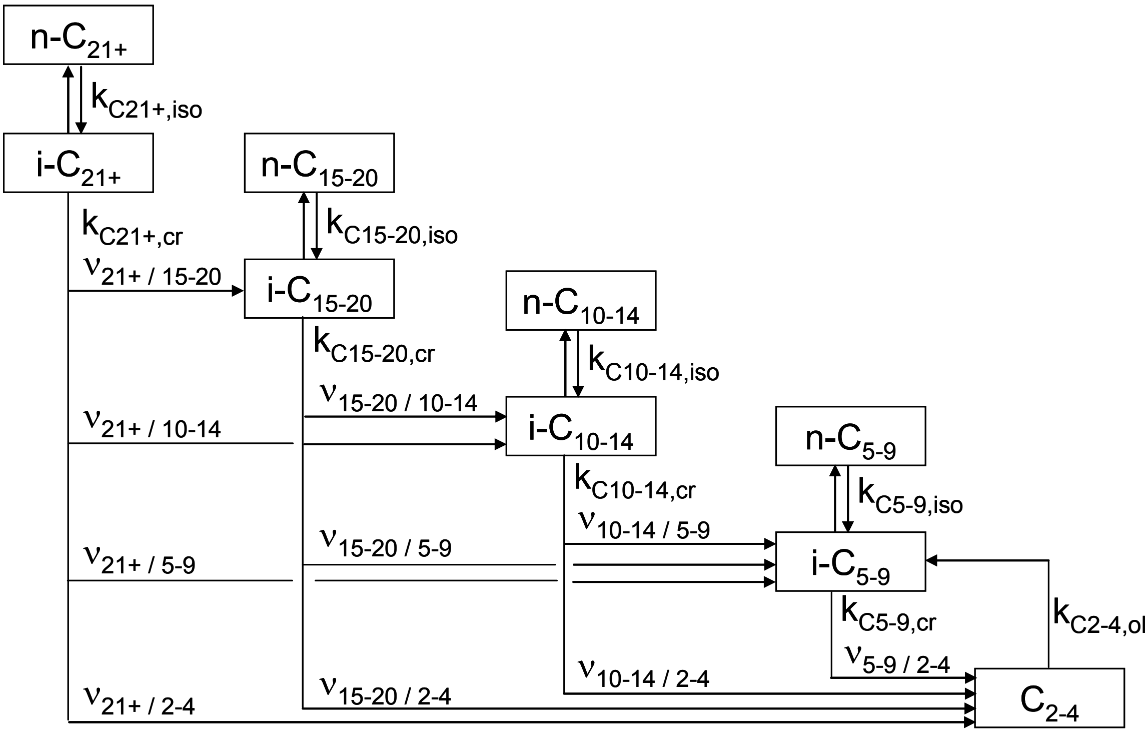
n-C21+
kC21+,iso
i-C21+
n-C15-20
kC21+,cr
kC15-20,iso
ν21+ / 15-20
i-C15-20
n-C10-14
kC15-20,cr
kC10-14,iso
ν15-20 / 10-14
ν21+ / 10-14
i-C10-14
n-C5-9
kC10-14,cr
kC5-9,iso
ν10-14 / 5-9
ν15-20 / 5-9
ν21+ / 5-9
i-C5-9
kC5-9,cr
kC2-4,ol
ν5-9 / 2-4
ν10-14 / 2-4
ν15-20 / 2-4
ν21+ / 2-4
C2-4

Fig. 7.1: Hydroisomerisation, hydrocracking and oligomerisation reactions network proposed for FT products on a Pt/zeolite catalyst according to the experimental data obtained (see Chapter 6).

Even with a pure model hydrocarbon or a binary mixture as feed (e.g. 1-octene, ethene/propene, Chapter 6.1) a large number of products is formed. In the dual-layer or in the physical-mixture configuration, the number of hydrocarbon molecules involved in these reactions is very large (approx. 350, as estimated from gas chromatograms). To simplify the reaction network the following assumptions are made:

- Hydrocarbons are divided into nine fractions: C_{21+}, C_{15-20}, C_{10-14}, C_{5-9} (respectively with n- and iso-alkanes) and C_{2-4} (which includes iso-C_4).
- Methane is not included. Pt/zeolite catalyst with 1 wt-% of Pt presents a strong hydrogenation function. For that reason primary cracking with symmetrical product distribution with no methane as product can be assumed. The smallest molecule that can undergo cracking reactions is C_8.
- Isomerisation reactions are reversible (Scherzer et al. 1996).

- Hydrocracking of n-alkane is preceded by hydroisomerisation (Steijns et al. 1981).
- Hydrocarbon cracking reactions generate two smaller molecules. Stoichiometric coefficients are required to describe the possibility that cracked products remain in the same fraction (e.g. C_{60} cracks into two C_{30} molecules). In addition, all the molecules are produced with the same probability:

$$S_i\left(N_{C,i}\right)= \begin{cases} 0 \quad , & i \in \left[N_{C,i}-3 \ldots\right] \\ \dfrac{\left(\dfrac{1}{N_{C,i}-6}\right)}{\sum\limits_{i=4}^{N_{C,i}-4}\left(\dfrac{1}{N_{C,i}-6}\right)}, & i \in \left[4 \ldots N_{C,i}-4\right] \\ 0 \quad , & i \in \left[N_{C,i}-3 \ldots\right] \end{cases} \tag{7.1}$$

- Fraction $C_{2\text{-}4}$ can undergo oligomerisation reactions leading mainly to iso-$C_{5\text{-}9}$ molecules (see Chapter 6.1).
- Alkenes and alcohols are not included in the reaction network since they are nearly completely hydrogenated on the bifunctional catalyst.

Tab. 7.1: Stochiometric coefficients ($\nu_{i\,/\,i'}$) for FT hydrocarbon cracking reactions assuming that all molecules are produced with the same probability (Eq. 7.1) for $C_{8\text{-}200}$ molecules (see Tab. 12.7).

$\nu_{21+\,/\,15\text{-}20}$	0.09	$\nu_{15\text{-}20\,/\,10\text{-}14}$	0.37	$\nu_{10\text{-}14\,/\,5\text{-}9}$	0.75	$\nu_{5\text{-}9\,/\,2\text{-}4}$	0.30
$\nu_{21+\,/\,10\text{-}14}$	0.07	$\nu_{15\text{-}20\,/\,5\text{-}9}$	0.49	$\nu_{10\text{-}14\,/\,2\text{-}4}$	0.22		
$\nu_{21+\,/\,5\text{-}9}$	0.07	$\nu_{15\text{-}20\,/\,2\text{-}4}$	0.10				
$\nu_{21+\,/\,2\text{-}4}$	0.01						

As the Pt/Beta catalyst used in the experiments showed a much lower cracking activity than Pt/ZSM-5 catalyst (Tab. 6.3, Fig. 6.30a), it was considered interesting to apply the reaction network model to the combination of FT (Co and Fe) and Pt/ZSM-5 catalysts.

7.2 Model formulation and validation of rate equations, example Pt/ZMS-5

Until today it appears no kinetic model has been published that considers the influence of CO and water vapour partial pressure on the hydrocarbon reactions with bifunctional catalysts. The experimental results obtained in the present study are not sufficient to develop a kinetic model which includes these effects explicitely.

Results from the kinetic model from Steijns et al. 1981 presented in Chapter 3.2.6 for reactions of n-C_8, n-C_{10} and n-C_{12} on Pt/Y catalyst are already presented in Chapter 6.1.1 for 1-octene reactions on Pt/ZSM-5 catalysts without the presence of CO. Figure 6.2 shows a relatively good agreement between calculated and experimental values of C_8 conversion and isomers and cracked product yields. However this kinetic model can not describe the experimental results obtained in the presence of CO (Fig. 7.2 grey curves). The experimental results indicate that CO decreases the isomers cracking rate (Fig. 6.3). Hence, the value of the preexponential cracking factor for C_8 ($k_{0,cr}$) presented in Table 3.9 was decreased by a factor 15 to yield a modified factor $k^*_{0,cr}$ (in Tab. 7.2). The factor was found by minimising the summed square of residuals between experimental and calculated data (Eq. 5.35). The k_0-values for isomerisation remain unchanged.

Tab. 7.2: Kinetic constants, adsorption and equilibrium constants for 1-C_8H_{16} reactions on Pt/ZSM-5 with synthesis gas (H_2/CO) in feed. Reaction conditions see Table 5.7. Kinetic model see Chapter 3.2.6. Reactor model see Chapter 5.4.

	$k_{0,iso,MB}$ mol/(s·kg)	$k_{0,iso,DB}$ mol/(s·kg)	$k^*_{0,cr}$ mol/(s·kg)	K_L (bar^{-1})	K_{eq} (-)
C_8	$3.06 \cdot 10^{13}$	$1.33 \cdot 10^{13}$	$1.10 \cdot 10^{12}$	8	7.6

Figure 7.2 shows a good agreement between experimental and calculated conversion and yield values for 1-C_8H_{16} reactions at 230-250 °C and the presence of CO (black curves and points). The kinetic model of Steijns et al. 1981 is valid in the temperature range of 130-250 °C (Chapter 3.2.6). Hence, the deviation between experimental and calculated data may be higher at 300 °C. The isomer yield curve includes the sum of mono- and dibranched hydrocarbons.

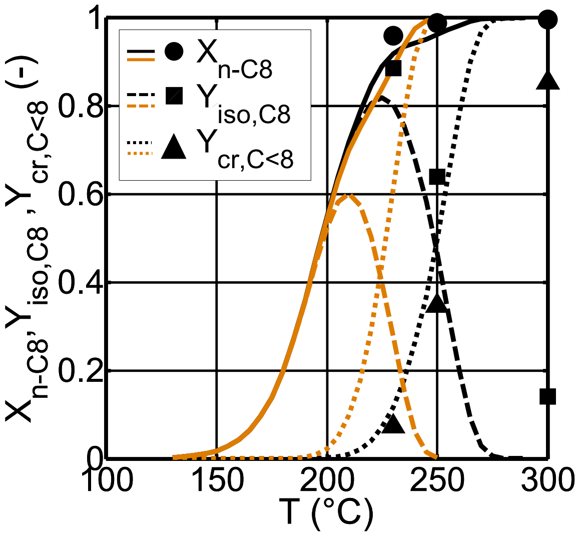

Fig. 7.2: Reactions of 1-C_8H_{16} with CO and H_2 on Pt/ZSM-5 catalysts. Points: experimental. Black curves: calculated with kinetic parameter values from Table 7.2. Grey curves: calculated with kinetic parameters from Steijns et al. 1981, Froment 1987. Reaction rates: Eq. 3.20-3.22. Reaction conditions see Table 5.7.

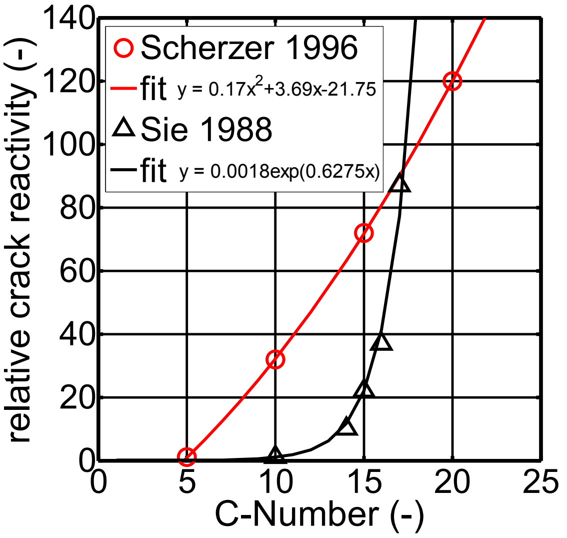

Fig. 7.3: Relative cracking reactivity of pure n-alkanes over a bifunctional catalyst. Symbols: from Sie 1988 and Scherzer et al. 1996. (Reference value 1: C_5 (Scherzer), C_{10} (Sie)). Curves: fitting.

For mixtures containing n-alkanes ($C_{4\text{-}70}$) Pellegrini et al. 2004, 2007 developed a kinetic model for cracking and isomerisation reactions on a Pt/amorphous-SiO_2/Al_2O_3 catalyst (see Chapter 3.2.6). This kinetic model is based on Steijns et al. 1981. Both models consider that all components are present in the gas phase. This assumption can also be applied in the present study, due to the relatively low partial pressure of the long-chain hydrocarbons produced during the FTS ($\alpha < 0.9$, Chapter 6.2).

The reaction conditions that Steijns et al. 1981 applied are closer to the present case than those from Pellegrini et al. 2004, 2007. Steijns et al. 1981 also used a Pt (1 wt-%)/zeolite catalyst. For that reason, it was considered reasonable to start with the kinetic model proposed by Steijns et al. 1981 in the present case.
The isomerisation and cracking reaction rates of Steijns et al. 1981 neglect the adsorption of the cracked products (Eq. 3.20-3.22). However, regarding the dual-layer configuration, at the inlet of the Pt/zeolite layer, all hydrocarbon molecules produced during the FTS are present. For that reason, the adsorption term of the isomerisation and cracking reaction rates was modified in order to include the adsorption of all n-alkanes and isomers (Eq. 7.2-7.3). In the product analysis, the branched hydrocarbons are calculated cumulatively for each C-number. Hence, only one isomerisation reaction rate is defined, not distinguishing between mono- and dibranched hydrocarbons (Eq. 7.2). The cracking reaction rate includes the modified rate constant ($k^*_{i,cr}$) which implicitly incorporates the effect of CO on the isomers cracking reactions (Eq. 7.3).

$$r_{i,iso} = \frac{k_{i,iso} \cdot \left(p_{n-Alkane,i} - p_{iso,i} / K_{dist,i}\right) - k^*_{i,cr} \cdot p_{iso,i}}{p_{H_2} \cdot \left[1 + \sum_i^{NC} \left(K_{L,i} \cdot p_{n-Alkane,i} + K_{L,i} \cdot p_{iso,i}\right)\right]} \tag{7.2}$$

$$r_{i,cr} = \frac{k^*_{i,cr} \cdot p_{iso,i}}{p_{H_2} \cdot \left[1 + \sum_i^{NC} \left(K_{L,i} \cdot p_{n-Alkane,i} + K_{L,i} \cdot p_{iso,i}\right)\right]} \tag{7.3}$$

The parameter $K_{L,i}$ (similar to an adsorption constant) of n-alkanes and isomers in the same C-fraction is assumed to be the same, as Steijns et al. 1981 also assumed. Considering Equation 7.2-7.3, one isomerisation and one cracking reaction rate constant ($k_{i,iso}$ and $k^*_{i,cr}$ respectively) and one adsorption constant ($K_{L,i}$) are required for each fraction.

Steijns et al. 1981 and Froment 1987 calculated the equilibrium constants ($K_{eq,i}$ in Eq. 3.20-3.21) for the reversible isomerisation reactions using thermodynamic data of Stull et al. 1969. They calculated values for C_{10} at 227 °C, assumed to be constant in the temperature range 150-250 °C (Tab. 3.9). The same values are adopted for C_8 and C_{12}. A thermodynamic analysis of n-alkane isomerisation is particularly difficult because of the relatively scarce data available on thermodynamic properties of isomers containing more than 10 carbon atoms (for C_{10}, the number of possible isomers is 75). Even more, the ratio n- / isomers of cracked products from n-alkanes (e.g. FT hydrocarbons) with bifunctional catalysts is governed by reaction kinetics. The ratio of individual monomethyl alkane to the corresponding n-alkane can be higher than calculated for thermodynamic equilibrium, due to the formation of isomers by cracking reactions (Schulz et al. 1972). Therefore, it was not considered appropriate to use the term “equilibrium constant”. It was renamed as distribution coefficient ($K_{dist,i}$ in Eq. 7.2). Then, one distribution coefficient is required for each fraction, except for C_{2-4}.

Then, the rate equations include seventeen parameters in total. Considering the number of experimental data, estimations are made based on published information. For example, Steijns et al. 1981 collected data for the hydroisomerisation and hydrocracking reactions of C_8-, C_{10}- and C_{12}-alkane. Extrapolation to large molecules can be made based on Rapaport 1962, Stangeland 1974, Sie et al. 1988 and Scherzer et al. 1996. They reported correlations between the number of C-atoms of a hydrocarbon and its cracking reactivity under mild hydrocracking conditions (p = 3-5 MPa, T = 300-350 °C from Sie et al. 1991), (see Fig. 7.3).

Conversion levels in the hydrocracking of petroleum fractions are usually in the 50-90 % range (Sie 1997). The decrease of the C_{21+} fraction achieved in the present experiments by combining FT catalyst (Co, Fe) and Pt/ZSM-5 is in the 40-57 % range (Fig. 6.30a, 6.35a). For that reason, the correlation from Scherzer et al. 1996 was chosen to calculate the cracking reactivity for each C-number (Fig. 7.3). Then, a mean value was calculated for each fraction. Assuming that $C_{5\text{-}9}$ group has a reference cracking reactivity of 1, the reactivity increases with C-number as follows: $C_{5\text{-}9}$/ $C_{10\text{-}14}$/ $C_{15\text{-}C20}$/ C_{21+} (1/ 3.7/ 7.5/ 33.7). A correlation for the relative isomerisation reactivity of the different fractions could not be found in the literature. Hence, it was assumed to be the same as for the cracking reactions.

However, by testing the kinetic model it was found that the relative cracking reactivity values from Scherzer et al. 1996 were too high for the Pt/ZSM-5 catalyst used in this study. Better agreement was found with the following values: $C_{5\text{-}9}$/ $C_{10\text{-}14}$/ $C_{15\text{-}C20}$/ C_{21+} (1/ 3.7/ 3.7/ 9), (see Tab. 7.3). The lower relative cracking reactivity may be due to the low partial pressure of long-chain hydrocarbons. In a hydrocracking unit in the petroleum refinery, the high-molecular-weight hydrocarbons are present in the liquid phase allowing longer contact time with the catalyst and having a greater chance of being cracked. In the experiments carried out in this study, the low partial pressure of these hydrocarbons may result in the gaseous state and therefore lower contact times.

The kinetic parameter values for C_8 collected by Steijns et al. 1981 and Froment 1987 were adopted for the fraction $C_{5\text{-}9}$ at 230 °C (Tab. 7.3), except the cracking rate constant which was adopted from the 1-octene reactions in Table 7.2 (taking into account the effect of CO on isomer cracking reactions).

The experimental results presented in Chapter 6.1.3 indicate that ethene and propene undergo oligomerisation reactions on Pt/ZSM-5 and Pt/Beta catalysts leading mainly to isomers in the $C_{5\text{-}9}$ fraction. In the literature, butene is also reported to undergo oligomerisation reactions (Quann et al. 1991, Tabak et al. 1986). The combination FT and Pt/zeolite catalyst decreases the alkene selectivity through hydrogenation reactions. However, alkenes with $N_C < 5$ are still present in the reactor outlet (Fig. 6.27, Fig. 6.33). From the experimental results mentioned, it was assumed that the fraction $C_{2\text{-}4}$ undergoes oligomerisation reactions not distinguishing between alkanes and alkenes (Fig. 7.1). The presence of H_2 or synthesis gas in feed decreases the oligomerisation rate of alkenes (see Chapter 6.1.3). Following these experimental results, the oligomerisation reaction rate was assumed to be analogous to that of cracking (Eq. 7.4). Inclusion of the oligomerisation reactions adds an additional kinetic parameter ($k_{i,ol}$). In order to form an iso-C_8 from ethene or propene, first oligomerisation must occur. This indicates that oligomerisation of $C_{2\text{-}4}$ fraction must be at least as fast as the isomerisation of $C_{5\text{-}9}$ fraction (Tab. 7.3, see also Chapter 7.2.3).

$$r_{ol} = \frac{k_{ol} \cdot p_{C2-4}}{p_{H_2} \cdot \left[1 + \sum_{i}^{NC} \left(K_{L,i} \cdot p_{n-Alkane} + K_{L,i} \cdot p_{iso} \right) \right]} \tag{7.4}$$

The rate of isomerisation and cracking reactions (Eq. 7.2-7.3) is also affected by the adsorption of the hydrocarbons on the catalyst ($K_{L,i}$). In general, larger molecules adsorb stronger and react faster than smaller molecues. For the C_{5-9} and C_{10-14} fractions, the adsorption constant was taken from Steijns et al. 1981 and Froment 1987. Pellegrini et al. 2007 presented an equation to calculate the adsorption constant ($K_{L,i}$) depending on the number of C-atoms of a molecule (Eq. 7.5). Sie et al. 1991 had already described qualitatively an adsorption curve as a function of the number of C-atoms which follows an approximately exponential increase, corresponding to a linearly increasing heat of adsorption with increasing number of C-atoms. However, above a critical chain length (N_c ~ 35), the effect levels off since the degree of adsorption approaches 100 %. The equation by Pellegrini et al. 2007 was used in the present study to calculate the adsorption constant for the C_{15-20} fraction. For the C_{21+} fraction this equation was used but considering that up C_{35} the adsorption constant remains constant, like Sie et al. 1991 described (Tab. 7.3)

$$K_{L,i} = 0.1 \cdot \exp(0.39 \cdot N_C) \quad ; \text{for } N_c \leq 35 \tag{7.5a}$$

$$K_{L,i} = 0.1 \cdot \exp(0.39 \cdot 35) \quad ; \text{for } N_c > 35 \tag{7.5b}$$

The distribution coefficient for isomerisation ($K_{dist,i}$) was assumed to be the same for all fractions given the lack of data (Tab. 7.3-7.4). It has the same value as the equilibrium constant for C_8 that Steijns et al. 1981 proposed ($K_{eq,1}$ in Tab. 3.9).

As presented in Chapter 6.3.2, a dual-layer configuration with Fe and Pt/ZSM-5 catalyst was also investigated. In that case, FT and hydrocarbon reactions take place at 250-270 °C. Table 7.4 presents the kinetic parameters for hydrocarbon reactions on Pt/ZSM-5 at 250 °C. The rate constants for isomerisation and hydrocracking reactions were calculated following the Arrenhius' law. The oligomerisation rate constant ($k_{i,ol}$) was determined by trial and error at 230 °C. Its value at 250 °C was determined by assuming that the activation energy is the same as for isomerisation and cracking reactions. Since the temperature range is rather limited (230-250 °C), the adsorption and distribution dependency on temperature was not considered.

The alkenes produced by FTS were assumed to be completely hydrogenated at the inlet of the Pt/ZSM-5 layer. The hydrogen consumption of the hydrogenation reactions was considered, as well as that of the cracking reactions. Pt/ZSM-5 catalyst has no synthesis activity and a negligible CO/CO_2-shift activity at 230 °C (Fig. 6.1). Hence, it was assumed that CO, CO_2 and H_2O do not react on the Pt/ZSM-5 catalyst. Assuming that only "ideal" cracking reactions take place on Pt/ZSM-5 catalyst, no CH_4 is produced, (see Fig. 12.21-12.22).

Tab. 7.3: Model parameter values for Pt/ZSM-5 at 230 °C, kinetic, adsorption and equilibrium constants for hydroisomerisation, hydrocracking and oligomerisation reactions in the presence of CO. p = 1 MPa, $(p_{H2}/p_{CO})_{in}$ = 2.

	$k_{i,iso}$ mol/(s·kg)	$k^*_{i,cr}$ mol/(s·kg)	$k_{i,ol}$ mol/(s·kg)	$K_{L,i}$ (bar^{-1})	$K_{dist,i}$ (-)
C_{2-4}	-	-	0.25	1	-
C_{5-9}	0.19	$6.79 \cdot 10^{-3}$	-	8	7.6
C_{10-14}	$k_{5-9,iso} \cdot 3.7$	$k^*_{5-9,cr} \cdot 3.7$	-	20	7.6
C_{15-20}	$k_{5-9,iso} \cdot 3.7$	$k^*_{5-9,cr} \cdot 3.7$	-	120	7.6
C_{21+}	$k_{5-9,iso} \cdot 9$	$k^*_{5-9,cr} \cdot 9$	-	30000	7.6

Tab. 7.4: Model parameter values for Pt/ZSM-5 at 250 °C Kinetic, adsorption and equilibrium constants for hydroisomerisation, hydrocracking and oligomerisation reactions in the presence of CO. p = 1 MPa, $(p_{H2}/p_{CO})_{in}$ = 2.

	$k_{i,iso}$ mol/(s·kg)	$k^*_{i,cr}$ mol/(s·kg)	$k_{i,ol}$ mol/(s·kg)	$K_{L,i}$ (bar^{-1})	$K_{dist,i}$ (-)
C_{2-4}	-	-	0.87	1	-
C_{5-9}	0.66	$2.40 \cdot 10^{-2}$	-	8	7.6
C_{10-14}	$k_{5-9,iso} \cdot 3.7$	$k^*_{5-9,cr} \cdot 3.7$	-	20	7.6
C_{15-20}	$k_{5-9,iso} \cdot 3.7$	$k^*_{5-9,cr} \cdot 3.7$	-	120	7.6
C_{21+}	$k_{5-9,iso} \cdot 9$	$k^*_{5-9,cr} \cdot 9$	-	30000	7.6

7.2.1 Dual layer

The experimental results from Chapter 6.3 show a very low cracking activity of Pt/ZSM-5 at temperatures below 230 °C and at H_2/CO-ratio below 2 at reactor inlet. For that reason the model presented in Chapter 7.2 was tested at 230 °C and an H_2/CO-ratio of 2.

The modified residence time in the second layer (τ_{mod}*) is defined as weight mass of Pt/ZSM-5 catalyst divided by the volume flow at reactor inlet at standard conditions:

$$\tau_{\mathrm{mod}}{}^{*} = \frac{m_{Pt/ZSM-5}}{\dot{V}_{n,in}} \tag{7.6}$$

The reactor model presented in Chapter 5.4 together with the reaction rates of isomerisation, cracking and oligomerisation (Eq. 7.2-7.4) were used to calculate the molar fraction profiles of the different hydrocarbon fractions along the Pt/ZSM-5 catalyst layer underneath of the Co/Al_2O_3 catalyst layer (Fig. 5.8b, Fig. 7.4-7.7). The fractions C_{10-14} and C_{15-20} were combined and presented as C_{10-20} (representing the diesel fuel fraction). The experimental data at τ_{mod}* = 0 represent the measured outlet gas composition from separate FTS experiments, corresponding to different residence times in the Co/Al_2O_3 layer.

The calculated hydrocarbon molar fractions reflect the measured decrease of n-C_{5-9} and the increase of iso-C_{5-9} fractions (Fig. 7.4), as well as the increase of the iso-C_{10-20} fraction. However, the kinetic model does not reflect the increase of the n-C_{10-20} fraction (Fig. 7.5). The decrease of the n-C_{21+} fraction results in an increase of iso-C_{21+} (Fig. 7.6). However, the kinetic model predicts a stronger increase of iso-C_{21+} than found in the experimental results. Inclusion of the oligomerisation reactions in the kinetic model results in a decrease of the C_{2-4} fraction (Fig. 7.7a). The calculated hydrogen molar fraction values start slightly below the experimental values due to the consideration of hydrogenation reactions at the second layer inlet (Fig. 7.7b, see also Chapter 7.2).

Figure 7.8a presents a parity plot which shows the agreement between calculated and experimental hydrocarbon molar fractions for all tested residence times. Most of the values are in the range ± 30%.

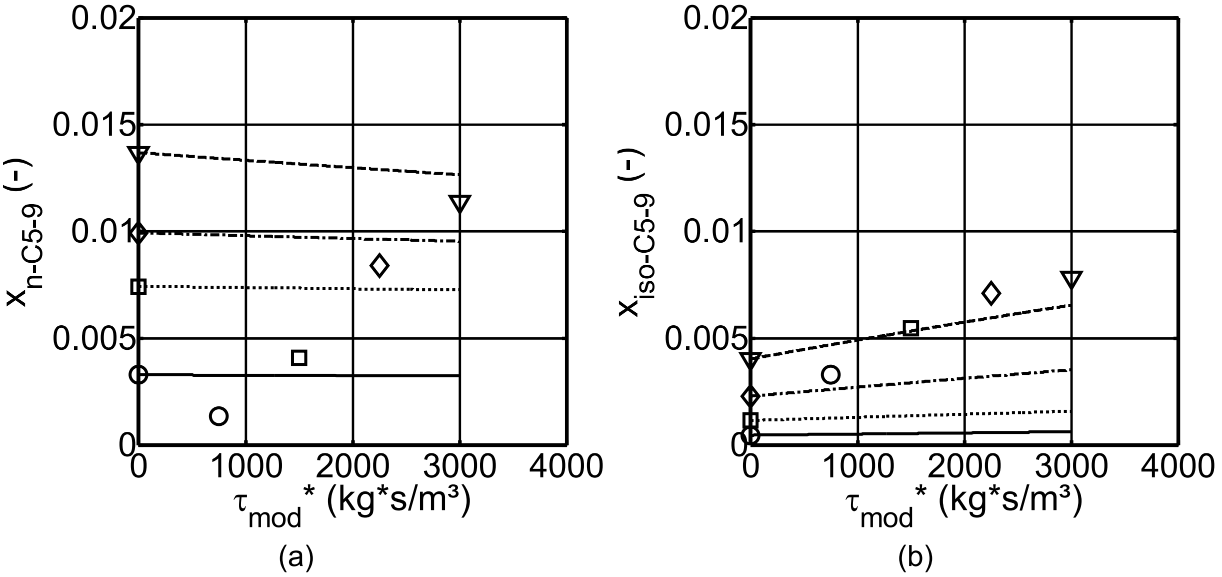

Fig. 7.4: Calculated and experimental molar fractions (curves, symbols) of n-C_{5-9} (a) and iso-C_{5-9} (b) in Pt/ZSM-5 catalyst layer below the Co/Al_2O_3 catalyst layer (dual-layer configuration). τ_{mod} = 4000 (triangles), 3000 (rhombus), 2000 (squares) and 1000 (circles) kg·s/m^3. T = 230 °C, p = 1 MPa, $(p_{H2}/p_{CO})_{in}$ = 2. Kinetics: Tab. 7.3, Eq. 7.2-7.4.

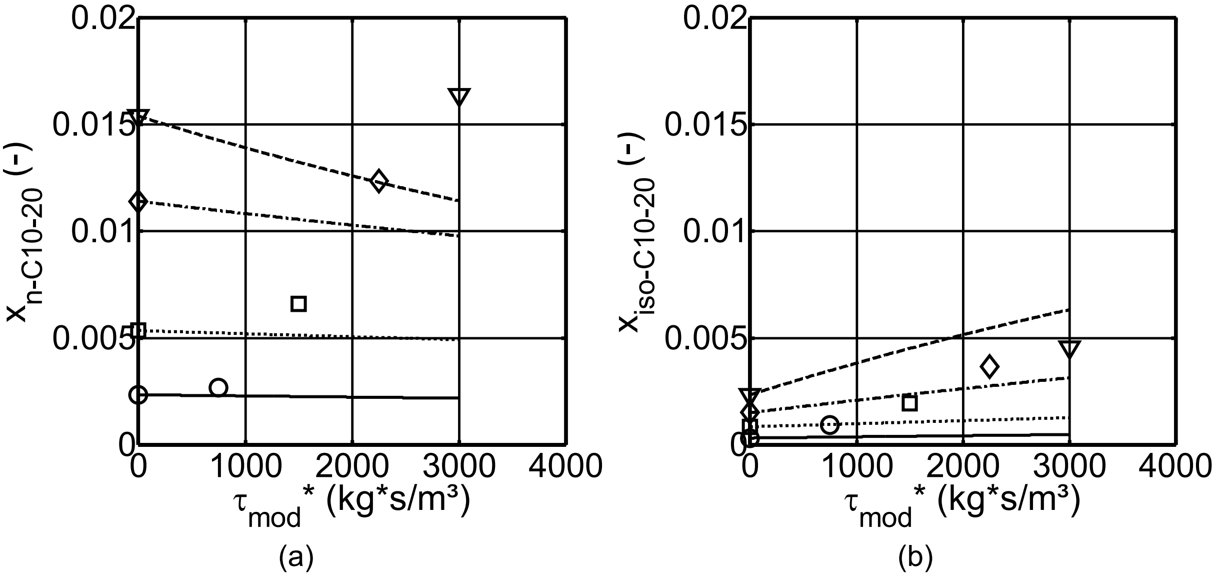

(a) (b)

Fig. 7.5: Calculated and experimental molar fractions (curves, symbols) of n-C_{10-20} (a) and iso-C_{10-20} (b) in Pt/ZSM-5 catalyst layer below the Co/Al_2O_3 catalyst layer (dual-layer configuration). Reaction conditions and kinetics: see Fig. 7.4.

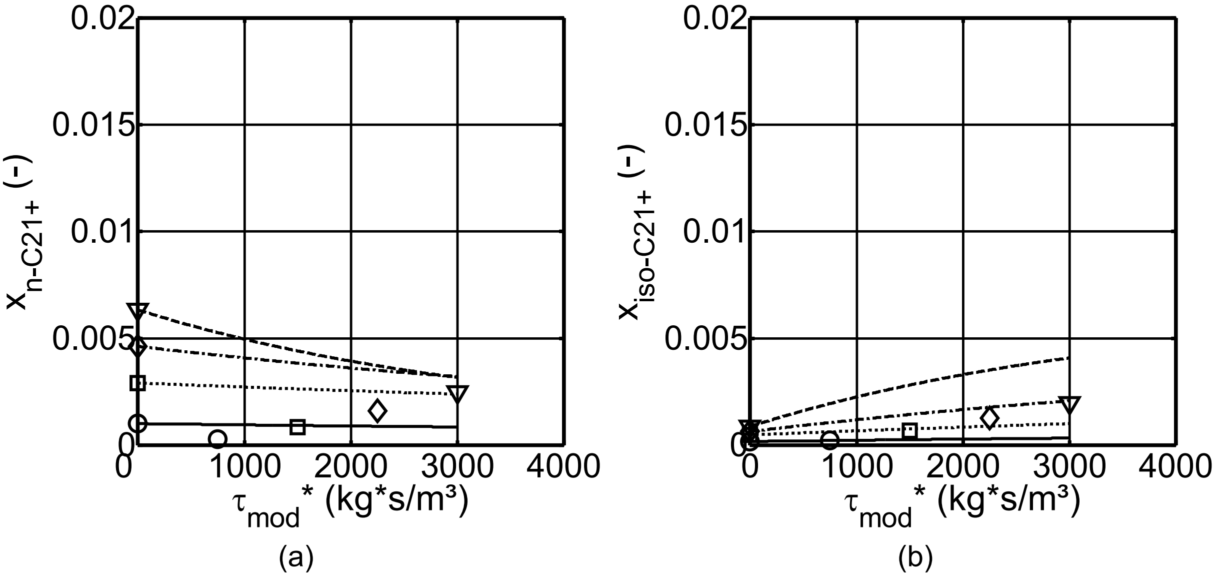

(a) (b)

Fig. 7.6: Calculated and experimental molar fractions (curves, symbols) of n-C_{21+} (a) and iso-C_{21+} (b) in Pt/ZSM-5 catalyst layer below Co/Al_2O_3 catalyst layer (dual-layer configuration). Reaction conditions and kinetics: see Fig. 7.4.

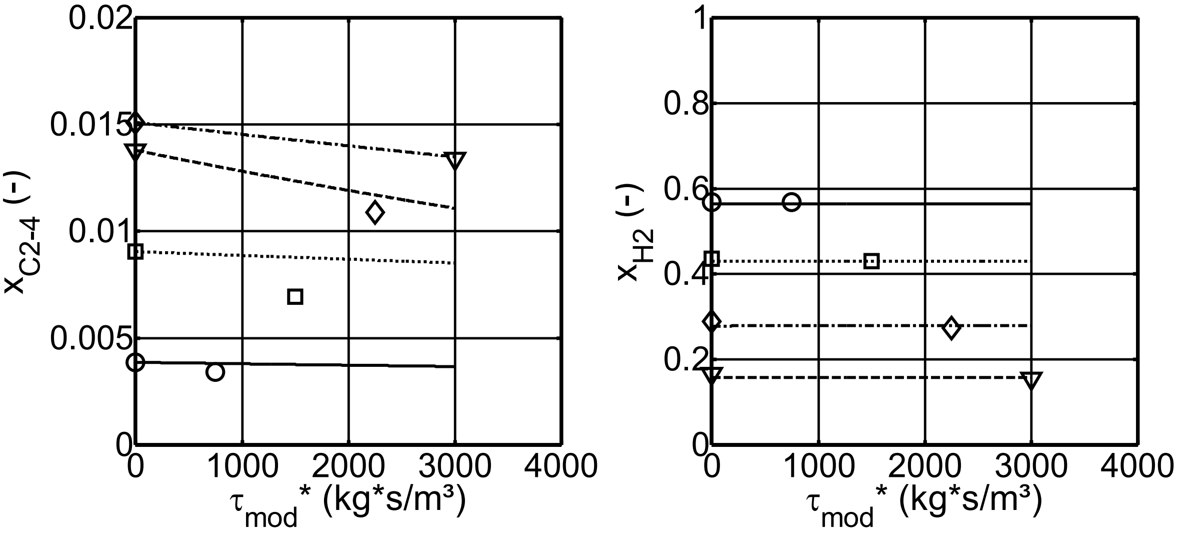

(a) (b)

Fig. 7.7: Calculated and experimental molar fractions (curves, symbols) of n-C_{2-4} (a) and H_2 (b) in Pt/ZSM-5 catalyst layer below the Co/Al_2O_3 catalyst layer (dual-layer configuration). Reaction conditions and kinetics: see Fig. 7.4.

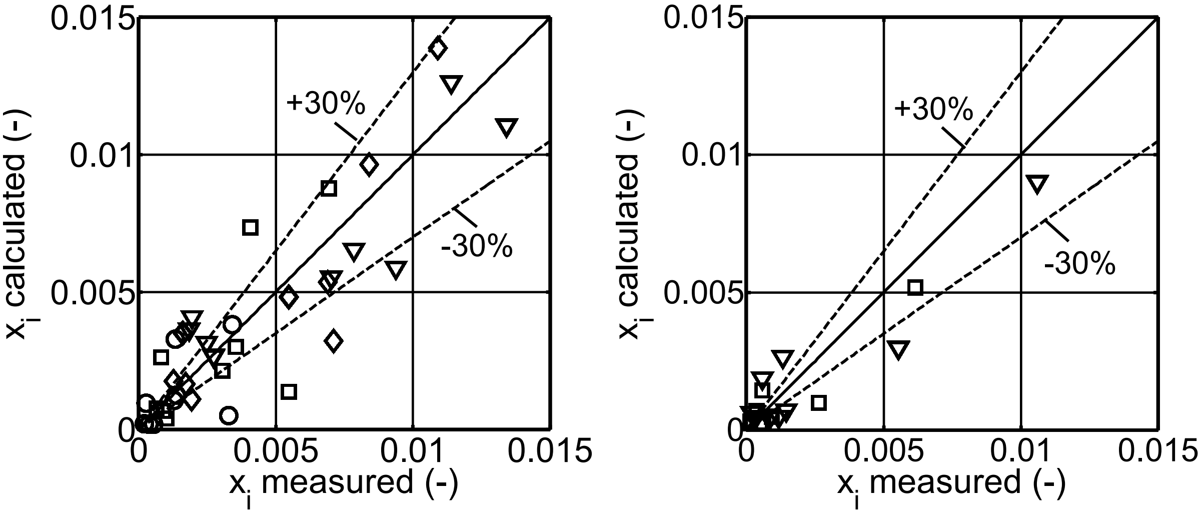

(a) (b)

Fig. 7.8: Parity plots: measured and calculated hydrocarbon molar fractions at all tested residence times. (a) Pt/ZSM-5 underneath Co/Al_2O_3 at 230 °C, (b) Pt/ZSM-5 underneath the K-promoted Fe at 250 °C. Reaction conditions and kinetics: see Fig. 7.4. Symbols: see Fig. 7.4-7.7.

The kinetic model for hydrocarbon reactions on Pt/ZSM-5 was also tested for the dual-layer configuration with the K-promoted Fe catalyst at 250 °C using the kinetic parameters presented in Table 7.4. The hydrogen consumption for alkenes and alcohols hydrogenation was also taken into account at Pt/ZSM-5 catalyst bed inlet with Fe showing higher yields of alkenes and alcohols than Co. Due to the CO/CO_2-shift activity of the K-promoted Fe catalyst, the hydrocarbon partial pressure is lower than with the Co/Al_2O_3 catalyst (see Chapters 6.2.1-6.2.2). The molar fraction profiles for the two residence time values investigated are presented in the Annex (Fig. 12.23-12.26). In these cases, the agreement between calculated and experimental values of the fraction n-C_{10-20} is better than in combination with the Co catalyst (Fig. 12.24a, Fig. 7.5a), with lower absolute values. Like in combination with Co, the kinetic model predicts a higher iso-C_{21+} molar fraction value than observed in the experiments (Fig. 12.25b, Fig. 7.6b). Considering all hydrocarbon fractions, the agreement between calculated and experimental values is not as good as in combination with Co. The deviation exceeds in most of the cases the range ± 30 % (Fig. 7.8b).

On the one hand, the experimental and calculated results presented show plausibility and agreement. Numerical optimisation routines were not applied given the limited number of experimental data and the errors in the combined experiments which mainly affect the fraction C_{15-20} (see Chapter 12.8). The main source of error here is the combination of the gas and liquid phase analyses (see Chapter 6.2). On the other hand, the limited agreement indicates the need to further improve the kinetic model. CO and H_2O may compete with H_2 and hydrocarbons for adsorption on the acidic sites of the zeolite. This competition could have an influence on the reaction rate. In addition shape-selectivity may influence diffusion of molecules into the pores and, thus, reaction rates.

7.2.2 Physical mixture

The kinetic model was also applied to the physical-mixture configuration with the Co/Al_2O_3 and Pt/ZSM-5 catalysts. In a physical-mixture configuration, FT synthesis, isomerisation, cracking, oligomerisation and hydrogenation reactions take place simultaneously along the reactor length. The hydrocarbon reactions were described with the reaction rates presented in Equation 7.2-7.4 and the kinetic parameters from Table 7.3. The FT synthesis reaction rates are given in Equation 5.31 and the kinetic parameter values in Table 6.1. The fixed-bed-reactor model used is presented in Chapter 5.4.

The formation of hydrocarbons during the FT synthesis and their distribution in the different fractions was calculated with the ideal Anderson-Flory-Schulz distribution (ASF) presented in Equation 3.8. According to the experimental results in Chapter 6, an α value equal to 0.85 was used to describe the chain-growth probability of hydrocarbons on the Co/Al_2O_3 catalyst at 230 ºC (Fig. 6.13a).
However, the ideal ASF distribution does not distinguish between n- and iso-alkane or alkene. The product distribution of Co/Al_2O_3 shows very low selectivities of alkenes at 230 °C and H_2/CO-ratio of 2 (Fig. 6.14a). Hence, in the present study no distinction is made between alkanes and alkenes. The distribution n-/iso-alkane used in this kinetic model was adopted from the experimental results with the Co/Al_2O_3 catalyst alone (Tab. 7.5).

Tab. 7.5: Isomer content in carbon-number fractions as obtained with the Co/Al_2O_3 catalyst alone.

	C_{2-4}	C_{5-9}	C_{10-20}	C_{21+}
Isomers in $N_{C,i}$ (%)	0.7	23.0	11.7	12.0

With Co-based FT catalysts, the formation of CO_2 can often be neglected and so was done in Chapter 6.2.1.1. However, the formation of CO_2 was included in the kinetic model of the physical-mixture configuration. In the literature there is no kinetic equation for the CO/CO_2-shift reaction on Co-based reactions (Eq. 3.5). Hence, according to the experimental values it was assumed that 4 % of the reacted CO converts to CO_2 and H_2 (Fig. 7.11a).

Figures 7.9-7.11 show the molar fraction profiles of all organic and inorganic compounds along the reactor length, expressed as modified residence time (with $m_{cat} = m_{Co\text{-}cat} + m_{Pt/ZSM\text{-}5}$). The agreement between calculated and experimental values for the physical mixture is not as good as for the dual-layer configuration (Fig. 7.11b, Fig. 7.8a). The model predicts higher n-alkane and lower isomer molar fractions than obtained in the experiments. In the physical mixture model, errors are not only caused by deficiencies in the hydroprocessing reaction model (see Chapter 7.2), but also by deficiencies in the FT selectivity model. Here, the hydrocarbon product distribution obtained from FT catalysts deviates from the ideal ASF distribution (see chapter 3.1.1.5). For example, Schulz et al. 1999 reported that the ASF product distribution is changed by the occurrence of secondary reactions (i.e. α-alkene readsorption, incorporation, hydrogenation and isomerisation of α-alkene). They also present a kinetic model which allows the formation of different compounds to be described (alkanes, alkenes and oxygenates). These compounds desorb in distinct ratios independent of carbon number. There is controversy in the literature about the fundamentals of this chain-length dependency. Potential causes for a chain-length- dependent contact time are physisorption, solubility and diffusivity (van der Laan 1999b). This indicates that changes in the solubility and physisorption strength must be included in a detailed FT product model. In addition, higher methane selectivity is observed than predicted from ASF (Fig. 7.10a), and often attributed to “extra-methane centres”.

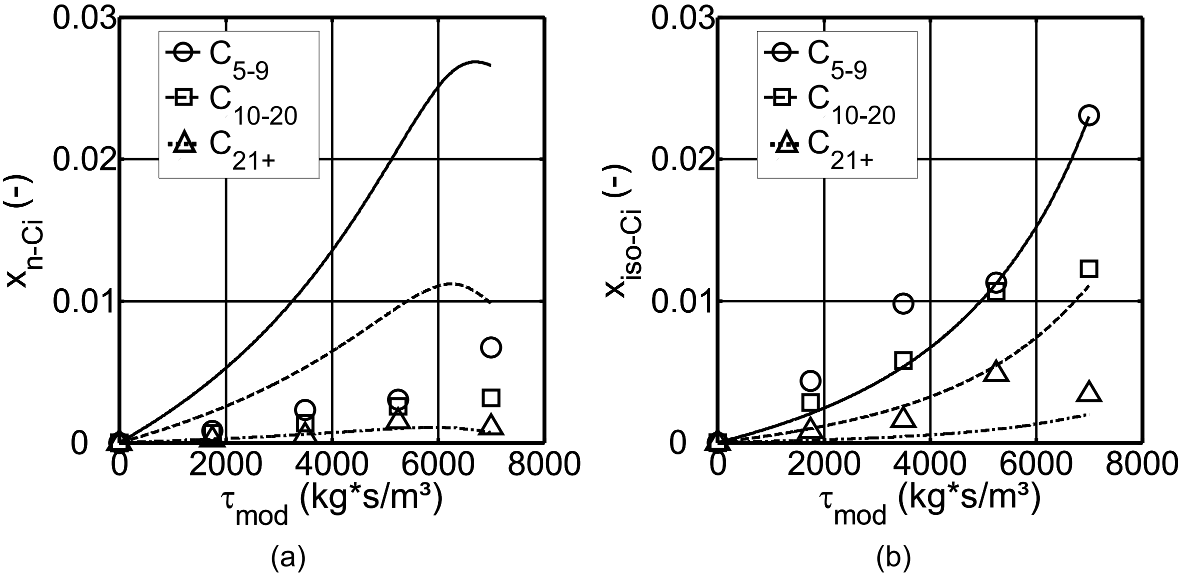

(a) (b)

Fig. 7.9: Calculated and experimental molar fractions (curves, symbols) of the n-alkanes (a) and iso-alkanes (b) in the physical mixture of Co/Al_2O_3 and Pt/ZSM-5 catalysts. T = 230 °C, p = 1 MPa, $(p_{H2}/p_{CO})_{in} = 2$. Kinetics FT reactions: Tab. 6.1, Eq. 5.31. Kinetics hydrocarbon reactions: Tab. 7.3, Eq. 7.2-7.4.

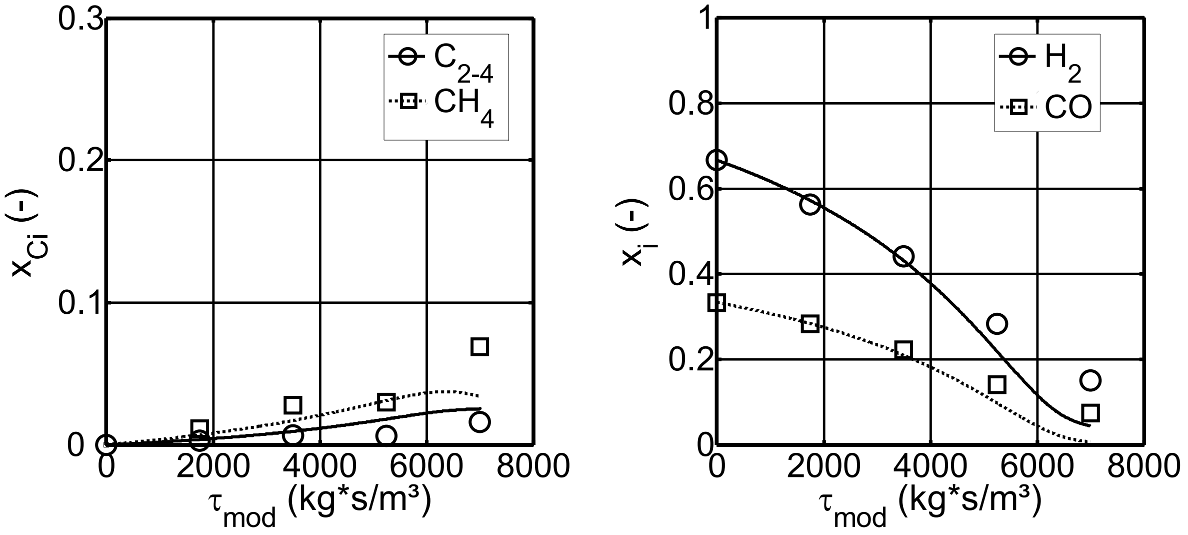

(a) (b)

Fig. 7.10: Calculated and experimental molar fractions (curves, symbols) of $C_{2\text{-}4}$ and CH_4 (a) and CO and H_2 (b) in the physical mixture of Co/Al_2O_3 and Pt/ZSM-5 catalysts. Reaction conditions and kinetics: see Fig. 7.9.

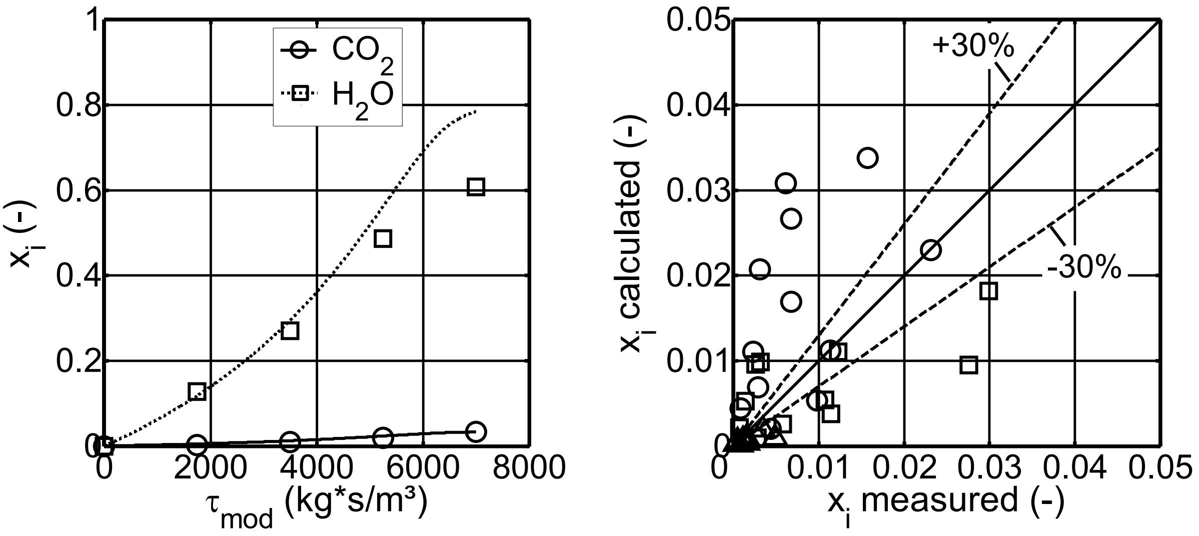

(a) (b)

Fig. 7.11: (a) Calculated and experimental (curves, symbols) molar fraction of CO and H_2O. (b) Parity plot: measured and calculated hydrocarbon molar fractions at all investigated residence time. Physical mixture of Co/Al_2O_3 and Pt/ZSM-5 catalysts. Reaction conditions and kinetics: see Fig. 7.9. Symbols: same as in Fig. 7.9-7.11a.

7.2.3 Reaction rates of hydroprocessing reactions

All the assumptions made in the model can be visualized in a plot of calculated rates along the length of the catalyst bed for dual-layer and physical-mixture configurations (Fig. 7.12-7.13):

i) For the development of the reactions network and the kinetic model it was assumed that the cracking reaction of n-alkanes is preceded by isomerisation on a

Pt/zeolite catalyst. In both reactor configurations (dual layer and physical mixture) isomerisation rates are faster than cracking rates for all fractions (Fig. 7.12).

ii) At the reactor outlet, the ratio $r_{i,iso}/r_{i,cr}$ is very similar for the C_{5-9} and C_{10-20} fractions. However, this ratio decreases for the fraction C_{21+}. This confirms the assumption that long-chain hydrocarbons would preferably undergo cracking reactions rather than isomerisation. In the dual-layer configuration, the ratio $r_{i,iso}/r_{i,cr}$ of fraction C_{21+} decreases by a factor three and in the physical mixture by a factor four compared with fraction C_{5-9} (at reactor outlet), (Fig. 7.12).

iii) In the physical-mixture configuration, at reactor inlet, isomerisation, cracking and oligomerisation reaction rates are equal to zero. First the hydrocarbons have to be formed via FT synthesis (Fig. 7.13).

iv) At the outlet of Pt/ZSM-5 layer (also reactor outlet) the relative reactivity ($r_{i,j}/r_{C5-9}$) of the C_{5-9}/ C_{10-20}/ C_{21+} fractions is equal to 1/ 3.6/ 5.6 for cracking reactions and 1/ 3.4/ 2 for isomerisation reactions. This indicates again the higher cracking reactivity of long-chain hydrocarbons. The relative reactivity ($r_{i,j}/r_{C5-9}$) in the physical mixture at reactor outlet is equal to 1/ 1.8/ 0.8 and 1/ 1.4/ 0.2 for cracking and isomerisation reactions respectively (C_{5-9}/ C_{10-20}/ C_{21+}). In that case, both cracking and isomerisation rates of the C_{21+} fraction are lower than those of the C_{5-9} fraction. This relates to the low partial pressure of the fraction C_{21+} in this configuration since hydrocarbons are formed and cracked simultaneously.

v) Oligomerisation of C_{2-4} is faster than the isomerisation or cracking of fraction C_{5-9} (Eq. 7.4) for both dual-layer and physical-mixture configurations (Fig. 7.12).

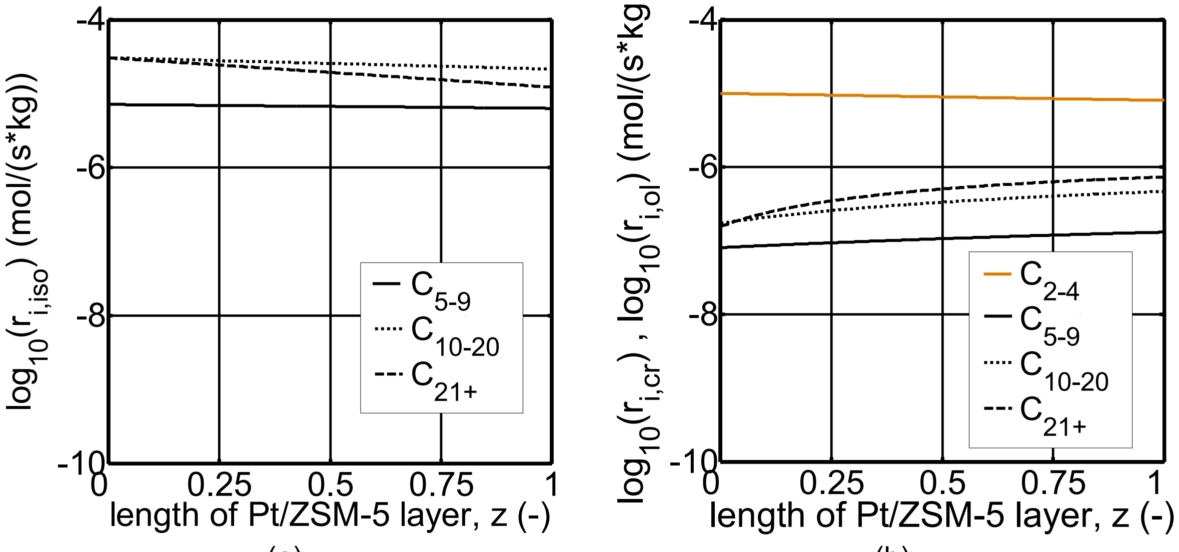

(a) (b)

Fig. 7.12: Dual-layer configuration - Co/Al_2O_3 + Pt/ZSM-5. (a) Isomerisation, (b) cracking and oligomerisation reaction rates calculated with the partial pressures obtained at the outlet of FT layer at τ_{mod} = 4000 kg·s/m^3 (Fig. 7.4-7.7 triangles). T = 230 °C, p = 1 MPa, $(p_{H2}/p_{CO})_{in}$ = 2. Kinetics hydrocarbon reactions: Tab. 7.3, Eq. 7.2-7.4.

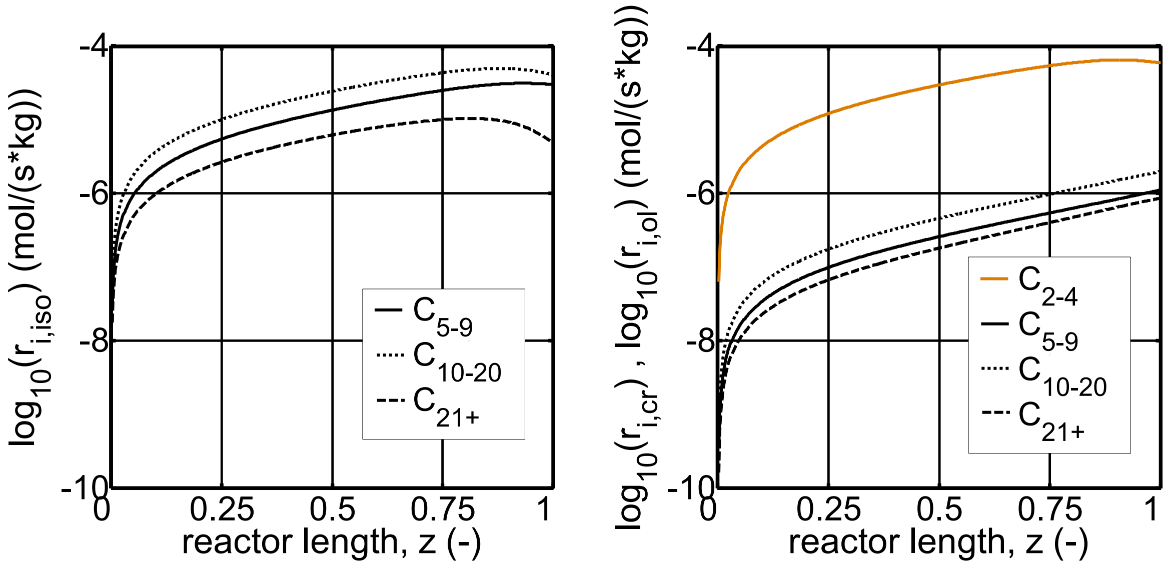

(a) (b)

Fig. 7.13: Physical-mixture configuration - Co/Al_2O_3 + Pt/ZSM-5. (a) Isomerisation, (b) cracking and oligomerisation reaction rates. Partial pressures see Figures 7.9-7.11a. T = 230 °C, p = 1 MPa, τ_{mod} = 7000 kg·s/m^3, $(p_{H2}/p_{CO})_{in}$ = 2. Kinetics FT reactions: Tab. 6.1, Eq. 5.31. Kinetics hydrocarbon reactions: Tab. 7.3, Eq. 7.2-7.4.

8 Conclusions and outlook

Conclusions

The present exploratory study of hydroprocessing reactions in combination with FT synthesis leads to the following main results:

1) Combining FT and hydroprocessing catalysts

- Measurable effects on hydrocarbon product distribution with combinations of Co or Fe FT-catalysts and hydroprocessing example catalysts (Pt/ZSM-5, Pt/Beta) include an increase of the gasoline and diesel yields, and limited improvement of the product quality (e.g. octane number of gasoline fraction).
- Cracking, isomerisation, hydrogenation and oligomerisation reactions take place on Pt/ZSM-5 and Pt/Beta catalysts at FT synthesis temperatures (230-300 ºC) and in the presence of CO and H_2O.
- Selection and development of improved hydroprocessing catalyst and adjustment of reaction conditions appear promising.

2) Comparison of hydroprocessing catalysts

- Different hydrocarbon product distributions are obtained on Pt/ZSM-5 and Pt/Beta catalysts: higher isomerisation and lower cracking product yields on Pt/Beta catalyst, to be attributed to zeolite structure and properties (e.g. pore and crystal size, acidic strength).

3) Effect of reaction conditions

- Isomerisation reactions dominate cracking reactions at lower temperatures (~ 200-230 ºC).
- Secondary cracking reactions take place at higher temperatures (> 250 °C), increasing methane selectivity.
- CO has a deleterious effect on the de/hydrogenation activity of Pt, consequently slowing down the isomer cracking reactions. Thus, H_2/CO-ratio at reactor inlet has an influence on the hydrocarbon product distribution.

4) Effect of catalyst-bed configuration

- Different product distribution is obtained depending on the catalyst-bed configuration (i.e. dual layer, physical mixture), which may be attributed to the CO partial pressure profiles.

5) Reaction network model

- Good agreement can be seen between experimental and calculated values for the 1-octene reactions on Pt/ZSM-5 with and without CO in feed.
- The calculated values for the dual-layer and the physical-mixture configurations show plausibility, but accentuate the need for including the partial pressures of CO and H_2O in the hydrocarbon reactions rates.

6) Overall process implications:

- With a combination of FTS and product upgrading in one reactor, a mixture of gasoline and diesel fuel with improved qualities will be the main product.
- Addition of hydroprocessing catalyst to FT catalyst will lead to larger FT reactor volume.
- Recirculation of the unconverted wax fraction may help to minimize the reactor volume (Fig. 8.1).
- A reduction of investment can be expected as the separate hydroprocessing process is eliminated. This reduction, however, will be limited by the increase in FTS reactor cost. The investment for the H_2-separation unit can definitely be saved (Fig. 8.1).

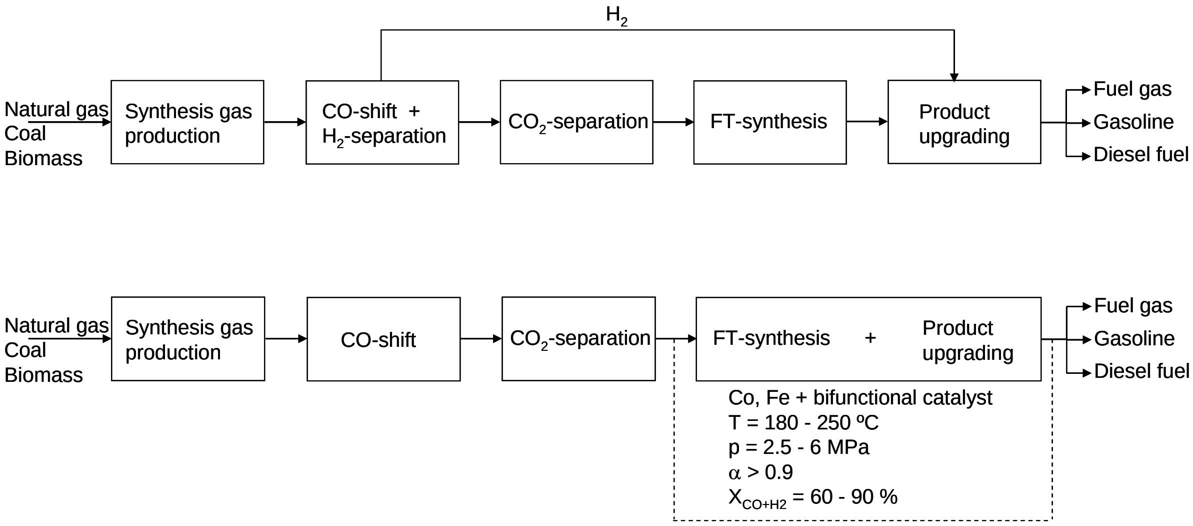
H2
Natural gas
Coal
Biomass
Synthesis gas production
CO-shift + H2-separation
CO2-separation
FT-synthesis
Product upgrading
Fuel gas
Gasoline
Diesel fuel
Natural gas
Coal
Biomass
Synthesis gas production
CO-shift
CO2-separation
FT-synthesis + Product upgrading
Fuel gas
Gasoline
Diesel fuel
Co, Fe + bifunctional catalyst
T = 180 - 250 °C
p = 2.5 - 6 MPa
α > 0.9
XCO+H2 = 60 - 90 %

Fig. 8.1: Overall flow scheme for the conversion of organic feedstock to liquid hydrocarbon fuels. Top: state of the art (based on Eilers et al. 1990, Hamelinck et al. 2004). Bottom: combination FTS and product upgrading in one reactor with recirculation of the unconverted wax fraction.

Outlook

Based on the results achieved, further investigations can be recommended:

1) Search for new types of hydroprocessing catalysts

- Different hydrogenation catalyst function (other than Pt) and metal/acid-ratio may influence the type and degree of cracking reactions (i.e. primary, secondary, hydrogenolysis).
- Improvement of the ion-exchange method for introducing the noble metal into the zeolite pores is recommended to counteract pore blockage and provide homogeneous noble metal dispersion.
- Different types of cracking function should be systematically investigated in order to find a tailor-made catalyst with higher isomer selectivity in the gasoline range and low branched hydrocarbon selectivity in the diesel range, without cracking $C_{<20}$ molecules.

2) Detailed experiments for further development of the hydrocarbon reaction kinetics

- Detailed experiments with model compounds of each hydrocarbon group (e.g. C_5, C_{12}, C_{15}, C_{20}, C_{30}, C_{40}) on hydroprocessing catalyst with the presence of CO and H_2O are recommended. The reaction conditions (i.e. T, p, p_i) should be similar to the FT synthesis conditions. Experiments should be performed at low and high conversion degree in order to vary the significance of either isomerisation or cracking reactions.
- Experiments at typical operating pressure of industrial FT applications (2-6 MPa) should be performed. Variation in total pressure may have an influence on the gas-liquid phase equilibrium, and therefore on the contact time of hydrocarbon molecules with the hydroprocessing catalyst.
- Further development of the kinetic models is necessary and should consider the CO and H_2O influence, and liquid and gas phase equilibrium.
- Stability / lifetime of hydroprocessing catalysts with long-term experiments (> 1 month) should be tested.

3) New combination concepts

- Combination of FT and bifunctional catalysts in a perfectly mixed reactor (slurry) should be performed and compared with the physical-mixture configuration in the fixed-bed reactor.
- Combination of Fe-based and hydroprocessing catalysts at high FTS temperature (320-350 °C) seems an attractive way to achieve high gasoline yield and good quality (i.e. high octane number).

9 Summary

Introduction and background

Fischer-Tropsch synthesis (FTS), which converts synthesis gas to hydrocarbons, offers a way to produce synthetic fuels from different raw materials such as natural gas, coal or biomass (GTL, CTL or BTL, X-to liquids). At present, commercial GTL and CTL plants are operated by Sasol and Shell and one BTL plant will start up in 2008. The maximum gasoline and diesel fuel selectivity of the FTS is limited by approximately 40 wt-% respectively. Product upgrading, including mainly hydrogenation, isomerisation and cracking reactions on bifunctional catalysts (Pt/zeolite), is applied in order to increase the synthetic fuel yield (Fig. 9.1).

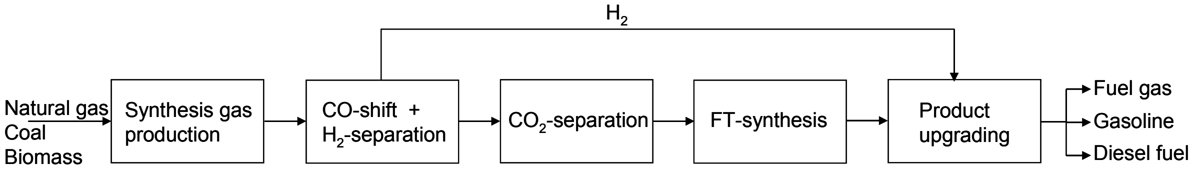

Fig. 9.1: Overall flow scheme for the conversion of organic feedstock to liquid hydrocarbon fuels via Fischer-Tropsch synthesis. State of the art (based on Eilers et al. 1990, Hamelinck et al. 2004).

The combination of FTS (on Co or Fe catalysts) with hydrocarbon reactions (on bifunctional catalysts) in one reactor may simplify the overall process by decreasing the number of process steps. Although the volume of the FT reactor may be larger - since it must contain two catalysts - the overall investment could be lowered (H_2-separation unit not required).

Objective of the study

The objective of the study was to explore effects and limiting factors of the combination FTS and hydrocarbon reactions under FTS conditions (temperature, gas phase composition).

Preliminary experiments with model compounds on Pt/zeolite catalyst had to be performed to better understand the hydrocarbon reactions on selected catalysts (Pt/ZSM-5, Pt/Beta). Fischer-Tropsch experiments with Co- and Fe-based catalyst had to be performed to have a basis for quantifying the effect of combining FTS and hydrocarbon reactions. The combination was tested in a dual-layer and in a physical-mixture configuration. In addition, mathematical calculations should help to understand the kinetics of the hydrocarbon reactions on a Pt/zeolite catalyst under FTS conditions.

Literature survey

Already in 1978 Chang and co-workers reported about a combination of Fe-based FT catalyst and HZSM-5-zeolite at 370 °C. The main products were hydrocarbons in the gasoline range. In the last few years, several authors have reported about such a combination in a dual-layer, in a physical-mixture configuration (Tsubaki et al. 2003, Botes et al. 2004, Li et al. 2004, Liu et al. 2005, Yoneyama et al. 2005, Ngamcharussrivichai et al. 2006, Martínez et al. 2007) or, most recently, in a capsuled catalyst (He et al. 2005). However, none of these studies presented a complete product analysis and the time-on-stream was very short (< 1 day). In most of the cases, the FT catalyst was combined with a pure zeolite without any noble metal that could help in hydrocracking reactions and for avoiding/retarding catalyst deactivation. Only Martínez et al. 2007 studied the effect of H_2O partial pressure on cracking reactivity of n-C_{16}. They concluded that H_2O competes with n-C_{16} molecules for adsorption on the zeolite acid sites. None of the studies mentioned above reported about the CO partial pressure effect on the isomerisation and cracking reactions.

Preliminary studies

It is known that hydrocracking reactions of hydrocarbons on bifunctional catalysts usually take place in the absence of CO and H_2O at higher temperature (300-450 °C) and pressure (5-20 MPa) than the low-temperature Fischer-Tropsch synthesis (220-250 °C, 2-6 MPa). The hydrocracking process also requires a high hydrogen partial pressure.

Steijns et al. 1981 and Froment 1987 presented a kinetic model for n-C_8, n-C_{10}, n-C_{12} isomerisation and cracking reactions on Pt/USY catalyst at FTS temperature and pressure. This kinetic model was used to carry out different case studies under similar conditions as those in this study. This model showed potential for the combination FT and Pt/zeolite catalysts in one reactor, even at a pressure of 1 MPa. The calculated data predicted that the hydrocarbons mentioned could be converted 100% to cracked products at 250 °C. These model hydrocarbons are not representative for the wax fraction (C_{21+}). Nevertheless, Sie et al. 1988 reported an increase of the cracking activity by increasing the number of C-atoms of a molecule. However, this kinetic model does not include any effect of CO and H_2O.

Procedure and experimental methods

As FT catalyst, a Co/Al_2O_3 catalyst with no reduction promoter and a K-promoted Fe catalyst, both provided by industrial manufacturers, were chosen. The FT-catalysts should produce a measurable quantity of wax in order to study the effect of the cracking reactions taking place on the bifunctional catalyst (noble metal/acidic component).

In this study, zeolites were chosen as acid components, and among them HZSM-5 (from Institut für Chemische Verfahrenstechnik, Universität Karlsruhe) and HBeta (from Süd-Chemie AG). The HZSM-5 zeolite has a lower number of acidic sites, external surface and pore size but larger crystals and stronger acidic sites than the HBeta zeolite. ZSM-5 zeolite has a strong shape selectivity. Large molecules (i.e. aromatics, naphtenes) cannot be formed in its pores due to the constrained pore space. These differences between the two zeolites result in a different activity.

Both zeolites were loaded with 1 wt-% Pt (as noble metal) with the ion-exchange method. The bifunctional catalyst was mixed with γ-Al_2O_3 and HEC and extrudated. Then, the extrudates were milled to the desired particle size (d_p = 100-160 μm, the same size as the FT catalyst particles). The bifunctional catalysts were characterised by TEM, SEM, TPD, BET and NLDFT analysis.

For all the experiments, a lab-scale fixed-bed reactor was used. The first experiments were carried out with model compounds (1-octene, ethene/propene) on a bifunctional catalyst bed (i.e. Pt/ZSM-5, Pt/Beta) with and without presence of CO indicating the influence of CO on catalyst activity. Fischer-Tropsch experiments with the Co- and the Fe-based catalysts were performed with variation of the following reaction parameters: temperature, residence time and synthesis gas composition. These experiments were the basis for quantifying the effects of the combination of FT and bifunctional catalysts. The combination was tested in a dual-layer and in a physical-mixture configuration. The catalyst mass was the same in all configurations ($m_{FT\text{-}cat}$ = 2 g, $m_{Pt/zeolite}$= 1.5 g).

The inorganic compounds were analysed in an online gas chromatograph (HP6890N) equipped with a TCD. The organic compounds in the gas phase were analysed by means of the ampoule technique (Schulz et al. 1984) in an adapted offline GC equipped with a FID (HP5890). The organic compounds in the liquid phase (wax) were also analysed offline in another GC equipped with a FID (HP5890 Series II Plus). The analyses data of the two phases were combined which resulted in some uncertainties in the overlapping range (~ $C_{12\text{-}23}$).

Experimental results and discussion

Preliminary experiments with model compounds on bifunctional catalysts

The experiments with 1-octene and H_2/Ar or H_2/CO on Pt/ZSM-5 and Pt/Beta at 230-300 °C under pressure (0.5 MPa) showed that 1-octene was completely hydrogenated, even in the presence of CO. Isomerisation and cracking reactions also took place under these conditions. However, the CO slowed down the cracking reactions of isomers (Fig. 9.2). With Pt/ZSM-5 and the presence of CO only at higher temperature (> 270 °C) the cracking reactions dominated the isomerisation reactions. In the absence of CO, the cracking products obtained on Pt/ZSM-5 catalyst followed a symmetrical distribution (Fig. 9.3a), whereas in the presence of CO, the main products were isomers of C_8. A symmetrical product distribution could only be observed at 300 °C (Fig. 9.3b). Pt/Beta showed a higher isomerisation and a lower cracking activity than Pt/ZSM-5 (Fig. 9.2b). Beta-zeolite is used commercially as isomerisation catalyst. The main product of 1-octene reactions on Pt/Beta were isomers of C_8.

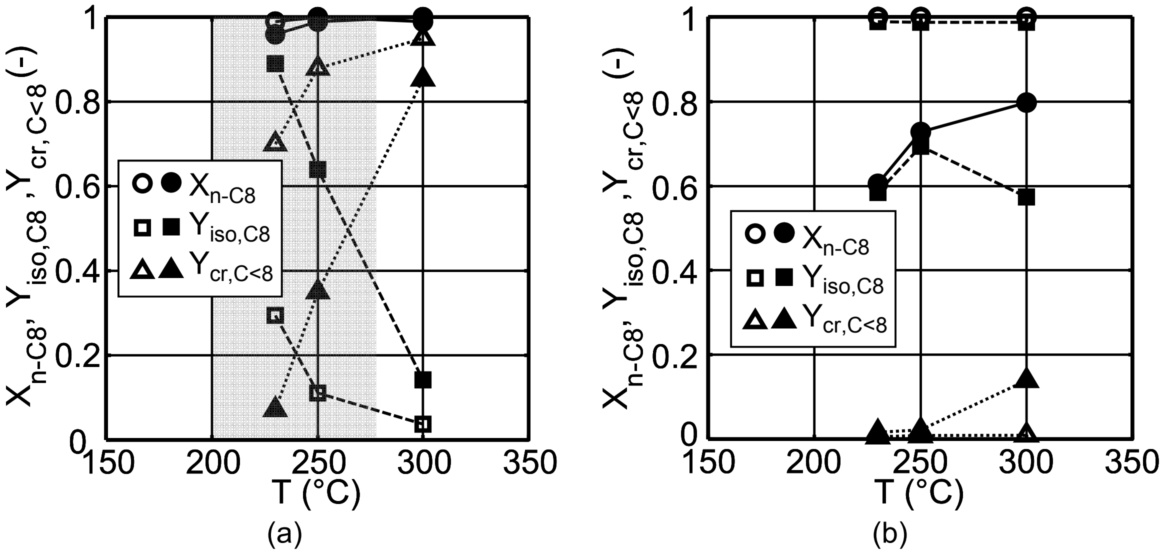

(a) (b)

Fig. 9.2: Reactions of 1-C_8H_{16} without CO (open symbols) and with CO (full symbols). Feed: 1-C_8H_{16} + H_2 + Ar or CO. Catalyst: (a) Pt/ZSM-5, (b) Pt/Beta. Points: experimental, curves: trends. Grey range: low temperature FTS. p = 0.5 MPa, WHSV = 0.22 h^{-1}. Other reaction conditions see Table 5.7.

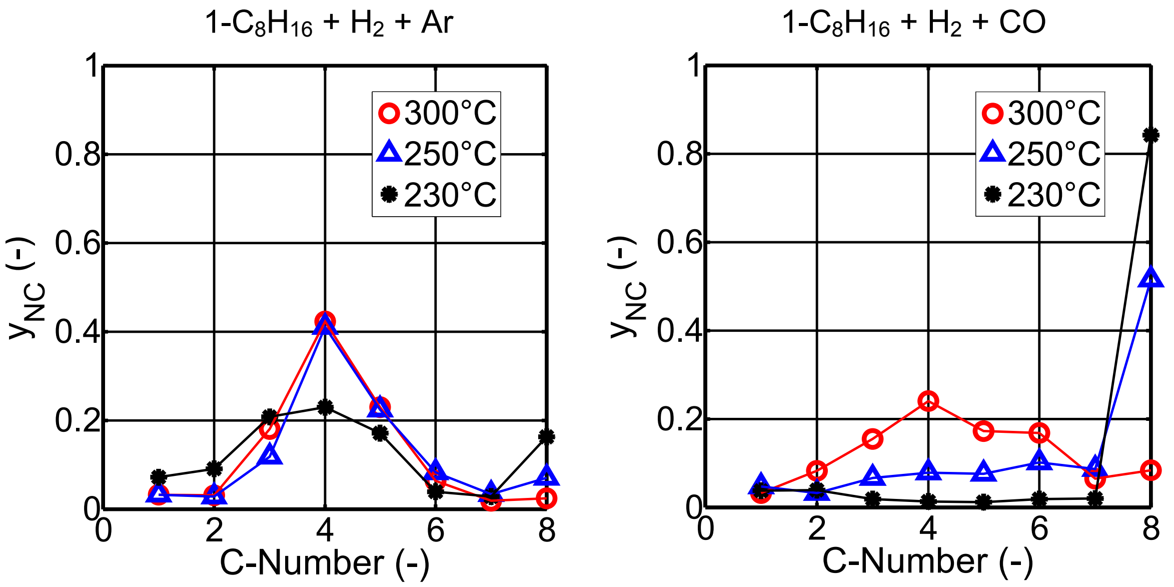

(a) (b)

Fig. 9.3: Effect of CO and temperature on hydrocarbon molar fractions after hydrogenation, hydrocracking and hydroisomerisation reactions of 1-octene with Pt/ZSM-5 catalyst. Points: experimental, curves: trends. Definition of $y_{NC,iso}$ see Equation 5.19. p = 0.5 MPa, WHSV = 0.22 h^{-1}. Other reaction conditions see Table 5.7.

Ethene and propene underwent oligomerisation reactions. Furthermore, the products of these reactions underwent isomerisation and cracking reactions which led to a continuous distribution of components (Tab. 9.1). In the presence of H_2, ethene and propene were completely hydrogenated (Tab. 9.1). However, in the presence of synthesis gas they were only partially hydrogenated due to the deleterious effect of CO on the Pt hydrogenation activity. Nevertheless, oligomerisation, isomerisation and cracking reactions took place (Tab. 9.1).

Tab. 9.1: Effect of H_2 and synthesis gas (H_2/CO) on the reactions of ethene/propene on Pt/ZSM-5 catalyst. Reaction conditions: T = 215-270 °C, p = 1 MPa.

Feed	Products
$C_2H_4 + C_3H_6 + N_2$	C_4-C_{13}: mainly branched alkenes
$C_2H_4 + C_3H_6 + N_2 + H_2$	C_2H_6 and C_3H_8
$C_2H_4 + C_3H_6 + N_2 + H_2 + CO$	$C_2H_6 + C_3H_8 + C_4$-C_{13}: mainly branched alkenes and alkanes

Fischer-Tropsch synthesis - Reference

As expected, the Co- and the Fe-based catalyst exhibit different FT and CO/CO_2-shift activities, and also a different product distribution. The Co/Al_2O_3 showed higher FT activity than the Fe-based catalyst. The CO/CO_2-shift activity of the Co/Al_2O_3 can be neglected, indicating that nearly all reacted CO was converted into hydrocarbons. However, the Fe-based catalyst showed higher CO/CO_2-shift activity resulting in a decrease of the hydrocarbon yield due to CO_2 formation.

N-alkanes were the main hydrocarbon products of both catalysts. However, the K-promoted Fe catalyst showed a higher n-alkenes and slightly higher isomers selectivity than the Co. The n-alkenes selectivity decreased by increasing the C-number with Co, while with Fe the n-alkenes selectivity was independent of the number of C-atoms. Alkenes selectivity increased with CO partial pressure and by decreasing the modified residence time (τ_{mod}) with the Co catalyst. Methane selectivity of the Co catalyst was higher than with Fe, even at lower temperature. The product distribution of the Fe catalyst could be described with two different chain-growth probabilities (α).

Combination of FT and bifunctional catalysts

The combination FT (Co or Fe) and bifunctional catalysts (Pt/ZSM-5, Pt/Beta) showed that the long-chain hydrocarbons (C_{21+}) were partially cracked even in the presence of CO and H_2O (Tab. 9.2). Consequently, the gasoline and diesel fraction selectivity increased. The different catalyst-bed configurations tested (i.e. dual-layer, physical-mixture) and the experiments with different H_2/CO-ratios elucidated again that the partial pressure of CO slowed down the cracking reactions of isomers. Hence, the isomers selectivity was higher in the physical-mixture resulting in an increase of the octane number of the gasoline fraction (Tab. 9.2). Alkenes were nearly completely hydrogenated on the Pt/zeolite catalyst.
Like in the preliminary experiments with model compounds, Pt/ZSM-5 and Pt/Beta showed different activity in the dual-layer configuration. Pt/Beta showed higher isomerisation activity than Pt/ZSM-5, especially in the diesel fraction (Tab. 9.2). Beta zeolite has larger pores allowing the diffusion and formation of larger molecules. ZSM-5 zeolite tends to crack the large hydrocarbons molecules in order to reduce their size and favours their diffusion through its smaller pores.

The methane selectivity remained nearly constant by the combination Co and Pt/ZSM-5 or Pt/Beta indicating that mainly “ideal” cracking reactions took place. The combination of Fe and Pt/ZSM-5 was performed at higher temperatures than that of Co (250-270 °C and 200-230 °C respectively). In that case, the methane selectivity increased, most probably due to secondary cracking reactions at higher temperature (270 °C). As already mentioned, the Fe catalyst showed lower FT activity than the Co. At 250 °C, the CO conversion on the Fe catalyst was lower than that of the Co catalyst at 230 °C. This resulted in a higher CO partial pressure at the inlet of the Pt/ZSM-5 layer and in a lower cracking activity (Fig. 9.4). At 270 °C, the CO partial pressure at the inlet of the Pt/ZSM-5 layer was similar to that with the combination with Co at 230 °C. Hence, nearly the same decrease of the C_{21+} fraction was observed.

The lower temperature and pressure applied in this combination, the presence of CO and water vapour, and the absence of recirculation of the non-converted C_{21+} fraction lead to lower gasoline and diesel selectivities than those achieve in industrial processes like the Shell Middle Distillate Synthesis (SMDS, with separate FTS and product upgrading).

Tab. 9.2: Effect of bifunctional catalysts on hydrocarbon fraction yield (on C-basis) and octane number (estimate, based on approx. 50 % of the identified isomers). Experimental data include gas and liquid phase analysis. Reaction conditions: T = 230 °C, $(p_{H2}/p_{CO})_{in} = 2$, $\tau_{mod} = 4000$ kg·s/m^3 (referred to $m_{FT\text{-}cat.}$), p = 1 MPa.

		Co	Co + Pt/ZSM-5	Co + Pt/Beta	Co + Pt/ZSM-5
		alone	dual-layer	dual-layer	physical-mixture
$y_{C1\text{-}4}$	(C-%)	14.8	16.5	14.3	17.9
$y_{gasoline,C5\text{-}9}$	(C-%)	17.5	19.4	23.3	31.7
$y_{iso\ in\ C5\text{-}9}$	(%)	23.0	40.0	41.3	91.0
$y_{diesel,C10\text{-}20}$	(C-%)	38.7	47.5	37.9	33.2
$y_{iso\ in\ C10\text{-}20}$	(%)	11.7	22.0	42.7	41.0
y_{C21+}	(C-%)	29.0	16.6	24.5	17.2
$\Sigma\ y_{gasoline\ +\ diesel}$	(C-%)	56.2	66.9	61.2	64.9
RON	(-)	~ 37	~ 39	~ 39	~ 63

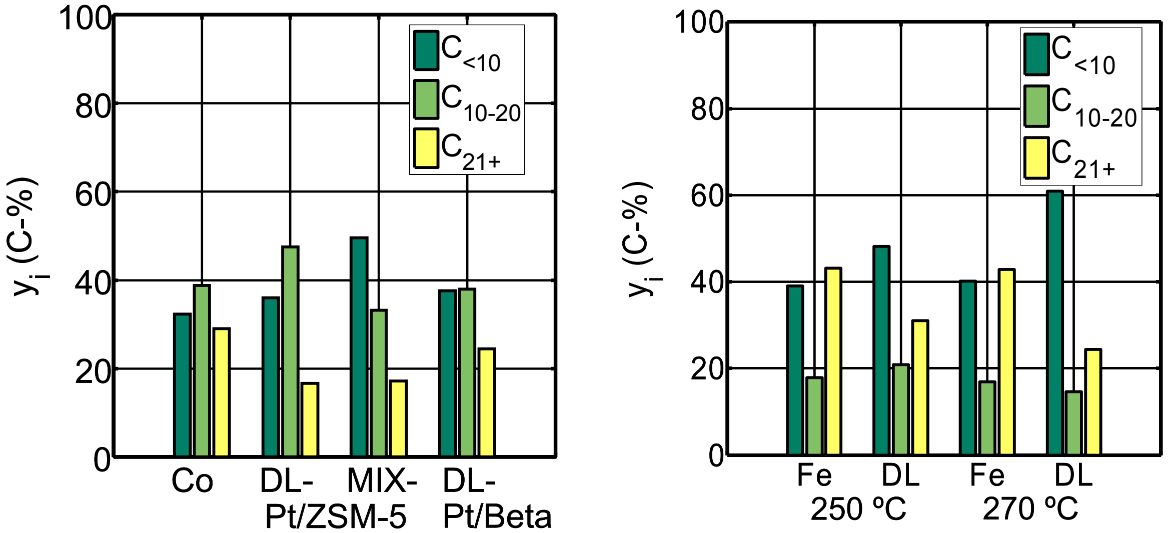

(a) (b)

Fig. 9.4: Effect of bifunctional catalyst, catalyst-bed configuration and temperature on hydrocarbon fraction yields (on C-basis). (a) Co-based configurations, (b) Fe-based configurations. DL: dual layer, MIX: physical mixture. Reaction conditions: $(p_{H2}/p_{CO})_{in} = 2$, p = 1 MPa, $\tau_{mod} = 4000$ kg·s/m^3 (referred to $m_{FT\text{-}cat.}$), $m_{HP\text{-}cat.} / m_{FT\text{-}cat.} = 0.75$.

Reaction network model

On the basis of the experimental results obtained, a reaction network was presented for the hydrocarbon reactions taking place on Pt/zeolite catalyst. Due to the large amount of molecules involved in these reactions, the hydrocarbons were divided into different groups ($C_{5\text{-}9}$, $C_{10\text{-}14}$, $C_{15\text{-}20}$, C_{21+}) distinguishing between n- and iso-alkanes. Alkenes were not included in the reaction network since they were nearly completely hydrogenated on the Pt/zeolite catalyst. However, the hydrogen consumption of the hydrogenation and cracking reactions was considered.

First of all, the kinetic model presented by Steijns et al. 1981 and Froment 1987 for model hydrocarbon reactions on Pt/zeolite catalyst was tested for the reactions of C_8.

The calculated results were compared with the experimental results from the 1-octene reactions on Pt/ZSM-5. A good agreement was observed in the 230-250 °C temperature range (this kinetic model is only valid up to 250 °C) when no CO was present in the feed (Fig. 9.5). As already mentioned, the CO partial pressure decreases the cracking activity of the isomers. For that reason, the cracking rate constant was decreased. Then, also a good agreement between calculated and experimental data was observed with the presence of CO (Fig. 9.6).

The kinetic model was further developed for the Pt/ZSM-5 catalyst. The kinetic data of C_8 reactions were adopted for the fraction $C_{5\text{-}9}$. The data for the higher fractions had to be extrapolated due to the lack of kinetic data in the literature. The isomerisation and cracking rate constants were obtained by multiplying the rate constant of fraction $C_{5\text{-}9}$ by a relative activity factor. This was found to be 1/ 3.7/ 3.7/ 9 for $C_{5\text{-}9}$/ $C_{10\text{-}14}$/ $C_{15\text{-}20}$/ C_{21+}. The hydrocarbons adsorption on the Pt/ZSM-5 catalyst was also considered and calculated for each fraction with an equation presented by Pellegrini et al. 2007, considering that above approximately C_{35} the adsorption is nearly 100 %. It means that the adsorption constant for higher C-numbers remains constant (Sie et al. 1991). The distribution coefficient of n- and iso-alkanes was chosen to be the same for all fractions due to the lack of thermodynamic data for isomers with N_C > 10. The value was taken from the fraction $C_{5\text{-}9}$ (Steijns et al. 1981, Froment 1987). According to the experimental results, the oligomerisation reaction rate was to be higher than the isomerisation rate of fraction $C_{5\text{-}9}$.

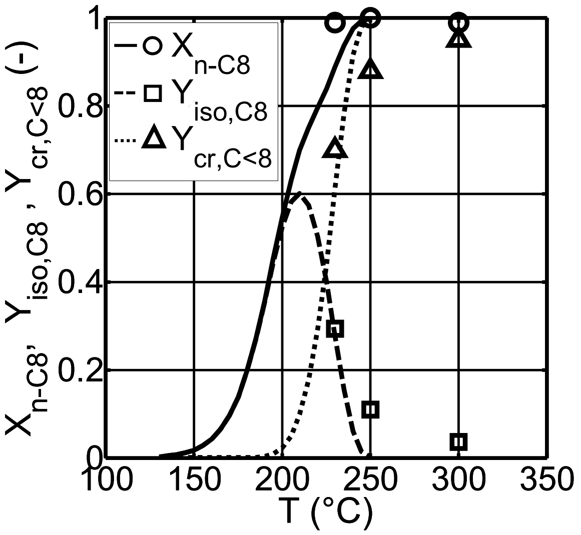

Fig. 9.5: Reactions of 1-C_8H_{16} without CO. Feed: 1-C_8H_{16} + H_2 + Ar. Catalyst: Pt/ZSM-5. Points: experimental, curves: calculated with Steijns et al. 1981, Froment 1987 kinetic model with Pt/USY catalyst (see Chapter 3.2.6). p = 0.5 MPa, WHSV = 0.22 h^{-1}. Other reaction conditions see Table 5.7.

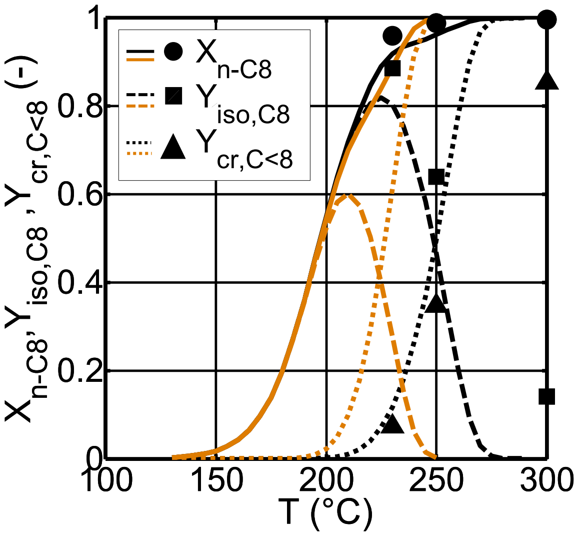

Fig. 9.6: Reactions of 1-C_8H_{16} with CO and H_2 on Pt/ZSM-5 catalyst. Points: experimental. Black curves: calculated with kinetic parameter values from Table 7.2. Grey curves: calculated with kinetic parameters from Steijns et al. 1981, Froment 1987. Reaction rates: Eq. 3.20-3.22. p = 0.5 MPa, WHSV = 0.22 h^{-1}. Other reaction conditions see Table 5.7.

The developed kinetic model was tested for the dual-layer and the physical-mixture configuration with Co and Pt/ZSM-5 at 230 °C and also for the dual-layer configuration with Fe and Pt/ZSM-5 at 250 °C. The calculated data showed plausibility but also confirmed the hypothesis that the cracking activity of isomers may be a function of the CO partial pressure. Hence, the calculated data accentuated the need for including the partial pressure of CO and H_2O in the hydrocarbon reaction rates.

Conclusions and Outlook

The achieved results indicate a potential of combining FT and hydrocarbons reactions in one reactor. It could be shown that hydrogenation, isomerisation, cracking and oligomerisation reactions take place on a Pt/zeolite catalyst at FTS temperatures and in the presence of CO and H_2O. The most critical point of this combination seems to be the deleterious effect of CO on the cracking reactions of isomers. For that reason, the wax fraction (C_{21+}) was only partially cracked.

The experimental results also indicated that the type of zeolite and the catalyst-bed configuration have an influence on the diesel/gasoline ratio obtained. It seems that the final fuel products will be a mixture of gasoline and diesel fuel, as long as no diesel-selective hydroprocessing catalyst is found.

Recycling of the uncracked wax fraction would be necessary resulting in a larger size reactor for the FT synthesis, thus increasing the FTS reactor cost. The investment for the H_2-separation unit can definitely be saved (Fig. 9.7).

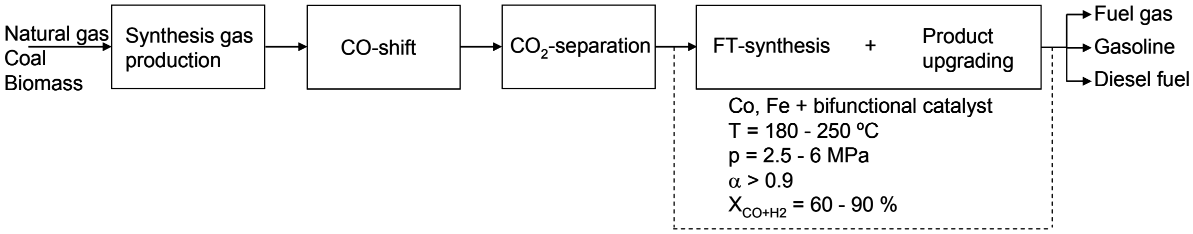

Fig. 9.7: Overall flow scheme for the conversion of organic feedstock to liquid hydrocarbon fuels with combining FTS and product upgrading in one reactor.

Detailed experiments with model compounds and CO and H_2O are necessary in order to better understand their effects on hydrocarbon reactions. The total pressure effect on these reactions should also be investigated since FTS usually takes place at higher pressure than applied in this study. Furthermore, the stability of the Pt/zeolite catalyst should also be investigated with long-term experiments. These experiments should be a good basis to further improve the kinetic model for hydrocarbon reactions on Pt/zeolite catalysts.

Zusammenfassung

Einleitung und Hintergrund

In der Fischer-Tropsch Synthese (FTS) wird Synthesegas zu Kohlenwasserstoffen umgesetzt. Auf diesem Weg ist es möglich, synthetische Kraftstoffe aus verschiedenen Rohstoffen wie Erdgas, Kohle oder Biomasse (GTL, CTL oder BTL, X-to liquids) herzustellen.
Zum jetzigen Zeitpunkt werden GTL und CTL Anlagen von Sasol und Shell betrieben, die Inbetriebnahme einer BTL Anlage ist für 2008 geplant. Die maximalen Benzin- und Dieselselektivitäten der FTS liegen bei etwa 40 %. Um die Ausbeute an synthetischen Kraftstoffen zu erhöhen, schließt sich an die eigentliche Synthese eine Produktaufarbeitung an. Diese besteht aus Hydrieren-, Isomerisieren- und Crackreaktionen an bifunktionellen Katalysatoren (Pt/Zeolith) (Abb.9.1).

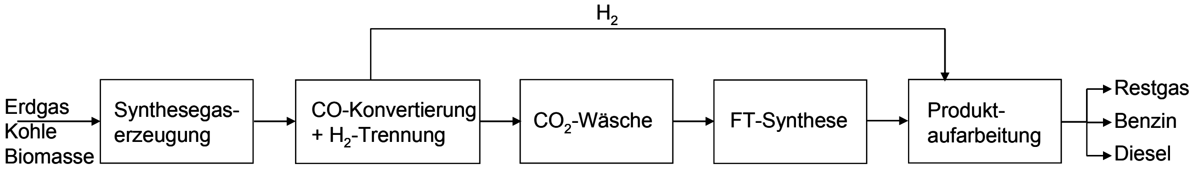

Abb. 9.1: Fließbild der Erzeugung flüssiger Kohlenwasserstoffe aus verschiedenen Rohstoffen via Fischer-Tropsch Synthese. Stand des Wissen (Basierend auf Eilers et al. 1990, Hamelinck et al. 2004).

Die Kombination von FTS (an Co oder Fe Katalysatoren) mit Kohlenwasserstoffreaktionen (an bifunktionellen Katalysatoren) in einem Reaktor ermöglicht die Vereinfachung des Gesamtprozesses durch die Reduzierung der Prozessschritte, wodurch die Gesamtinvestitionen gesenkt werden können. Zwar muss ein größerer FT Reaktor, der dann beide Katalysatoren enthält, verwendet werden, gleichzeitig kann aber auf eine kostenintensive H_2-Trennung verzichtet werden.

Zielsetzung der Arbeit

Ziel der Untersuchungen war, Effekte und Haupteinflussgrößen, aber auch Grenzen der Kombination von FTS und Produktaufarbeitung unter FTS Bedingungen (Temperatur, Gaszusammensetzung) zu untersuchen.

Zunächst wurden Experimente mit Modellkomponenten durchgeführt, um die Kohlenwasserstoffreaktionen an den verwendeten Katalysatoren besser zu verstehen (Pt/ZSM-5, Pt/Beta). Als Basis für eine Quantifizierung der Kombination FTS und Produktaufarbeitung wurden Fischer-Tropsch Experimente mit Co- und Fe-basierten Katalysatoren ohne anschließende Produktaufarbeitung durchgeführt. Im Anschluss wurde die Kombination der Katalysatoren in einer Zweischichtanordnung und einer Physikalischen Mischung untersucht.
Zusätzlich durchgeführte mathematische Berechnungen sollen helfen, die Kinetik der Kohlenwasserstoffreaktionen an einem Pt/Zeolith Katalysator unter FTS Bedingungen zu verstehen.

Literaturübersicht

Bereits 1978 berichteten Chang et al. über die Kombination eines Fe-basierten Katalysators und eines HZSM-5 Zeolithen bei 370 °C. Als Hauptprodukt der Synthese erhielten sie dabei Benzin. In den letzten Jahren berichteten diverse Autoren über diese Kombination in Form einer Zweischichtenanordnung, als Physikalische Mischung (Tsubaki et al. 2003, Botes et al. 2004, Li et al. 2004, Liu et al. 2005, Yoneyama et al. 2005, Ngamcharussrivichai et al. 2006, Martínez et al. 2007) oder als Kapselkatalysatoren (He et al. 2005). Allerdings präsentierte keine dieser Studien eine geschlossene Produktanalyse, und die Versuchsdauer war sehr kurz (< 1 Tag). In den meisten Studien war der Produktaufarbeitungskatalysator ein Zeolith ohne Edelmetall, obwohl dieses für gezielte Crackreaktionen günstig wäre und sich positiv auf die Katalysatorlebensdauer auswirkte. Außerdem untersuchten nur Martínez et al. (2007) den Effekt des Wasserdampfpartialdrucks auf die Crackaktivität am Beispiel von C_{16}. Als Schlussfolgerungen berichten sie eine Adsorptionskonkurrenz zwischen Wasser und n-C_{16} an den sauren Zentren der Zeolithen. Der Einfluss des CO-Partialdrucks auf die Kohlenwasserstoffreaktionen wurde von keiner der erwähnten Forschergruppen untersucht.

Vorüberlegungen / Rechnerische Vorstudie

Es ist bekannt, dass Hydrocrack-Reaktionen üblicherweise in Abwesenheit von CO und H_2O, sowie bei höherer Temperatur (300-450 °C) und höherem Druck (5-20 MPa) stattfinden als die Niedrigtemperatur Fischer-Tropsch Synthese.
Steijns et al. (1981) und Froment et al. (1987) entwickelten ein kinetisches Modell für Kohlenwasserstoff-Hydrocracken und Hydroisomerisieren Reaktionen am Beispiel von n-C_8, n-C_{10}, n-C_{12} an einem Pt/USY Katalysator bei FTS Temperaturen und Drücken. In der vorliegenden Arbeit wurde das gleiche kinetische Modell verwendet, um verschiedene Fallstudien zu berechnen. Die Reaktionsbedingungen wurden dabei analog zu den Versuchen ausgewählt. Die rechnerischen Ergebnisse zeigen selbst bei 1 MPa Potential für die Kombination von FT und Pt/Zeolith Katalysatoren in einem Reaktor. Es wird vorausgesagt, dass die Modellkomponenten bei 250 ºC vollständig zu Crackprodukten umgesetzt werden können. Die Modellkomponenten sind zwar nicht für die Wachsfraktion (C_{21+}) charakteristisch, allerdings berichten Sie et al. (1988), dass die Crackaktivität mit der Anzahl der C-Atome steigt. Es kann somit auch von einer vollständigen Umsetzung der langkettigen Kohlenwasserstoffe ausgegangen werden. CO- und Wasserdampfeinflüsse berücksichtigt das kinetische Modell allerdings nicht.

Experimentelle Vorgehensweise und Methoden

Ein Co/Al_2O_3 Katalysator ohne Reduktionspromotoren und ein K-dotierter Fe Katalysator eines kommerziellen Herstellers wurden als FT Katalysatoren gewählt. Die FTS-Katalysatoren sollten eine messbare Wachsausbeute erzeugen, um die Effekte der Crackreaktionen mit bifunktionellen Katalysatoren (Edelmetall/saure Komponente) zu quantifizieren. Als saure Komponente wurden Zeolithen ausgewählt, HZSM-5 (Institut für Chemische Verfahrenstechnik, Universität Karlsruhe) und HBeta (Süd-Chemie AG). Der HZSM-5 Zeolith besitzt eine niedrigere Anzahl an sauren Zentren, geringere spezifische Oberfläche und Porengröße, aber größere Kristalle und stärkere Acidität als der HBeta Zeolith. Eine besondere Eigenschaft von ZSM-5 ist seine Formselektivität. Größere Moleküle (z.B. Aromaten,

Naphtene) können nicht gebildet werden, weil deren kritischer Durchmesser nicht der ZSM-5 Porengröße entspricht. Die unterschiedlichen Eigenschaften der Zeolithen resultieren in unterschiedlichen Aktivitäten.
Beide Zeolithen wurden mit 1 Gew-% Pt (als Edelmetall) nach der Ionenaustauschmethode imprägniert. Die bifunktionellen Katalysatoren wurden mit γ-Al_2O_3 und HEC gemischt und extrudiert. Danach wurden sie auf die gewünschte Partikelgröße gemahlen (d_p = 100-160 μm, dieselbe Größe wie die FT Katalysatorpartikel). Die bifunktionellen Katalysatoren wurde durch TEM, SEM, TPD, BET und NLDFT Analysen charakterisiert.

Alle Experimente wurden in einer Festbettapparatur im Labormaßstab durchgeführt. Die Experimente lassen sich in drei Gruppen unterteilen:

i) Kohlenwasserstoff-Modellkomponenten Reaktionen (1-Okten, Ethen/Propen) an bifunktionellen Katalysatoren (Pt/ZSM-5, Pt/Beta) in An- und Abwesenheit von CO, um dessen Einfluss auf die Katalysatoraktivität festzustellen.
ii) Fischer-Tropsch Synthese mit Co- und Fe-basierten Katalysatoren mit Variation von Temperatur, Verweilzeit und Synthesegaszusammensetzung. Diese Versuche dienen als Referenz, um nachfolgend exemplarisch die Kombination von FTS und KW- Reaktionen zu bewerten.
iii) Kombination von FTS und KW-Reaktionen in einer Zweischichtanordnung und einer Physikalischen Mischung. Die Katalysatormasse wurde für jede Anordnung konstant gehalten ($m_{FT\text{-}Kat}$ = 2 g, $m_{Pt/Zeolith}$ = 1,5).

Zur Analyse der anorganischen Komponenten wurde ein on-line Gaschromatograph (HP6890N) mit Wärmeleitfähigkeitsdetektor (WLD) verwendet. Zur Analyse der Kohlenwasserstoffe in den Produktgasproben wurde die so genannte Ampullentechnik verwendet (Schulz et al. 1984). Dabei wurden die Ampullen in einem adaptierten off-line Gaschromatographen mit Flammenionisationsdetektor (FID) analysiert (HP5890). Die Analyse des bei Raumtemperatur festen Heißkondensats (Wachs) erfolgte durch off-line Gaschromatographie mit Flammenionisationsdetektor (HP5890 Series II plus). Die Kombination der beiden Analysen führte zu Abweichungen im Übergangsbereich (~ $C_{12\text{-}23}$).

Experimentelle Ergebnisse und Diskussion

Orientierende Versuche mit Modellkomponenten an bifunktionellen Katalysatoren

Die Experimente mit 1-Okten und H_2/Ar bzw. H_2/CO an Pt/ZSM-5 und Pt/Beta (230-300 °C, 0.5 MPa) zeigten, auch bei Anwesenheit von CO, eine vollständige Hydrierung des 1-Okten. Zusätzlich fanden unter diesen Reaktionsbedingungen Isomerisierung- und Crackreaktionen statt. Allerdings verlangsamte das CO die Iso-Alkane Crackreaktionen (Abb. 9.2).
Mit dem Pt/ZSM-5 Katalysator konnte bei Abwesenheit von CO eine symmetrische Produktverteilung festgestellt werden (Abb. 9.3a). Demgegenüber waren bei Anwesenheit von CO iso-C_8 die Hauptprodukte. Nur bei hohen Temperaturen (> 270 °C) dominierten die Crackreaktionen. Eine symmetrische Produktverteilung wurde erst bei 300 °C beobachtet (Abb. 9.3b).
Der Pt/Beta Katalysator zeigte eine höhere Isomerisierungsaktivität aber eine geringere Crackaktivität als der Pt/ZSM-5 (Abb. 9.2.b). Die Hauptprodukte waren iso-C_8. Wegen dieses Verhaltens wird Beta Zeolith auch in der Industrie als Isomerisierungskatalysator verwendet.

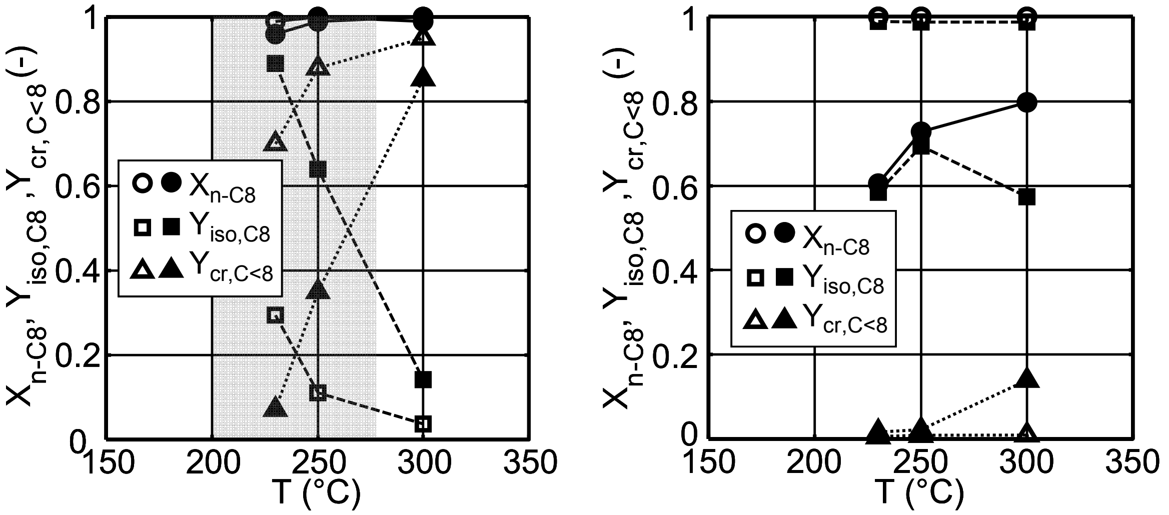

(a) (b)

Abb. 9.2: 1-C_8H_{16} Reaktionen bei Ab- (Offene Symbole) und Anwesenheit von CO (Gefüllte Symbole). Feed: 1-C_8H_{16} + H_2 + Ar or CO. Katalysator: (a) Pt/ZSM-5, (b) Pt/Beta. Punkte: Experimentell, Kurven: Trends. Grauer Bereich: niedrige Temperatur FTS. p = 0,5 MPa, WHSV = 0,22 h^{-1}. Andere Reaktionsbedingungen siehe Tabelle 5.7.

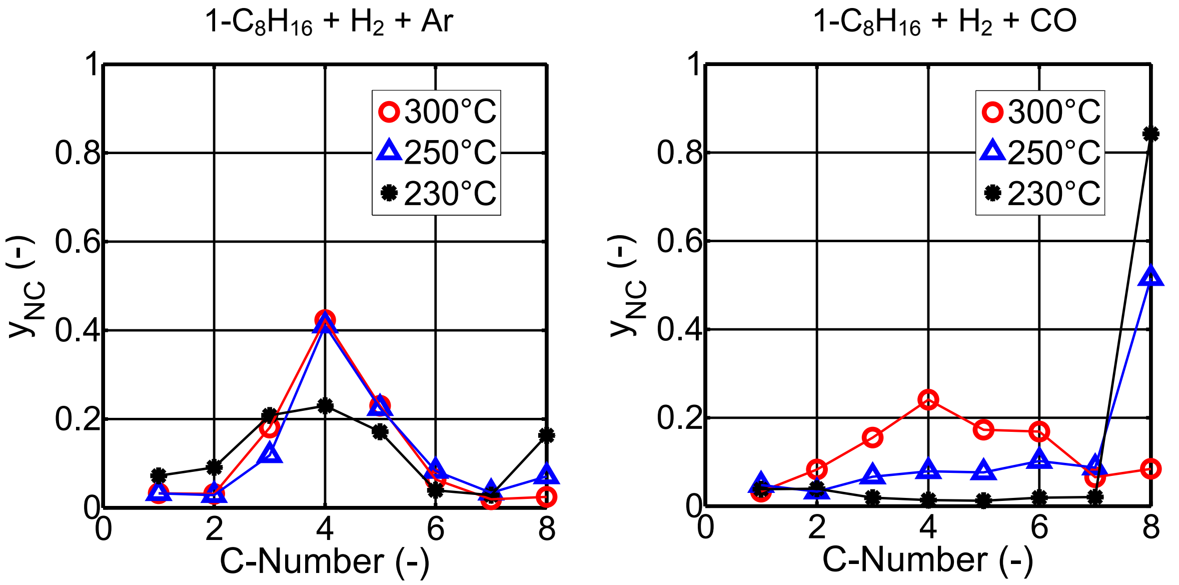

(a) (b)

Abb. 9.3: CO- und Temperatureinfluss auf die Kohlenwassserstoff-Produktverteilung bei 1-Okten Hydrier-, Hydroisomerisier- und Hydrocrackingreaktionen an Pt/ZSM-5 Katalysator. Punkte: Experimentell, Kurven: Trends. Definition von $y_{NC,iso}$ siehe Gleichung 5.19. p = 0,5 MPa, WHSV = 0,22 h^{-1}. Andere Reaktionsbedingungen siehe Tabelle 5.7.

Ethen und Propen wurden zu langkettigen Kohlenwasserstoffen oligomerisiert. Diese wurden anschließend isomerisiert und gecrackt, was zu einer kontinuierlichen Produktverteilung führte (Tab. 9.1). Bei Anwesenheit von H_2 wurden Ethen und Propen vollständig hydriert (Tab. 9.1). Allerdings wurden bei Anwesenheit von Synthesegas Ethen und Propen wegen des negativen Effekts von CO auf die Hydrieraktivität des Platins nur partiell hydriert. Oligomerisier-, Isomerisieren- und Crackreaktionen fanden hingegen statt (Tab. 9.1)

Tab. 9.1: H_2 und Synthesegaseinfluss (H_2/CO) auf die Ethen/Propen Reaktionen an Pt/ZSM-5 Katalysator. Reaktionsbedingungen: T = 215-270 °C, p = 1 MPa.

Feed	Produkte
$C_2H_4 + C_3H_6 + N_2$	C_4-C_{13}: hauptsächlich verzweigte Alkene
$C_2H_4 + C_3H_6 + N_2 + H_2$	C_2H_6 und C_3H_8
$C_2H_4 + C_3H_6 + N_2 + H_2$ + CO	C_2H_6 + C_3H_8 + C_4-C_{13}: hauptsächlich verzweigte Alkene und Alkane

Fischer-Tropsch Synthese - Referenz

Die FT Syntheseexperimente mit Co- und Fe-basierten Katalysatoren zeigten das erwartete Ergebnis unterschiedlicher FT und CO/CO_2-Konvertierungsaktivität und unterschiedlicher Produktverteilung. Der Co/Al_2O_3 Katalysator zeigte dabei eine höhere FT Aktivität als der Fe-basierte Katalysator. Am Co/Al_2O_3 Katalysator sind CO/CO_2-Konvertierungsreaktionen vernachlässigbar. Die Geschwindigkeit der CO-Umsetzung ist gleich der Bildungsgeschwindigkeit organischer Verbindungen auf Kohlenstoffbasis. Im Gegensatz dazu zeigte der Fe-basierte Katalysator eine hohe CO/CO_2-Konvertierungsaktivität. Die CO_2 Bildung führt zu einer Abnahme der Kohlewasserstoffausbeute.

Unverzweigte Alkane waren die Hauptprodukte von beiden Katalysatoren, die Alken- und Isomerenselektivität am Fe Katalysator war jedoch höher. Die Selektivität der unverzweigten Alkene nahm am Co Katalysator bei steigender C-Zahl ab, während sich die Alkenselektivität am Fe Katalysator unabhängig von der C-Zahl zeigte. Am Co Katalysator nahm die Alkenselektivität mit steigendem CO-Partialdruck und abnehmende Verweilzeit (τ_{mod}) zu. Der Co Katalysator zeigte auch bei niedrigen Temperaturen eine höhere Methanselektivität als der Fe Katalysator. Die Produktverteilung des Fe-Katalysators wurde durch zwei verschiedene Kettenwachstumswahrscheinlichkeiten (α) beschrieben.

Kombination von FT und bifunktionellen Katalysatoren

Die Experimente mit der Kombination von FTS und bifunktionellen Katalysatoren zeigten, dass langkettige Kohlenwasserstoffe (C_{21+}) auch bei Anwesenheit von CO- und Wasserdampf partiell gecrackt werden konnten (Tab. 9.2). Infolgedessen nahm die Benzin- und Dieselselektivität zu. Die beiden untersuchten Anordnungen (Zweischichten und Physikalische Mischung), sowie die verschiedenen H_2/CO-Verhältnisse ließen erkennen, dass der CO-Partialdruck die Crackreaktionen der Isomere verlangsamte. Bei der Physikalischen Mischung war der CO-Partialdruck geringer, dies führte zu einer höheren Isomerenselektivität und dadurch zu einer Zunahme der Oktanzahl der Benzinfraktion (Tab. 9.2). Die Alkene wurden am Pt/Zeolith Katalysator fast vollständig hydriert.

Pt/ZSM-5 und Pt/Beta Katalysatoren zeigten sowohl in der Zweischichtanordnung, als auch bei den Experimenten mit Modellkomponenten unterschiedliche Aktivität. Der Pt/Beta besaß eine höhere Isomerisierungsaktivität als Pt/ZSM-5, besonderes in der Dieselfraktion (Tab. 9.2), da die größeren Poren des Beta Zeoliths die Bildung und Diffusion von größeren Molekülen erlauben. Der ZSM-5 neigt dazu, größere Moleküle zu cracken, um die Diffusion durch seine Poren zu erleichtern.

Mit der Kombination von Co und Pt/ZSM-5 bzw. Pt/Beta blieb die Methanselektivität nahezu konstant, was auf primäres Cracken zurückgeführt werden kann. Die Kombination von Fe und Pt/ZSM-5 wurde bei höheren Temperaturen untersucht als die Co Kombinationen (250-270 °C bzw. 200-230°C), wodurch eine Zunahme der Methanselektivität festgestellt werden konnte (sekundäres Cracken bei 270 °C). Wie schon zuvor erwähnt, besitzt der Fe Katalysator eine geringere FT Aktivität als der Co Katalysator, was zu einem niedrigeren CO-Partialdruck bei 250 °C im Vergleich zum Co Katalysator bei 230 °C führte. Ein höherer CO-Partialdruck am Eintritt der Pt/ZSM-5 Katalysatorschicht führte zu geringerer Crackaktivität (Abb. 9.4). Bei 270 °C war der CO-Partialdruck mit Fe vergleichbar mit dem bei 230 °C mit Co. Deshalb wurde auch eine fast identische Abnahme der C_{21+} Fraktion beobachtet.

Im Vergleich zu kommerziellen Prozessen, wie beispielsweise der „Shell Middle Distillate Synthesis“ (SMDS, mit getrennter FTS und Produktaufarbeitung) führten die experimentellen Bedingungen der vorliegenden Untersuchung (Geringe Temperatur, niedriger Druck, Anwesenheit von CO und Wasserdampf, keine Rückführung der nicht konvertierten C_{21+} -Fraktion) zu geringerer Benzin- und Dieselselektivität.

Tab. 9.2: Bifuktioneller Katalysator Einfluss auf die Kohlenwasserstoffausbeute (C-Basierte) und auf die Oktanzahl (Anhaltswerte, basierend auf etwa 50 % der ermittelten Isomere). Gas- und Flüssigphase Analyse vereint. Reaktionsbedingungen: T = 230 °C, $(p_{H2}/p_{CO})_{ein} = 2$, $\tau_{mod} = 4000$ kg·s/m³ (Bezug auf $m_{FT\text{-}Kat.}$), p = 1 MPa.

		Co	Co + Pt/ZSM-5	Co + Pt/Beta	Co + Pt/ZSM-5
		Allein	Zweischichten	Zweischichten	Physikalische Mischung
$y_{C1\text{-}4}$	(C-%)	14,8	16,5	14,3	17,9
$Y_{Benzin,C5\text{-}9}$	(C-%)	17,5	19,4	23,3	31,7
$y_{iso\ in\ C5\text{-}9}$	(%)	23,0	40,0	41,3	91,0
$y_{diesel,C10\text{-}20}$	(C-%)	38,7	47,5	37,9	33,2
$y_{iso\ in\ C10\text{-}20}$	(%)	11,7	22,0	42,7	41,0
y_{C21+}	(C-%)	29,0	16,6	24,5	17,2
$\sum y_{Benzin\ +\ Diesel}$	(C-%)	56,2	66,9	61,2	64,9
RON	(-)	~ 37	~ 39	~ 39	~ 63

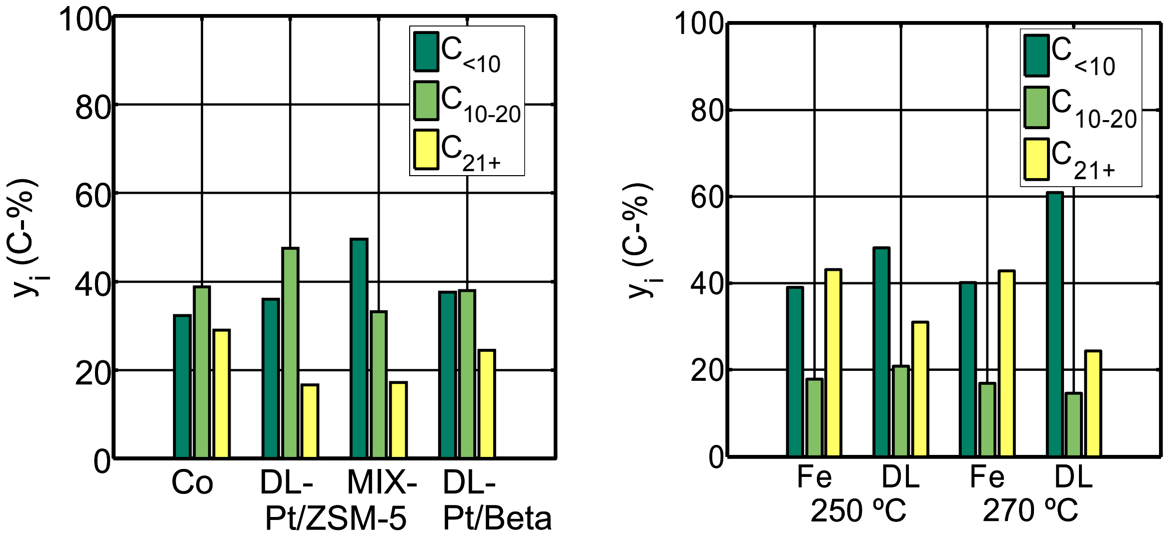

(a) (b)

Abb. 9.4: Bifunktioneller Katalysator-, Anordnung- und Temperatureinfluss auf die Kohlenwasserstoffausbeute (C-Basierte). (a) Co-basierte Anordnungen, (b) Fe-basierte Anordnungen. DL: Zweischichten, MIX: Physicalische Mischung. Reaktionsbedingungen: $(p_{H2}/p_{CO})_{ein}$ = 2, p = 1 MPa, τ_{mod} = 4000 kg·s/m^3 (Bezug auf $m_{FT\text{-}Kat.}$), $m_{HP\text{-}Kat.}$ / $m_{FT\text{-}Kat.}$ = 0,75.

Reaktionsnetzwerk - Modellierung

Auf Basis der gewonnenen Ergebnisse war es möglich, ein Reaktionsnetzwerk für die Kohlenwasserstoffreaktionen an Pt/ZSM-5 Katalysator festzulegen. Das Produktspektrum der Kohlenwasserstoffreaktionen ist sehr breit, deshalb wurden die Kohlenwasserstoffe in Gruppen eingeteilt (C_{5-9}, C_{10-14}, C_{15-20}, C_{21+}) und lediglich zwischen n-Alkanen und Isomeren unterschieden. Die Alkene werden am Pt/Zeolith Katalysator fast vollständig hydriert, weshalb sie nicht in dem Reaktionsnetzwerk berücksichtigt wurden. Allerdings wurde der Wasserstoffverbrauch dieser Hydrier-, sowie auch der Crackreaktionen berücksichtigt.

Als Erstes wurde das kinetisches Modell für Modellkohlenwasserstoffen an Pt/Zeolith Katalysator von Steijns et al. (1981) und Froment (1987) für die C_8-Reaktionen angewendet. Die erhaltenen Ergebnisse wurden mit den experimentellen Ergebnissen der 1-Okten Reaktionen an Pt/ZSM-5 verglichen. Eine gute Übereinstimmung wurde vor allem im Temperaturbereich 230-250 °C (das kinetische Modell ist nur gültig bis 250 °C) in Abwesenheit von CO beobachtet (Abb. 9.5). Wie schon erwähnt, verlangsamt der CO-Partialdruck die Crackreaktionen der Isomeren, deshalb wurde die Crackgeschwindigkeit Konstante gesenkt. Auf diese Weise wurde auch in Anwesenheit von CO eine gute Übereinstimmung zwischen experimentellen und berechneten Daten erzielt (Abb. 9.6).

Im Anschluss wurde das kinetische Modell für den Pt/ZSM-5 Katalysator weiter entwickelt. Die Kinetikdaten der C_8-Reaktionen wurden für die gesamte Fraktion C_{5-9} angenommen. Wegen des Fehlens kinetischer Daten in der Literatur für die höheren Fraktionen, wurden diese ausgehend von den bekannten Werten extrapoliert. Die Isomerisieren- und Crackgeschwindigkeitskonstanten wurden durch multiplizieren der Geschwindigkeitskonstanten der Fraktion C_{5-9} mit einem relativen Crackreaktivitätsfaktor erhalten. Wird die C_{5-9}-Fraktion mit einer relativen

Crackreaktivität von 1 angenommen, steigt die Reaktivität folgendermaßen: $C_{5\text{-}9}$/ $C_{10\text{-}14}$/ $C_{15\text{-}20}$/ C_{21+} entsprechend 1/ 3,7/ 3,7/ 9. Zusätzlich wurde die Kohlenwasserstoffadsorption an Pt/ZSM-5 Katalysator berücksichtigt. Diese wurde mit einer Gleichung von Pellegrini et al. 2007 für jede Fraktion berechnet, allerdings unter die Berücksichtigung, dass oberhalb von circa C_{35} vollständige Adsorption stattfindet, d.h. dass die Adsorptionskonstanten für hohe C-Zahlen konstant werden (Sie et al. 1991).

Wegen des Fehlendes thermodynamischer Daten für Isomere mit $N_{C>10}$ wurden die Verteilungskoeffizienten für n- und Iso-Alkane ausgehend von der $C_{5\text{-}9}$-Fraktion (Steijns et al. 1981, Froment 1987) für alle Fraktionen gleich angenommen. Entsprechend den experimentellen Ergebnissen müsste die Oligomerisation Reaktionsgeschwindigkeit eigentlich größer als die der Isomerisation der $C_{5\text{-}9}$-Fraktion gewählt werden.

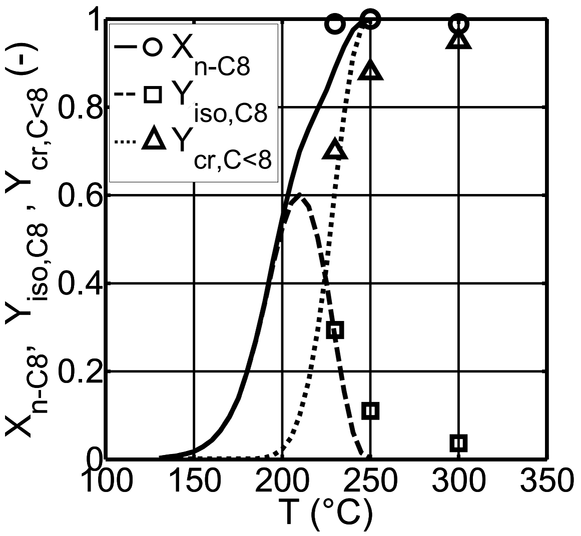

Abb. 9.5: Reaktionen von $1\text{-}C_8H_{16}$ bei Abwesenheit von CO. Feed: $1\text{-}C_8H_{16}$ + H_2 + Ar. Katalysator: Pt/ZSM-5. Punkte: Experimentell, Kurven: berechnet mit Steijns et al. 1981, Froment 1987 kinetisches Modell an Pt/USY Katalysator (siehe Kapitel 3.2.6). p = 0,5 MPa, WHSV = 0,22 h^{-1}. Andere Reaktionsbedingungen siehe Tabelle 5.7.

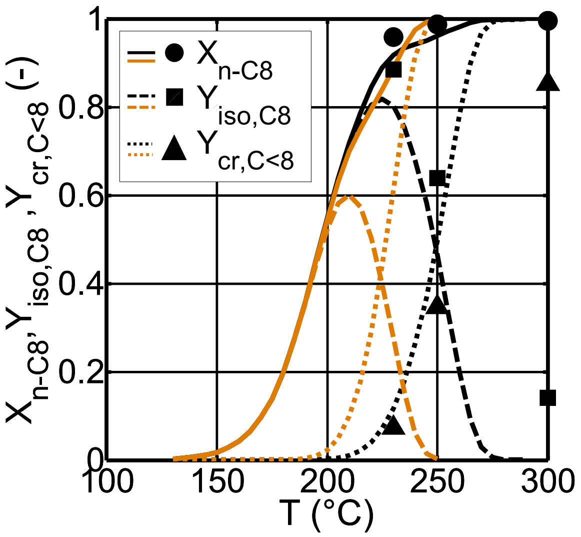

Abb. 9.6: Reaktionen von $1\text{-}C_8H_{16}$ bei Anwesenheit von CO an Pt/ZSM-5 Katalysator. Punkte: Experimentell. Schwarze Kurven: berechnet mit kinetischen Daten aus Tabelle 7.2. Graue Kurven: berechnet mit kinetischen Daten von Steijns et al. 1981, Froment 1987. Reaktions-Geschwindigkeit: Gl. 3.20-3.22. p = 0,5 MPa, WHSV = 0,22 h^{-1}. Andere Reaktionsbedingungen siehe Tabelle 5.7.

Das entwickelte kinetische Modell wurde für die Zweischichtanordnung und die Physikalische Mischung mit Co und Pt/ZSM-5 bei 230 °C und für die Zweischichtanordnung mit Fe und Pt/ZSM-5 bei 250 °C getestet. Die berechneten Daten zeigten Plausibilität und eine qualitative Übereinstimmung mit den experimentellen Daten. Es wird aber auch die Notwendigkeit der Berücksichtigung der CO- und Wasserdampfpartialdrücke in den Geschwindigkeitsgleichungen deutlich. Vor allem scheint der CO-Partialdruck die Crackaktivität der Isomeren zu beeinflussen.

Schlussfolgerungen und Ausblick

Die erzielten Ergebnisse bestätigen das Potential der Kombination von FTS und Kohlenwasserstoffereaktionen in einem Reaktor und geben einen detaillierten Einblick in die ablaufenden Mechanismen. Es wurde gezeigt, dass Hydrieren-, Isomerisieren-, Cracken- und Oligomerisierenreaktionen an Pt/Zeolith Katalysatoren bei FTS Temperaturen und Anwesenheit von CO und Wasserdampf statt fanden. Der negative Effekt von CO an der Isomeren Crackreaktionen – die Wachsfraktion (C_{21+}) wurde nicht vollständig gecrackt – ist wahrscheinlich der kritischste Punkt der Kombination.
Die experimentellen Ergebnisse zeigten auch, dass der Zeolithtyp und die Katalysatoranordnung Einfluss auf das Benzin/Diesel Verhältnis haben. Es ist anzunehmen, dass neben Dieselkraftstoff Benzin das Hauptprodukt für die Kombination sein wird, so lange kein Diesel-selektiver Katalysator gefunden wird.
Eine Rückführung der nicht gecrackten Wachsfraktion wird erforderlich, was zu größeren FT Synthese Reaktoren führt und somit auch zu höheren Kosten. Allerdings können immer noch die Investitionskosten für die H_2-Trennung gespart werden (Abb. 9.7)

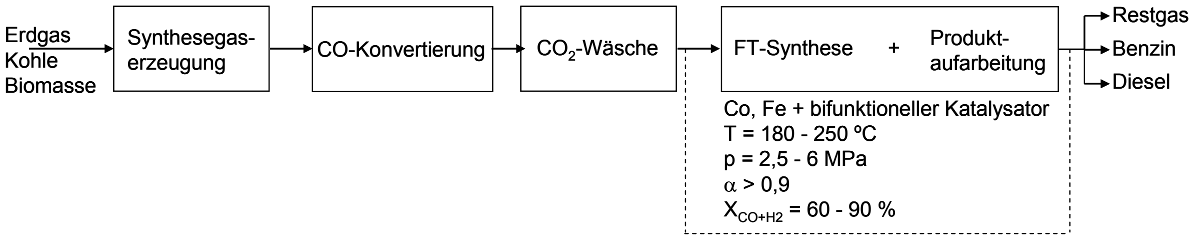

Abb. 9.7: Fließbild der Erzeugung flüssiger Kohlenwasserstoffe aus verschiedenen Rohstoffen via Fischer-Tropsch Synthese mit Kombination von FTS und Produktaufarbeitung in einem Reaktor.

Detaillierte Experimente mit Modellkomponenten bei Anwesenheit von CO und Wasserdampf sind notwendig, um deren Effekt auf die Kohlenwasserstoffreaktionen besser zu verstehen. Der gesamt Druckeinfluss an diesen Reaktionen sollte auch untersucht werden, da industrielle FTS-Anlagen normalerweise bei hohen Drücken betrieben werden. Außerdem sollte die Stabilität des Pt/Zeolith Katalysators mit längerer Versuchdauer untersucht werden. Diese Experimente könnten gleichzeitig als Referenz für die Weiterentwicklung des kinetischen Modells für Kohlenwasserstoffreaktionen an Pt/Zeolith Katalysatoren dienen.

10 References

Abbott J., Clark N.J., Baker B.G., Effects of sodium, aluminium and manganese on the fischer-tropsch synthesis over alumina-supported iron catalysts, Applied Catalysis 26 (1986) 141-153

Al-Ammar A.S., Webb G., Hydrogenation of acetylene over supported metal catalysts. Part 1. - Adsorption of [^{14}C]acetylene and [^{14}C]ethylene on silica supported rhodium, iridium and palladium and alumina supported palladium, J. Chem. Soc., Faraday Trans. 75 (1978) 1900-1911

Anderson R., Catalysts for the Fischer-Tropsch Synthesis, van Nostrand Reinhold, New York, 4th Edition (1956)

Arnold H., Döbert F., Gaube J., in: Ertl G. (Ed.), Handbook of heterogeneous catalysis, VCH Verlagsgesellschaft GmbH, Weinheim, Vol. 5 (1997) 2165-2186

ASTM Committee D-2 Data Series DS 4B, Physical Constants of Hydrocarbon and Non-Hydrocarbons compounds, 2nd Edition, American Petroleum Institut (1991)

Baerns M., Hofmann H., Renken A., Chemische Reaktionstechnik. Georg Thieme Verlag, Stuttgart, New York, Lehrbuch der Technischen Chemie, 1. Ausgabe (1987)

Barrer R.M., MacLeod D.M., Activation of montmorillonite by ion exchange and sorption complexes of tetra-alkyl ammonium montmorillonites, Trans. Faraday Soc. 51 (1955) 1290-1300

Bechtel, Aspen process flowsheet simulation model of a Battelle biomass-based gasification, Fischer-Tropsch liquefaction and combined-cycle power plant. Pittsburgh, Department of Energy, USA (1998)

Beech Jr.J.H., Saeger R.B., Ware R.A., United States Patent 5382743, Applicant: Mobil Oil Corporation, (1995)

Bessell S., Investigation of bifunctional zeolite supported cobalt Fischer-Tropsch catalysts, Applied Catalysis A: General 126 (1995) 235-244

Bhatia S., Zeolite Catalysis: Principles and Applications, CRC Press, Florida (1990) 75, 260

Blauwhoff P.M.M., Gosselink J.W., Sie S.T., Stork W.J.H., in: Weitkamp J., Puppe L. (Eds.), Catalysis and Zeolites: Fundamentals and Applications, Springer, Berlin (1999) 1955-1986

Botes F.G., Böhringer W., The addition of HZSM-5 to Fischer-Tropsch process for improved gasoline production, Applied Catalysis A: General 267 (2004) 217-225

Botes F.G., The effect of higher operating temperature on the Fischer-Tropsch/HZSM-5 bifunctional process, Applied Catalysis A: General 284 (2004) 21-29

BP Statistical Review of World Energy 2007. Available online: www.bp.com/statisticalreview (2007)

Bukur D., Sivaraj C., Supported iron catalysts for slurry phase Fischer-Tropsch synthesis, Applied Catalysis A: General 231 (2002) 201-214

Butter S.A., Hanson F.V., Sherry H.S., United States Patent 4,207,248, Applicant: Mobil Oil Corporation (1980)

Chang C.D., Lang W.H., United States Patent 4,086,262, Applicant: Mobil Oil Corporation, (1978)

Chang C.D., in: Ertl. G., Knözinger H., Weitkamp J. (Eds.), Handbook of Heterogeneous Catalysis, Wiley-VCH, Vol. 4 Part B (1997) 1894

Chen N.Y., Miale J.N., United States Patent 4,420,561, Applicant: Mobil Oil Corporation (1983)

Choi P., Jun K., Lee S., Choi M., Lee K., Hydrogenation of carbon dioxide over alumina supported Fe-K catalysts, Catalysis Letters 40 (1996) 115-118

Claeys M., Selektivität, Elementarschritte und kinetische Modellierung bei der Fischer-Tropsch Synthese, Dissertation, Universität Karlsruhe (1997)

Claeys M., van Steen E., in: Steynberg A.P., Dry M.E. (Eds.), Fischer-Tropsch Technology, Studies in Surface Science and Catalysis 152, Elsevier (2004) 601

Corma A., Martínez A., in: Schüth F., Sing K.S.W., Weitkamp J. (Eds.), Handbook of Porous Solids, Wiley-VCH, Weinheim, (2002) 2825

Dancuart L.P., de Haan R., de Klerk A., in : Steynberg A.P., Dry M.E. (Eds.), Fischer-Tropsch Technology, Studies in Surface Science and Catalysis 152, Elsevier (2004) 482

Davis B.H., Sing K.S.W., in: Schüth F., Sing K.S.W., Weitkamp J. (Eds.), Handbook of Porous Solids, Wiley-VCH, Weinheim, (2002) 18

Donnelly T.J., Satterfield C.N., Product Distributions of the Fischer-Tropsch Synthesis on Precipitated Iron Catalysts, Applied Catalysis 52 (1989) 93-114

Dry M.E., Shingles T., Boshoff J., Oosthuizen G.J., Heats of chemisorption on promoted iron surfaces and the role of alkali in Fischer-Tropsch synthesis, Journal of Catalysis 15 (1969) 190-199

Dry M.E., The Fischer-Tropsch synthesis, in: Anderson J.R., Boudart M. (Eds.), Catalysis Science and Technology, Springer Verlag Berlin, Vol. 1 (1981) 159

Dry M.E., Practical and theoretical aspects of the catalytic Fischer-Tropsch process, Applied Catalysis A: General 138 (1996) 319-344

Dry M.E., The Fischer-Tropsch process: 1950-2000, Catalysis Today 71 (2002) 227-241

Dry M.E., in: Steynberg A.P., Dry M.E., (Eds.), Fischer-Tropsch Technology, Studies in Surface Science and Catalysis 152, Elsevier (2004) 196

Eilers J., Posthuma S., Sie S.T., The Shell Middle Distillate Synthesis Process (SMDS), Catalysis Letters 7 (1990) 253-270

Emig G., Dittmeyer R., in: Ertl G., Knözinger H., Weitkamp J., Handbook of Heterogeneous Catalysis, V.3, VCH Verlagsgesellschaft GmbH, Weinheim (1997) 1209-1252.

Espinoza R.L., Steynberg A.P., Jager B., Vosloo A.C., Low temperature Fischer-Tropsch synthesis from a Sasol perspective, Applied Catalysis A: General 186 (1999) 13-26

Fischer F., Tropsch H., Über die Herstellung synthetischer Ölgemische (Synthol) durch Aufbau aus Kohlenoxyd und Wasserstoff, Brennstoff-Chemie 4 (1923) 276-285

Fischer F., CO-Hydrierung, Brennstoff-Chemie 7 (1926) 97

Fitzer E., Fritz W., Emig G., Technische Chemie – Einführung in die chemische Reaktionstechnik, Springer Verlag Berlin, New York, Heidelberg, 4. Edition (1995)

Fleisch T.H., Sills R.A., Briscoe M.D., 2002-Emergence of the Gas-to-Liquids Industry: a Review of Global GTL Developments, Journal of Natural Gas Chemistry 11 (2002) 1-14

Fröhling J.C., Zusammensetzung von Dieselkraftstoffen aus deutschen Raffinerien, Forschungsbericht 583, Hamburg: DGMK (2002)

Froment G.F., Kinetics of the hydrosiomerization and hydrocracking of paraffins on a platinum containing bifunctional Y-zeolite, Catalysis Today 1 (1987) 455-473

Giesche H., in: Schüth F., Sing K.S.W., Weitkamp J. (Eds.), Handbook of Porous Solids, Wiley-VCH, Weinheim, (2002) 309

Gorte R.J., in: Schüth F., Sing K.S.W., Weitkamp J. (Eds.), Handbook of Porous Solids, Wiley-VCH, Weinheim, (2002) 432

Grandvallet P., Jong K.P., Mooiweer H.H., Kortbeek A.G.T.G., Kraushaar-Czarnetzki B., European Patent Application 0,501,577, Applicant: Shell Int. Res., (1992)

Haag W.O., Lago R.M., Weisz P.B., Transport and reactivity of hydrocarbons molecules in a shape selective zeolite, Faraday Discuss. Chem. Soc., 72 (1981) 317-330

Hamelinck C.N., Faaij A.P.C., den Uil H., Boerrigter H., Production of FT transportation fuels from biomass; technical options, process analysis and optimisation, and development potential, Energy 29 (2004) 1743-1771

He J., Yoneyama Y., Xu B., Nishiyama N., Tsubaki N., Designing a Capsule Catalyst and Its Application for Direct Synthesis of Middle Isoparaffins, Langmuir 21 (2005a) 1699-1702

He J., Yoneyama Y., Xu B., Nishiyama N., Tsubaki N., Designing a New Kind of Capsule Catalyst and Its Application for Direct Synthesis of Middle Isoparaffins from Synthesis Gas, Chemistry Letters 34 (2005b) 148-149

Huff G., Satterfield C., Intrinsic Kinetics of the Fischer-Tropsch Synthesis on a Reduced Fused-Magnetite Catalyst, Ind. Eng. Chem. Proc. Des. Dev. 23 (1984) 696-705

IEA, China and India´s Energy Development in Global Perspective, Yo Osumi, Beijing (2006)
http://www.iea.org/textbase/speech/2006/yo_apec.pdf

Iglesia E., Reyes S.C., Madon R.J., Soled S.L., Selectivity Control and Catalyst Design in the Fischer-Tropsch Synthesis: Sites, Pellets, and Reactors, Advances in Catalysis 39 (1994) 221-302

Iglesia E., Soled S.L., Baumgartner J.E., Reyes S.C., Synthesis and catalytic properties of eggshell cobalt catalysts for the Fischer-Tropsch synthesis, Topics in Catalysis 2 (1995) 17-27

IZA (2007), International Zeolite Association, http://www.iza-structure.org/databases/

Jacobs P.A., Martens J.A., in: van Bekkum H., Flanigen E.M., Jansen J.C. (Eds.), Introduction to Zeolite Science and Practice, Studies in Surface Science and Catalysis, Elsevier, Amsterdam, 58 (1991) 445

Jager B., Espinoza R., Advances in low-temperature Fischer-Tropsch Synthesis, Catalysis Today 23 (1995) 17-28

Jothimurugesan K., Gangwal S.K., Titania-Supported Bimetallic Catalysts Combined with HZSM-5 for Fischer-Tropsch Synthesis, Ind. Eng. Chem. Res. 37 (1998) 1181-1188

Kaiser R., Chromatographie in der Gasphase, Band III, 2. Auflage (Bibliographisches Institut, Mannheim (1969)

Katofsky R.E., The production of fluid fuels from biomass. PU/CEES report 279. Princeton, Center for Energy and Environmental Studies, Princeton University (1993)

De Klerk A., Oligomerization of Fischer-Tropsch Olefins to Distillates over Amorphous Silica-Alumina, Energy & Fuels 20 (2006) 1799-1805

De Klerk A., Environmentally friendly refining: Fischer-Tropsch versus crude oil, Green Chemistry 9 (2007) 560-565

Knottenbelt C., Mossgas “gas-to-liquid” diesel fuels - an environmentally friendly option, Catalysis Today 71 (2002) 437-445

Kölbel H., Ralek M., The Fischer-Tropsch Synthesis in the Liquid Phase, Catalysis Reviews - Science and Engineering 21 (1980) 225-274

Kreitman K.M., Baerns M., Butt J.B., Manganese-oxide-supported iron Fischer-Tropsch synthesis catalysts: Physical and catalytic characterization, Journal of Catalysis 105 (1987) 319-334

Kresge C.T., Leonowicz M.E., Roth W.J., Vartuli J.C., Beck J.S., Ordered mesoporous molecular sieves synthesized by a liquid crystal template mechanism, Nature 359 (1992) 710-712

Kuipers E.W., Vinkenburg I.H., Oosterbeek H., Chain length dependence of α-olefin readsorption in Fischer-Tropsch synthesis, Journal of Catalysis 152 (1995) 137-146

Kvisle S., Nilsen H.R., Fuglerud T., Grønvold A., Vora B.V., Pujado P.R., Borger P.T., Andersen J.M., Methanol to Olefins: State of the Art and Prespectives, Erdöl, Erdgas, Köhle, 18.Jahrgang 7/8 (2002) 361-365

Leckel D., Hydrocracking of Iron-Catalyzed Fischer-Tropsch Waxes, Energy & Fuels 19 (2005) 1795-1803

Ledakowicz S., Nettelhoff H., Kokuun R., Dewecker W., Kinetics of the Fischer-Tropsch Synthesis in the slurry Phase on a Potassium-Promoted Iron Catalyst, Ind. Eng. Chem. Proc. Res. Dev. 24 (1985) 1043-1049

Li X., Luo M., Asami K., Direct synthesis of middle iso-paraffins from synthesis gas on hybrid catalysts, Catalysis Today 89 (2004) 439-446

Liebner W., Wagner M., MtSynfuels, die effiziente und wirtschaftliche Alternative zu Fischer-Tropsch-Treibstoffen, DGMK-Tagungsbericht, Energetische Nutzung von Biomassen, 19-21. April (2004)

Liu Z-W., Li X., Asami K., Fujimoto K., Iso-paraffins synthesis from modified Fischer-Tropsch reaction - Insights into Pd/beta and Pt/beta catalysts, Catalysis Today 104 (2005a) 41-47

Liu Z-W., Li X., Asami K., Fujimoto K., Selective production of iso-paraffins from syngas over Co/SiO_2 and Pd/beta hybrid catalysts, Catalysis Communications 6 (2005b) 503-506

Lyondell, 2007, Olefins and Fuels www.lyondell.com/Lyondell/Products/Licensing/OlefinsAndFuels

Marcilly Ch., in: Galarneau A., Di Renzo F., Fajula F., Vedrine J. (Eds.), Zeolites and Mesoporous Materials at the Dawn of the 21st Century, Studies in Surface Science and Catalysis 135 (2001) 37

Martens J.A., Jacobs P.A., in: van Bekkum H., Flanigen E.M., Jacobs P.A., Jansen J.C. (Eds.) 2nd Edition, Studies in Surface Science and Catalysis, Elsevier, Amsterdam, 137 (2001) 633

Martínez A., Rollán J., Arribas M.A., Cerqueira H.S., Costa A.F., Aguiar E.F.S., A detailed study of the activity and deactivation of zeolites in hybrid Co/SiO_2-zeolite Fischer-Tropsch catalysts, Journal of Catalysis 249 (2007) 160-171

Maxwell I.E., Zeolite Catalysis in Hydroprocessing Technology, Catalysis Today 1 (1987) 385-413

Maxwell I.E., Stork W.H.J., in: van Bekkum H., Flanigen E.M., Jansen J.C. (Eds.), Introduction to Zeolite Science and Practice, Studies in Surface Science and Catalysis, Elsevier, Amsterdam, 58 (1991) 571

Maxwell I.E., Minderhoud J.K., Stork W.H.J., van Veen J.A.R., in: G. Ertl., Knözinger H., Weitkamp J. (Eds.), Handbook of Heterogeneous Catalysis, V. 4, Wiley-VCH, Weinheim, (1997) 2017

Miale J.N., Chen N.Y., Weisz P.B., Catalysis by crystalline aluminosilicates. IV. Attainable catalytic cracking rate constants, and superactivity, Journal of Catalysis 6 (1966) 278-287

Mol J.C., in: Ertl. G., Knözinger H., Weitkamp J. (Eds.), Handbook of Heterogeneous Catalysis, Wiley-VCH, Weinheim, V. 5 (1997) 2387

Newsome D.S., The Water-Gas Shift Reaction, Catalysis Reviews - Science and Engineering 21 (1980) 275-318

Ngamcharussrivichai C., Liu X., Li X., Vitidsant T., Fujimoto K., An active and selective production of gasoline-range hydrocarbons over bifunctional Co-based catalysts, Fuel 86 (2006) 50-59

Nieminen V., Kangas M., Salmi T., Murzin D.Y., Kinetic Study of n-Butane Isomerization over Pt-H-Mordenite, Ind. Eng. Chem. Res. 44 (2005) 471-484

Niwa M., Katada N., Measurements of acidic property of zeolites by temperature programmed desorption of ammonia, Catalysis Surveys from Japan 1 (1997) 215-226

O´Connor C.T., Kojima M., Alkene Oligomerization, Catalysis Today 6 (1989) 329-350

O´Connor C.T., in: Ertl G., Knözinger H., Weitkamp J., (Eds.), Handbook of Heterogeneous Catalysis, Wiley-VCH, Weinheim, V. 5 (1997) 2380

Pellegrini L., Locatelli S., Rasella S., Bonomi S., Calemma V., Modeling of Fischer-Tropsch products hydrocracking, Chemical Engineering Science 59 (2004) 4781-4787

Pellegrini L., Bonomi S., Gamba S., Calemma V., Molinari D., The “all components hydrocracking model”, Chemical Engineering Science 62 (2007) 5013-5020

Pichler H., Schulz H., Neue Erkenntnisse auf dem Gebiet der Synthese von Kohlenwasserstoffe aus CO und H_2, Chem. Ing. Tech. 42 (1970) 1162-1174

Pischinger S., Müther M., Fricke F., Kolbeck A., From Fuel to Wheel: How Modern Fuels Behave in Combustion Engines, DGMK-Tagungsbericht: Opportunities and Challenges at the Interface between Petrochemistry and Refinery (2007) 177-189

Post M.F.M., van’t Hoog A.C., Minderhoud J.K., Sie S.T., Diffusion Limitations in Fischer-Tropsch Catalysts, AIChE Journal Vol. 35, No. 7 (1989) 1107-1114

Post M.F.M., in: van Bekkum H., Fanigen E.M., Jansen J.C. (Eds.), Introduction to Zeolite Science and Practice, Studies in Surface Science and Catalysis, Elsevier, Amsterdam, 58 (1991) 391

Quann R.J., Krambeck F.J., in: Sapre A.V., Krambeck F.J. (Eds.), Chemical Reactions in Complex Mixtures, Van Nostrand Reinhold, New York (1991) 143-161

Rao V.U.S., Gormley R.J., Bifunctional catalysis in syngas conversions, Catalysis Today 6 (1990) 207-234

Rapaport I.B., Chemistry and Technology of Synthetic Liquid Fuels, 2nd Edition, Israel Program for Scientific Translation, Jerusalem (1962)

Refining Processes, Hydrocarbon Processing, November (2002) 85-148

Riedel T., Schaub G., Jun K.W., Lee K.W., Kinetics of CO_2 Hydrogenation on a K-promoted Fe catalyst, Ind. Eng. Chem. Res. 40 (2001) 1355-1363

Riedel T., Reaktionen von CO_2 bei der Fischer-Tropsch Synthese - Kinetik und Selektivität, Dissertation, Universität Karlsruhe (2003)

Rouquerol J., Avnir D., Fairbridge C.W., Everett D.H., Haynes J.M., Pernicone N., Ramsay J.D.F., Sing K.S.W., Unger K.K, Recommendations for the Characterization of Porous Solids, Pure Applied Chemistry 66 (1994) 1739-1758

Rouquerol F., Rouquerol J., Sing K.S.W., in: F. Schüth, K.S.W. Sing, Weitkamp J. (Eds.), Handbook of Porous Solids, Wiley-VCH, Weinheim, (2002) 236

Ruthven D.M., Principles of Adsorption and Adsorption processes, Wiley-Interscience Publication, New York (1984) 25, 334

Sachtler W.M.H., Metal Clusters in Zeolites: An Intriguing Class of Catalysts, Acc. Chem., Res., 26 (1993) 383-387

Sarup B., Wojciechowski B.W., Studies of the Fischer-Tropsch Synthesis on a Cobalt Catalyst. III. Mechanistic Formulation of the Kinetics of Selectivity for Higher Hydrocarbon Formation, Canadian Journal of Chemical Engineering 67 (1989) 62-74

SasolChevron, 2007, Record $6 Billion GTL Initiative. Qatar Petroleum and Sasol Chevron progress a 200,000 Barrel a day GTL expansion and integrated project plan, http:/www.sasolchevron.com/pr_01a.htm

Satterfield C.N., Sherwood T.K., The Role of Diffusion in Catalysis, Addison/Wesley, Reading, UK (1963)

Scherzer J., Gruia A.J., Hydrocracking Science and Technology, Marcel Dekker, Inc., New York (1996)

Schulz H.F., Weitkamp J.H., Hydrocracking and hydroisomerization of n-Dodecane, Ind. Eng. Chem. Prod. Res. Dev. 11 (1972) 46-53

Schulz H., Trends in Research and Development of Coal Conversion to Liquid Fuels and Basic Chemicals in Europe, Pure and Applied Chemistry 51 (1979) 2225-2241

Schulz H., Böhringer W., Kohl C.R.N., Will A., Entwicklung und Anwendung der Kapillar-GC-Gesamtprobentechnik für Gas/Dampf-Vielstoffgemische, DGMK-Forschungsbericht 320, DGMK Hamburg (1984) 1-6

Schulz H., Beck K., Erich E., Mechanism of the Fischer-Tropsch process, Studies in Surface Science and Catalysts 46 (1988), 3rd Natural gas Conversion Symposium, 457

Schulz H., Niederberger H.L., Kneip M., Weil F., Synthesis Gas Conversion on Fischer-Tropsch Iron/HZSM5 Composite Catalysts, in Natural Gas Conversion, Studies in Surface Science and Catalysis 61 (1991) 313-323

Schulz H., van Steen E., Claeys M., in: Curry-Hyde H.E., Howe R.F. (Eds.), Studies in Surface Science and Catalysis 81 (1994) 455

Schulz H., van Steen E., Claeys M., Specific inhibition as the kinetic principle of Fischer-Tropsch synthesis, Topics in Catalysis 2 (1995) 223-234

Schulz H., Short history and present trends of Fischer-Tropsch synthesis, Applied Catalysis A: General 186 (1999) 3-12

Schulz H., Nie Z., Ousmanov F., Construction of the Fischer-Tropsch regime with cobalt catalysts, Catalysis Today 71 (2002) 351-360

Schulz H., Principles of selectivity in Fischer-Tropsch Synthesis, Proceedings of the DGMK/SCI-Conference Synthesis Gas Chemistry, October 4-6, Dresden, Germany (2006)

Schulz H., Skript Gaschromatographie - Grundlagen und Anwendungen in Brennstoff- und Umwelttechnik, Universität Karlsruhe, 2007

Schüth F., Sing K.S.W., Weitkamp J. (Eds.), Handbook of Porous Solids, Wiley-VCH, Weinheim, (2002) 25

Shell, 2007, Shell Middle Distillate synthesis (Malaysia), www.shell.com.my/smds/

Shroff M.D., Kalakkad D.S., Coulter K.E., Köhler S.D., Harrington M.S., Jackson N.C., Sault A.G., Datye A.K., Activation of Precipitated Iron Fischer-Tropsch Synthesis Catalysts, Journal of Catalysis 156 (1995) 185-207

Sie S.T., Eilers J., Minderhoud J.K., Consequences of Fischer-Tropsch chain growth kinetics for process model selection and product selectivity, Proc. 9th Internat. Congr. Catalysis, Philips M.J. and Ternan M., (Eds.), The Chemical Institute of Canada, Ottawa 2 (1988) 743-750

Sie S.T., Senden M.M.G., van Wechem H.M.H., Conversion of Natural Gas to Transportation Fuels via the Shell Middle Distillate Synthesis Process (SMDS), Catalysis Today 8 (1991) 371-394

Sie S.T., in: G. Ertl., Knözinger H., Weitkamp J. (Eds.), Handbook of Heterogeneous Catalysis, Wiley-VCH, Weinheim, V. 4 (1997) 1998

Sing K.S.W., Schüth F., in: Schüth F., Sing K.S.W., Weitkamp J. (Eds.), Handbook of Porous Solids, Wiley-VCH, Weinheim, (2002) 25

Stangeland B.E., A Kinetic Model for the Prediction of Hydrocracker Yields, Ind. Eng. Chem. Proc. Des. Dev. 13 (1974) 71-76

Steijns M., Froment G., Jacobs P., Uytterhoeven J., Weitkamp J., Hydroisomerization and Hydrocracking. 2. Product Distributions from n-Decane and n-Dodecane, Ind. Eng. Chem. Prod. Res. Dev. 20 (1981a) 654-660

Steijns M., Froment G., Hydroisomerization and Hydrocracking. 3. Kinetic Analysis of Rate Data for n-Decane and n-Dodecane, Ind. Eng. Chem. Prod. Res. Dev. 20 (1981b) 660-668

Steynberg A.P., Espinoza R.L., Jager B., Vosloo A.C., High temperature Fischer-Tropsch synthesis in commercial practice, Applied Catalysis A: General 186 (1999) 41-54

Steynberg A.P., Dry M.E., Davis B.H., Breman B.B., in: Steynberg A.P., Dry M.E. (Eds.), Fischer-Tropsch Technology, Studies in Surface Science and Catalysis 152, Elsevier (2004) 64

Stöcker M., Methanol-to-hydrocarbons: catalytic materials and their behaviour, Microporous and Mesoporous Materials 29 (1999) 3-48

Stöcker M., Gas phase catalysis by zeolites, Microporous and Mesoporous Materials 82 (2005) 257-292

Storch H.G., Golumbic N., Anderson R.B., The Fischer Tropsch and Related Syntheses, Wiley, New York, 1951

Stull D.R., Westrum E.F., Sinke G.C., The Chemical Thermodynamics of Organic Compounds, Willey, New York (1969)

Tabak S.A., Krambeck F.J., Garwood W.E., Conversion of Propylene and Butylene over ZSM-5 Catalysts, AIChE Journal 32 (1986) 1526-1531

Tatsumi T., in: Schüth F., Sing K.S.W, Weitkamp J. (Eds.), Handbook of Porous Solids, Wiley-VCH, Weinheim, (2002) 903

Terasaki O., in: Karge H.G., Weitkamp J. (Eds.), Molecular Sieves. 2 Science and Technology. Structures and structure Determination, Springer-Verlag, Berlin-Heidelberg (1999) 71-105

Tesche B., in: Schüth F., Sing K.S.W., Weitkamp J. (Eds.), Handbook of Porous Solids, Wiley-VCH, Weinheim, (2002) 106

Tsubaki N., Yoneyama Y., Michiki K., Fujimoto K., Three-component hybrid catalyst for direct synthesis of isoparaffin via modified Fischer-Tropsch synthesis, Catalysis Communications 4 (2003) 108-111

Turro N.J., Fehlner J.R, United States Patent 4,971,664, Applicant: Inrad, Inc., (1990)

Unruh D., Fischer-Tropsch Synthese mit Synthesegasen aus Biomasse - Verbesserung der Kohlenstoffnutzung durch Anwendung eines Membranreaktors, Dissertation, Universität Karlsruhe (2006) van der Laan G., Beenackers A., Kinetics and Selectivity of the Fischer-Tropsch synthesis: A Literature Review, Catalysis Reviews Science and Engineering 41 (1999a) 255-318

van der Laan G., Kinetics, selectivity and scale up of the Fischer-Tropsch synthesis, Dissertation, University of Groningen (1999b)

VDI-Wärmeatlas, Einführung in die Lehre von der Wärmeübertragung (A13), Dimensionslose Kenngrößen (Bc1), Berechnungsmethoden für Stoffeigenschaften (Da33), Siede- und Sublimationstemperaturen bei verschiedenen Drücken in °C (Dc7), Verein Deutsche Ingenieure, VDI-Gesellschaft Verfahrenstechnik und Chemieingenieurwesen (GVC), 4. Auflage (1984)

Wang Z.B., Kamo A., Yoneda T., Komatsu T., Yashima T., Isomerization of n-heptane over Pt-loaded zeolite ß catalysts, Applied Catalysis A: General 159 (1997) 119-132

Weidert D.J., Olefin-Transformation - A Means to Ease Your MTBE Woes, AIChE March 5-9 (2000) Spring Meeting

Weitkamp J., Farag H., Acta. Phys. Chem. Hung. 24 (1978) 327

Weitkamp J., Jacobs P.A, Martens J.A., Isomerization and hydrocracking of C_9 through C_{16} n-alkanes on Pt/HZSM-5 zeolite, Applied Catalysis 8 (1983) 123-141

Weiss A.H., LeViness S., Nair V., Guzci L., Sarkany A., Schay Z., Proceeding of the 8th International Congress of Catalysis 5 (1984) 591-600

Weisz P.B., Prater C.D., Interpretation of measurements in experimental catalysis, Advances in Catalysis 6 (1954) 143-196

Weisz P.B., Zeolites - New horizons in catalysis, Chemtech (1973) 498-505

Yashima T., Wang Z.B., Kamo A., Yoneda T., Komatsu T., Isomerization of n-hexane over Platinum loaded zeolite catalysts, Catalysis Today 29 (1996) 279-283

Yates I., Satterfield C., Intrinsic kinetics of the Fischer-Tropsch Synthesis on a cobalt catalyst, Energy & Fuel 5 (1991) 168-173

Yoneyama Y., He J., Morii Y., Azuma S., Tsubaki N., Direct synthesis of isoparaffin by modified Fischer-Tropsch synthesis using hybrid catalyst of iron catalyst and zeolite, Catalysis Today 104 (2005) 37-40

Yori J.C., D´Amato M.A., Costa G., Parera J.M., Influence of Platinum and Hydrogen on n-Butane Isomerization on H-Mordenite, React. Kinet. Cat. Lett. 56 (1995) 129-135

Zimmerman W.H., Bukur D.B., Reaction Kinetics Over Iron Catalysts Used for the Fischer-Tropsch Synthesis, Canadian Journal of Chemical Engineering 68 (1990) 292-301

11 Notation

Symbols (Latin)

Symbol	Description	Definition	Dimension
A	Area	L^2	m^2
a	Inhibition coefficient	Eq. 3.11-3.13	-
b	Inhibition coefficient	Eq. 3.12-3.13	-
C_i	Concentration	N_i/V	mol/m^3
c_p	Specific heat capacity	$(dH/dT)_p$	J / (mol·K)
d	Diameter	L	m
D_i	Diffusion of component i	$- J_i / (dC_i/dz)$	m^2/s
E_A	Apparent activation energy	-	J/mol
i	Counter	-	-
f	Function	-	-
f_j	factor	Eq. 5.1	-
F	Force	m*du/dt	$kg\cdot m/s^2$
h_{ext}	External heat transfer coefficient	$Q / (A\cdot\Delta t\cdot \Delta T)$	$W/(m^2\cdot K)$
$\Delta_R H_T^0$	Heat of reaction at standard pressure and temperature T	$\sum_{j}^{product}(\nu_{ij}\Delta H_{i,T}) - \sum_{j}^{reactant}(\nu_{ij}\Delta H_{i,T})$	J/mol
j	Counter	-	-
J	Molar flux	$\dot{N} / A$	$mol/(m^2\cdot s)$
k_i	Reaction rate constant	-	mol/(s·kg·Pa), mol/(s·kg)
$k^*_{i,cr}$	Cracking rate constant with CO presence	$k_{i,cr}$ / 15	mol/(s·kg)
$k_{0,i}$	Preexponential factor in Arrenhius law	-	mol/(s·kg·Pa), mol/(s·kg)
$k^*_{0,cr}$	Preexponential factor in Arrenhius law for cracking reactions with CO presence	-	mol/(s·kg)
K_{dist}	Distribution coefficient	$p_{iso}/p_{n\text{-}alkane}$	-
K_{eq}	Equilibrium constant	$p_{iso}/p_{n\text{-}alkane}$	-
K_p	Equilibrium constant	Eq. 3.14	-
K_L	Adsorption constant	Eq. 3.19	bar^{-1}
L	Length	Basic dimension	m
m	Mass	Basic dimension	kg
m	Counter	-	-
$\dot{m}$	Mass flow	dm_i/dt	kg/s
M	Molecular mass	-	kg/kmol
N	Number	-	-
N_C	Number of C-atoms	-	-
N_i	Amount of substance	Basic dimension	mol
$\dot{N}$	Molar flow	dN_i/dt	mol/s
n	Counter	-	-
p	Pressure	F/A	$kg/(m\cdot s^2)$

p_i	Partial pressure	$\dot{N}_i / \sum_{i=1}^{n} \dot{N}_i \cdot p$	$kg/(m \cdot s^2)$
P	Parameter	-	-
Q	Heat input or heat lost	Basic dimension	J
r_j	Reaction rate	Eq. 5.22	$mol/(kg \cdot s)$
R	Universal gas constant (8.314)	-	$J/(mol \cdot K)$
R	Radius	L	m
r_i	Total rate	Eq. 5.23	mol/s
s	Thickness	L	m
$S_{C,j}$	Selectivity	Eq. 5.14	-
t	Time	Basic dimension	s
T	Temperature	Basic dimension	K, °C
u	Velocity	dL/dt	m/s
$\bar{u}$	Mean velocity	dL/dt	m/s
V	Volume	L^3	m^3
$\dot{V}$	Volume flow	dV/dt	m^3/s
V_A	Avogadro volume: $22.414 \cdot 10^{-3}$	-	m^3/mol
WHSV	Weight Hour Space Velocity	Eq. 5.20	s^{-1}
X_i	Conversion	Eq. 5.12	-
x_i	Molar fraction	$N_i / \Sigma N_i$	-
x_i	Independent variable	-	-
$Y_{C,j}$	Yield	Eq. 5.13	-
y_i	Molar fraction	Eq. 5.15	-
y_i	Dependent variable	-	-
z	Reactor axial length coordinate	L	M
z*	Dimensionless number	z/L	-

Symbols (Greek)

Symbol	Description	Definition	Dimension
α	Chain-growth probability	Eq. 3.10	-
χ^2	Sum square of residuals	Eq. 5.34	-
χ	Labyrinth factor or tortuosity	$D_{i\text{ ,free space}} / D_{i\text{, porous medium}}$	-
∂	Complexor / operator	-	-
ε	Porosity	V_g / V_s	-
Φ	Thiele modulus	Eq. 3.15, 12.24	-
η	Effectiveness factor		-
$\eta_{H2/CO}$	Dynamic viscosity	τ / (du/dz)	$N \cdot s/m^2$
λ	Thermal conductivity	-	$W/(m \cdot K)$
$\nu_{i,j}$	Stochiometric coefficient of component I in reaction j	-	-
$\nu_{H2,CO}$	Kinematic viscosity	η / ρ	m^2/s

θ	Dimensionless number	t / τ	-
ρ	Density	m/V	kg/m^3
τ_{mod}	Modified residence time	Eq. 5.21	$(kg \cdot s/m^3)$
τ^*_{mod}	Modified residence time	Eq. 7.6	$(kg \cdot s/m^3)$
ζ_j	Extent of reaction j	$(N_{i,j} – N_{i,j,in})/ \nu_{i,j}$	mol
Ψ	Vacancies volume	$V_{vacancies} / V_{total}$	-

Indices

Symbol	Description
A	Avogadro
ax	Axial
C	Carbon
c	Zeolite crystal
cat	Catalyst
CPr	Cyclopropane
cr	Cracking
DB	Dibranched
dist	Distribution
eff	Effective
eq	Equilibrium
ext	External
g	Gas
grad	Gradient
HC	Hydrocarbons
HHV	High heating value
i, i´, j	Counter for components and reactions
in	Inlet
int	Internal
iso	Isomer, isomerisation
Kn	Knudsen
L	Langmuir
lam	Laminar
m	Mass
max	Maximum
MB	Monobranched
min	Minimum
mod	Modified
N_C	Hydrocarbon with N C-atoms
NC	Hydrocarbons
n	Standard conditions, $p = 1.013 \cdot 10^5$ Pa, T = 273.15 K
n	Number of C-atoms
n	Molar (Eq. 3.8)
ol	Oligomerisation
out	Outlet
p	Pellet, particle, propagation (Eq. 3.10), pressure (Fig. 5.6)
Ref	Reference
R	Reaction
s	Solid
S	Catalyst bed

SH	Shift
t	Termination (Eq. 3.10)
tur	Turbulent
z	Local coordinate

Dimensionless numbers

Abbreviation	Denomination	Definition
Bo	Bodenstein number	Eq. 12.1
Nu	Nusselt number	Eq. 12.10
Pe	Péclet number	Eq. 12.4
Pr	Prandtl number	Eq. 12.16
Re	Reynolds number	Eq. 12.5
Sc	Schmidt number	Eq. 12.6

Abbreviations

Symbol	Description
a	Year
A	Acid site
AD	Adsorption
AES	Auger Electron Microscopy
AFM	Atomic Force Microscopy
Al	Aluminium
ALPO	Aluminophosphate
approx.	Approximately
aq.	Aqueous
Ar	Argon
ASF	Anderson-Schulz-Flory
AUX	Auxiliar
BET	Brunauer-Emmett-Teller
BP	British Petroleum
bpd	Barrel per day
BTL	Biomass to Liquids
CFB	Circulating Fluidised Bed
C	Carbon
Ca	Calcium
CH_4	Methane
CH_2	Monomer
CFPP	Cloud Filter Plugging Point
Cl	Chlorine
Co	Cobalt
CO	Carbon monoxide
CO_2	Carbon dioxide
COD	Conversion of low-molecular-weight Olefins to Distillate
CPr	Cyclopropane
cr.	Cracking, cracked products
CTL	Coal to Liquids

Cu	Copper
De	Dealuminated
DB	Dibranched
DL	Dual layer
EDX	Energy Dispersive (X-ray) Spectroscopy
e.g.	for example, “exempli gratia”
Eq.	Equation
etc.	et cetera
Fe	Iron
FFB	Fixed Fluidised Bed
Fig.	Figure
FIC	Flow Indicator Controller
FID	Flame Ionization Detector
FT	Fischer-Tropsch
FTS	Fischer-Tropsch Synthesis
GC	Gas Chromatograph
grad	Gradient
GTL	Gas-to-Liquids
H	Hydrogen
HC	hydrocarbons
He	Helium
HEC	Hydroxyethylcellulose
Hg	Mercury
HP	Hydroprocessing
HTFT	High-Temperature Fischer-Tropsch
H_2O	Water
H_2S	Hydrogen sulphide
i	Internal
ICP-OES	Inductively Coupled Plasma Optical Emission Spectrometry
id	Internal diameter
i.e.	that is, “id est”
IEA	International Energy Agency
IR	Infrared
is.	Isomerisation
iso	Isomers
IUPAC	International Union of Pure and Applied Chemistry
K	Potassium
LM	Light Microscopy
LSR	Light Straight Run
LTFT	Low-Temperature Fischer-Tropsch
M	Metal
MB	Monobranched
MCM-41	Mobil Catalytic Material number 41
MIX	Physical mixture
Mn	Manganese
MOGD	Mobile Olefine to Gasoline and Distillate
MS	Mass Spectroscometry
MTBE	Methyl tertiary-butyl ether
MTG	Methanol to Gasoline
MTO	Methanol to Olefins
MTP	Methanol to Propylene

NLDFT	Non-Local Density Functional Theory
N	Nitrogen
Ni	Nickel
NMR	Nuclear Magnetic Resonance
O	Oxygen
Ol.	Oligomerisation
PC	Pressure Controller
PCP	Protonated Cyclopropane
Pd	Palladium
PEC	Primary Energy Consumption
PFR	Plug-flow reactor
PI	Pressure Indicator
prim.	Primary
PSA	Pressure Swing Adsorption
Pt	Platinum
PVC	Polyvinyl Chloride
R	Radical
rel.	Relative
Re	Rhenium
RON	Research octane number
rpm	revolutions per minute
Ru	Ruthenium
sec.	Secondary
SAPO	Silicoaluminophosphate
SAS	Sasol Advanced Synthol
SEM	Scanning Electron Microscopy
SH	Shift
Si	Silicon
SMDS	Shell Middle Distillate Synthesis
SPGK	Shell Polygasoline Kero Process
STM	Scanning Tunnelling Microscopy
t	Tonne
Tab.	Table
TAME	Tert-Amyl methyl ether
TCD	Thermal Conductivity Detector
TEM	Transmission Electron Microscopy
tert.	Tertiary
Ti	Titanium
TI	Temperature Indicator
TIP	Total Isomerisation Process
tos	Time on stream
TPD	Temperature-programmed desorption
USY	Ultra stable Y zeolite
vol.	Volume
WGS	Water-gas-shift
WHSV	Weight Hour Space Velocity
wt	Weight
XPS	X-ray Photoelectron Spectroscopy
Z	Zeolite
Zr	Zirconium
ZSM-5	Zeolite Socony Mobil-5

12 Appendix

12.1 Gas chromatography

12.1.1 Inorganic compounds

Tab. 12.1: Gas chromatography specifications (HP6890N).

Gas chromatograph	HP 6890N
Detector	Thermal Conductivity Detector (TCD), T = 270 °C Flame Ionization Detector (FID), T = 270 °C
Column HP1(after V1)	J&W column Megabore^{R} serial no.US5362544H Stationary phase: HP-1 Dimethylpolysiloxane L = 30 m, d_i = 0.534 mm, s_{film} = 2.65 µm
Column HP1(after V2) (for organic compounds)	J&W column Widebore^{R} serial no.US5412614H Stationary phase: HP-1 (Dimethylpolysiloxane) L = 50 m, d_i = 0.321 mm, s_{film} = 0.52 µm
Column Plot Q	J&W column Megabore^{R} serial no.US4923415H Stationary phase: HP-Plot Q (Porapak-Q and Porapak-N) L = 30 m, d_i = 0.539 mm, s_{film} = 40 µm
Molesieve	J&W column Megabore^{R} serial no.US4727415H Stationary phase: HP-Molesieve L = 30 m, d_i = 0.533 mm, s_{film} = 25 µm
Carrier/reference gas	Ar
Temperature program	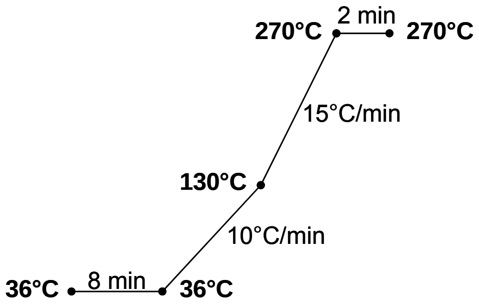 270°C 2 min 270°C 15°C/min 130°C 10°C/min 36°C 8 min 36°C Maximum temperature 290°C Set point temperature 35°C
Analysis duration	28 min

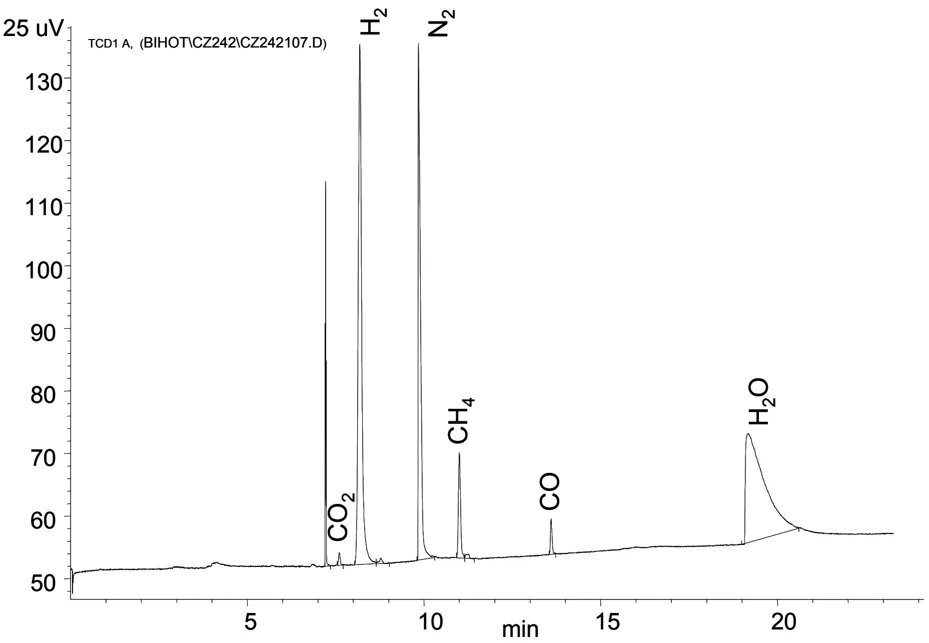

Fig. 12.1: Typical chromatogram of the inorganic gases and methane with nitrogen as reference gas (HP6890N).

12.1.2 Organic compounds

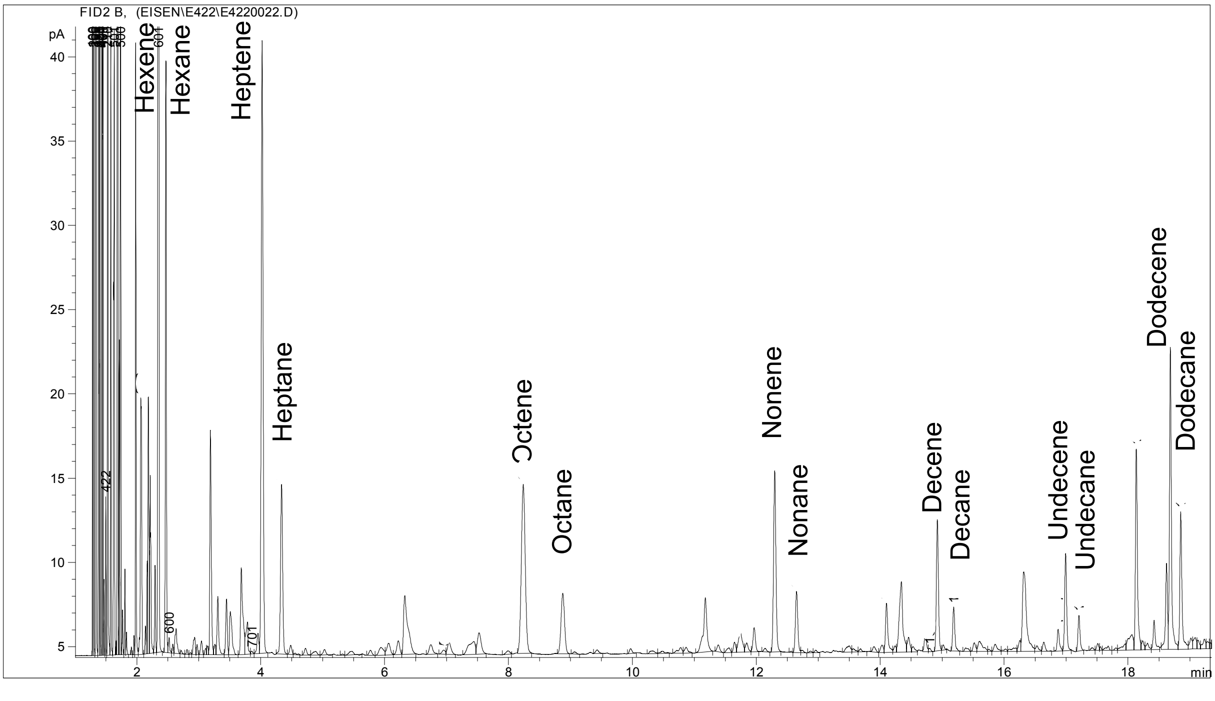

Fig. 12.2: Typical chromatogram of the organic compounds in the gas phase with cyclopropane as reference gas (HP6890N).

Tab. 12.2: Gas chromatography specifications (HP5890).

Gas chromatograph	HP 5890 (ampoule analysis)
Detector	Flame Ionization Detector (FID)
Column	Fused Silica L = 50 m, d_i = 0.25 mm, s_{film} = 0.25 μm
Carrier gas	H_2
Sample volume	20 μl
Ampoule breaker temp.	240 °C (max. 260 °C)
Temperature program	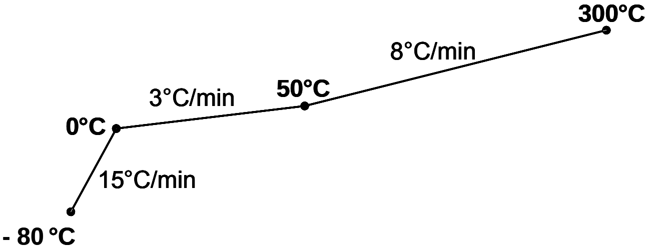
Analysis duration	60 min

Tab. 12.3: Gas chromatography specifications (HP 5890 Series II plus).

Gas chromatograph	HP 5890 Series II plus (wax analysis)
Detector	Flame Ionization Detector (FID), T = 375 °C
Column	HP-SiMDiST L =15 m, d_i = 0.530 mm, s_{film} = 0.15 μm
Carrier gas	He
Pressure	2.5 psi
Sample volume	1 μl
Temperature program	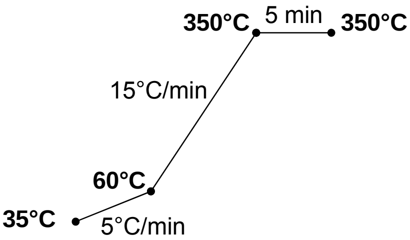
Analysis duration	30 min

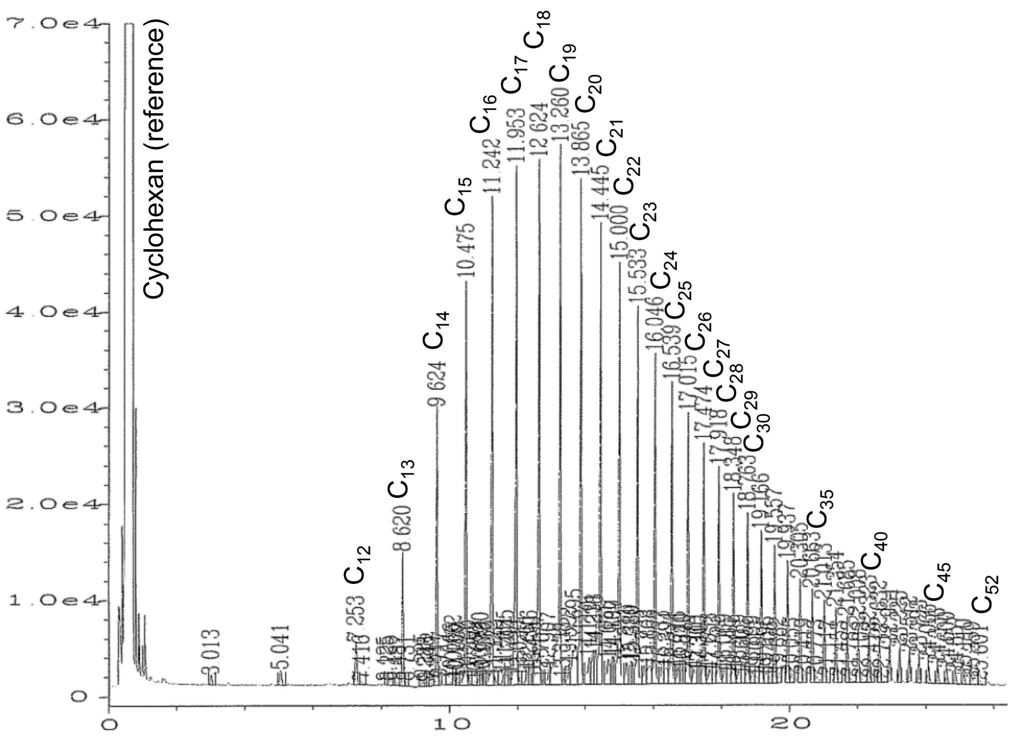

Fig. 12.3: Typical chromatogram of the organic products in the liquid phase (wax), (HP 5890 Series II Plus).

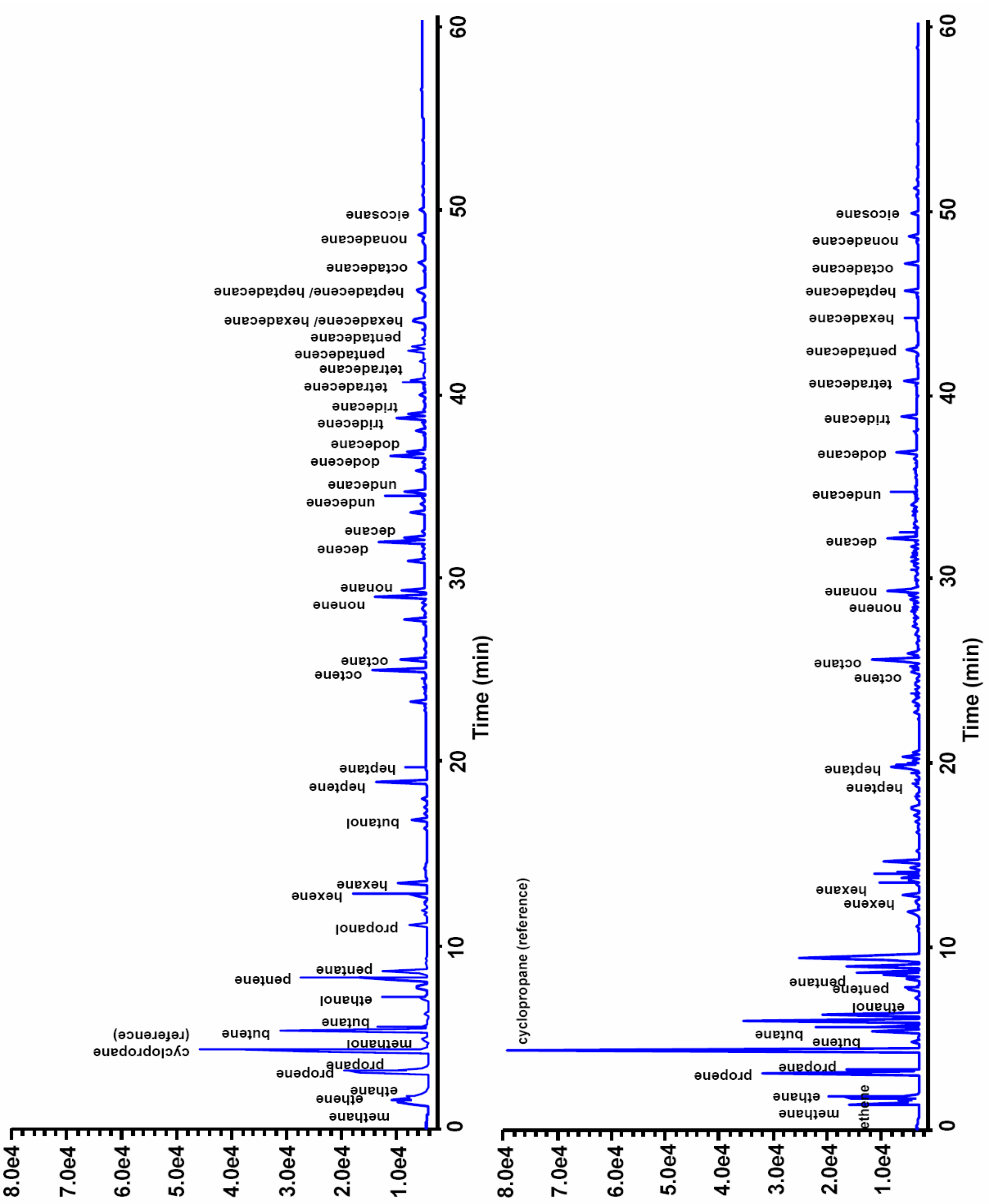

A
K-promoted Fe catalyst alone

B
K-promoted Fe + Pt/ZSM5

Fig 12.4: Example gas chromatograms from the gas phase (HP5890).

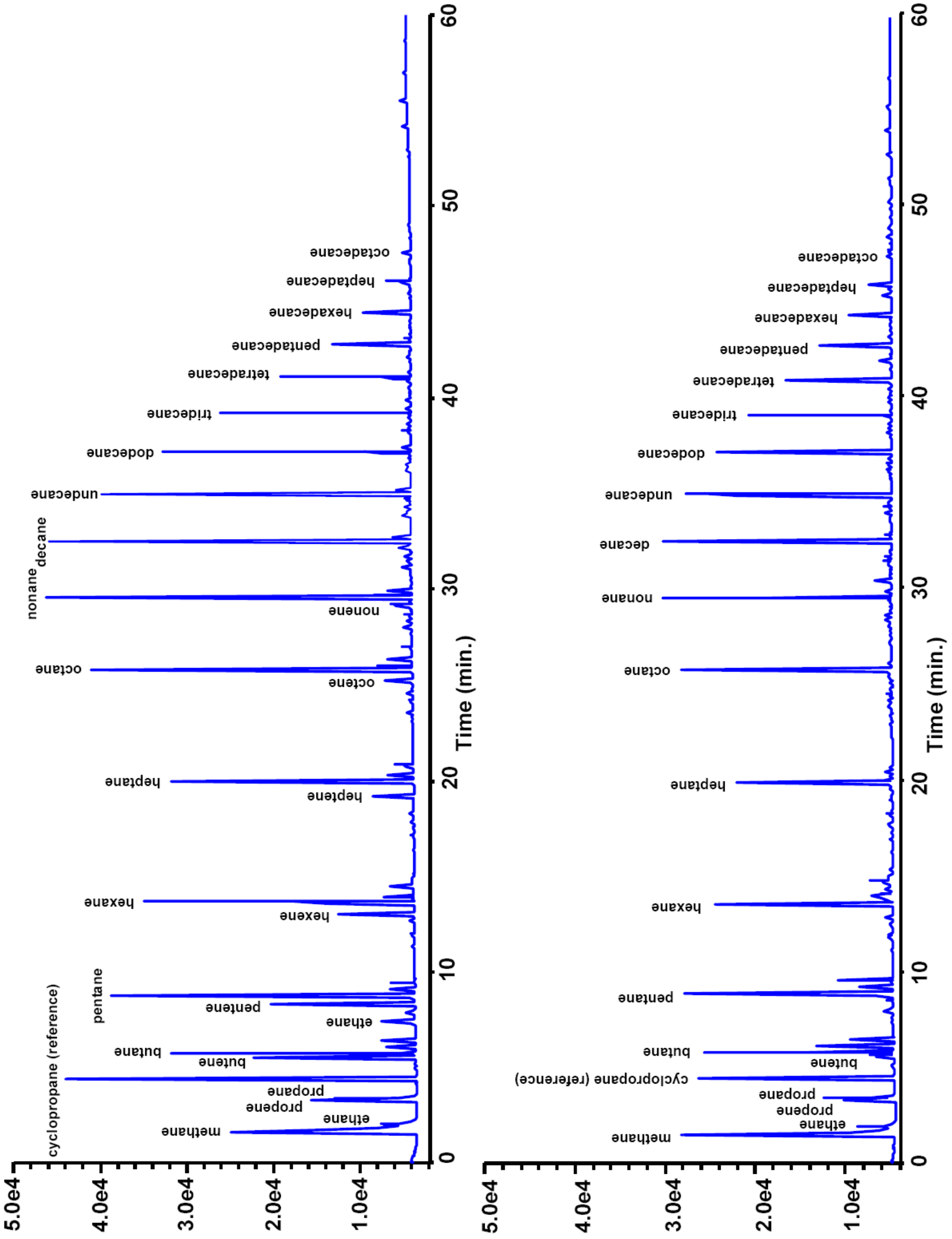

A
Co/Al_2O_3 alone

B
Co/Al_2O_3 + Pt/ZSM5 (dual layer)

Fig 12.5: Example gas chromatograms from the gas phase (HP5890).

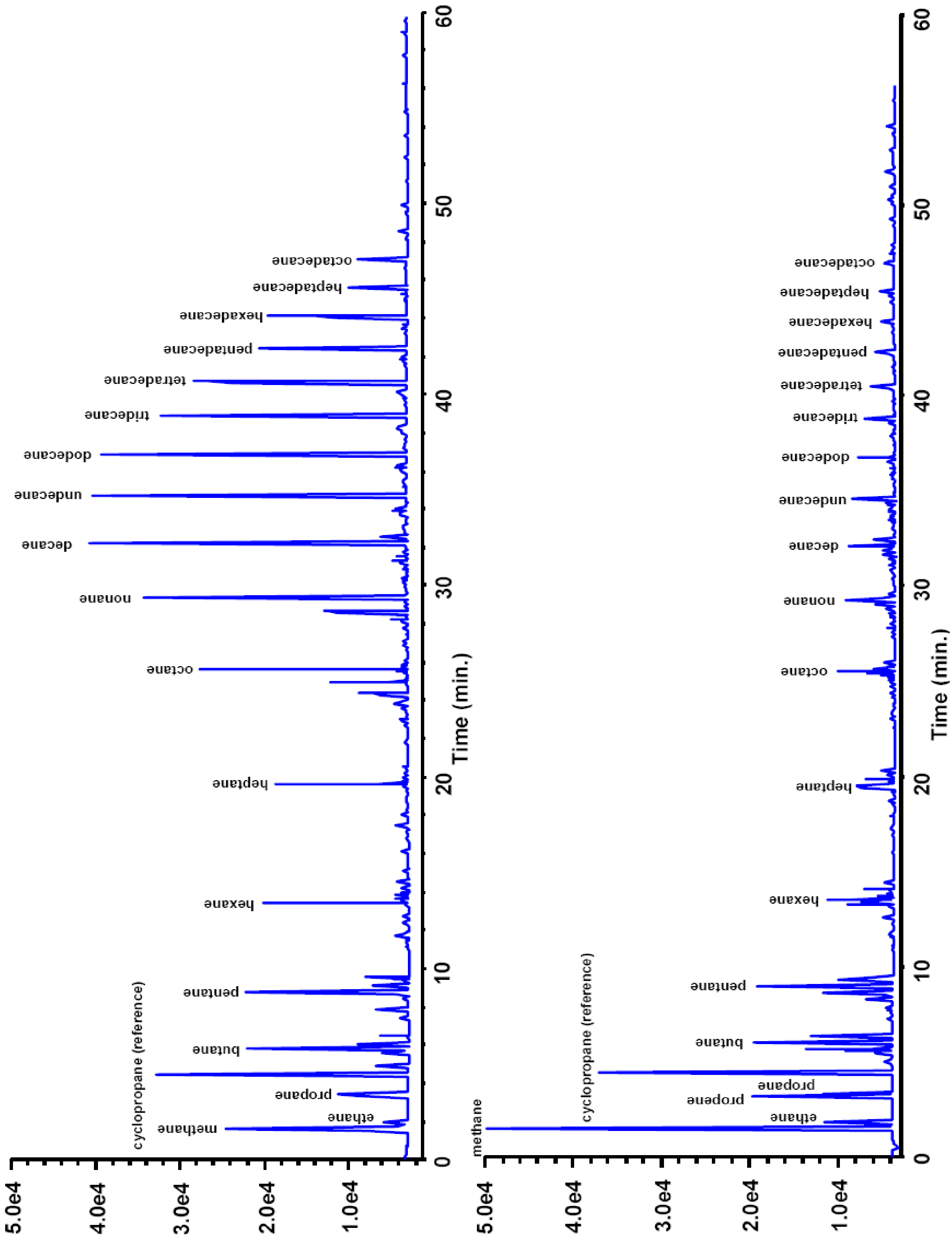

A
Co/Al_2O_3 + Pt/Beta (dual layer)

B
Co/Al_2O_3 + Pt/ZSM5 (physical mixture)

Fig 12.6: Example gas chromatograms from the gas phase (HP5890).

12.2 FID factors for oxygenates compounds

Tab. 12.4: Factor for oxygenate compounds calculated with the method described in Kaiser 1969.

Oxygenate compound	f_i
Methanol	1.82
Ethanol	1.29
Propanol	1.18

12.3 Additional experimental results

12.3.1 Ethene/propene reactions on Pt/ZSM-5

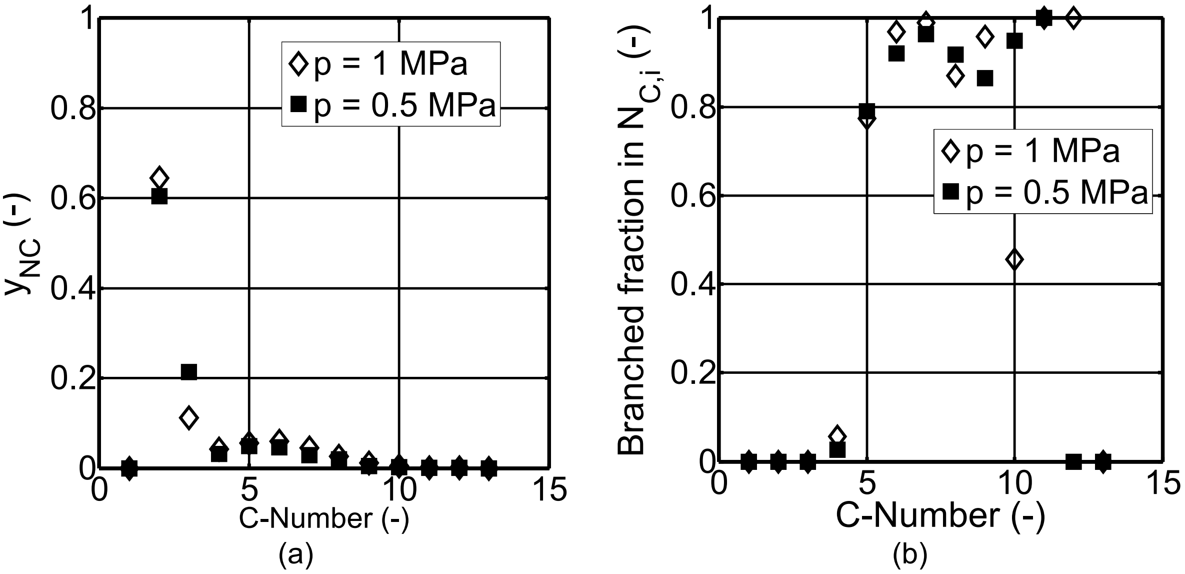

Fig. 12.7: Effect of pressure on the product distribution. (a) Molar fraction, (b) branched fraction in $N_{C,i}$. Catalyst: Pt/ZSM-5. Feed: $C_2H_4 + C_3H_6 + N_2 + H_2 + CO$. Reaction conditions: T = 250 °C, τ_{mod} = 2000 kg·s/m^3. Other reaction conditions see Table 5.8.

12.3.2 Ethene/propene reactions on Pt/Beta

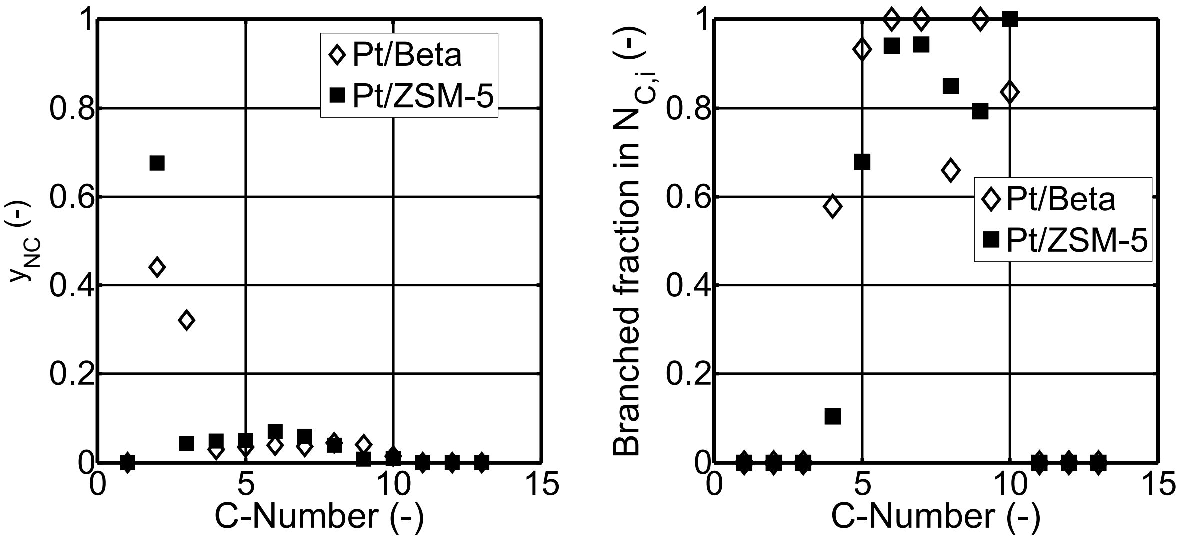

(a) (b)

Fig. 12.8: Comparison of the product distribution on Pt/ZSM-5 and Pt/Beta catalysts. (a) Molar fraction, (b) branched fraction in $N_{C,i}$. Feed: $C_2H_4 + C_3H_6 + N_2$. Reaction conditions: T = 250 °C, τ_{mod} = 13600 kg·s/m^3, p = 1 MPa. Other reaction conditions see Table 5.8.

12.3.3 Fischer-Tropsch Synthesis

Co/Al_2O_3 catalyst

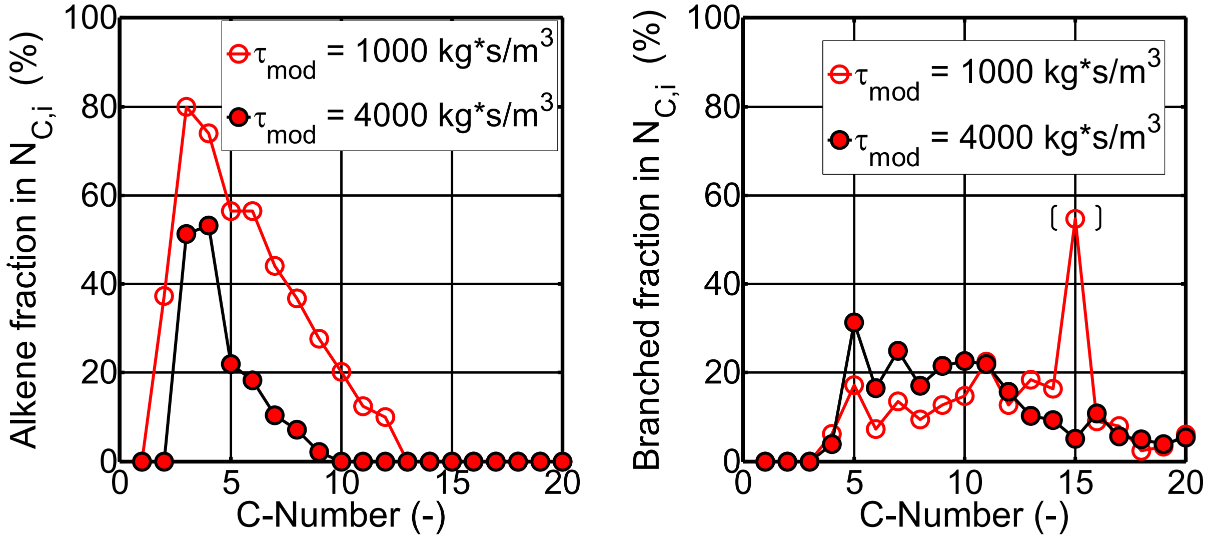

(a) (b)

Fig. 12.9: Effect of residence time on alkenes (a) and branched hydrocarbons (b) content in carbon-number fractions in the gas phase. Catalyst: Co/Al_2O_3. Reaction conditions: T = 230 °C, $(p_{H2}/p_{CO})_{in}$ = 2, p = 1 MPa. (○) Fig. 12.9b: most probably an analysis error.

K-promoted Fe catalyst

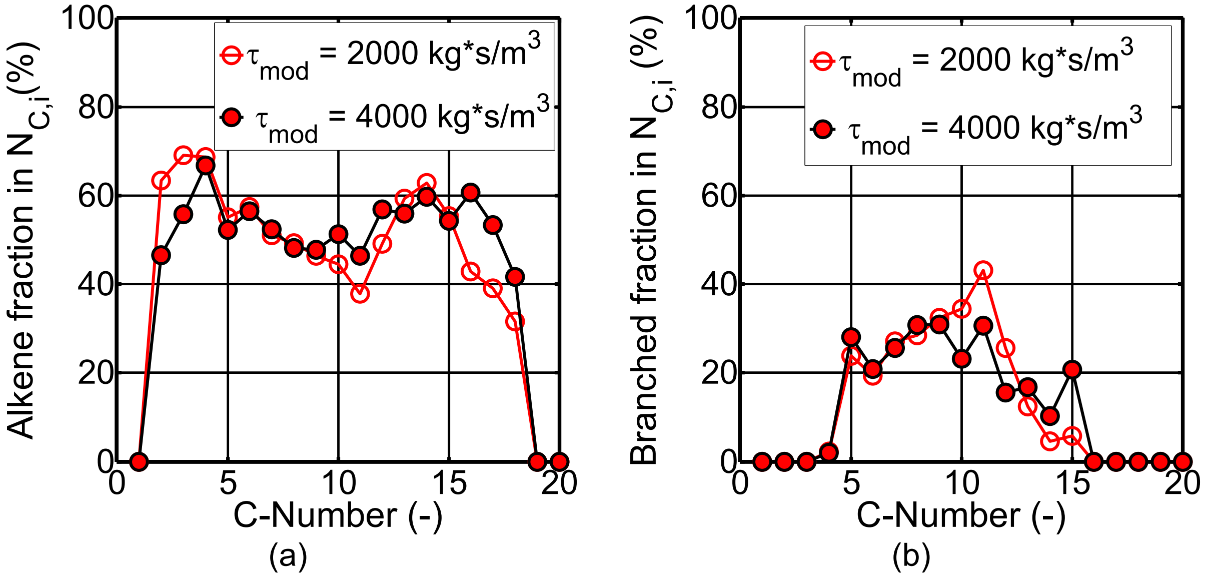

Fig. 12.10: Effect of residence time on alkenes (a) and branched hydrocarbons (b) content in carbon-number fractions in the gas phase. Catalyst: K-promoted Fe. Reaction conditions: T = 250 °C, $(p_{H2}/p_{CO})_{in}$ = 2, p = 1 MPa.

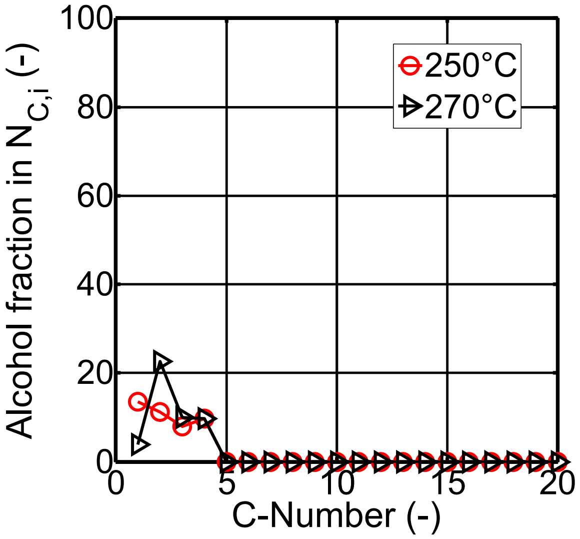

Fig. 12.11: Effect of temperature on alcohol content in carbon-number fractions in the gas phase. Catalyst: K-promoted Fe. Reaction conditions: $(p_{H2}/p_{CO})_{in}$ = 2, p = 1 MPa, τ_{mod} = 4000 kg·s/m^3.

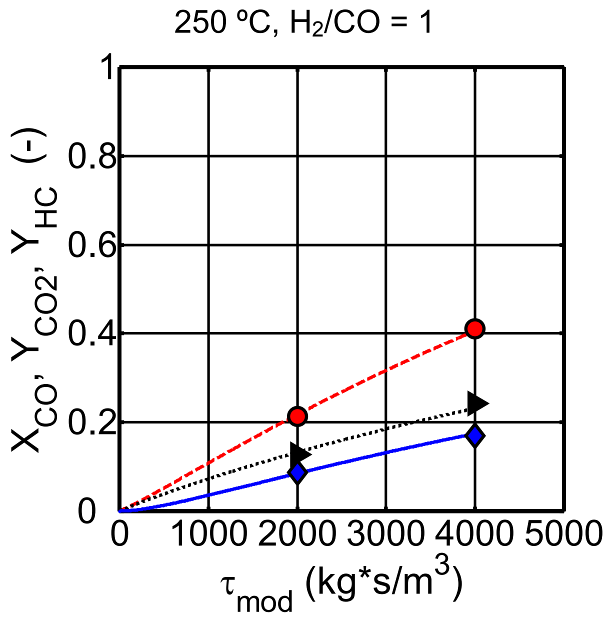

(a)

Fig. 12.12: CO conversion (diamonds, solid curve), CO_2 (circles, dashed curve) and hydrocarbons (triangles, dotted curve) yield. Catalyst: K-promoted Fe. Points: experimental, curves: calculated with kinetic model (Tab. 6.2, Eq. 5.31-5.32). p = 1 MPa.

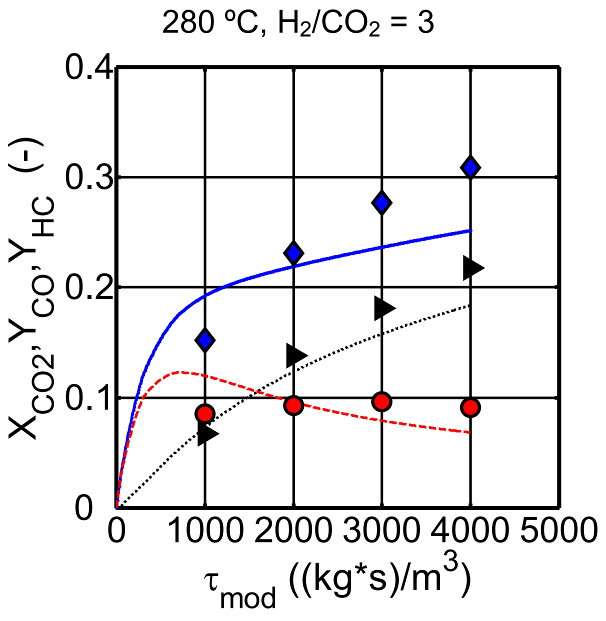

(b)

Fig. 12.13: CO_2 conversion (diamonds, solid curve), CO (circles, dashed curve) and hydrocarbons (triangles, dotted curve) yield. Catalyst: K-promoted Fe. Points: experimental, curves: calculated with kinetic model (Tab. 6.2, Eq. 5.31-5.32). p = 1 MPa.

12.3.4 Combination FT and bifunctional catalysts

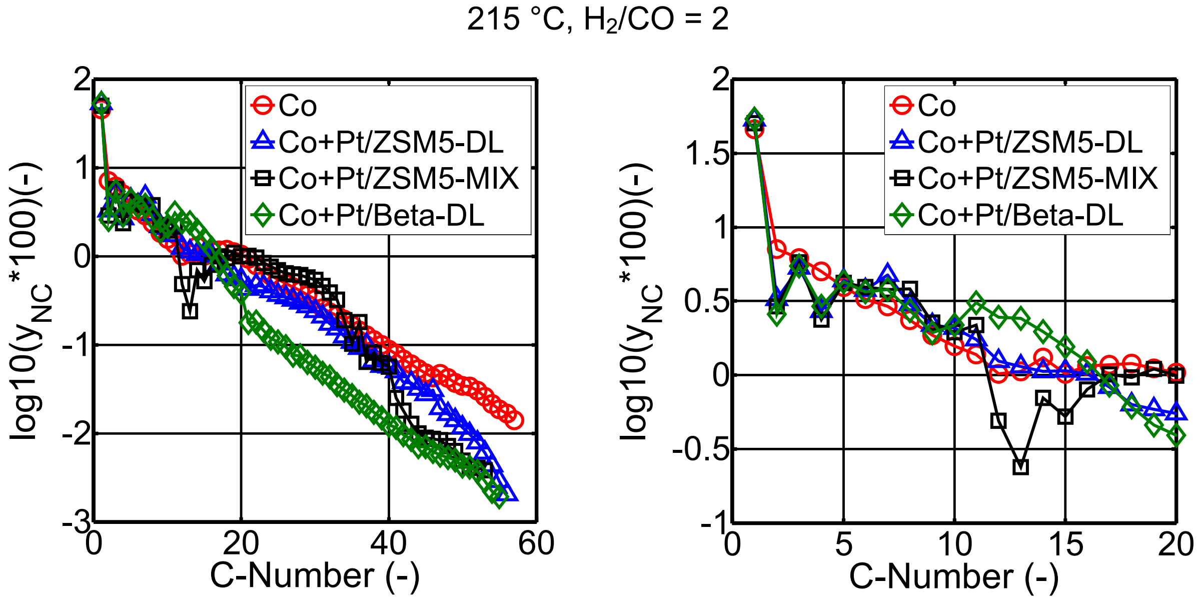

(a) (b)

Fig. 12.14: Effect of temperature, bifunctional catalyst and catalyst-bed configuration on hydrocarbons distribution. Catalysts: Co/Al_2O_3, Pt/ZSM-5, Pt/Beta. Reaction conditions: p = 1 MPa, τ_{mod} = 4000 kg·s/m^3 (referred to $m_{FT\text{-}cat.}$), $m_{HP\text{-}cat.}$ / $m_{FT\text{-}cat.}$ = 0.75.

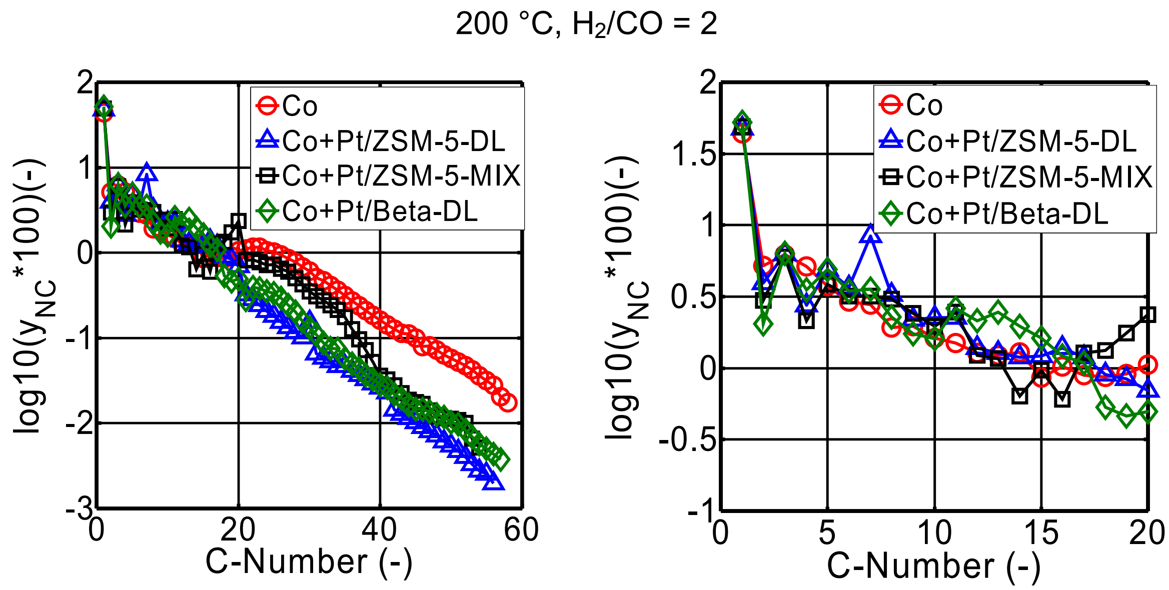

(a) (b)

Fig. 12.15: Effect of temperature, bifunctional catalyst and catalyst-bed configuration on hydrocarbons distribution. Catalysts: Co/Al_2O_3, Pt/ZSM-5, Pt/Beta. Reaction conditions: p = 1 MPa, τ_{mod} = 4000 kg·s/m^3 (referred to $m_{FT\text{-}cat.}$), $m_{HP\text{-}cat.}$ / $m_{FT\text{-}cat.}$ = 0.75.

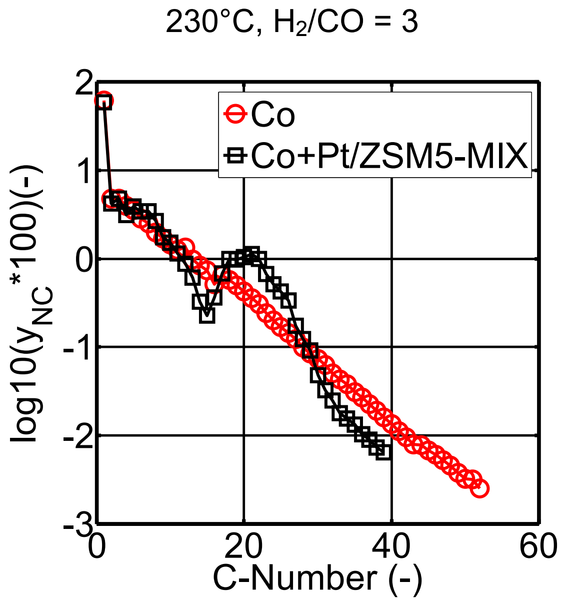

Fig. 12.16: Effect bifunctional catalyst on hydrocarbons distribution. Catalysts: Co/Al_2O_3, Pt/ZSM-5. Reaction conditions: T = 230 °C, τ_{mod} = 4000 kg·s/m^3 (referred to $m_{FT\text{-}cat.}$), $m_{HP\text{-}cat.}$ / $m_{FT\text{-}cat.}$ = 0.75, p = 1 MPa.

12.4 Analysis of Pt/ZSM-5 and Pt/Beta after one month on stream

Pt/ZSM-5 and Pt/Beta catalysts after one month on stream were analysed by means of gas chromatography in order to know if some hydrocarbons have deposited in the catalyst (see Chapter 6.3.2).

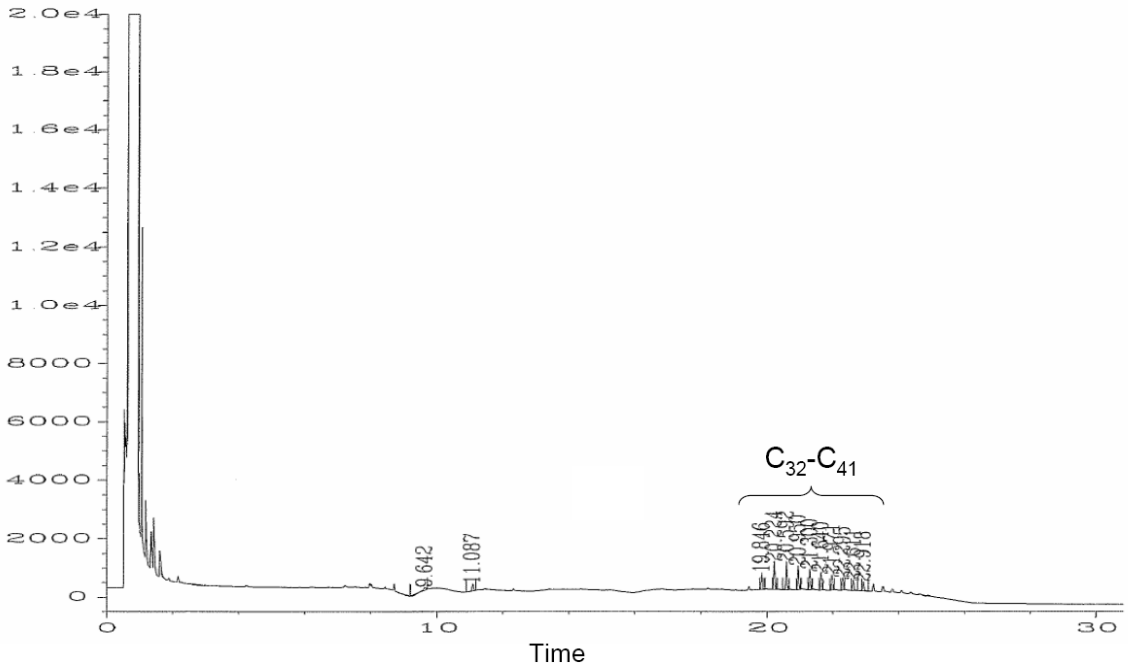

Fig. 12.17: Gas chromatogram (HP5890 Series II plus) of the extracted hydrocarbons deposited in the Pt/Beta catalyst after one month on stream.

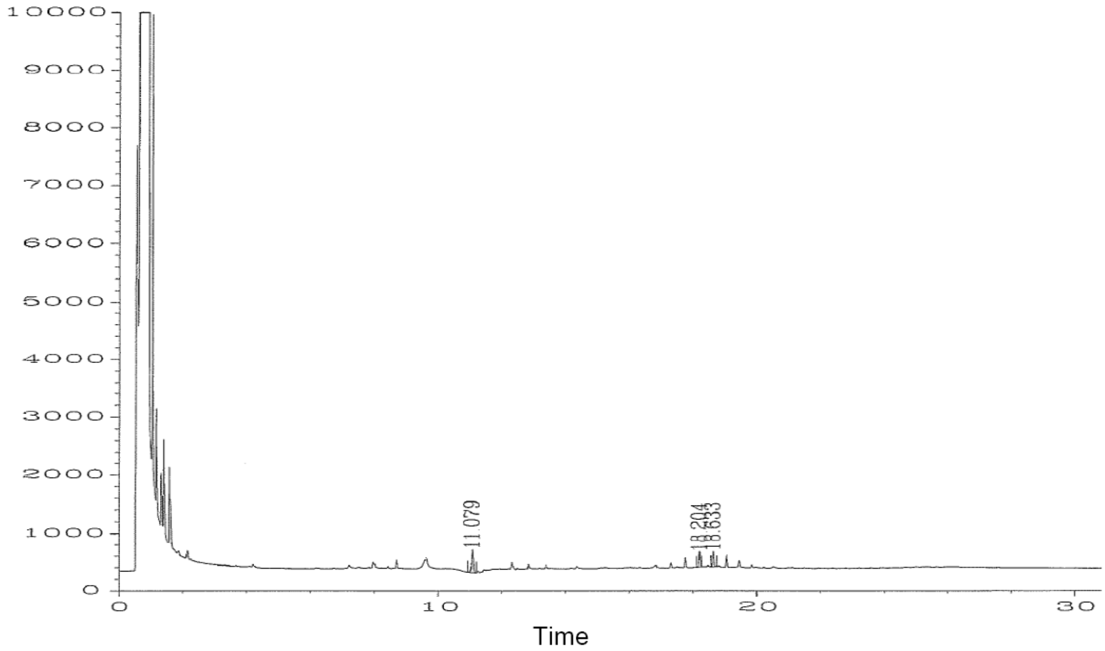

Fig. 12.18: Gas chromatogram (HP5890 Series II plus) of the extracted hydrocarbons deposited in the Pt/ZSM-5 catalyst after one month on stream.

Thermal gravimetrical analyses of Pt/Beta catalyst were carried out by Sachtleben Chemie GmbH with Thermoanalyse STA449 Jupiter (Netzsch GmbH) under synthetic air or nitrogen atmosphere with the following procedure:

Weighted sample : 115 mg
Temperature program : 30-1200 °C
Heating rate : 5 K/min

The curve progression of Figure 12.19 can be attributed to the following effects:

- 30-145 °C : humidity
- 145-510 °C : -9.5 % most probably due to oxidation or thermal decomposition of organic C
- 510-1200 °C: thermal decomposition of inorganic C

The curve progression of the fresh Pt/Beta catalyst in Figure 12.20 was attributed to the bounded humidity.

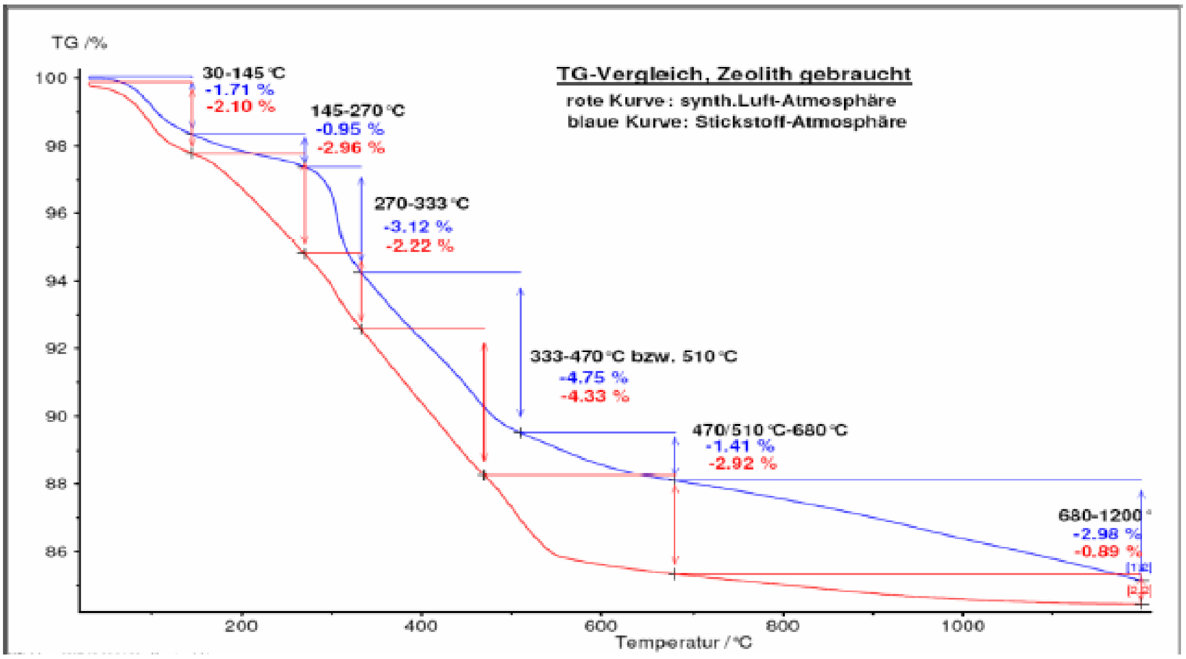

Fig. 12.19: Thermal gravimetrical analysis of Pt/Beta catalyst after one month on stream. Measurements under nitrogen and synthetic air atmosphere by Sachtleben Chemie GmbH.

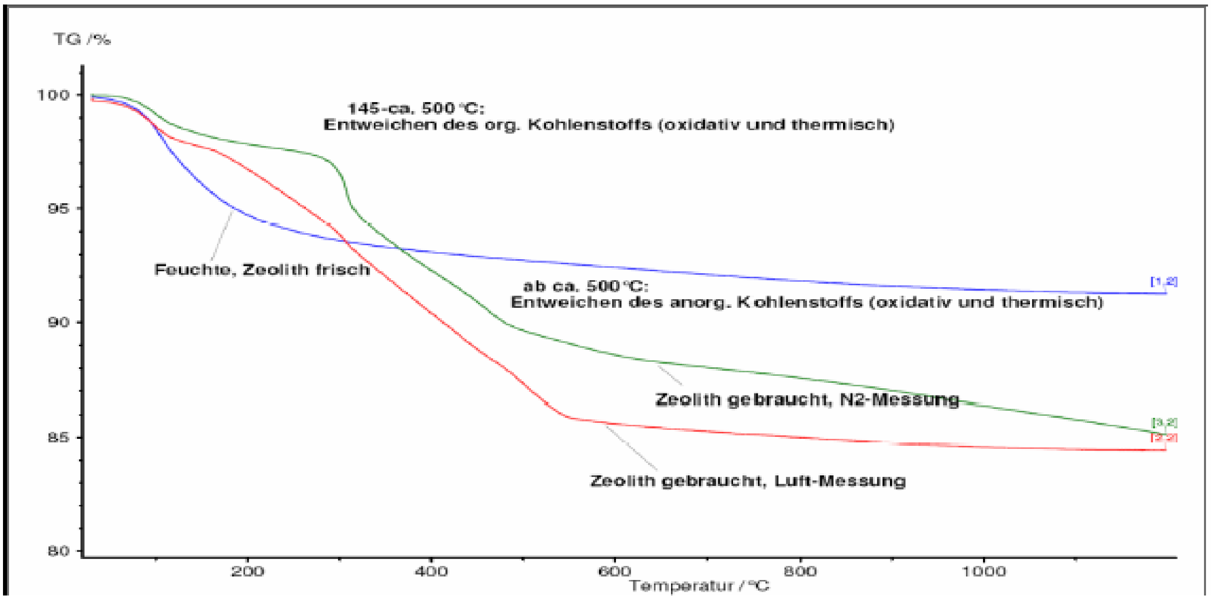

Fig. 12.20: Thermal gravimetrical analysis of Pt/Beta catalyst after one month on stream and of fresh Pt/Beta catalyst. Measurements under nitrogen and synthetic air atmosphere by Sachtleben Chemie GmbH.

12.5 Temperature-programmed desorption (TPD) - Method

Tab. 12.5: Temperature-programmed desorption (TPD) - Method. Measurements carried out at the Institut für Chemische Verfahrenstechnik, Universität Karlsruhe (TH), (see Chapter 5.2).

Process	Gas (-)	Volume flow (ml/min)	T_{End} (°C)	Heating rate (°C/min)	t (min)
Heating	He (5.0)	25	500	10	10
Cooling down	He (5.0)	25	50	10	-
NH_3-Sorption	10 % NH_3 in He	25	50	-	60
Cleaning	He (5.0)	25	50	-	60
NH_3-Desorption	He (5.0)	25	600	15	10
Cooling down	He (5.0)	25	-	-	-

12.6 Complementary calculations for the plug-flow reactor model

For the kinetic analysis of the experimental data, the assumption of an isothermal ideal plug-flow reactor (PFR) was made. In the following, criteria for this assumption are discussed.

Axial dispersion

Axial transport must be slower than the convective transport in order to be neglected. The Bodenstein number relates the convective and the dispersion velocity (Eq. 12.1). Fitzer et al. 1995 reported that for Bo > 50 ideal plug-flow behaviour can be assumed (Baerns et al. 1987 reported Bo > 100).

$$Bo_{ax} = \frac{u \cdot L_S}{D_{ax}} \tag{12.1}$$

Using the material balance equation presented in Equation 5.27 and defining the following dimensionless parameters: $z^* = z/L$ and $\theta = t/\tau = t \cdot u/L_s$ (Baerns et al. 1987), Equation 12.3 is obtained by assuming constant gas velocity along the reactor length.

$$\frac{\partial C_i}{\partial t} = -\frac{\partial (C_i \cdot u_g)}{\partial z} + D_i \cdot \frac{\partial^2 C_i}{\partial z^2} + \rho_S / \varepsilon \cdot \sum_{j=1}^{N} \nu_{i,j} \cdot r_j \tag{12.2}$$

$$\frac{\partial C_i}{\partial \theta} = -\frac{\partial C_i}{\partial z^*} + \underbrace{\frac{D_i}{u \cdot L_S}}_{1/Bo} \cdot \frac{\partial^2 C_i}{\partial z^{*2}} + \frac{L_S}{u} \rho_S / \varepsilon \cdot \sum_{j=1}^{N} \nu_{i,j} \cdot r_j \tag{12.3}$$

From Equation 12.3 it can be deduced that for high Bodenstein numbers the diffusive transport is very small compared to the convective transport and, therefore, can be neglected. Baerns et al. 1987 indicated that for gas flows in a fixed-bed reactor and taking in account the catalyst layer, the Péclet number can be defined as follows:

$$Pe_{ax} = \frac{\bar{u} \cdot d_p}{D_{ax}} = \left(\frac{0.3}{\mathrm{Re}_p \cdot Sc} + \frac{0.5}{1 + 3.8/(\mathrm{Re}_p \cdot Sc)} \right)^{-1} \tag{12.4}$$

Equation 12.4 is valid for $0.008 < \mathrm{Re}_p < 400$ and $0.28 < Sc < 2.2$, with Reynolds and Schmidt numbers defined as:

$$\mathrm{Re}_p = \frac{\bar{u} \cdot d_p}{\nu_{H2,CO}} \tag{12.5}$$

$$Sc = \frac{\nu_{H2,CO}}{D_{H2,CO}} \tag{12.6}$$

Then, the Bodenstein number can be calculated as:

$$Bo_{ax} = Pe_{ax} \cdot \frac{L_S}{d_p} \tag{12.7}$$

The minimal flow velocity at reactor inlet at reaction conditions (p = 1 MPa, T = 250 °C) applied in this study was 0.0025 m/s. The minimal velocity was calculated considering the lowest volume flow used (30 ml n/min) and a cross-sectional area of $3.8 \cdot 10^{-5}$ m^2 (taking in account the thermocouple guide tube). For a maximal catalyst layer length of 0.2 m (including dilution with SiC particles) and particle diameter of 100 μm, the Bodenstein number is 84 (> 50).

Wall effects

The porosity of the catalyst bed could decrease close to the reactor walls and results in a local higher velocity. Emig et al. 1997 presented a criterion that must be satisfied in order to neglect the wall effects:

$$\frac{d_{reactor}}{d_p} > 10 \tag{12.8}$$

For an effective reactor diameter of 0.002 m (taking into account the thermocouple guide tube) and particle diameter between 100 and 200 μm (taking in account the SiC particle size) the wall effects can be neglected.

Heat transfer

The heat transfer in a catalyst bed -assuming a gas-solid system- is composed of the heat transfer between the gas phase and the catalyst surface and the heat transfer inside the catalyst particle. The external-heat transfer coefficient (h_{ext}) is a function of the Nusselt number and the ratio between thermal conductivity and diameter of the catalyst particle.

$$h_{ext} = Nu_S \cdot \frac{\lambda_{H2/CO}}{d_p} \tag{12.9}$$

$$Nu_S = (1 + 1.5 \cdot (1 - \psi)) \cdot Nu_{sphere} \tag{12.10}$$

$$Nu_{sphere} = Nu_{\min} + \sqrt{Nu^2{}_{lam} + Nu_{tur}{}^2} \tag{12.11}$$

$$Nu_{\min} = 2 \tag{12.12}$$

$$Nu_{lam} = 0.664 \cdot \mathrm{Pr}^{1/3} \cdot \mathrm{Re}^{1/2}{}_{p,S} \tag{12.13}$$

$$Nu_{tur} = \frac{0.037 \cdot \mathrm{Pr} \cdot \mathrm{Re}^{0.8}{}_{p,S}}{1 + 2.443 \cdot \mathrm{Re}_{p,S}{}^{-1} \cdot \left(\mathrm{Pr}^{2/3} - 1\right)} \tag{12.14}$$

$$\mathrm{Re}_{p,S} = \frac{\bar{u} \cdot dp}{\nu_{H2/CO} \cdot \psi} \tag{12.15}$$

$$\mathrm{Pr} = \frac{\eta_{H2/CO} \cdot c_{p,H2/CO}}{\lambda_{H2/CO}} \tag{12.16}$$

The heat-transfer coefficient is equal to:

h_{ext} = 8147 W/(m^2·K)

Heat transfer between the gas phase and the catalyst surface can be neglected if (Baerns et al. 1987):

$$\left| \frac{-\Delta H_R \cdot r_{p,eff} \cdot d_p}{h \cdot T_g} \right| < 0.3 \cdot \frac{R \cdot T_g}{E_{A,j}} \tag{12.17}$$

For the K-promoted Fe catalyst, the maximal effective FT reaction rate at reactor inlet at 250 °C is equal to 15.2 mol/(s·m^3). At this temperature, the FT reaction enthalpy is equal to -158.5 kJ/mol and the FT activation energy is equal to 92 kJ/mol. This results for h_{ext} = 8147 W/(m^2·K) and d_p = 100 μm in:

$5.64 \cdot 10^{-5} < 1.42 \cdot 10^{-2}$

which reflects the heat transfer between the gas phase and the catalyst surface can be neglected. In order to neglect the temperature gradient inside the catalyst particle, Equation 12.18 must be accomplished (Baerns et al. 1987).

$$\left| \frac{-\Delta H_R \cdot r_{p,eff} \cdot d^2{}_p}{\lambda_{cat,eff} \cdot T_s} \right| < 0.3 \cdot \frac{R \cdot T_s}{E_{A,j}} \tag{12.18}$$

Considering that the temperature at the catalyst surface is the same as that in the gas phase ($T_s = T_g$) and the effective thermal conductivity of the catalyst bed ($\lambda_{cat,\ eff}$) is equal to 0.25 W/(m·K) (Emig et al. 1997), the temperature gradient inside the catalyst particle can be neglected:

$1.84 \cdot 10^{-4} < 1.89 \cdot 10^{-1}$

For both situations considered, heat transfer is faster in the presence of a liquid phase (as in the present case of FT synthesis).

Mass transfer

With the following equation from Baerns et al. 1987, the significance of external material transport limitation can be determined:

$$\frac{k_{eff}^{\ 1} \cdot d_p^{\ 1.5}}{11 \cdot \sqrt{u \cdot D_{H2/CO}}} < 0.1 \qquad (12.19)$$

Assuming a reaction rate of first order and 0.002 kg of FT catalyst, the left side of Equation 12.19 is equal to $3.2 \cdot 10^{-5}$ (with $k_{eff} = 7.96 \cdot 10^{-2}$ s^{-1}, $d_p = 1 \cdot 10^{-4}$ m, $u = 2.54 \cdot 10^{-3}$ m/s and $D_{H2/CO} = 2.01 \cdot 10^{-5}$ m^2/s). For that reason the external mass transport can be neglected.

The internal mass transport can be neglected if the following equation is accomplished:

$$\frac{k_{eff}^{\ 1} \cdot d_p^{\ 2}}{4 \cdot D_{CO,eff}} < 1 \qquad (12.20)$$

The diffusion coefficient for H_2 is expected to be higher than that of CO. For that reason, the effective diffusion coefficient for CO is used. It can be calculated by means of the CO diffusion coefficient in the pores ($D_{CO,pore}$), the catalyst porosity (ε_p) and the labyrinth factor or tortuosity (χ_p):

$$D_{CO,eff} = D_{CO,pore} \cdot \chi_p \cdot \varepsilon_p \qquad (12.21)$$

The CO diffusion coefficient in the pores (here assumed for a gas phase) is composed of the CO Knudsen diffusion coefficient and the binary diffusion coefficient ($D_{H2/CO}$):

$$D_{CO,pore} = \left(\frac{1}{D_{CO,Kn}} + \frac{1}{D_{H2,CO}} \right)^{-1} \qquad (12.22)$$

The Knudsen diffusion of CO can be calculated with the following equation (d_{pore} in cm and $D_{CO,Kn}$ in cm^2/s, Baerns et al. 1987):

$$D_{CO,Kn} = 4850 \cdot d_{pore} \cdot \sqrt{\frac{T}{M_{CO}}} \tag{12.23}$$

At 250 °C assuming a pore diameter of $8 \cdot 10^{-9}$ m (see Tab. 5.1), a porosity of 0.25 and an estimated labyrinth factor of 0.3, the Knudsen diffusion coefficient ($D_{CO,Kn}$) is equal to $1.68 \cdot 10^{-6}$ m^2/s and the effective pore diffusion coefficient ($D_{CO,eff}$) is equal to $1.21 \cdot 10^{-7}$ m^2/s (with $D_{CO,pore} = 1.54 \cdot 10^{-6}$ m^2/s). Then, the left side of Equation 12.20 is equal to $1.71 \cdot 10^{-3}$ which indicates that the pore diffusion can be neglected.

The Thiele modulus (Φ) can be calculated with Equation 12.24 and is equal to $4.14 \cdot 10^{-2}$. Assuming a spherical geometry for the catalyst particles, the effectiveness factor (η) can be calculated with Equation 12.25, and as expected its value is closed to 1.

$$\Phi = r_p \cdot \sqrt{\frac{k_{eff}^{\ 1}}{D_{CO,eff}}} \tag{12.24}$$

$$\eta = \frac{3}{\Phi} \cdot \left(\frac{1}{\tanh(\Phi)} - \frac{1}{\Phi} \right) \tag{12.25}$$

Under typical low temperature FT reaction conditions the major part of the hydrocarbon product will be in the liquid phase. Post et al. 1989 reported that the molecular diffusivity of hydrogen in the liquid phase in the catalyst pores is in the range $0.9 \cdot 10^{-9}$-$1.8 \cdot 10^{-9}$ m^2/s. Then, the left side of Equation 12.20 could be in some cases larger than 1 and the internal transport limitation could be significant.

Tab. 12.6: Characteristic property values and calculated dimensionless numbers for the axial dispersion, heat and mass transport (VDI-Wärmeatlas 1984, Baerns et al. 1987). Data calculated at 250 °C, 1 MPa, $(p_{H2}/p_{CO})_{in} = 2$.

Parameter	Symbol	Value	Units
Binary diffusion coefficient	$D_{H2/CO}$	$2.01 \cdot 10^{-5}$	m^2/s
Kinematic viscosity	$\nu_{H2/CO}$	$7.10 \cdot 10^{-6}$	m^2/s
Dynamic viscosity	$\eta_{H2/CO}$	$1.75 \cdot 10^{-5}$	$N \cdot s/m^2$
Thermal conductivity	$\lambda_{H2/CO}$	$1.96 \cdot 10^{-1}$	$W/(m \cdot K)$
Maximal FT reaction rate at reactor inlet	$r_{FT,0,V,max}$	15.2	$mol/(s \cdot m^3)$
Reynolds number (particle)	Re_p	$3.58 \cdot 10^{-2}$	(-)
Schmidt number	Sc	$3.53 \cdot 10^{-1}$	(-)
Reynolds number (catalyst bed)	$Re_{p,S}$	$8.94 \cdot 10^{-2}$	(-)
Prandtl number	Pr	$8.97 \cdot 10^{-1}$	(-)
Nusselt number (catalyst bed)	Nu_S	4.15	(-)

12.7 Additional kinetic model results

This chapter includes calculated and experimental molar fraction of the inorganic compounds and CH_4 for the dual-layer configuration with Co/Al_2O_3 + Pt/ZSM-5 catalysts, and the calculated and experimental molar fraction of both organic and inorganic compounds for the dual-layer configuration with Fe + Pt/ZSM-5 catalysts.

12.7.1 Dual layer: Co/Al_2O_3 + Pt/ZSM-5

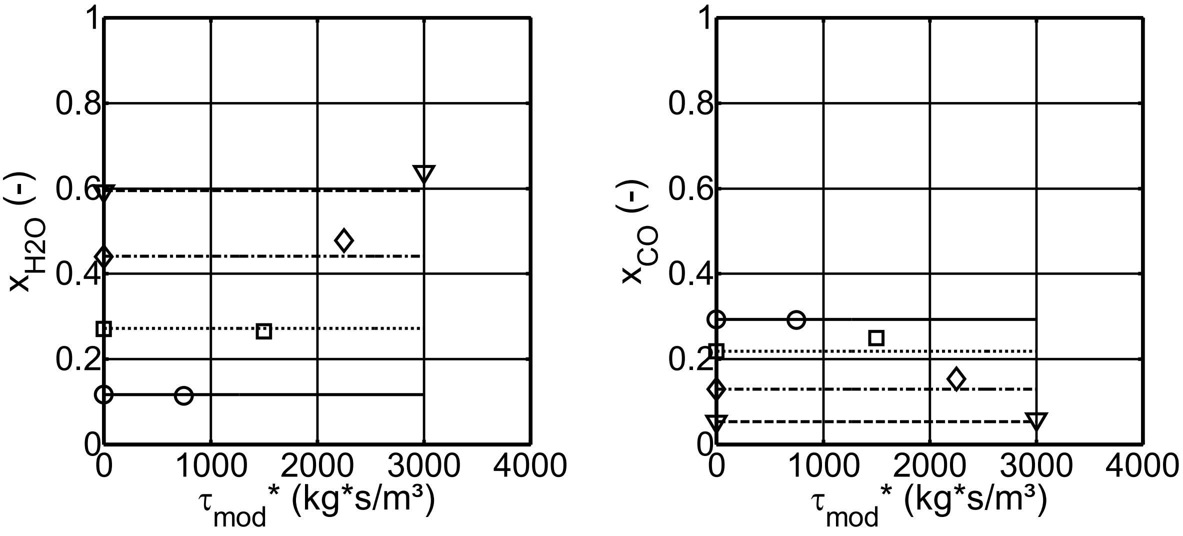

(a) (b)

Fig. 12.21: Calculated and experimental molar fractions (curves, symbols) of H_2O (a) and CO (b) in Pt/ZSM-5 catalyst layer below the Co/Al_2O_3 catalyst layer (dual-layer configuration), τ_{mod} = 4000 (triangles), 3000 (rhombus), 2000 (squares) and 1000 (circles) kg·s/m^3. T = 230 °C, p = 1 MPa, $(p_{H2}/p_{CO})_{in}$ = 2. Kinetics: Tab. 7.3, Eq. 7.2-7.4.

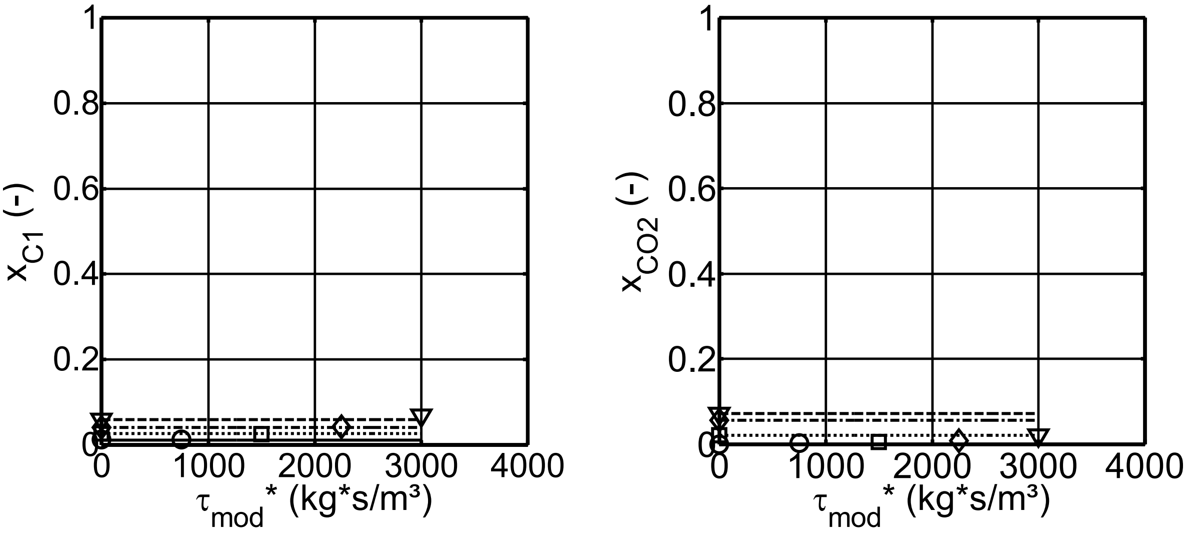

(a) (b)

Fig. 12.22: Calculated and experimental molar fractions (curves, symbols) of CH_4 (a) and CO_2 (b) in Pt/ZSM-5 catalyst layer below the Co/Al_2O_3 catalyst layer (dual-layer configuration). Reaction conditions and kinetics: see Fig. 12.21.

12.7.2 Dual layer: K-promoted Fe + Pt/ZSM-5

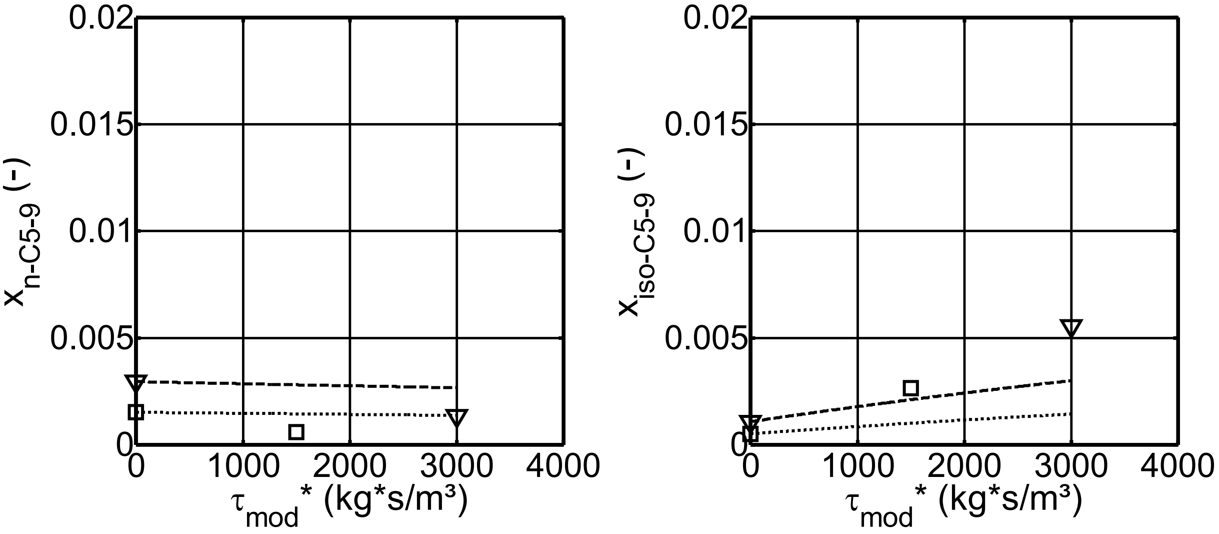

(a) (b)

Fig. 12.23: Calculated and experimental molar fractions (curves, symbols) of the n-$C_{5\text{-}9}$ (a) and iso-$C_{5\text{-}9}$ (b) fractions in Pt/ZSM-5 catalyst layer below the K-promoted Fe catalyst layer (dual-layer configuration). Reaction conditions and kinetics: see Fig. 12.21.

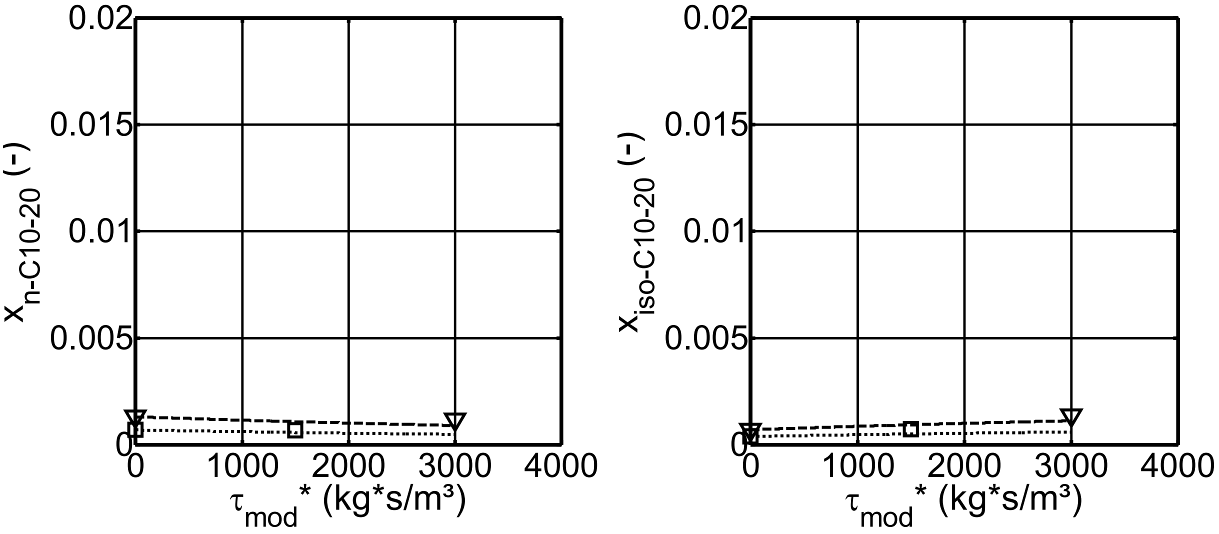

(a) (b)

Fig. 12.24: Calculated and experimental molar fractions (curves, symbols) of the n-$C_{10\text{-}20}$ (a) and iso-$C_{10\text{-}20}$ (b) fractions in Pt/ZSM-5 catalyst layer below the K-promoted Fe catalyst layer (dual- layer configuration). Reaction conditions and kinetics: see Fig. 12.21.

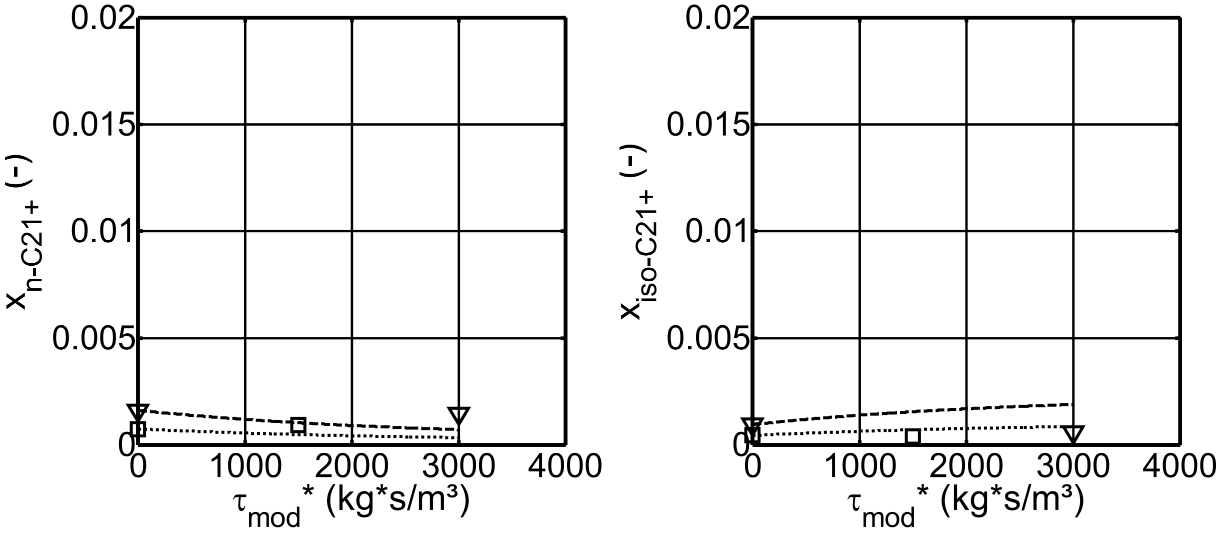

(a) (b)

Fig. 12.25: Calculated and experimental molar fractions (curves, symbols) of the n-C_{21+} (a) and iso-C_{21+} (b) fractions in Pt/ZSM-5 catalyst layer below the K-promoted Fe catalyst layer (dual-layer configuration). Reaction conditions and kinetics: see Fig. 12.21.

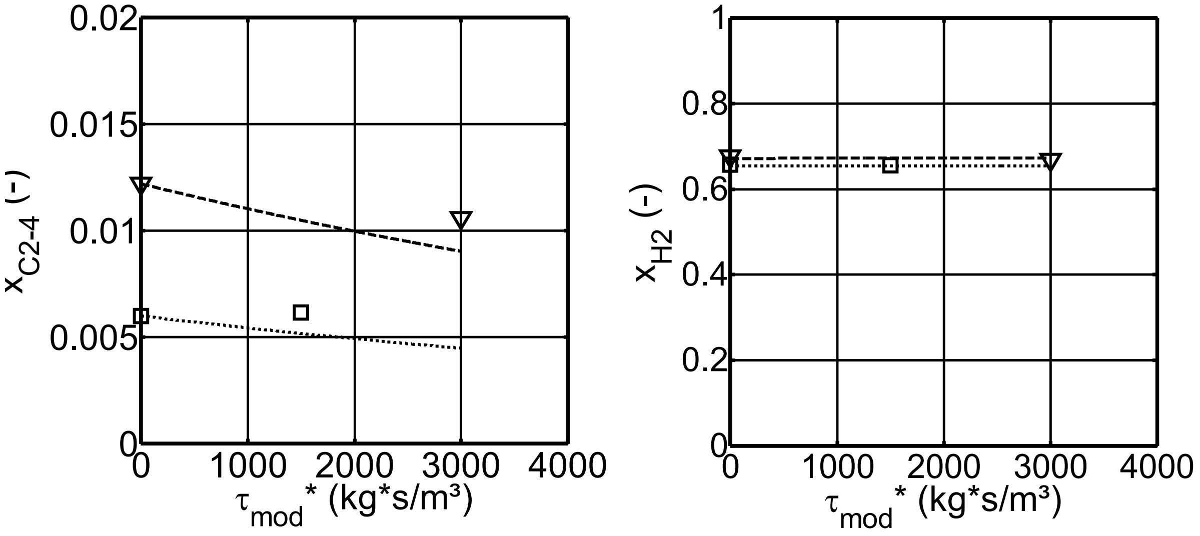

(a) (b)

Fig. 12.26: Calculated and experimental molar fractions (curves, symbols) of the $C_{2\text{-}4}$ fraction (a) and H_2 (b) in Pt/ZSM-5 catalyst layer below the K-promoted Fe catalyst layer (dual-layer configuration). Reaction conditions and kinetics: see Fig. 12.21.

12.7.3 Stoichiometric coefficients

Tab. 12.7: Example of calculation scheme of stoichiometric coefficients for the C_{21+} fraction ($\nu_{\geq 21/j}$) assuming that all molecules are produced with the same probability (Eq. 7.1).

	C-number of cracking molecules														$\upsilon_{21+/i}$
C-Number	**8**	**9**	**10**	**11**	**...**	**20**	**21**	**22**	**23**	**24**	**...**	**200**		in	Stoichiometric coefficients
1															
2															
3															
4	1,00	0,50	0,33	0,25		0,077	0,071	0,067	0,063	0,059		0,005	**C2-4**	0	0,01
5		0,50	0,33	0,25		0,077	0,071	0,067	0,063	0,059		0,005			
6			0,33	0,25		0,077	0,071	0,067	0,063	0,059		0,005			
7				0,25		0,077	0,071	0,067	0,063	0,059		0,005			
8						0,077	0,071	0,067	0,063	0,059		0,005			
9						0,077	0,071	0,067	0,063	0,059		0,005	**C5-9**	0	0,07
10						0,077	0,071	0,067	0,063	0,059		0,005			
11						0,077	0,071	0,067	0,063	0,059		0,005			
12						0,077	0,071	0,067	0,063	0,059		0,005			
13						0,077	0,071	0,067	0,063	0,059		0,005			
14						0,077	0,071	0,067	0,063	0,059		0,005			
15						0,077	0,071	0,067	0,063	0,059		0,005	**C10-14**	0	0,07
16						0,077	0,071	0,067	0,063	0,059		0,005			
17							0,071	0,067	0,063	0,059		0,005			
18								0,067	0,063	0,059		0,005			
19									0,063	0,059		0,005			
20										0,059		0,005	**C15-20**	0	0,09
21												0,005			
22												0,005			
23												0,005			
24												0,005			
25												0,005			
....												**...**			
196												0,005			
197															
198															
199															
200													**C21+**	180	0,76
Sum:	1	1	1	1	**...**	1	1	1	1	1	**...**	1		180	1

12.8 Estimation of errors

An analysis of the possible sources of error is required in order to evaluate the experimental results. Possible sources of error include the measurement equipment and gas bottles used (e.g. integration of peak area by gas chromatography, mass flows, temperature controllers, composition of the reference gas N_2 with cyclopropane, etc.). These errors may affect the quantities derived from the measured data: conversion, yield, selectivity, molar fraction, reaction rates, etc. For that reason, the uncertainty of a function ($f(x_1, x_2,\ldots,x_n)$) was calculated based on the uncertainty of the independent variables (Δx_j) by using the law of error propagation. The uncertainty of a given variable is given by:

$$x_j \pm \Delta x_j \tag{12.26}$$

If the variables are uncorrelated, the uncertainty of a function f (Δ_f) can be calculated with the following equation:

$$\Delta f = \Delta f\left(x_1, x_2, \ldots, x_n, \Delta x_1, \Delta x_2, \ldots, \Delta x_n\right) = \sum_{i=1}^{n}\left(\frac{\partial f}{\partial x_i}\Delta x_i\right) \tag{12.27}$$

The uncertainty values of the most relevant variables or magnitudes are summarised in Table 12.8.

Tab. 12.8: Uncertainty of the most relevant variables or magnitudes and of the most relevant functions. Own calculations based on the law of error propagation (Eq. 12.27), with some data taken from Unruh 2006 and Riedel 2003.

Variable/Magnitude x_i	Uncertainty in % (Δx_j)	Function f	Calculated uncertainty Δ_f
$A_{i,TCD}$	2	X_{CO}, X_{CO2}	3
$A_{i,FID}$	1	Y_{CO}, Y_{CO2}	4
$y_{CPr,Ref}$	2	Y_{HC}	7
y_{N2}	2	S_{HC}	10
$\dot{n}_i$	3	Y_{wax}	14
$m_{Co\text{-}cat}$	5	r_i	11

CO or CO_2 conversion is a function of the integrated areas of CO or CO_2 and N_2 from the gas chromatography analysis (TCD). The uncertainty of the conversion of CO or CO_2 can be calculated with the following equations (see also Chapter 5.3.4):

$$X_{CO\ or\ CO2} = 1 - \frac{A_{CO\ or\ CO2,out}}{A_{N2,out}} \cdot \frac{A_{N2,in(Bypass)}}{A_{CO\ or CO2,in(Bypass)}} \tag{12.28}$$

$$\Delta X_{CO\ or\ CO2} = \sum_{A_i}^{A_n} \left| \frac{\partial X_{CO\ or\ CO2}}{\partial A_i} \cdot \Delta A_i \right| \tag{12.29}$$

The CO or CO_2 yield function is also based on the TCD analysis. Its uncertainty can be calculated with the following equations:

$$Y_{CO\ or\ CO2} = \frac{A_{CO\ or\ CO2,out}}{A_{N2,out}} \cdot \frac{A_{N2,in(Bypass)}}{A_{CO\ or CO2,in(Bypass)}} \tag{12.30}$$

$$\Delta Y_{CO\ or\ CO2} = \sum_{A_i}^{A_n} \left| \frac{\partial Y_{CO\ or\ CO2}}{\partial A_i} \cdot \Delta A_i \right| \tag{12.31}$$

The yield of an organic compound ($Y_{HC,i}$) in the gas phase is a function of the CO measured by the TCD analysis and the organic compounds measured in the FID analysis (see also Chapter 5.3.4). Its uncertainty is calculated as follows:

$$Y_{HC,i,gas\ phase} = \frac{A_{HC,i,out,FID}}{A_{C\Pr,out,FID}} \cdot \frac{A_{N2,in(Bypass)}}{A_{CO,in(Bypass)}} \cdot \frac{y_{C\Pr}}{y_{N2}} \tag{12.32}$$

$$\Delta Y_{HC,i,gas\ phase} = \sum_{A_i}^{A_n} \left| \frac{\partial Y_{HC,i,gas\ phase}}{\partial A_i} \cdot \Delta A_i \right| + \sum_{y_i}^{y_n} \left| \frac{\partial Y_{HC,i,gas\ phase}}{\partial y_i} \cdot \Delta y_i \right| \tag{12.33}$$

As explained in Chapter 5.3.4, in the liquid phase obtained from the wax trap no reference gas was present. For that reason the wax yield was determined by an overall carbon balance.

$$Y_{HC,i,wax} = X_{CO} - Y_{CO2} - Y_{HC,i,gas\,phase} \tag{12.34}$$

$$\Delta Y_{wax} = \Delta X_{CO} + \Delta Y_{CO2} + \Delta Y_{HC,i,gas\,phase} \tag{12.35}$$

The hydrocarbon selectivity ($S_{HC,i}$) uncertainty can be determined in the same way as that of hydrocarbon yield ($Y_{HC,i}$).

If the CO/CO_2-shift activity of a Co-based catalyst can be neglected the reaction rate of hydrocarbon production can be calculated with Equation 12.36 and its uncertainty with Equation 12.37:

$$r_{FT} = \frac{1}{m_{Co-cat.}} \cdot \dot{n}_{N2,in} \cdot \frac{A_{CO,in(Bypass)}}{A_{N2,in(Bypass)}} \cdot X_{CO} \tag{12.36}$$

$$\Delta r_{FT} = \left| \frac{\partial r_{FT}}{\partial m_{Co}} \cdot \Delta m_{Co} \right| + \left| \frac{\partial r_{FT}}{\partial \dot{n}_{N2,in}} \cdot \Delta \dot{n}_{N2,in} \right| + \sum_{A_i}^{A_n} \left| \frac{\partial r_{FT}}{\partial A_i} \cdot \Delta A_i \right| + \Delta X_{CO} \tag{12.37}$$

As explained in Chapter 5.3.2, the product distribution of the organic compounds in the gas phase was determined by analysis of the ampoules taken. Two of them were analysed (one after the other in the same breaker) and the mean value was calculated. The standard deviation (i.e. measures the spread of data about the mean) of the molar flow on C-basis for each C-number was in the range $3.2 \cdot 10^{-6}$ and $1.1 \cdot 10^{-8}$ (worst and best case respectively). The higher standard deviation was observed in the range C_{17-20} (overlapping range with the wax analysis).

Tables 12.9-12.10 present an example of how both liquid and gas phase analysis are combined following Equations 5.6-5.10. The combination of the two analyses is presented in Figure 6.12.

Tab. 12.9: Example for combination of liquid and gas phase analyses: molar flows, CO conversion and CO_2 yield for FTS with Co/Al_2O_3 catalyst. Reaction conditions: T = 230 °C, p = 1 MPa, τ_{mod} = 4000 kg·s/m^3, $(p_{H2}/p_{CO})_{in}$ = 2.

$\dot{N}_{CO,in}$	mol/min	$4.41 \cdot 10^{-4}$	(at standard conditions)
X_{CO}	(-)	0.93	(calculated from TCD analysis)
Y_{CO2}		0.09	(calculated from TCD analysis)
$\dot{N}_{C,HC,out}$	mol/min	$3.71 \cdot 10^{-4}$	(calculated with Eq. 5.8)
$\dot{N}_{C,HC,ampoule}$	mol/min	$1.59 \cdot 10^{-4}$	(calculated from ampoule analysis)
$\dot{N}_{C,HC,wax}$	mol/min	$2.12 \cdot 10^{-4}$	(calculated with Eq. 5.10)
$\dot{N}_{C,HC,wax}$	mol/min	$2.31 \cdot 10^{-4}$	(calculated by weighting the wax accumulated in the wax trap, t = 24h)

Tab. 12.10: Example for combination of liquid and gas phase analyses: molar flows (on C-basis) for the hydrocarbons in the gas (ampoule) and liquid (wax) phase, total molar flow and hydrocarbon molar fractions for FTS with Co/Al_2O_3 catalyst. Reaction conditions: T = 230 ºC,
p = 1 MPa, τ_{mod} = 4000 kg·s/m^3, $(p_{H2}/p_{CO})_{in}$ = 2.

C-Number (-)	$\dot{N}_{C,HC,ampoule}$ mol/min	C-Number (-)	$y_{j,wax}$ (-)	$\dot{N}_{C,HC,wax}$ mol/min	C-Number (-)	$\dot{N}_{C,HC,out}$ mol/min	$\dot{N}_{HC,out}$ mol/min	y_{NC} (-)
1	3,25E-05	12	0,037	7,87E-06	1	3,25E-05	3,25E-05	5,09E-01
2	5,04E-06	13	0,035	7,51E-06	2	5,04E-06	2,52E-06	3,95E-02
3	9,76E-06	14	0,053	1,13E-05	3	9,76E-06	3,25E-06	5,09E-02
4	7,52E-06	15	0,055	1,17E-05	4	7,52E-06	1,88E-06	2,95E-02
5	1,51E-05	16	0,062	1,32E-05	5	1,51E-05	3,03E-06	4,74E-02
6	1,26E-05	17	0,064	1,36E-05	6	1,26E-05	2,10E-06	3,29E-02
7	1,36E-05	18	0,062	1,31E-05	7	1,36E-05	1,95E-06	3,05E-02
8	1,20E-05	19	0,062	1,31E-05	8	1,20E-05	1,50E-06	2,34E-02
9	1,15E-05	20	0,061	1,28E-05	9	1,15E-05	1,28E-06	2,00E-02
10	1,05E-05	21	0,060	1,27E-05	10	1,05E-05	1,05E-06	1,65E-02
11	9,56E-06	22	0,053	1,11E-05	11	9,56E-06	8,69E-07	1,36E-02
12	6,61E-06	23	0,043	9,18E-06	12	1,45E-05	1,21E-06	1,89E-02
13	4,76E-06	24	0,039	8,18E-06	13	1,23E-05	9,44E-07	1,48E-02
14	3,12E-06	25	0,037	7,84E-06	14	1,44E-05	1,03E-06	1,61E-02
15	1,92E-06	26	0,030	6,44E-06	15	1,36E-05	9,09E-07	1,42E-02
16	1,27E-06	27	0,028	5,92E-06	16	1,45E-05	9,03E-07	1,41E-02
17	6,98E-07	28	0,026	5,43E-06	17	1,43E-05	8,42E-07	1,32E-02
18	4,47E-07	29	0,022	4,69E-06	18	1,35E-05	7,51E-07	1,18E-02
19	2,70E-07	30	0,021	4,37E-06	19	1,34E-05	7,04E-07	1,10E-02
20	2,00E-07	31	0,018	3,84E-06	20	1,30E-05	6,51E-07	1,02E-02
		32	0,016	3,40E-06	21	1,27E-05	6,03E-07	9,45E-03
		...	...	...	...	...	...	...
		52	0,002	3,51E-07	52	3,51E-07	6,76E-09	1,06E-04
		53	0,001	2,65E-07	53	2,65E-07	4,99E-09	7,82E-05
Total	1,59E-04	Total	1,000	2,12E-04	Total	3,71E-04	6,38E-05	1,00E+00

12.9 Applications of zeolites as catalysts

Tab. 12.11: Oil refining and petrochemistry isomerisation processes catalysed by zeolites

Processes	Isomerisation of n-alkane				Isomerisation of n-alkene
	LSR naphtha	Separation n-/iso-alkane	long-chain alkane	$n-C_4H_{10}$	
Feedstock	$n-C_5-C_6$ (straight-run)	mixture n-/iso-alkane	middle distillate, lube oils	n-butane	n-alkene from catalytic or steam-cracking units
Product	Iso-C_5-C_6	Pure n-alkane	Isoalkane	Isobutane and fuel gas	Isobutene and isopentene
Objective	To boost the octane number of the unleaded gasoline pool	Increase the conversion of the LSR naphtha process [1, 3]	Improve cold-flow properties (pour / cloud / freeze point, viscosity)	To boost the octane number	Components for the MTBE or TAME production
T (°C)	240-280 (~ 250) [1, 2, 6]	150-270		300-400 [10, 11]	< 400 [2, 3]
p (MPa)	2-5 [1]	1.32 [5]		0.1[11, 12]	0.1-5 [12]
p_{H2} (MPa)	3 [3, 6]	-		-	-
Catalyst	bifunctional	5 A [1, 3, 5]	bifunctional [2,3]	bifunctional [3]	acid [2, 3, 8]
Metal (wt-%)	Pt, Pd (~ 0.2) [1, 3]	-	Pt [2,4]	Pt[4]	-
Zeolite	De-H-Mordenite Omega, Beta [2, 3]	Ca A [1,3]	Beta, (SAPO-11) [2,3]	H-Mordenite [3]	ZSM-22, Theta-1, ZSM-23, ferrierite [2, 3]
Reactor	Fixed bed [4]	5 columns in parallel [5]		Fixed bed [10, 11]	Fixed bed [7]
Commercial Processes	Shell (Hysomer) [1, 3, 6], Ipsorb Isom (Axens) [4], UOP (Penex) [4]	Union Carbide (now UOP, Isosiv) [3], Texaco (TSF), Leuna (Parex-Leuna), ELF (N-Iself) [5], Exxon and BP	Mobil, Chevron [2]	Commercial processes make use of $HCl/AlCl_3$ or $Pt/AlCl_3$ catalysts [3]	Lyondell (Isomplus) [4, 7, 8], Shell [10]
	UOP (Total isomerisation process, TIP) [1,3]				

[1] Maxwell 1987, [2] Corma et al. 2002, [3] Stöcker 2005, [4] Refining Processes 2002, [5] Ruthven 1984, [6] Bhatia 1990, [7] Weidert 2000, [8] Lyondell 2007, [9] Grandvallet et al. 1992, [10] Nieminen et al. 2005, [11] Yori et al. 1995, [12] Beech et al. 1995 [13] Maxwell et al. 1991 [14] Sie et al. 1991, [15] Leckel 2005, [16] Chang 1997, [17] Liebner et al. 2004, [18] Kvisle et al. 2002, [19] de Klerk 2006, [20] Knottenbelt 2002, [21] Chen et al. 1983.

Tab. 12.12: Oil refining and petrochemistry processes catalysed by zeolites

Processes	Isobutane alkylation	Catalytic reforming of nahptha	Catalytic cracking	Catalytic hydrocracking	Catalytic dewaxing	Alkylation of aromatics	Aromatization of $C_{2\text{-}4}$ alkanes
Feedstock	Isobutene, C_3-C_5 alkene	n-alkane and cyclohexane $C_{5\text{-}10}$	Vacuum gasoil	Heavy-oil fractions	Lubricating oil base stocks, gas oils	Aromatics and alkene	$C_{2\text{-}4}$ alkanes
Product	Alkylate (mainly C_{7+} iso-alkane)	High-octane iso-alkane and aromatics	Light alkene, gasoline, diesel	Naphtha, kerosene and gas oil	n-/iso-alkane with lower C-number	Ethylbenzene, cumene, alkylnaphthalene, alkylbenzene sulfonates	Aromatics
Objective	Increase RON	Increase RON	More valuable low-molecular-weight hydrocarbons	Higher middle distillate/gasoline ratio	Improve the cold-flow properties of the lubricating oil	Intermediates, fine chemicals and petrochemicals	Precursors compounds for the petrochem. industry, RON components
T (°C)	50-100 [2,3]	425-525 [3] (300-350)	~ 500 [3]	300-450 [2, 3]	~ 400 [3, 6]	380-450 [3]	< 500 for C_{3+} ~ 575 for C_{2+} [3, 13]
p (MPa)		3-5 [1]	0.3		2-5 [6]	2-3 [3]	0.2-1 [13]
p_{H2} (MPa)	present [4]	0.5-3.0 [3]	-	5-20 [2, 3]	250-450 m^3 H_2 / m^3 oil [6]		
Catalyst	acid	bifunctional	acid	bifunctional	acid	acid	bifunctional
Metal	-	Pt	-	Pt, Pd or Mo,W / Ni,Co [4]	-	-	Ga, Zn, Pt, Ag, Ni [2, 3]
Zeolite	REHY or H-Y H-EMT, H-Beta [2, 3]	Ba K-L, De-ZSM-12, Beta, Cs-Beta [3]	Y + matrix + additive (e.g. ZSM-5) [3]	USY, Al-MCM-41, mordenite, L, Omega, Beta [3]	ZSM-5, ZSM-11, ZSM-23, SAPO-11, Beta [3]	ZSM-5, Beta, ZSM-12, Y, MCM-22 [3]	Ga/H-ZSM-5, K-L [2, 3]
Reactor		Fixed bed [2, 3]	Fluid bed [6]	Fixed bed	Tricke bed [6]		Moving bed
Commercial processes	UOP Indirect Alkylation (InAlk) AlkyClean [4]	UOP, Chevron [1, 2, 3]	ExxonMobil, Kellogg Brown & Root, Inc., Shell, UOP, Stone & Webster Inc., [4]	UOP/Unocal (Unicracking), Chevron (Isocracking-Isomax), Shell, IFP [3]	ExxonMobile (MSDW), Chevron (Isodewaxing), Haldor Topsøe [3]	Mobil-Badger, ExxonMobil (EBMAX), Deltech Corp. [3]	BP/UOP Cyclar Process, Mobil M2 Forming process, Chevron AROMAX [3]

Tab 12.13: Natural gas upgrading / gas conversion processes catalysed by zeolites

Processes	Gas to liquids (GTL) - Hydrocracking	CO hydrogenation	Methanol to gasoline (MTG)	Ethanol to gasoline	Methanol to alkene		Alkene to gasoline or distillate		
					MTO	MTP	MOGD	COD	SPGK
Feedstock	FT-wax	Synthesis gas	Alkene from MTO	Ethanol from fermentation	Methanol	Methanol	C_{2-10} alkene [6]	C_{2-4} alkene [19]	C_{2-5} alkene [13]
Product	Middle distillate or gasoline	Hydrocarbons	Aromatics and alkanes (gasoline fraction)	Gasoline	Alkene (mainly propene and butane)	Mainly propylene	Middle distillate [a] or gasoline [b]	Middle distillate [20]	Middle distillate or gasoline
Objective	Increase diesel, gasoline selectivity	Production of chemicals and petrochemicals products [2]	Synthetic gasoline	Automotive fuels from fermentation products	Intermediate step of MTG or chemical products	Propylene for the petrochemical industry	Synthetic fuels	Synthetic fuels from HTFTS [20]	Synthetic fuels
T (°C)	300-350 [14]	~ 350 [2]	~ 400 [3, 13]	400 [6]	350-600 [16, 18]	470-515 [16]	190-310 [a] 290-375 [b]	150-350	200-280 [13]
p (MPa)					0.2-0.4 [16]	2-3.5 [16]	4-10 [a] 0.4-3 [b]	3.5-8.5	1-5 [13]
p_{H_2} (MPa)	3-5 [14]				-	-	-	-	-
Catalyst	bifunctional	bifunctional [2]	acid	bifunctional [6]	acid [18]	acid [3]	acid	acid	acid
Metal	NiMo [15]	Fe, Co, Pd [2]	-	Zn, Mn [6]	-	-	-	-	-
Zeolite	SiO_2/Al_2O_3 [15]	ZSM-5, Y [2]	ZSM-5 [3, 13]	ZSM-5 [6, 21]	(SAPO-34)[18]	H-ZSM-5, ZSM-34 [3]	H-ZSM-5 [6]	COD-9 [21]	H-mordenite [13]
Reactor	Tricke-flow [14]		Fluidised / fixed bed [3, 13]		Fluidised bed [18]	Fixed bed [17]	Fixed bed / fluidised bed	Fixed bed	
Commercial processes	Shell (SMDS), Sasol/Chevron, ExxonMobil (AGC-21) [3, 15]		Mobil [3, 13], Topsoe (TIGAS) [13]		UOP Nord Hydro (MTO) [3]	Lurgi (MTP) [3]	Mobil (MOGD) [6]	Mossgas (COD) [17, 20], Lurgi (Mt-Synfuels)	Shell (SPGK) [13]

Lebenslauf

Persönliche Daten

Name:	Alba Mena Subiranas
Geburtsdatum:	06.09.1980
Geburtsort:	Vic, Spanien
Staatsangehörigkeit:	spanisch
Familienstand:	ledig

Schulausbildung

1984 - 1994	Grundschule, Mittelstufe: Escola Segimon Comas Codinach, Sant Quirze de Besora (Spanien)
1994 - 1998	Oberstufe: Escola Sant Miquel dels Sants, Vic (Spanien)
Juni 1998	Abitur (Spanien)

Studium

1998 - 2003	Studium des Chemieingenieurwesens an der Universitat de Barcelona (Spanien)
2003	Diplomarbeit an der Universität Karlsruhe (TH)
2004 - 2005	Aufbaustudium der Betriebswirtschaftslehre an der Universitat Oberta de Barcelona, Fernuniversität
seit 2006	Studium der Ostasienwissenschaften an der Universitat Oberta de Barcelona, Fernuniversität

Berufstätigkeit

2004 - 2007	Wissenschaftliche Mitarbeiterin am Engler-Bunte-Institut der Universität Karlsruhe (TH), Bereich Gas, Erdöl und Kohle
seit 2008	Ingenieurin in der Gruppe Conceptual Process Design bei BASF SE, Ludwigshafen